TUNABLE NARROWBAND THOMSON SOURCE BASED ON A LASER-PLASMA ACCELERATOR

Dissertation
zur Erlangung des Doktorgrades
an der Fakultät für Mathematik, Informatik und Naturwissenschaften
Fachbereich Physik
der Universität Hamburg

vorgelegt von

MARTIN MEISEL

Hamburg
2023

Gutachter der Dissertation:	Dr. Jens Osterhoff
	Prof. Dr. Wolfgang Hillert
Zusammensetzung der Prüfungskommission:	Prof. Dr. Daniela Pfannkuche
	Dr. Jens Osterhoff
	Prof. Dr. Wolfgang Hillert
	Prof. Dr. Gudrid Moortgat-Pick
	Dr. Andreas Maier
Vorsitzende der Prüfungskommission:	Prof. Dr. Daniela Pfannkuche
Datum der Disputation:	28.04.2023
Vorsitzender Fach-Promotionsausschuss PHYSIK:	Prof. Dr. Günter H. W. Sigl
Leiter des Fachbereichs PHYSIK	Prof. Dr. Wolfgang J. Parak
Dekan der Fakultät MIN:	Prof. Dr.-Ing. Norbert Ritter

Martin Meisel: *Tunable Narrowband Thomson Source based on a Laser-Plasma Accelerator,* Dissertation zur Erlangung des Doktorgrades an der Fakultät für Mathematik, Informatik und Naturwissenschaften, Fachbereich Physik der Universität Hamburg,

ABSTRACT

A compact, high-energy, tunable, ultra-short pulse duration, narrowband X-ray source with high brilliance could unlock novel developments in a wide range of scientific and medical X-ray applications, such as **X**-ray **F**luorescence **I**maging (XFI) with **g**old **n**ano**p**articles (GNPs). Compared to light sources driven by large-scale radiofrequency-based accelerators, **T**homson **S**cattering (TS) sources based on electrons from a compact laser-plasma accelerator are a promising alternative for providing high-energy and high-quality X-ray beams. These could provide the necessary compactness for a future transition into clinical environments for many applications relying on X-ray radiation. Even though X-ray sources based on the combination of TS and **L**aser-**P**lasma **A**cceleration (LPA) have been demonstrated before, the X-ray spectral bandwidth was insufficiently narrow for XFI. LPAs driven by 10-TW class lasers typically produce electron bunches with multi-percent-level bandwidths and milliradians divergences. As a result, Thomson X-ray beam generation suffers from severe spectral broadening, resulting in X-ray beams with many tens of percent bandwidths that are impractical for most X-ray applications.

In a proof-of-principle experiment designed to mitigate these restriction, an **A**ctive **P**lasma **L**ens (APL) was utilised for focusing of the electron beam, allowing for tunable X-ray beams with reduced bandwidths to be produced. Without any changes to the electron bunch properties, only the focusing strength of the APL was varied to tune the X-ray beam energy between 34 keV and 81 keV. Beam imaging reduced the electron beam divergence and acted as a chromatic filter for the electron beam. Although an electron bunch with an initial FWHM energy spread of more than 100 % was used in the TS interaction, the average FWHM bandwidth of the generated X-ray beam was measured to be (25.6 ± 2.5) %. While the total bandwidth measured in this proof-of-principle experiment exceeds the typical requirements for novel X-ray applications, this bandwidth is no longer dominated by electron beam properties, as is usually the case for LPA-based TS sources. With further optimisation of the scattering laser in the TS interaction, the total bandwidth can be significantly reduced. The demonstrated bandwidth filtering Thomson source based on a laser-plasma accelerator with APL focusing is a key development that has the potential to be beneficial in a variety of compact X-ray applications and to enable their implementation outside of research environments.

ZUSAMMENFASSUNG

Kompakte, durchstimmbare Schmalband-Röntgenquellen, die hochenergetische und ultrakurze optische Pulse erzeugen, können neue Entwicklungen in wissenschaftlichen und medizinischen Röntgenanwendungen vorantreiben. Ein Beispiel für eine solche medizinische Anwendung ist die Bildgebung im menschlichen Körper mittels Röntgenfluoreszenz von Gold-Nanopartikeln. Typischerweise basieren die benötigten Röntgenquellen auf großflächigen Hochfrequenzbeschleunigern, was sie für medizinische Anwendungen in Krankenhäusern uninteressant macht. Im Gegensatz dazu sind Thomson-Röntgenquellen, die Elektronen aus kompakten Laser-Plasma-Beschleunigern verwenden, eine vielversprechende Alternative für die Bereitstellung hochenergetischer und qualitativ hochwertiger Röntgenstrahlen. Diese können die notwendige Kompaktheit für den Übergang vieler Anwendungen, die auf brillante Röntgenstrahlung angewiesen sind, in das klinische Umfeld bieten. Obwohl Röntgenquellen basierend auf der Kombination von Thomson-Streuung und Laser-Plasma-Beschleunigung bereits realisiert wurden, war die Bandbreite der resultierenden Röntgenstrahlenspektren nicht schmal genug für eine Anwendung wie die Röntgenfluoreszenz. Laser-Plasma-Beschleuniger, die von 10-TW Lasersystemen angetrieben werden, erzeugen typischerweise Elektronenstrahlen mit Energiebreiten im Prozentbereich und Divergenzen von einigen Milliradian. Infolgedessen leidet die Thomson-Röntgenstrahlerzeugung unter einer starken spektralen Verbreiterung, was zu Röntgenstrahlen mit Bandbreiten von mehreren zehn Prozent führt, die für viele Röntgenanwendungen unbrauchbar sind.

Um diese Einschränkungen zu beseitigen, wurde zum ersten Mal eine aktive Plasmalinse verwendet, um den Elektronenstrahl zu fokussieren, was zu einem durchstimmbaren Röntgenstrahl mit reduzierter Bandbreite führt. Ohne Veränderung an den Eigenschaften der Elektronenpakete wurde lediglich die Fokussierstärke der Plasmalinse variiert, um die Röntgenstrahlenergie zwischen 34 keV und 81 keV einzustellen. Die Fokussierung reduziert die Elektronenstrahldivergenz und wirkt als Energiefilter für den Elektronenstrahl. Obwohl die Thomson-Streuung unter Verwendung von Elektronenstrahlen mit FWHM-Energiebreiten von mehr als 100 % durchgeführt wurde, wurde die durchschnittliche FWHM-Bandbreite des resultierenden Röntgenstrahls mit (25.6 ± 2.5) % gemessen. Während die in diesem Experiment gemessene Gesamtbandbreite typische Anforderungen für neuartige Röntgenanwendungen

übersteigt, wird die Bandbreite nicht mehr von den Elektronenstrahleigenschaften dominiert, wie dies häufig bei derartigen Röntgenquellen der Fall ist. Durch eine weitere Optimierung des gestreuten Laserstrahls kann die Gesamtbandbreite deutlich reduziert werden. Die demonstrierte bandbreitengefilterte Thomson-Röntgenquellen auf Basis von Laser-Plasma-Beschleunigern mit Plasmalinsen-Fokussierung ist eine entscheidende Entwickelung, die das Potenzial hat, für eine Vielzahl kompakter Röntgenanwendungen nützlich zu sein und ihren Einsatz außerhalb von Forschungsumgebungen ermöglicht.

CONTENTS

LIST OF FIGURES

LIST OF TABLES

ACRONYMS

ADC **A**nalog-to-**D**igital **c**onverter

APL **A**ctive **P**lasma **L**ens

ASTRA **A** **S**pace Charge **Tra**cking **A**lgorithm

BOND **B**eam **O**ptimisation and **N**ovel **D**iagnostic

CCD **C**harged-**C**oupled **D**evice

CdTe **c**admium **t**elluride

C-S **C**ourant-**S**nyder

CPA **C**hirped **P**ulse **A**mplification

DaMon **Da**rk current **Mon**itor

DESY **D**eutsches **E**lektronen-**Sy**nchrotron

EMP **E**lectro**m**agnetic **P**ulse

FBPIC **F**ourier-**B**essel **P**article-**I**n-**C**ell

FEL **F**ree-**e**lectron **L**aser

FLASH **F**ree-electron l**as**er in **H**amburg

FLASHForward **F**uture-**OR**iented **W**akefield **A**ccelerator **R**esearch and **D**evelopment at FLASH

FWHM **F**ull **W**idth at **H**alf **M**aximum

GNP **g**old **n**ano**p**article

HEXITEC **H**igh **E**nergy **X**-ray **I**maging **Tec**nology

HG **H**ermite **G**aussian

HV **H**igh **V**oltage

ICT **I**ntegrating **C**urrent**T**ransformer

PEEK **P**oly**e**ther**e**ther**k**etone

LPA **L**aser-**P**lasma **A**cceleration

LySo lutetium-yttrium oxyorthosilicate

MHD **m**agneto-**h**ydro**d**ynamics

NP **n**ano**p**article

OAP **O**ff-**A**xis **P**arabolic mirror

PIC **P**article-**i**n-**c**ell

PFN **P**ulse-**F**orming **N**etwork

RMS **R**oot **M**ean **S**quare

RSS **R**esidual **S**um of **S**quares

SRSI **S**elf-**R**eferenced **S**pectral **I**nterferometry

TS **T**homson **S**cattering

Wake-T **Wake**field particle **T**racker

XFI **X**-ray **F**luorescence **I**maging

XPW Cross-Polarized Wave

1 INTRODUCTION

This story began when Heinrich Geissler invented the first gas discharge tube more than 150 years ago [1]. These early tubes paved the way for the development of products such as cathode ray tubes and X-ray sources. In particular, the discovery of X-ray radiation by W. C. Röntgen in 1895 [2] was followed by the development of first X-ray sources with clinical applications only one year later. Because of their short wavelengths, X-ray radiation can resolve structures at the atomic level and penetrate deep into or through materials, providing insight into opaque systems such as the human body. The development of powerful pulsed X-ray sources has attracted considerable attention in recent years due to the vast range of potential applications [3]. Novel applications for bright X-ray beams that require or benefit greatly from a narrow spectral bandwidth and tunable energies include radiation therapy [4], crystallographical applications [5], and advanced imaging modalities such as X-ray absorptiometry [6], fluorescence tomography [7], and K-edge imaging [8].

Another example of a novel medical X-ray application is the non-invasive method of **X**-ray **F**luorescence **I**maging (XFI) [9]. In XFI, small amounts of elements can be detected in a dedicated sample by observing the emitted characteristic X-ray photons after being excited with a suitable incident photon energy. To study samples in the human body, chemical elements with a high atomic number are functionalised with specific peptides and injected into an organism. These **n**ano**p**articles (NPs) follow the natural behaviour of the peptides and accumulate in certain regions of interest. After external irradiation, element-characteristic X-ray photons are emitted and can be detected to localise and quantify the NP concentration. The detection quality is highly dependent on the X-ray source used to excite the NPs. A suitable element for XFI is the noble metal gold [10–13], as it is non-toxic, chemically inert, and usually not present in the human body.

To perform XFI using **g**old **n**ano**p**articles (GNPs) in the human body, an X-ray beam with an incident energy of 90 keV and a **F**ull **W**idth at **H**alf **M**aximum (FWHM) spectral bandwidth of less than 15 % is required [14, 15]. As conventional X-ray tubes cannot provide X-ray beams with such narrow bandwidths and sufficient photon flux at these high energies, XFI is currently being investigated using large synchrotrons where the energy of the incident radiation can be precisely tuned [16]. However,

because these machines span hundreds of metres or more in circumference, they are unsuitable for use in a medical environment. The combination of **L**aser-**P**lasma **A**cceleration (LPA) and **T**homson **S**cattering (TS) is a possible solution, as it allows for the generation of high-energy, high-quality X-ray beams while significantly reducing their size compared to conventional accelerator-based X-ray sources.

TS describes the scattering of laser light and relativistic electrons to produce X-ray photons [17–19]. Such a type of light source is also driven by relativistic electron beams, which are typically provided by large-scale particle accelerators. As the maximum acceleration gradient achievable using radio-frequency technology is currently limited to about 100 MV/m [20], any reduction in size requires the use of novel acceleration techniques. Tajima and Dawson proposed the concept of LPA in 1979 [21], predicting acceleration gradients in excess of 100 GV/m. With developments in accelerator and laser technologies, LPA became experimentally accessible with high-power laser pulses of sufficiently short pulse duration using a technique known as **C**hirped **P**ulse **A**mplification (CPA) [22]. Using LPA, electron beams with GeV energies can now be produced in cm-scale plasma structures, matching the compactness required for an X-ray source in a medical environment.

Even though X-ray sources based on the combination of TS and LPA have been demonstrated before [23–28], they have lacked sufficiently narrowband spectra for XFI with GNPs. While LPA has the potential to generate high-quality electron beams, energy spreads of several percent and beam divergences of the order of a few milliradians are typically reported when using 10-TW class lasers [29–36]. The extent of this beam divergence, as well as the large energy spread compared to radio-frequency-based accelerators, are the primary causes of broad Thomson X-ray spectra on the order of tens of percent. In the context of this thesis, an **A**ctive **P**lasma **L**ens (APL) has been utilised to gain control over the radiated X-ray beam energies, reduce its spectral bandwidth and relax the requirements on the electron bunch parameters. APLs were first recognised by Panofsky and Baker in 1950 [37] and were demonstrated on ion beams in 1991 [38]. They were proposed by Tilborg et al. in 2015 for focusing LPA electron beams [39] and have attracted more interest in modern particle acceleration owing to their unique advantages. An APL is able to provide azimuthally symmetric focusing for charged particle beams with magnetic field gradients on the order of kT/m, setting them apart from conventional beam-optic elements such as quadrupole magnets and solenoid magnets. Therefore, it allows for compact beamline designs and is well suited for independently controlling the electron bunch properties in a scattering interaction.

Following the theoretical work of [40, 41], a tunable Thomson source based on a laser-plasma accelerator has been set up as a proof-of-principle experiment. The structure of the thesis is as follows: Pt. I discusses the concepts of LPA as well as the experimental structures used to generate the electron beams required for the subsequent Thomson source. The electron beams are characterised in terms of their beam profile and beam divergence. Another feature that indicates the quality of an electron beam is the beam emittance, which refers to the volume occupied by the beam in the space spanned by the electrons' position and momentum. Modern light sources require sub-µm normalised electron emittances, and their measurement is crucial for the successful development and optimisation of the Thomson source. Part II introduces the APL, which is used to study the beam emittance and measure the electron energy spectrum. Furthermore, it is an essential component of the TS setup. Part III explains the principles of TS and describes the development of the tunable Thomson source. The mean X-ray energy and spectral bandwidth contributions of the X-ray source are investigated. Finally, Sec. 11 provides a summary of the work as well as an outlook for future experiments based on the results.

Part I

LASER-DRIVEN ELECTRON BEAM SOURCE

X-ray light sources, such as synchrotrons or **F**ree-**e**lectron **L**asers (FELs), are driven by relativistic electron beams with energies in the GeV range. Usually, the electron beams are generated in conventional accelerators based on radio-frequency microwave cavities, which have acceleration gradients of up to 100 MV/m limited by structural breakdowns [20]. As a result, such machines require tens of meters of accelerating structures in order to achieve GeV-scale electron beam energies. Plasma-based accelerators, on the other hand, are of great interest due to their ability to sustain extremely large acceleration gradients and currents. They can support fields in excess of 100 GV/m and thus provide a method for producing GeV energy gain in cm-scale plasma structures [42]. The possibility to construct such electron beam sources in a compact manner allows for the compactness of the proposed Thomson source for X-ray generation.

The purpose of this part is to present the experimental structures and fundamentals used to generate electron beams for the subsequent realisation of a Thomson source. For that, the theoretical basics of plasmas and plasma acceleration are described in Sec. 2. Section 3 describes the laser system used in the experiments as well as the experimental laboratory, where the **L**aser-**P**lasma **A**cceleration (LPA) experiments were carried out. Finally, Sec. 4 discusses the electron generation from the LPA source.

2 PLASMAS AND ACCELERATION

2.1 PROPERTIES OF PLASMAS

A plasma is a state of matter in which charged particles remain in an unbound state but for which they cannot be referred to as free particles. However, not any ionised gas can be called a plasma. For the use of plasmas for a plasma accelerator, it is practical to define plasma as a quasi-neutral gas of charged and neutral particles which exhibits collective behaviour [43]. These collective effects, which underlie the following definition, ultimately allow for electron acceleration in a plasma-based accelerator. On the basis of [43–45], the defining properties of plasmas are explained below.

2.1.1 Debye Shielding

Free charge carriers can shield the electric fields from other charged particles in a plasma, making it appear electrically neutral on large scales. The Debye length is a measure of length at which charges shield each other and the electric potential drops to $1/e$. It is defined as [45]

$$\lambda_D = \sqrt{\frac{\epsilon_0 k_B}{e^2}\left(\frac{n_e}{T_e} + \sum_i^N \frac{Z_i n_i}{T_i}\right)^{-1}}, \tag{2.1}$$

with the vacuum permittivity ϵ_0, the elementary charge e and the Boltzmann constant k_B. n_e and T_e specify the electron density and temperature, respectively. Similarly, n_i and T_i describe the ions' density and temperature. N represents the number of ion types, with each ion having a charge of Z_i. Due to shielding, the plasma appears quasi-neutral on scales where $L \gg \lambda_D$. This also implies that the total size of an ionised gas must be larger than its Debye length in order for it to behave collectively and be treated as a plasma.

A measure for the number of particles of species x with density n_x in a Debye sphere with radius λ_D is given by [43]

$$\Lambda = \frac{4\pi}{3} n_x \lambda_D^3. \tag{2.2}$$

The plasma parameter Λ allows us to distinguish between two cases. $\Lambda \ll 1$ corresponds to a barely populated Debye sphere, where particles couple strongly and there is no collective behaviour because scattering dominates their motion. A plasma with $\Lambda \gg 1$, on the other hand, is called weakly coupled because the Debye sphere is densely populated and collective behaviour outweighs scattering processes. Only the second, weakly coupled, case is considered to be a plasma [44, 46].

2.1.2 Plasma Frequency

As previously stated, there is no electric screening effect on length scales less than λ_D. As a consequence, an infinitesimal displacement δx of an electron results in a restoring force from the ion background. According to [44], the electric field inside the plasma is calculated using the Poisson equation and is represented by

$$E_0 = \frac{e}{\epsilon_0} n_e \, \delta x. \tag{2.3}$$

Owing to this field, the displaced electron tends to its equilibrium state as its motion is described by

$$m_e \frac{d^2}{dt^2} \delta x = -eE_0, \tag{2.4}$$

where m_e is the rest mass of an electron. By inserting Eq. 2.3 into Eq. 2.4 the equation of motion reads as

$$\frac{d^2}{dt^2} \delta x + \frac{e^2 n_e}{m_e \epsilon_0} \delta x = 0. \tag{2.5}$$

Therefore the electrons follow the differential equation of a harmonic oscillator. The solution to this is a harmonic oscillation with the natural frequency

$$\omega_p = \sqrt{\frac{e^2 n_e}{m_e \epsilon_0}}, \tag{2.6}$$

which is referred to as plasma frequency. The fundamental time scale on which collective plasma effects occur is defined by the inverse plasma frequency. The plasma wavenumber defined by $k_p = \omega_p / c$ is a commonly used quantity in this context.

2.1.3 Criteria for Plasmas

To summarise the above-mentioned plasma concepts, an ionised gas must meet the three following conditions in order to be considered a plasma [43]:

1. Quasi-neutrality, which means that the Debye screening length must be greater than the plasma's length scale ($\lambda_D \ll L$).
2. Collective interactions must dominate over single-scattering events ($\Lambda \gg 1$).
3. The frequency of typical collective plasma behaviour must dominate over the mean time τ between collisions with neutral atoms ($\omega_p \tau > 1$).

2.2 PLASMA ACCELERATION BASICS

When an intense laser beam interacts with plasma, extremely high electric fields can be generated, which can be used to accelerate electrons. Tajima and Dawson proposed this concept of LPA in 1979 [21], and it became experimentally accessible with high-power laser pulses of sufficiently short pulse duration using a technique known as **C**hirped **P**ulse **A**mplification (CPA) [22]. The theory of LPA will be presented below. For a more detailed introduction on the subject refer to standard literature such as [21, 47, 48].

Modern laser pulses exceed intensities of $10^{18}\,\mathrm{W/cm^2}$ when focused down to spot sizes of tens of µm. When such an intense laser pulse passes through a plasma, the ponderomotive force $\mathbf{F}_p$ on the plasma electrons is non-negligible and displaces them along the negative intensity gradient. For an electron with rest mass m_e the ponderomotive force is given by [47]

$$\mathbf{F}_p = -m_e c^2 \boldsymbol{\nabla} a^2/2, \tag{2.7}$$

where c denotes the speed of light and a describes the normalised vector potential of the laser pulse averaged over one laser cycle. The normalised vector potential peak a_0 is also known as laser strength parameter, and it relates to the peak laser intensity as

$$a_0 \simeq 0.85 \cdot \lambda(\mu\mathrm{m}) \sqrt{I_0 (10^{18}\,\mathrm{W/cm^2})}, \tag{2.8}$$

where λ is the laser wavelength. While the plasma electrons are pushed away from the propagation axis of the laser pulse, the plasma ions remain stationary on the relevant time scale due to their much higher mass. When the laser pulse has passed, the electrons will be pulled back by the Coulomb force. This causes electrons to oscillate with the plasma frequency from Eq. 2.6. A plasma wave is formed by the charge separation and subsequent oscillation that occurs behind the laser pulse. The fields carried by this plasma wave are termed wakefields. The length of the cavity

thus formed is described by the plasma wavelength $\lambda_p = 2\pi c/\omega_p$ and depends on the plasma density as

$$\lambda_p(\mu m) \simeq 33/\sqrt{n_e(10^{18}\,cm^{-3})}. \tag{2.9}$$

Due to the charge separation, high electric fields are generated. The electric field that a plasma can sustain before it breaks down can be described in the cold non-relativistic wave-breaking limit as [47]

$$E_0(V/m) = \frac{cm_e\omega_p}{e} \simeq 96\sqrt{n_e(cm^{-3})}. \tag{2.10}$$

For example, an electron density of $n_e = 10^{18}\,cm^{-3}$ results in an accelerating field of $E_0 \simeq 96\,GV/m$, which is approximately three orders of magnitude greater than what is obtained in conventional accelerators. In addition, Eq. 2.9 results in a plasma wavelength of about 33 µm. Therefore, an electron bunch accelerated in such a wake-field has an intrinsic pulse duration on the fs-level. The electric fields described so far serve to accelerate electrons when they are in the correct phase.

Figures 2.1 and 2.2 depict examples of generated electron densities with their corresponding electric fields driven by a laser pulse, which were calculated using a **P**article-**i**n-**c**ell (PIC) code. PIC codes can be used to simulate the interaction of charged particles and electromagnetic fields, making them a powerful tool of studying plasma-based acceleration. In this case, **F**ourier-**B**essel **P**article-**I**n-**C**ell (FBPIC) [49, 50] is used to simulate a laser pulse with a normalised vector potential of $a_0 = 0.5$ driving a linear plasma wave, resulting in the electron density shown in Fig. 2.1a. For more informations about FBPIC refer to Sec. 10.1.2. In a flat plasma density the plasma electrons are pushed away from the axis directly behind the laser pulse, resulting in a positive longitudinal electric field that is decelerating for electrons (see Fig. 2.1b). As the electron density increases further behind, the longitudinal field becomes negative, implying that the wake is accelerating. In the linear regime ($a_0 < 1$), a sinusoidal shape can be used to estimate the longitudinal wave. In addition, as shown in Fig. 2.1c, transversely focusing fields occur in regions with low electron density. Only in regions with both accelerating and focusing fields can an electron bunch be accelerated while being tightly focused. The simulation reveals longitudinal accelerating fields of up to 8 GV/m for $a_0 = 0.5$. However, when the laser pulse has a normalised vector potential of $a_0 = 2$, stronger density perturbations occur, and a non-linear plasma wave with accelerating fields of up to 100 GV/m forms (see Fig. 2.2). Since nearly all electrons are pushed away from the axis, this non-linear regime ($a_0 \gg 1$) is also known as the bubble regime [51].

Electrons can be accelerated to energies in the GeV range in cm-scale plasma structures using such LPA techniques. However, several mechanisms, including laser

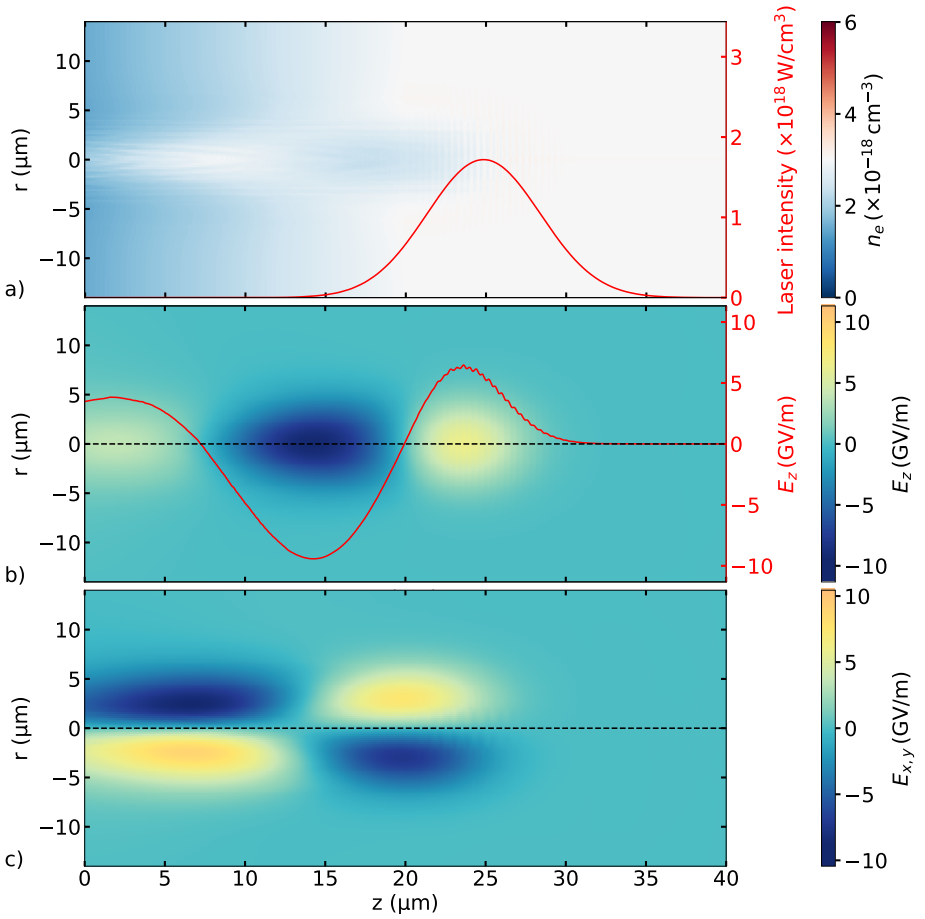

Figure 2.1: FBPIC is used to simulate a laser pulse with a normalised vector potential of $a_0 = 0.5$ driving a linear wakefield in a plasma with a density of 3×10^{18} cm^{-3}. (a) depicts the resulting electron density in the plasma as well as the on-axis intensity of the laser pulse (red line). The charge separation produces a longitudinal electric field, shown in (b) with the on-axis lineout (red line). The resulting transversal electric field is shown in (c).

diffraction, electron dephasing, pump depletion, and laser-plasma instabilities, can limit the energy gain [47]. The dominant effects for LPA are energy depletion and dephasing. Energy depletion means that the laser pulse loses energy when driving the wakefield, and this leads to a weaker wakefield due to the weaker laser pulse. Dephasing comprises the fact that the accelerated particles are relativistic and hence travel at the speed of light c, but the driving laser pulse holds a phase velocity smaller than c while penetrating the plasma. Over time, the particles leave the desired phase for acceleration and might even get decelerated in the worst case. For more information on the limiting factors in LPA refer to the aforementioned literature.

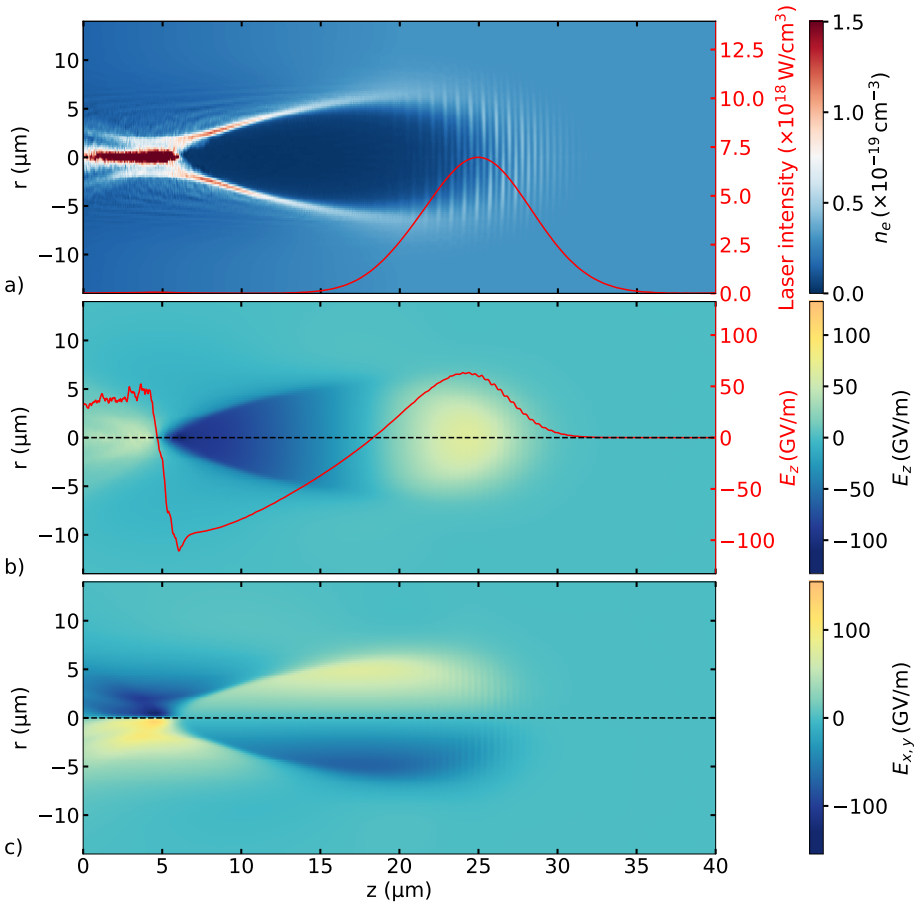

Figure 2.2: FBPIC is used to simulate a laser pulse with a normalised vector potential of $a_0 = 2$ driving a non-linear wakefield in a plasma with a density of $3 \times 10^{18}\,\mathrm{cm}^{-3}$. (a) depicts the resulting electron density in the plasma as well as the on-axis intensity of the laser pulse (red line). The charge separation produces a longitudinal electric field, shown in (b) with the on-axis lineout (red line). The resulting transversal electric field is shown in (c).

2.3 IONISATION INJECTION

Section 2.2 explains the acceleration, but an electron initially at rest might just get passed by the plasma wave and not necessarily get dragged along. In order to accelerate an electron bunch, it needs to be injected into the wakefield. Electrons are considered injected in a flat plasma density when they are situated at the accelerating phase of the wakefield and their longitudinal velocity matches the phase-velocity of the wakefield, which is defined by the laser pulse's group-velocity. In an experiment, a bunch can either be externally [52] or internally injected into the plasma wakefield. For example, plasma electrons at the bubble's end can collide and scatter into the

cavity, allowing them to be trapped. This is known as self-injection and occurs in the highly non-linear regime where $a_0 \gg 1$. It is a highly statistically dominated mechanism that typically results in unstable electron beam properties [53, 54].

A controlled injection is required for a reliable electron beam source. The electron beam source discussed in Sec. 4 is based on an injection technique called ionisation injection [55–57]. A low atomic-number gas, such as hydrogen or helium, is doped with a higher atomic-number gas, such as nitrogen. The low-atomic-number gas has a low ionization threshold and is fully ionised even at moderate laser intensities, forming background plasma. Meanwhile, the inner-shell electrons of the higher-atomic-number gas species require higher laser intensities to ionise, which are only present near the laser pulse's peak intensity. Since the ponderomotive force is proportional to the gradient of the laser intensity, electrons ionised around the intensity peak experience a weaker transverse kick. These inner-shell electrons are ionised directly on the laser axis where they fall back into the accelerating phase and can become trapped in the plasma cavity. However, the inner-shell electrons are passing through the laser-field and gain additional transverse momentum. As a result, ionization injection typically results in higher beam emittances [58]. This effect is particularly noticeable in the laser's polarisation axis, leading to elliptical beam profiles of the electron bunch. Another characteristic of this injection scheme is that it continues as long as the laser peak intensity is sufficient to ionise the required higher ionization states. This results in a higher bunch charge but also a broad electron energy spectrum originating from the difference in the total accelerating length depending on the position of injection. Controlling the injection duration is required for the generation of narrower electron energy spectra. A more localised injection can be achieved by using using two stages [34] or using multiple laser pulses [59, 60]. Other examples of schemes with localised injection are self-truncated ionisation injection [61, 62] and shock-front injection[35, 63, 64].

In general, electron injection for acceleration in a plasma cavity is considered complex because it relies on non-linear mechanisms. Even minor changes in the laser pulse or plasma parameters can cause instabilities in the electron beam parameters. The laser intensity, for example, influences both electron injection and the electric fields in the plasma cavity. As a result, shot-to-shot fluctuations or use of a decreased laser intensity can degrade the electron beam quality.

3 EXPERIMENTAL OVERVIEW

The theoretical and experimental studies were performed at **D**eutsches **E**lektronen-**S**ynchrotron (DESY) in Hamburg, Germany. Two laboratories were available for this purpose, namely a laser laboratory and an acceleration laboratory, called **B**eam **O**ptimisation and **N**ovel **D**iagnostic (BOND) laboratory. A floor plan of both laboratories together with the control room is shown in Fig. 3.1.

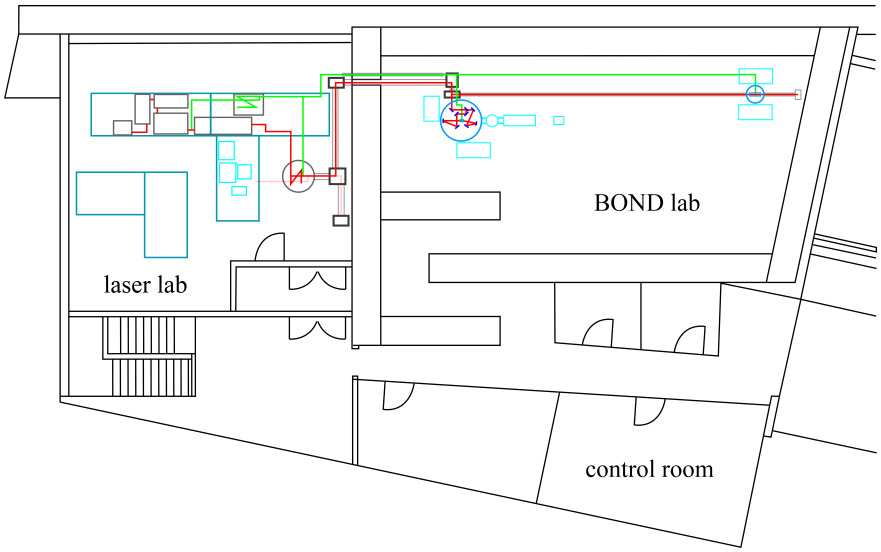

Figure 3.1: Layout of the laser laboratory housing the laser system and the BOND laboratory where the LPA and X-ray generation studies were set up. The laser beam path of the main laser beam is indicated by the red line, and the green line shows an additional probe laser beam. The experiments in the BOND laboratory were monitored and conducted from the control room. The drawing is adapted from [65]

The experiment's laser system is situated in the laser laboratory and can be used in the BOND laboratory for LPA experiments. It is shared with the **F**uture-**OR**iented **W**akefield **A**ccelerator **R**esearch and **D**evelopment at FLASH (FLASHForward) experiment. FLASHForward focuses primarily on studies involving beam-driven plasma-wakefield acceleration [66, 67]. Despite the author's contribution to various experiments of FLASHForward [66, 68, 69], these will not be elaborated on since they are beyond the scope of this thesis. The objective of this thesis is to describe work on

a proof-of-principle X-ray source for **X**-ray **F**luorescence **I**maging (XFI) within the PLASMED-X collaboration [14–16]. The experiment relied on various experimental components and diagnostics to run and set up. This section provides an overview of the key components for comprehending and carrying out the experiment.

3.1 LASER SYSTEM

To drive an LPA electron source, laser systems with intensities of $10^{18}\,\mathrm{W/cm^2}$ or higher are vital. Only after the advances in laser technologies in recent decades have these intensities become available. Particularly important is the method of generating high-intensity, ultra-short optical pulses with a technique called CPA. It was first introduced by Strickland and Mourou in 1985 [22] and they were awarded the Nobel Prize in 2018 in Physics.

Such high intensities cannot be produced directly by laser beam sources because non-linear optical effects would first destroy the laser beam quality and, eventually, the laser's amplifying medium. Since the temporal and spectral profiles of the laser pulse are related to each other through Fourier transformations, the bandwidth and pulse duration are linked to each other, so that a short pulse requires a large spectral bandwidth and vice versa [70]. The minimal **F**ull **W**idth at **H**alf **M**aximum (FWHM) bandwidth of a Gaussian laser pulse with a FWHM pulse duration of 25 fs and 800 nm is 38 nm. Because the pulse cannot be compressed temporally further without increasing its bandwidth, this minimal bandwidth is referred to as Fourier-limited. CPA works by reducing the peak power of a spectrally broad laser pulse before further amplifying it. To reduce the peak power, a short laser pulse is stretched by several orders of magnitude using dispersive elements, such as a grating pair. The stretched laser pulse can then be amplified without causing non-linear optical effects that degrade the laser beam quality. Following the final amplification, the pulse is recompressed, e.g. by another grating pair, resulting in a short pulse with a high peak power. For more details on ultra-short laser pulses refer to [70–72].

The laser laboratory is shown in Fig. 3.1. It houses a 25 TW, 800 nm Titanium:Sapphire laser system from Amplitude Technologies, which employs the CPA scheme. The main components are encased on a 2 m by 10 m optical table. Within the laser system, gratings are used to stretch the initially spectrally broad laser pulses before they pass through multiple amplification stages. Before the final amplification stage, a beam splitter divides the laser beam into a main laser beam and a secondary laser beam. The secondary laser beam, also known as the probe laser beam, contains 20 % of the

original pulse and is compressed in air by its separate grating pair, yielding a 3.5 mJ pulse with a FWHM duration of 25 fs. The remaining 80 % of the main laser beam is amplified by the final amplification unit, resulting in a pulse energy of up to 900 mJ. Because of the resulting high peak power, it is then compressed by gratings in a vacuum chamber. Both, the main- and the secondary laser beams can be sent into the BOND laboratory separately for experiments. The main laser beam is used to drive the LPA as well as as a scattering laser beam for the targeted all-optical driven X-ray source.

3.2 THE LASER–PLASMA ACCELERATION CHAMBER

Each LPA experiment takes place in the chamber illustrated in detail in Fig. 3.2. Here, it is a 1.4 m diameter vacuum chamber that houses the setup for the electron source. It includes a focusing **O**ff-**A**xis **P**arabolic mirror (OAP), a plasma target and several diagnostic facilities, motors and stages for alignment. In addition, all key components of the X-ray source from Pt. III are located within.

After final compression, the main laser beam, also known as the LPA laser beam, is transported into the experimental chamber and then focused by a 3" OAP with a focal length of 500 mm onto a 1 mm-diameter gas-jet nozzle [74]. The pulse front of the high-intensity laser pulse will generate plasma in the gas stream. Electrons can be injected and accelerated to travel in the same direction as the laser beam if done correctly. After a drift of 7.4 cm, an **A**ctive **P**lasma **L**ens (APL) [39, 75] can be driven into the beamline to capture and image the electron bunch. It is mounted on a vacuum-compatible hexapod, which allows for alignment and positioning in all three translational and rotational directions. The APL's **H**igh **V**oltage (HV) discharge cables are fed into the vacuum chamber via a dedicated APL HV feedthrough. Among other things, the APL can be used for emittance measurements [76] (see Sec. 7) and is a key component of the X-ray source [14, 77] (see Pt. III). Section 6 contains more information on the setup with the APL and its principles.

The gas load from the gas-jet was initially a limiting factor on the repetition rate of the LPA source in this setup. The ambient pressure in the compressor chamber must be kept below 10^{-4} mbar to protect the gratings and mirrors in the vacuum compressor from damage caused by the high-intensity laser beam. The APL, in addition to the gas-jet, contributes to the total gas load because it operates with a continuous gas flow. Therefore, a differential pumping system was installed in the chamber for both the gas-jet and the APL. The gas-jet is contained in a differential pumping cube, the top of

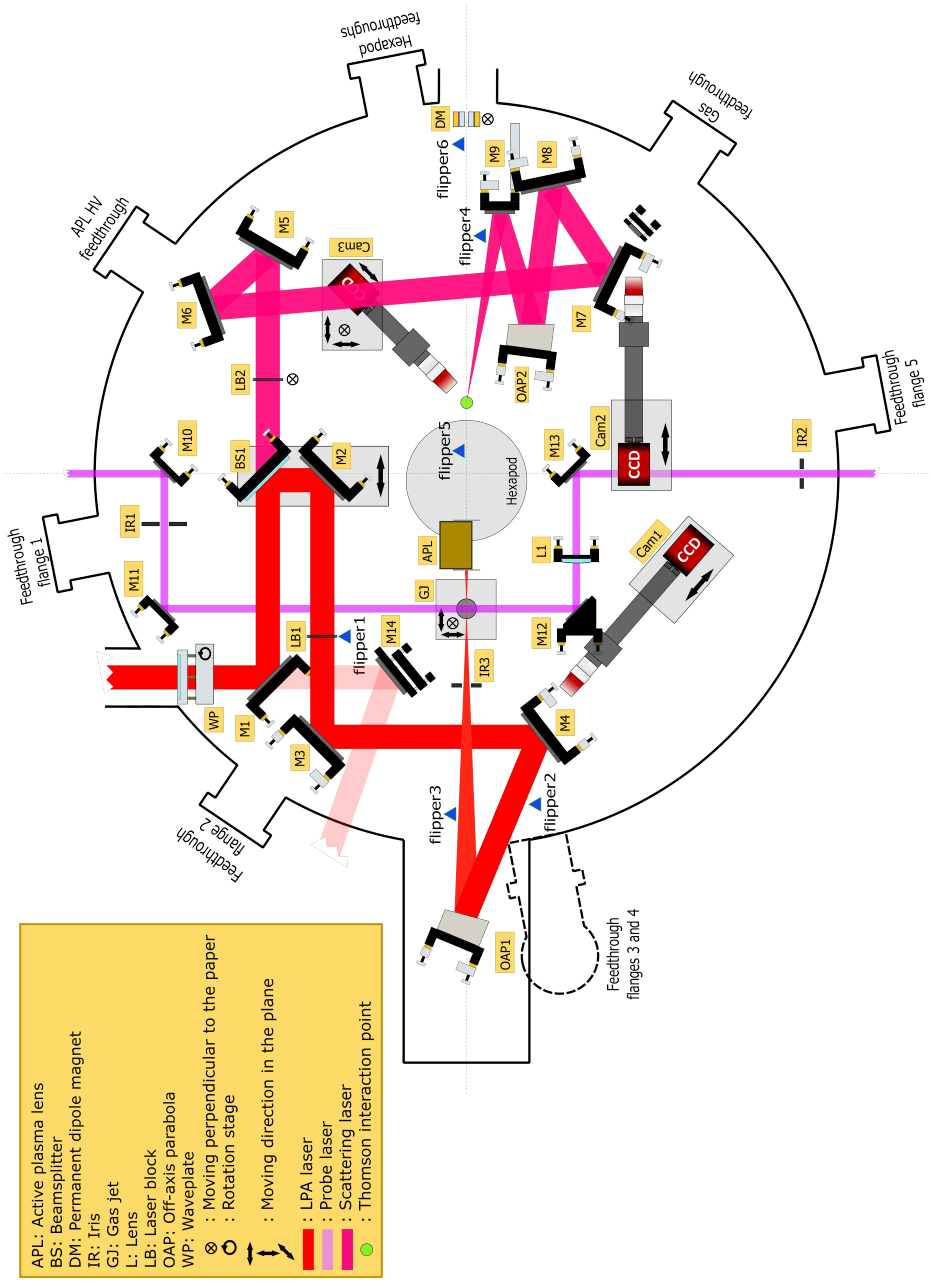

Figure 3.2: Sketch of the LPA chamber housing the beam paths of three laser beams. The LPA laser beam (red) is focused onto the gas jet labelled as GJ to create a plasma and drive the electron source. There, the probe laser beam (purple) passes transversely through the plasma channel as a part of the plasma density measurement. The active plasma lens is situated on the edge of a Hexapod next to the electron source. It is a key component for both the emittance measurement and the TS experiment, and will be discussed further in Pt. II. The beam splitter in the path of the LPA laser beam allows a part of its laser power to be split into the scattering laser beam (pink) which can be focused onto the Thomson interaction point (green disc). The vacuum-compatible cameras CAM1 and CAM2 can be used to image the focal spots of the LPA and scattering laser beam respectively. Camera CAM3 is mounted together with the spatial and temporal diagnostics to overlap the scattering laser beam with the electron beam. Part III discusses the scattering laser beam and its diagnostics, which are used to drive the TS process. Drawing adapted from [73].

which is connected to a large external pump. The cube has a 4 mm diameter entrance hole to in-couple the laser beam and a 7 mm diameter opening to out-couple the laser- and electron beam. The cube's bottom is connected with flexible bellows, allowing the gas-jet to move along the longitudinal and transversal axes relative to the laser beam. Special pockets in the APL sapphire slabs are pumped differentially by connecting them to the same external pumping line (see Sec. 6.3.2.2). In the experiment, the APL was run in continuous flow mode with pure argon at a backing pressure of < 0.1 mbar. The gas-jet used a 99.5 % helium with 0.5 % nitrogen dopant gas mixture by weight and operated at a backing pressure of (3.52 ± 0.08) bar at 1.4 Hz. To ensure a stable gas flow condition, the gas-jet was opened for 5 ms and the laser beam was fired 4 ms after its opening. In this mode of operation, the differential pumping system kept the ambient pressure in the interaction chamber around 3×10^{-3} mbar while keeping the ambient pressure in the vacuum compressor below 2×10^{-5} mbar. This system was also tested to run the gas-jet at the laser system's full repetition rate of 10 Hz while maintaining acceptable chamber pressures, removing the setup's limit on the gas load.

The differential pumping cube has two windows to let the probe laser beam, i.e. the secondary laser beam, pass the plasma transversely (compare with Fig. 3.2). The probe laser beam is transported outside the chamber and sent to a Mach-Zehnder interferometer. There, a part of the probe laser beam that traveled through plasma interferes with a part of the laser beam that only traveled through vacuum. The longitudinal plasma density can be reconstructed from the interference pattern [78–81].

For the design of an all-optical X-ray source on the basis of **T**homson **S**cattering (TS) (see Pt. III), a fraction of the main laser beam was used as the scattering laser beam. The 5 mm thick magnesiumfluorid beam splitter BS1 reflects two-thirds of the total laser energy into the LPA laser beam while transmitting the other one-third into the scattering laser beam. The beam splitter, as well as an additional mirror, are located on a stage to allow for femtosecond temporal alignment between these two laser arms. A 3" OAP with a focal length of 500 mm focuses the scattering laser beam, while the folding mirror M9 redirects the laser beam focus onto the electron-laser interaction point. Together with camera CAM3, the diagnostics for temporal and spatial overlap are located on three motorised stages, allowing movement in all three directions. For details on the scattering arm and the overlap diagnostics refer to Sec. 9.

3.3 DIAGNOSTICS

Several diagnostic facilities and references are required to conduct a meaningful LPA experiment. This section presents the essential diagnostics of the laser pulse and the electron bunch in order to understand the context of this thesis.

3.3.1 Laser Diagnostics

The laser system was described in Sec. 3.1. Regular maintenance and optimisation are required for its daily operation, which demands several diagnostics for monitoring and characterization of the laser pulses. For example, several near- and far-field cameras are set up to measure the position and pointing of the laser beam within the beamline. This section describes the diagnostics for critical laser parameters to drive a laser-wakefield accelerator, which will also be required as input for realistic simulations.

3.3.1.1 *Laser Pulse Energy in Interaction*

The very high laser intensity gradient, as explained in Sec. 2.2, is what drives the wakefield in a plasma and requires measurement of laser pulse energy, pulse duration and focal spot size for its quantification. Using a commercial energy meter, the maximum output energy after the final amplification stage and before compression was measured to be 814 mJ, with a **R**oot **M**ean **S**quare (RMS) stability of 1.0 % of 1000 consecutive laser shots. However, due to losses in the beamline and not operating the laser system at full power, the actual pulse energy on target was lower. A pre-interaction diagnostic is set up for this purpose, which uses the leakage laser light of the first mirror M1 in the LPA chamber (compare Fig. 3.2). The laser light is imaged on a near- and far-field $12-$bit **C**harged-**C**oupled **D**evice (CCD) camera to check the alignment into the vacuum chamber. By measuring the laser energy of the LPA laser beam directly in front of the plasma target with an energy meter, the near-field camera image was calibrated for laser pulse energy. Analogously, before the interaction point, the energy of the scattering laser beam was measured and calibrated to the same camera image. The pulse energy of both laser beams can thus be obtained with a relative error of about 3.5 % by processing the near-field camera image.

Within the pre-interaction diagnostic, a fast photo diode is also installed and connected to an **A**nalog-to-**D**igital **c**onverter (ADC). It allows the laser beam timing at the position of the APL to be measured relative to its discharge profile, which is

assumed to have the same timing as the electron beam. To obtain the correct relative timing, identical cables were used to transport both signals to the ADC, and the total path difference between the laser signal at the photo diode and the APL was taken into account. The discharge current experienced by the electron beam in the APL can thus be obtained in this manner. Section 6.3.2.1 contains more information on the discharge current system.

3.3.1.2 *Laser Pulse Duration*

The pulse duration is another factor that influences the intensity of a laser pulse. A Dazzler [82] is included in the laser system to modify the shape of the optical beam and control the pulse duration. Dazzlers are pulse shaping systems that use an acousto-optic programmable filter. They enable independent and simultaneous spectral phase and amplitude programming of ultra-fast laser pulses. As a result, they allow the dispersion of later parts of the laser system chain to be compensated for.

The Dazzler can be used to manipulate the pulse shape, but a Wizzler [83] was used to measure its duration. It is located on the pre-interaction diagnostic table. By using a flip mirror before the OAP of the main laser beam, some laser light can be sent through a 1 mm thin vacuum window and transported into the Wizzler. It can provide a complete characterisation of a single ultra-short pulse by measuring the laser pulse duration using **S**elf-**R**eferenced **S**pectral **I**nterferometry (SRSI) [84]. In the Wizzler, the main pulse generates a replica via Cross-Polarized Wave (XPW) generation [85]. XPW generation is a third-order non-linear effect that produces a linearly polarised wave with orthogonal polarisation relative to the input wave. The temporal amplitude $E_{XPW}(t)$ of the XPW pulse is linked to the input temporal amplitude $E_{IN}(t)$ via

$$E_{XPW}(t) \propto |E_{IN}(t)|^2 \cdot E_{IN}(t). \tag{3.1}$$

Because the XPW effect acts as a temporal filter, the XPW pulse is shorter and therefore has a broader spectrum with a flatter phase than the input pulse. The replica and XPW pulses are both sent to a spectrometer, which measures an interference signal. This is known as SRSI, and it delivers the spectral phase and amplitude of the pulse in a single beam iteratively. Because the XPW process is sensitive to chirp, this technique only works for input pulses close to the Fourier-limit of < 50 fs. It is a stand-alone piece of hardware that can be linked to the Dazzler and provide laser-phase information. The Wizzler software uses feedback loops to optimise the pulse in seconds and enables the measurement of the pulse duration at 10 Hz. After optimising the main laser pulse with the Wizzler, a pulse duration of about (27.6 ± 0.3) fs was obtained. Figure 3.3 depicts the Wizzler measurement for 1000 consecutive laser beam shots.

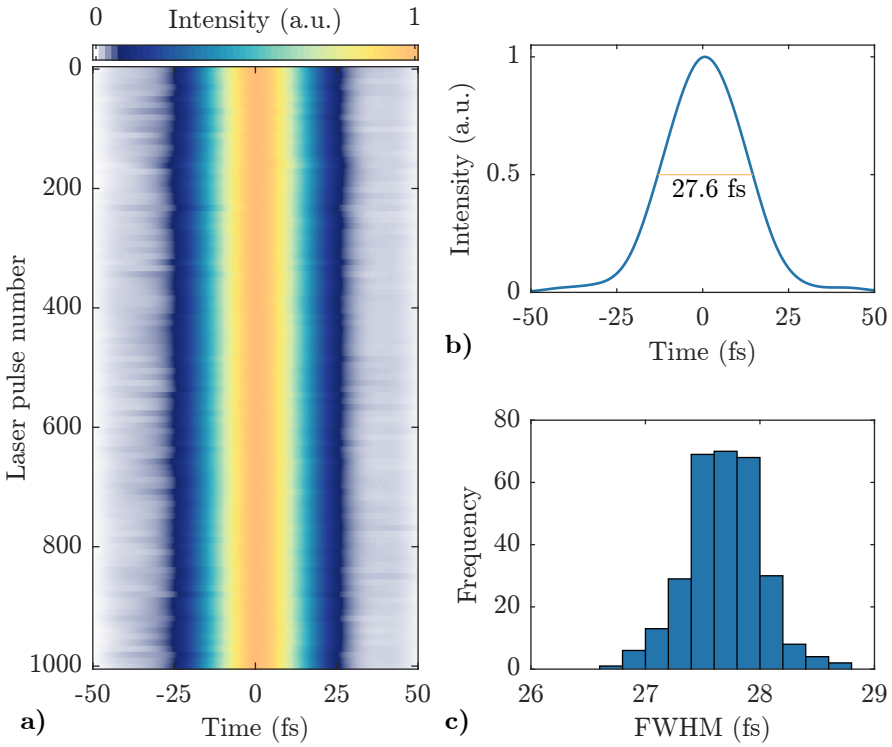

Figure 3.3: Measurement of the laser pulse duration using the Wizzler. (a) depicts a waterfall plot for 1000 consecutive laser pulses. The average temporal profile with its FWHM is shown in (b), with the individual FWHM pulse durations depicted in the histogram in (c).

3.3.1.3 *Focal Spot*

A laser-wakefield accelerator requires knowledge of the spatial distribution of the laser pulse energy at focus. To image the focal spot, a $14-$bit CCD camera is installed inside the vacuum chamber, along with an infinity-corrected objective with a magnification of 10. This diagnostic can be used to improve the quality of the focal spot by correcting for aberrations such as astigmatism or coma. Figure 3.2 includes the camera observing the main laser beam as Cam1. The average focal spot image and the pointing stability of 100 consecutive laser shots is shown in Fig. 3.4. The optimised focal spot has a mean FWHM beam size of $(10.4 \pm 0.1)\,\mu m$ on the horizontal axis and $(9.5 \pm 0.1)\,\mu m$ on the vertical axis, with pointing stability of $0.9\,\mu rad$ and $1.2\,\mu rad$, respectively. The intensity distribution in this plot is shown assuming a laser pulse with a FWHM pulse duration of $27.6\,fs$, a pulse energy of $154.3\,mJ$ and a wavelength of $800\,nm$. According to Eq. 2.8, this results in a normalised vector potential of $a_0 = 1.67 \pm 0.04$, which drives the plasma-wakefield. The calculation of a_0 is based on distributing the measured laser pulse energy according to the measured focal spot profile and a temporal Gaussian distribution with the specified FWHM pulse duration.

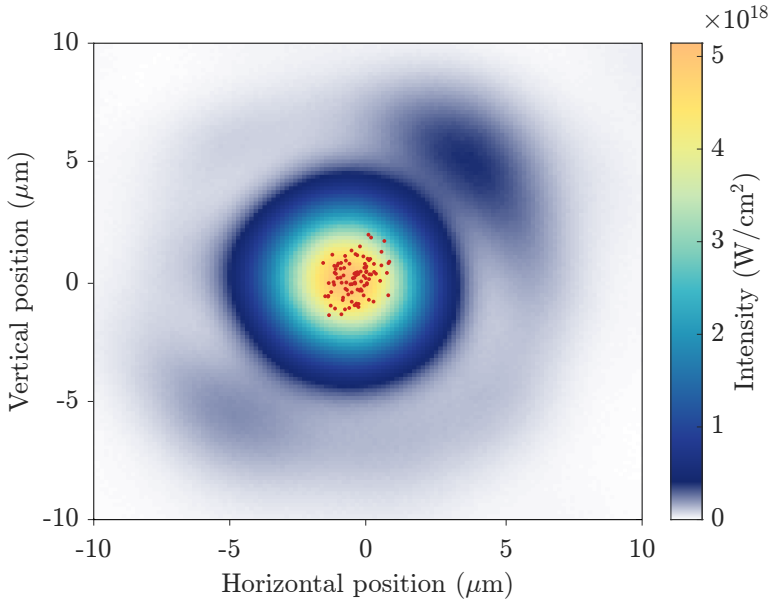

Figure 3.4: Average focal spot to drive the laser-plasma acceleration for 100 consecutive laser pulses. The intensity distribution is calculated for a laser pulse with a FWHM pulse duration of 27.6 fs, a pulse energy of 154.3 mJ and a wavelength of 800 nm. The red points represent the centre of mass for each shot, resulting in pointing stability of 0.9 µrad in the horizontal axis and 1.2 µrad in the vertical axis.

3.3.2 Electron Diagnostics

The evaluation of the electron beams that are generated requires that they are meaningfully characterised. Only then can the quality of an electron source be evaluated and improved. In the BOND laboratory, a variety of diagnostics are available for measuring electron beam pointing, divergence, charge, and energy. The following describes the working principles of these diagnostics.

3.3.2.1 *Electron Profile Screen*

The pointing and divergence of electron beams are measured on a profile screen, which consists of a DRZ-High screen imaged by a CCD camera. The DRZ-High screen is made up of a phosphor layer, a thin PET protective layer, and a plastic supporting layer. A phosphor-based screen converts the energy of particles passing through it into visible light via fluorescence and phosphorescence. The screen offers a high light yield per electron charge and can be used as a charge diagnostic when calibrated [86, 87]. The profile screen is angled at 45 degrees with respect to the electron beam axis and can be driven into the beam axis 1.47 m after the gas target. A $12-$bit CCD camera with an 8 mm f/1.4 lens images the backside of the screen, which covers about

35 mrad by 35 mrad. A 10 nm bandpass filter was included to reduce residual laser light around the 545 nm central wavelength of the DRZ-High. In addition, two layers of 50 µm thick aluminium block incoming laser light and plasma radiation from the front of the screen.

3.3.2.2 *Charge Detection Cavity*

Another distinguishing feature of LPA is the electron bunch charge. For an X-ray source on the basis of TS, the charge or charge density determines, among other things, the number of X-ray photons generated (see Sec. 8.3). The bunch charge can be measured with the profile screen from Sec. 3.3.2.1 [86, 87], an **I**ntegrating **C**urrent**T**ransformer (ICT) [88], or the so-called **Da**rk current **Mon**itor (DaMon) [89, 90]. Since the use of the profile screen is an invasive method due to its being positioned in the beam axis, it is not suitable if the electron bunch needs to be further studied or if X-rays are located on the same axis. The ICT is a non-invasive passive transformer used in plasma acceleration experiments to measure the charge of short electron bunches. However, its measurements are affected by the presence of an **E**lectro**m**agnetic **P**ulse (EMP), like that formed by powerful laser beams, plasma EMP, or discharge units [88, 91, 92]. The output signal of the ICT is dominated by EMP noise when using the discharge-based APL to capture the electron bunch, making this device unsuitable in combination with the APL. Therefore, the DaMon was used for all electron bunch charge measurements in this thesis. It is a stainless steel cavity with a frequency of 1.3 GHz in its first monopole mode. A beam passing through the cavity will stimulate this mode, resulting in a voltage signal. This process is unaffected by the position of the electron bunch within the cavity due to the use of said mode. The beam charge is directly proportional to the amplitude of the voltage signal, which exits the device via an antenna and is carried to an ADC. It is not sensitive to EMP noise, as shown by tests with low laser intensities and an APL. Bunch charges ranging from tens of femtocoulombs to hundreds of picocoulombs can be resolved by measuring this signal non-invasively [92].

3.3.2.3 *Electron Energy Spectrometer*

The electron energy is measured in a single-shot electron spectrometer about 2.7 m after the electron source. The BOND lab's dipole magnet is an electromagnet with a length of 500 mm and a maximum current of 311 A, yielding a magnetic field strength of 245 mT. A vacuum chamber continues inside the magnet, preventing electrons from being scattered by air. Due to the Lorentz force, the dipole field directs electrons to an energy-dependent position on a phosphor screen. A DRZ-High screen is installed in the forward direction by default and is mounted at a 140 degree angle relative to the beam axis.

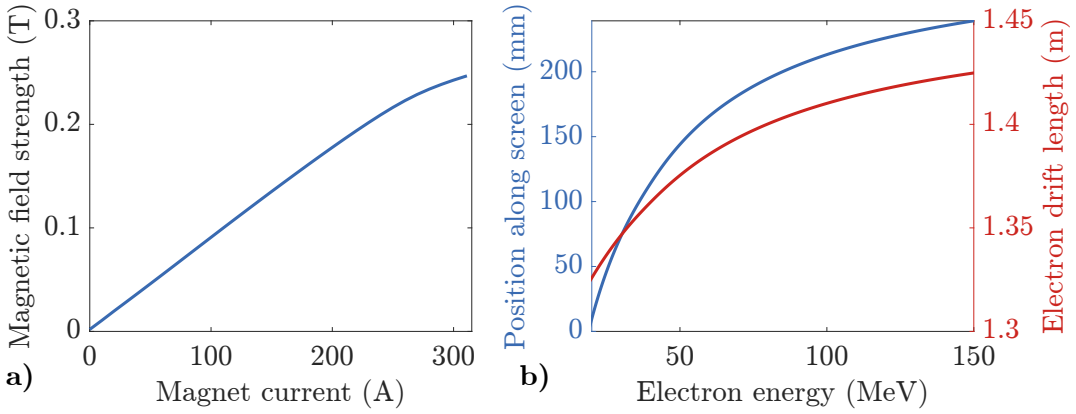

Figure 3.5: The calibration of the magnetic field strength in the electron spectrometer dipole for various magnet currents is shown in (a). A tracking simulation was performed at a magnet current of 100 A to retrieve the energy-dependent position on a scintillating screen and the drift length inside the spectrometer, with the tracking beginning 0.5 m before the dipole magnet.

Both the electrons' path length and their position on the screen are energy dependent and must be known. To perform tracking simulations, accurate magnetic field maps for magnet currents 180 A, 250 A, and 311 A are available. However, various magnet currents ranging from 90 A to 200 A were used in the experiment. Because the three known magnetic field maps differ only in amplitude, the magnetic field in the centre of the dipole was measured using a Hall probe for various magnet currents. Figure 3.5a depicts the scaling of magnetic field strength with applied magnet current. The calibration result indicates a linear behaviour up to currents of about 250 A. For a centrally incoming electron, particle tracking simulations were performed using the known magnetic field map to retrieve the energy-dependent position along the screen and the energy-dependent drift length through the dipole. Figure 3.5b depicts the simulation result for a magnet current of 100 A. The position along the screen is measured from its lower edge, and higher energies are situated higher on the screen. With regard to the drift length of the electrons, highly energetic electrons travel a longer distance before reaching the screen due to its angled orientation relative to the dipole magnet. Originally, the spectrometer used was not an imaging spectrometer, and the measured band-width appears broadened due to electron bunch divergence. Section 6 introduces an APL as an imaging device that, when combined with an electron spectrometer, can be used to create an imaging spectrometer (see Sec. 7). Furthermore, this combination provides a method for further characterising the electron beam by analysing its energy-dispersed focus (see the emittance reconstruction method in Sec. 7.1). To resolve the electron focal spot, the spectrometer's optical imaging system must fulfil additional demands.

When a single focusing device, such as the APL, is placed about 10 cm after the plasma source and the electrons are imaged on a screen at a distance of 250 cm, the electron beam size is magnified by about 25. With an electron beam size of 1 µm at the source, an electron focal size of 25 µm is expected. Furthermore, because electrons travel in vacuum through the magnet but the screen is placed outside, they must pass through a 1 mm aluminium vacuum window. Particle passage through matter is typically described in terms of small-angle multiple scattering. While the beam is within the matter, there is no significant change in its size, but there is an increase in its divergence. This additional divergence causes a particle distribution in a drift length to widen. This means that an angle is introduced in the aluminium window, which broadens the distribution while traversing the thickness of the subsequent screen. The RMS of the angle increase for electrons can be approximated by [93]

$$\theta_{\text{rms}} = \frac{13.6\,\text{MeV}}{\beta_r cp} z \sqrt{\frac{x}{X_0}} \left[1 + 0.038 \ln\left(\frac{x}{X_0}\right)\right], \tag{3.2}$$

where p, c and z are the momentum, velocity and charge number of the incident particles, respectively. In the case of relativistic electrons, $z = 1$ and the velocity is the speed of light, meaning $\beta_r = 1$. x/X_0 describes the thickness of the scattering medium in radiation lengths, where aluminium has a radiation length of $X_0 = 8.897\,\text{cm}$ [93]. For a 60 MeV electron beam passing a 1 mm thick aluminium window, an additional angle of $\theta_{\text{rms}} = 20\,\text{mrad}$ is introduced. Within a scintillator of 200 µm thickness directly after the window, this angle results in a maximum widening of the RMS beam size of about 4 µm. Assuming a 1 µm source size, the screen and imaging system must be capable of resolving at least a 29 µm RMS electron focal size. For even smaller source sizes, the optical system's resolution must be increased. This demand is only required to obtain the beam emittance and is not required to reconstruct the electron spectrum using an imaging technique.

Although a DRZ-High screen offers higher light yield, it lacks the resolution required to resolve the electron focal size. This screen has a resolution of approximately 260 µm, and the imaging system has a resolution of approximately 520 µm [92]. In addition, because the DRZ screen is thicker than the assumed 200 µm, electron scattering causes more severe beam broadening. For the purpose of resolving dispersed electron beam foci of the order of tens of micrometers, a lutetium-yttrium oxyorthosilicate (LySo) scintillator crystal replaces a section within the DRZ screen as shown in Fig. 3.6. It measures 30 mm by 27 mm and has a thickness of 200 µm. LySo crystals have a high light output and a low granularity. The emitted light peaks at a wavelength of 428 nm with a decay time of 40 ns to 42 ns. Beam sizes of 1.44 µm could be resolved using a 200 µm thick LySo screen [94]. A dedicated $12-$bit CCD with a sensor size

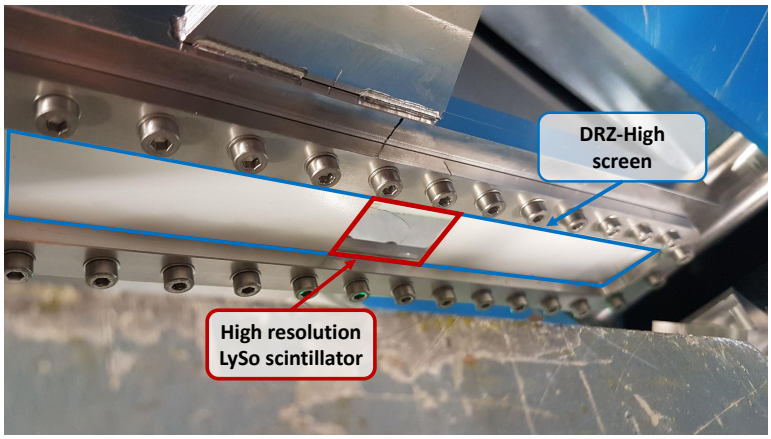

Figure 3.6: Photo of the white DRZ-High screen after the electron spectrometer. A small section of the DRZ screen was replaced by a high resolution LySo screen.

of 2448 px by 2048 px and a pixel size of 3.45 µm in combination with an adjustable objective images the installed LySo screen over a front-surfaced mirror. Transition radiation from electrons reaching the mirror is avoided by orienting the camera at a small angle relative to the mirror. The imaging system's resolution was determined to be approximately 10 µm using a negative 1951 USAF test target [76], which is sufficient to resolve the energy-dispersed electron focal spot.

4 ELECTRON BEAM GENERATION IN THE LPA CHAMBER

During preparation of this thesis, electron beam generation in the LPA chamber was established and improved for reproducibility and reliability. The electron source thus developed was used to collect data for several theses [14, 77, 92, 95–99] and publications [100, 101]. The pointing and spectral stability of generated electron beams are of great importance for various experiments and applications. In the case of TS experiments, the electron source must be stable over time. Due to X-ray detection difficulties, an integration of the photon spectrum over many shots is required. To prevent saturation of the X-ray detector, the X-ray flux must be adjusted, which requires stable pointing in combination with stable bunch charge output. While the use of an APL directly after the gas jet relaxes some requirements due to imaging and spectrally filtering the electron energy distribution (see Sec. 9.2), a reliable source is essential. Experiments involving APLs can suffer from a large on-axis Bremsstrahlung background when electrons scatter from the APL housing. In addition, fluctuation in the pointing and offset position of the electron source can affect the focusing capabilities and even lead to a shift of the electron focal spot (see Sec. 6.1.4). This section discusses the output of the ionisation injection-based electron source, as well as the experimental conditions. Section 7.2.1 will examine the electron beam energy distribution after implementing an APL to determine the electron energy spectrum unaffected by electron beam divergence.

The electron source must be optimised in order to be stable and meet the requirements of the planned experiment. To find a stable regime for LPA, extensive scans of laser focal point position, laser pulse energy, plasma density, and pulse shaping were performed. As a result, an 8-hour experiment with 72.000 consecutive shots with charge injection and acceleration was published [100]. While shot-to-shot fluctuations were observed, there was no detectable drift in the average beam charge of 14.5 pC. However, due to limitations in X-ray radiation detection (see Sec. 9.4.2), the X-ray flux had to be reduced by reducing the total electron beam charge. This was accomplished primarily by lowering the laser power and re-optimising the electron beams. The data presented below were collected on the same day as the X-ray data from Pt. III in order to interpret the capabilities of the Thomson source and were therefore performed with a reduced laser power. Figure 4.1 is a schematic drawing of the setup used for the

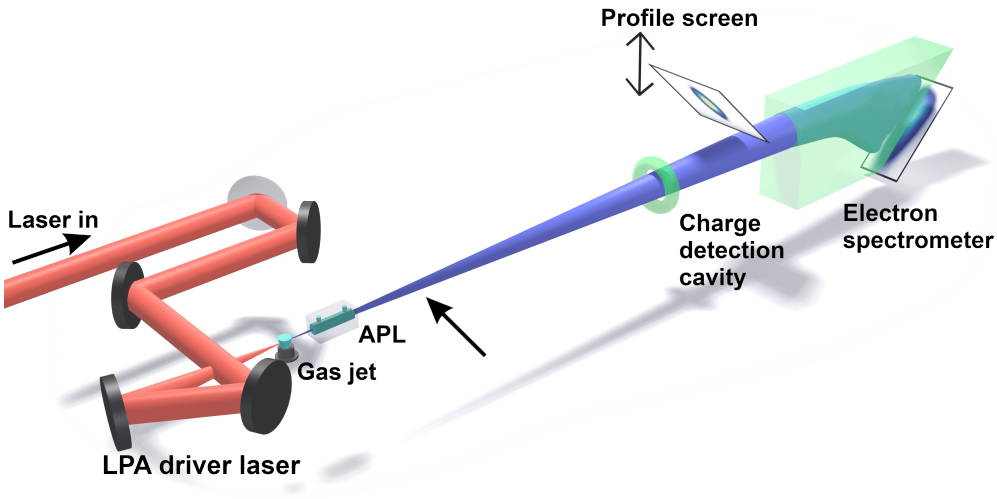

Figure 4.1: The setup for LPA experiments is depicted schematically. To ionise a plasma and drive a laser-wakefield electron source, the incoming laser beam (red) is transported and focused onto a gas jet. Electrons are injected via ionisation injection and then accelerated. The generated electron beam (blue) points in the same direction as the incoming LPA driver laser beam and can be captured by an APL. It passes through a charge detection cavity to measure beam charge, and a profile screen can be driven into the beam axis to observe beam pointing and divergence. It then enters the electron spectrometer and is spectrally resolved on a screen.

experiments. To generate an electron beam the LPA driver laser beam is focused onto a gas jet target in this simplified depiction. The laser beam both ionises the gas and drives a plasma wakefield. Ionisation injection is used to inject the electron beam into the wakefield. The generated electron beam points in the same direction as the laser beam and can be studied with the following diagnostics. In particular, beam charge, as well as beam divergence and pointing are considered. Section 7.2.1 discusses the electron spectrum after incorporating the APL into the setup and converting the diagnostic into an imaging spectrometer. Depending on whether or not the APL is in use, it is positioned in the beamline and the electron beam must pass through it (compare Fig. 6.7). Because of its limited aperture of 2 mm in diameter, this can have an effect on electron charge transport.

The repetition rate of the LPA drive laser beam was 1.4 Hz. To maintain a moderate level of energy deposition on the beamline optics, the laser system output was not operated at its maximum repetition rate of 10 Hz. Excessive heating can cause optics

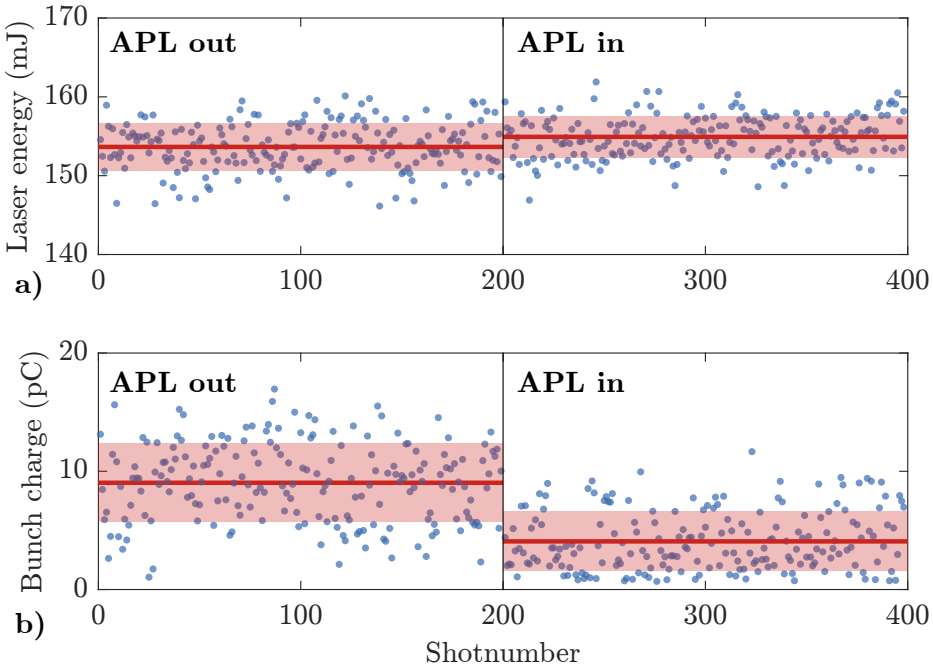

Figure 4.2: For both the APL in and out of the beamline, 200 consecutive shots were taken while the laser pulse energy (a) and bunch charge (b) were recorded. The blue dots represent the measurements for each shots. Only the time required to drive the APL into the beam-axis has passed between the two runs. The horizontal red line represents the mean of 200 shots, while the transparent area represents the standard deviation. A 0.8 % difference in laser pulse energy was observed between both APL positions, indicating that the LPA driver had not changed significantly. An overall average laser pulse energy of (154.3 ± 6.1) mJ was measured, while the average charge dropped from (9.0 ± 3.3) pC to (4.1 ± 2.5) pC.

to deform and change the spatio-temporal properties of the laser pulse, which must be corrected. As shown in Sec. 3.3.1.2, the FWHM duration of the laser pulse was minimised to 27.6 fs. The laser pulse energy was measured simultaneously with the acceleration of 200 consecutive electron bunches for two APL positions, respectively. The measured laser pulse energy for each shot is shown in Fig. 4.2a for both APL in and out of the beamline, demonstrating agreement of the two measurements within the error bars. The measured laser pulse energy for each shot is shown in Fig. 4.2a, and differs by 0.8 % depending on whether the APL is in or out of the beamline. However, the laser pulse energy is independent of the APL's position, and the change in its mean value is caused by a change in the laser system's output energy. The overall average pulse energy was determined to be (154.3 ± 6.1) mJ. These properties, combined with the laser focal spot from Sec. 3.3.1.3, result in a normalised vector potential of $a_0 = 1.67 \pm 0.04$. The pulsed supersonic gas jet has a 1 mm diameter

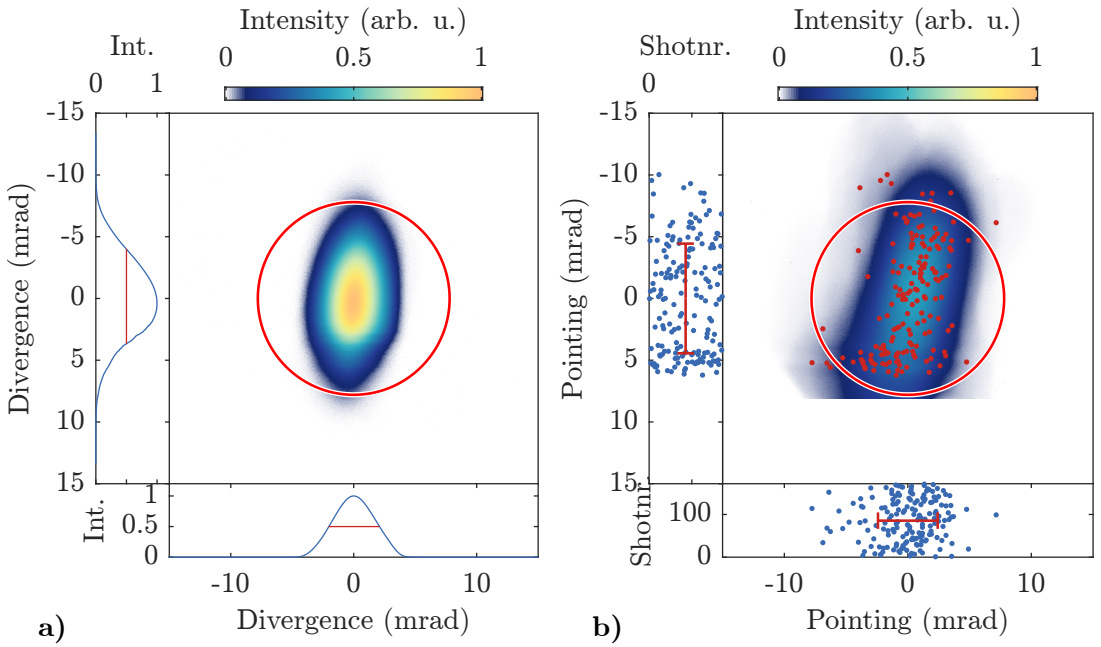

Figure 4.3: (a) shows the average beam profile of 200 consecutive electron shots using ionisation injection. Gaussian fits to the single shots yielded an average FWHM divergence of (3.8 ± 0.7) mrad in the horizontal and (7.8 ± 1.7) mrad in the vertical. (b) depicts the sum of all individual beam profiles measured on the screen, with red dots representing the beam pointing of each shot. The standard deviations of the pointing fluctuations were measured to be 4.4 mrad in the vertical plane and 2.4 mrad in the horizontal plane. The red circle represents the 7.8 mrad APL exit aperture through which the electron beams must pass.

nozzle and was operated at the same repetition rate as the laser beam with 99.5 % helium and 0.5 % nitrogen dopant by weight at a backing pressure of (3.52 ± 0.08) bar. A plasma channel is created by the laser pulse 0.7 mm above the gas jet nozzle. As mentioned in Sec. 3.2, the dedicated transverse probe beam was used to measure a plasma density of approximately $(2 \pm 0.3) \times 10^{19}$ cm^{-3}.

Prior to measuring the electron spectrum and emittance, as well as producing Thomson X-rays, the electron beams were optimised for pointing stability on the profile screen. The average electron beam profile of 200 consecutive shots is shown in Fig. 4.3a, yielding a vertical FWHM divergence of (7.8 ± 1.7) mrad and a horizontal FWHM divergence of (3.8 ± 0.7) mrad. Because the LPA driver laser beam is vertically polarised, the beam profile is elongated in the vertical plane. This is a common property of electron beams injected via ionisation injection, as explained in Sec. 2.3. Figure 4.3b depicts the integrated beam profile and the pointing of each single shot. The extent of the pointing fluctuations is comparable to the extent of the beam divergence. The standard deviations of the pointing fluctuations were measured to

be 4.4 mrad in the vertical plane and 2.4 mrad in the horizontal plane. The jitter of the source position is assumed to be given by the jitter of the focal spot, which was described in Sec. 3.3.1.3 and is given by 0.5 µm in the horizontal plane and 0.6 µm in the vertical plane. An increased pointing jitter can be caused by various effects and instabilities. Common sources are shot-to-shot changes in the characteristics of the laser pulses and the plasma density profiles. Additionally, operating the electron beam source with a reduced laser pulse energy near the threshold where charge can be injected can induce additional instabilities. This was done to prevent the X-ray detector from becoming saturated during the TS experiment.

This instability causes the loss of bunch charge in the beam optics close to the beamline. The APL has an exit aperture of 7.8 mrad, which is shown in Fig. 4.3 as a red circle. The average bunch profile itself fits through the APL, but the additional pointing jitter causes a significant charge loss. Figure 4.2b depicts the charge of these 200 consecutive shots as the setting 'APL out'. When moving the APL into the beamline without turning it on, the average charge dropped to 4.1 pC, as seen on the 'APL in' setting. With the charge loss, the total flux after the APL is about 0.3 nC/min. A charge loss reduces the available charge for the subsequent TS interaction and can create a substantial photon background on-axis owing to Bremsstrahlung.

Part II

LOW SLICE EMITTANCE ELECTRON BEAMS FROM AN LPA SOURCE

Part I discussed the realization of an **L**aser-**P**lasma **A**cceleration (LPA) electron beam source, which is the foundation of various applications, such as linear colliders [102] or modern light sources [103–106]. For all of the above, sub-µm normalised electron-emittances are required. Therefore, the measurement of emittance is critical for the successful development and optimisation of new applications, such as the proposed Thomson X-ray source. However, traditional emittance reconstruction methods can be problematic to apply to LPA generated beams due to their broad energy spectra and shot-to-shot fluctuations. Here, the emittance is measured using a different method first introduced by Weingartner et al. [107]. It relies on the analysis of a single shot of a polychromatic electron focus dispersed in an electron spectrometer. To capture and image the electron beams, an **A**ctive **P**lasma **L**ens (APL) is used instead of conventional quadrupole magnets. With their compact design and short focal lengths, APLs complement LPA electron beam sources. Furthermore, they are preferred for minimising chromatic emittance growth in a free drift [108, 109], can be used to build an imaging electron spectrometer, and are a key component in the Thomson scattering setup [40, 41].

In Sec. 5, the analytical consideration of linear beam dynamics and the concept of beam emittance are presented. Section 6 provides an introduction to APLs as well as the design and implementation of one in the experimental setup. In this context, the various sources of emittance growth are discussed. Finally, the APL is used to reconstruct the electron energy spectrum and the initial phase-space including the emittance, as discussed in Sec. 7.

5 LINEAR BEAM DYNAMICS AND BEAM PARAMETERS

Guiding and focusing systems are essential for transporting a charged particle beam through an accelerator. Magnetic and electric fields are utilised in order to control and accelerate the bunch along a desired path. A transfer matrix formalism can be used to describe such a trajectory, and it includes the evolving characteristic beam parameters. This section offers an introduction to the basic principles of linear beam dynamics and presents the concept of beam emittances. The theoretical basics of this section are on the basis of [76, 110–112].

5.1 TRANSFER MATRIX FORMALISM

To begin, the transfer matrix formalism is introduced to provide a description of particle movement along a beamline. Electromagnetic fields are used to guide a charged particle beam by using the Lorentz force. For a particle moving with the velocity $\mathbf{v}$ and carrying the electrical charge q the Lorentz force is given by

$$\mathbf{F}_L = q(\mathbf{E} + \mathbf{v} \times \mathbf{B}). \tag{5.1}$$

The vectors $\mathbf{E}$ and $\mathbf{B}$ represent the electric and magnetic field vectors, respectively. The increase of the longitudinal energy of an electron with elementary charge $q = e$ is given by $\int(\mathbf{E} + \mathbf{v} \times \mathbf{B})\, d\mathbf{r} = \int \mathbf{E}\, d\mathbf{r}$[1]. As a result, only electric fields are responsible for the particle acceleration. Because of the vector product in Eq. 5.1, the resulting force due to the magnetic field is always perpendicular to the particle's trajectory. It can be used for deflecting structures and in the case of many particles, also for focusing of particle bunches. For relativistic particles ($|\mathbf{v}| \approx c$), an electric field which exerts the same force as a magnetic field has the magnitude

$$|\mathbf{E}| = c \cdot |\mathbf{B}|, \tag{5.2}$$

with c being the speed of light. This implies that the force from a magnetic field of 1 T is equivalent to that of an electric field of 300 MV/m. While a magnetic field of

1 The particle velocity $\mathbf{v}$ is parallel to the longitudinal particle motion $\mathbf{r}$, therefore $\mathbf{v} \times \mathbf{B}$ is perpendicular to $\mathbf{r}$. Hence, the scalar product in the magnetic term cancels out in the energy relation.

1 T is technically feasible, generating its equivalent electric field is problematic in conventional setups [111]. Thus, magnetic fields are used for beam manipulation and focusing. This section looks at how magnetic fields affect the particle's motion.

It is convenient to consider the position and motion of each particle in relation to a reference trajectory, usually the design orbit. The coordinate system moves along the reference trajectory in the accelerator, while each individual particle is characterised within this moving system.

Instead of using time as the dependent variable, the distance s along the reference orbit is used. The motion of a particle is described in canonical phase-space by a six-dimensional vector (x, p_x, y, p_y, s, p_s), where x and y represent the horizontal and vertical displacements and s is the distance along the reference orbit. The corresponding canonical momentum components are p_x, p_y and p_s. Rather than the canonical phase-space, it is common to use the so called normalised phase-space with its geometrical coordinates

$$\mathbf{X}(s) = \begin{pmatrix} x \\ x' \\ y \\ y' \\ l \\ \delta \end{pmatrix}, \tag{5.3}$$

where l defines the longitudinal displacement from the reference particle. The horizontal and vertical slopes with respect to the reference orbit are given by $x' = {}^{dx}/_{ds}$ and $y' = {}^{dy}/_{ds}$, whereas $\delta = {}^{\Delta p}/_{p}$ describes the relative momentum deviation from the momentum p from a reference particle. These coordinates are canonical conjugated if all particles have constant momentum. Figure 5.1 depicts this right-handed (x,y,s), orthogonal coordinate system.

It is impossible to solve the equation of motion for charged particles in arbitrary electromagnetic fields explicitly. Basic beam dynamics are based on fields that are either independent or linearly dependent on the distance from the ideal trajectory. In this mathematical approach for describing a particle's motion, a beamline consists only of drift spaces, dipoles and quadrupole magnets, where the magnetic fields

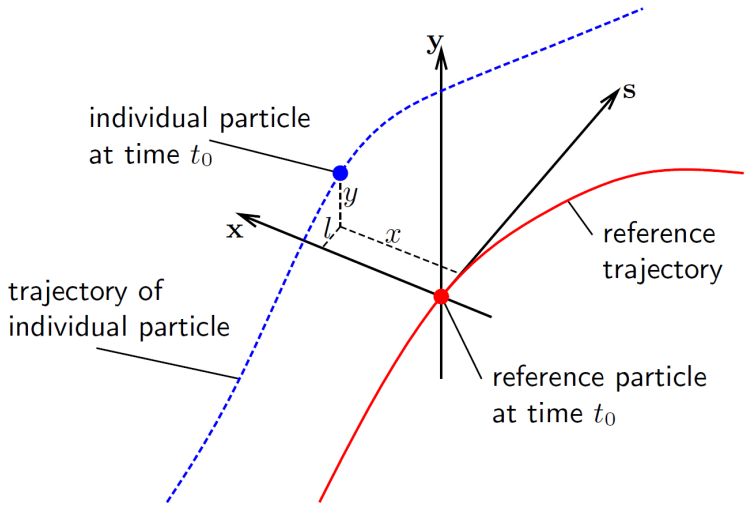

Figure 5.1: Definition of the coordinate system. The reference particle advances along its reference trajectory described by the distance s. The phase-space coordinates of an individual particle refer to a coordinate system in respect to the reference particle at the same time. Drawing taken from [110].

depend linearly on the deviation of the particle from the reference path. In that case, the equations of motion for transverse position-offset can be written as [111]

$$x''(s) + K_x(s)x(s) = \frac{\delta}{\rho_x(s)} \tag{5.4}$$

$$y''(s) + K_y(s)x(s) = \frac{\delta}{\rho_y(s)}, \tag{5.5}$$

where the parameters $\rho_x(s)$ and $\rho_y(s)$ denote the dipole bending radii of the reference trajectory at the position s. Furthermore, the relation

$$K_x(s) = \frac{1}{\rho_x^2(s)} - k(s) \tag{5.6}$$

$$K_y(s) = \frac{1}{\rho_y^2(s)} + k(s) \tag{5.7}$$

applies with

$$k(s) = \frac{q}{p} g(s). \tag{5.8}$$

$K_x(s)$ and $K_y(s)$ are called the focusing strength or magnet parameters, and consist of a dipole-dependent contribution through $\rho_{x,y}$ and a quadrupole-dependent contribution through the quadrupole strength $k(s)$. The quadrupole strength is a function of the incoming particle's charge q and momentum p, and it relates linearly to the gradient $g(s)$ of the magnetic field within the quadrupole. The following considerations are based on the hard-edge model for magnets. It is assumed that the

magnetic field begins and ends abruptly at the magnet's beginning and end, and that the field gradient is constant within the magnet. $K_{x,y}$ is a constant parameter in this case. Initially, a constant momentum is assumed, implying a vanishing relative momentum deviation $\delta = 0$. The differential equations 5.4 and 5.5 then describe a harmonic oscillation and their solution can be expressed using a matrix formalism as [111]

$$\begin{pmatrix} x(s) \\ x'(s) \end{pmatrix} = \mathbf{R}_x(s, s_0) \cdot \begin{pmatrix} x(s_0) \\ x'(s_0) \end{pmatrix} \tag{5.9}$$

$$\begin{pmatrix} y(s) \\ y'(s) \end{pmatrix} = \mathbf{R}_y(s, s_0) \cdot \begin{pmatrix} y(s_0) \\ y'(s_0) \end{pmatrix}, \tag{5.10}$$

where the transfer matrices R_x and R_y are explicitly given by

$$\mathbf{R}_{x,y}(s, s_0) = \begin{cases} \begin{pmatrix} \cos\left(\sqrt{K_{x,y}}d\right) & \frac{1}{\sqrt{K_{x,y}}}\sin\left(\sqrt{K_{x,y}}d\right) \\ -\sqrt{K_{x,y}}\sin\left(\sqrt{K_{x,y}}d\right) & \cos\left(\sqrt{K_{x,y}}d\right) \end{pmatrix} & \text{for } K_{x,y} > 0 \\ \begin{pmatrix} \cosh\left(\sqrt{|K_{x,y}|}d\right) & \frac{1}{\sqrt{|K_{x,y}|}}\sinh\left(\sqrt{|K_{x,y}|}d\right) \\ -\sqrt{|K_{x,y}|}\sinh\left(\sqrt{|K_{x,y}|}d\right) & \cosh\left(\sqrt{|K_{x,y}|}d\right) \end{pmatrix} & \text{for } K_{x,y} < 0 \end{cases} \tag{5.11}$$

with $d = s - s_0$.

Quadrupoles have $1/\rho = 0$ and $K_x = -K_y \equiv -k$ and are used for focusing and defocusing. In particular that a horizontally focusing quadrupole is defocusing vertically, and vice versa. A combination of several quadrupole magnets with alternating k is required to achieve transverse focusing in both planes. A dipole magnet, unlike a quadrupole magnet, has a vanishing gradient $g(s)$, so that the magnet parameter is only dependent on the dipole bending radius ρ. For a given beam direction the bending angle $\theta = d/\rho$ defines the transport matrix as

$$\mathbf{R}_{\text{bend}} = \begin{pmatrix} \cos(\theta) & \rho\sin(\theta) \\ -\frac{1}{\rho}\sin(\theta) & \cos(\theta) \end{pmatrix}. \tag{5.12}$$

There are no magnetic fields within a free drift space of length d. The magnet parameter becomes zero and the matrix for a free drift can be adapted from Eq. 5.12 as

$$\mathbf{R}_{\text{drift}} = \begin{pmatrix} 1 & d \\ 0 & 1 \end{pmatrix}. \tag{5.13}$$

So far matrices were derived to describe the transverse motion of particles in a drift, a dipole or a quadrupole. Including the longitudinal phase space with the already introduced longitudinal displacement l and the relative momentum deviation δ, the 6×6-dimensional transfer matrix yields

$$\begin{pmatrix} x \\ x' \\ y \\ y' \\ l \\ \delta \end{pmatrix} = \begin{pmatrix} R_{11} & R_{12} & 0 & 0 & 0 & R_{16} \\ R_{21} & R_{22} & 0 & 0 & 0 & R_{26} \\ 0 & 0 & R_{33} & R_{34} & 0 & R_{36} \\ 0 & 0 & R_{43} & R_{44} & 0 & R_{46} \\ R_{51} & R_{52} & R_{53} & R_{54} & R_{55} & R_{56} \\ 0 & 0 & 0 & 0 & 0 & 1 \end{pmatrix} \cdot \begin{pmatrix} x_0 \\ x'_0 \\ y_0 \\ y'_0 \\ l_0 \\ \delta_0 \end{pmatrix}. \tag{5.14}$$

An entry of 0 implies that there is no coupling between the individual particle coordinates. Therefore, R_{13}, R_{14}, R_{23}, R_{24}, R_{31}, R_{32}, R_{41} and R_{42} vanish owing to the assumption of no coupling between the transverse planes x and y. The zeros in column five represent the independence of transverse motion along the longitudinal axis, and the final row contains exactly one 1, indicating the preservation of momentum of a particle in a longitudinally non-accelerating structure. The matrix elements R_{16} and R_{36} characterise the dispersion, and the elements R_{26} and R_{46} describe the angular dispersion, meaning the change of the focusing properties depending on the momentum. Refer to [111] for a more detailed description.

A beamline consists of many elements with a piecewise constant focusing parameter K. The total beam transport matrix is the product of all transfer matrices R_j with $j =\in \{1, ..., n\}$ for each element in the beamline, i.e.

$$\mathbf{X}_f = \mathbf{R}_n \cdot \mathbf{R}_{n-1} \cdot ... \cdot \mathbf{R}_1 \cdot \mathbf{X}_i. \tag{5.15}$$

The subscription i and f symbolise the initial an final particle coordinates.

5.2 THE COURANT–SNYDER PARAMETERS

Because only linearly varying magnetic fields are considered, the particle trajectory in the transverse plane is represented by the Eqs. 5.4 and 5.5. It simplifies to the homogeneous differential Hill equation

$$x''(s) + K_x(s)\, x(s) = 0 \tag{5.16}$$

of the neglected relative momentum deviation $\delta = 0$. The following calculations are explicitly carried out for the the horizontal motion $x(s)$ but are also valid for the vertical case. The general solution is given by [111]

$$x(s) = A\sqrt{\beta_x(s)}\cos(\psi_x(s) + \psi_{x_0}) \tag{5.17}$$

with the phase

$$\psi_x(s) = \int_0^s \frac{ds'}{\beta_x(s')}, \tag{5.18}$$

and A as well as ψ_{x_0} being constants determined by the initial conditions. Equation 5.17 describes an oscillation with a varying amplitude $A \cdot \sqrt{\beta_x(s)}$ along the s-coordinate, which is called a betatron oscillation. By combining Eq. 5.17 with the Hill equation 5.16, it can be shown that an A^2 defined by (see [111])

$$\gamma_x(s)\,x^2(s) + 2\alpha_x(s)\,x(s)\,x'(s) + \beta_x(s)\,x'^2(s) = A^2 \tag{5.19}$$

is invariant. This expression is called the Courant-Snyder invariant and uses the abbreviations

$$\alpha_x(s) = -\frac{1}{2}\beta_x'(s) \text{ and } \gamma_x(s) = \frac{1+\alpha_x^2(s)}{\beta_x(s)}. \tag{5.20}$$

Equation 5.19 describes an ellipse whose shape and orientation are determined by the **C**ourant-**S**nyder (C-S) parameters α_x, β_x and γ_x, which are used to parametrise the betatron motion of a particle. According to Liouville's theorem, the phase space area given by $\pi \cdot A^2$ stays constant [111]. This is true, if the coordinates defined in Eq. 5.3 are canonically conjugated and the forces involved are conservative. The C-S parameters depend on the coordinate s, implying that the shape of the ellipse along the beamline changes while its area remains constant. A single particle always moves along an ellipse's perimeter. Because the ellipse's area is preserved, a second particle with a smaller betatron amplitude will always remain within the first particle's ellipse.

The solution of the Hill equation 5.16 can be written as the 2×2-matrix

$$\begin{pmatrix} x(s) \\ x'(s) \end{pmatrix} = \begin{pmatrix} R_{11} & R_{12} \\ R_{21} & R_{22} \end{pmatrix} \cdot \begin{pmatrix} x(s_0) \\ x'(s_0) \end{pmatrix}, \tag{5.21}$$

which implies that the phase space ellipse transforms with the evolution of x and x' from s_0 to s along the beamline. By using the invariant in Eq. 5.19 and $\det(\mathbf{R}) = 1$, which is fulfilled within Liouville's theorem, the x and x' dependence is replaced by the C-S parameters,

$$\begin{pmatrix} \beta_x(s) \\ \alpha_x(s) \\ \gamma_x(s) \end{pmatrix} = \begin{pmatrix} R_{11}^2 & -2R_{11}R_{12} & R_{12}^2 \\ -R_{11}R_{21} & R_{12}R_{21} + R_{11}R_{22} & -R_{12}R_{22} \\ R_{21}^2 & -2R_{21}R_{22} & R_{22}^2 \end{pmatrix} \cdot \begin{pmatrix} \beta_x(s_0) \\ \alpha_x(s_0) \\ \gamma_x(s_0) \end{pmatrix} \tag{5.22}$$

The resulting matrix is called the C-S matrix and describes the transformation of the C-S parameters along the beamline.

5.3 CONCEPT OF BEAM EMITTANCE

The horizontal emittance ϵ_x is related to the occupied phase space area A. In the context of this work, it is defined as[2] $\epsilon_x = A/\pi$. Figure 5.2 depicts the relationship between the emittance and the C-S parameters provided by

$$\gamma_x x^2 + 2\alpha_x x x' + \beta_x x'^2 = \epsilon_x. \tag{5.23}$$

The emittance is one of the quantities describing the quality of a particle beam. As stated in Sec. 5.2, Liouville's theorem involves the preservation of the phase space area, and thus the emittance is a conserved quantity of a particle beam. It is a measure of a beam's parallelism that defines the smallest opening the beam may squeeze though. A lower emittance in a particle collider indicates that the likelihood of particle interactions increases, resulting in a higher luminosity. In case of a synchrotron light source, a lower emittance corresponds to a higher brilliance. This section will present a statistical definition of the enclosed fraction of particles in phase space in order to define the emittance as a statistical quantity.

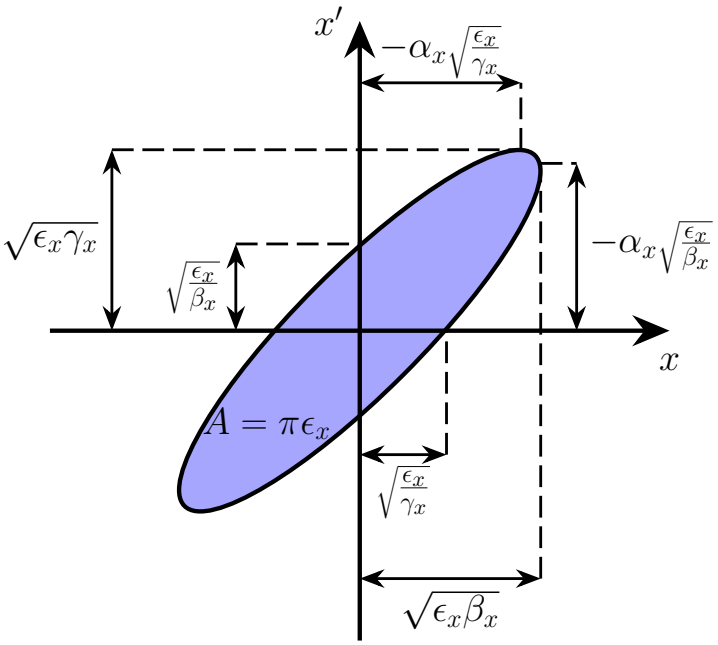

Figure 5.2: The phase-space ellipse in the transverse plane x as determined by the C-S parameters α_x, β_x, and γ_x, as well as the emittance ϵ_x. Except for a factor π, the emittance corresponds to the enclosed area of the ellipse.

2 A commonly used unit for the emittance is [mm · mrad], as used in this thesis. Occasionally, this quantity is specified in the unit [µm] or it is given with an additional factor π as [π · mm · mrad].

The evolution of the beam ellipse can be written using a two-dimensional symmetric beam matrix $\boldsymbol{\sigma}$, i.e. [111]

$$\begin{pmatrix} x & x' \end{pmatrix} \cdot \begin{pmatrix} \sigma_{11} & \sigma_{12} \\ \sigma_{21} & \sigma_{22} \end{pmatrix}^{-1} \cdot \begin{pmatrix} x \\ x' \end{pmatrix} = 1, \tag{5.24}$$

with $\sigma_{12} = \sigma_{21}$. Then the ellipse equation yields

$$\sigma_{22}x^2 + 2\sigma_{12}xx' + \sigma_{11}xx'^2 = \det\sigma \tag{5.25}$$

and a comparison with Eq. 5.23 identifies the beam matrix elements with the known C-S parameters as

$$\boldsymbol{\sigma} = \begin{pmatrix} \sigma_{11} & \sigma_{12} \\ \sigma_{21} & \sigma_{22} \end{pmatrix} = \epsilon_x \cdot \begin{pmatrix} \beta_x & -\alpha_x \\ -\alpha_x & \gamma_x \end{pmatrix}. \tag{5.26}$$

The two-dimensional phase space area is then given by

$$V_2 = \pi\sqrt{\det\boldsymbol{\sigma}} = \pi\sqrt{\sigma_{11}\sigma_{22} - \sigma_{12}^2} = \pi\epsilon_x, \tag{5.27}$$

which is consistent with the relation $\beta\gamma - \alpha_x^2 = 1$ from Eq. 5.20. This concept can be generalised for an n-dimensional hyper-ellipsoid with $\boldsymbol{\sigma}^{nD}$ being a $n \times n$-matrix. The n-dimensional emittance can then be defined as $\epsilon^{nD} = \sqrt{\det\boldsymbol{\sigma}^{nD}}$.

Statistical Definition of the Beam Matrix

The definition of the elements in the beam matrix, which describe the distribution of particles, is somewhat arbitrary. For a statistical distribution of particles, the hyper-ellipsoid that encloses them can contain almost all of them or only a fraction of them. As a result, statistical beam parameters must be defined to characterise the size, shape, and orientation of the hyper-ellipsoid. This can be achieved by introducing the second moments $\langle uv \rangle$ defined by

$$\langle uv \rangle = \frac{\int_{-\infty}^{\infty} (u - \langle u \rangle)(v - \langle v \rangle)\rho(x, x', y, y', l, \delta)\, dx\, dx'\, dy\, dy'\, dl\, d\delta}{\int_{-\infty}^{\infty} \rho(x, x', y, y', l, \delta)\, dx\, dx'\, dy\, dy'\, dl\, d\delta}, \tag{5.28}$$

where the first moment $\langle u \rangle$ is given by

$$\langle u \rangle = \frac{\int_{-\infty}^{\infty} u\rho(x, x', y, y', l, \delta)\, dx\, dx'\, dy\, dy'\, dl\, d\delta}{\int_{-\infty}^{\infty} \rho(x, x', y, y', l, \delta)\, dx\, dx'\, dy\, dy'\, dl\, d\delta}. \tag{5.29}$$

Here, ρ is the intensity distribution of the beam in six-dimensional phase-space and u and v represents x, x', y, y', l or δ. The $\langle x^2 \rangle$ and $\langle y^2 \rangle$ denote the variances of the beam distribution in the horizontal and vertical plane. Each plane the square root of the variance defines the **R**oot **M**ean **S**quare (RMS) beam size, i.e. $x_{rms} = \sqrt{\langle x^2 \rangle}$ and $y_{rms} = \sqrt{\langle y^2 \rangle}$. Using these moments the beam matrix can be written as

$$\sigma^{6D} = \begin{pmatrix} \langle x^2 \rangle & \langle xx' \rangle & \langle xy \rangle & \langle xy' \rangle & \langle xl \rangle & \langle x\delta \rangle \\ \langle xx' \rangle & \langle x'^2 \rangle & \langle x'y \rangle & \langle x'y' \rangle & \langle x'l \rangle & \langle x'\delta \rangle \\ \langle xy \rangle & \langle x'y \rangle & \langle y^2 \rangle & \langle yy' \rangle & \langle yl \rangle & \langle y\delta \rangle \\ \langle xy' \rangle & \langle x'y' \rangle & \langle yy' \rangle & \langle y'^2 \rangle & \langle y'l \rangle & \langle y'\delta \rangle \\ \langle xl \rangle & \langle x'l \rangle & \langle yl \rangle & \langle y'l \rangle & \langle l^2 \rangle & \langle l\delta \rangle \\ \langle x\delta \rangle & \langle x'\delta \rangle & \langle y\delta \rangle & \langle y'\delta \rangle & \langle l\delta \rangle & \langle \delta^2 \rangle \end{pmatrix} \tag{5.30}$$

$$= \begin{pmatrix} \boldsymbol{\sigma}_{xx} & \boldsymbol{\sigma}_{xy} & \boldsymbol{\sigma}_{xl} \\ \boldsymbol{\sigma}_{xy}^T & \boldsymbol{\sigma}_{yy} & \boldsymbol{\sigma}_{yl} \\ \boldsymbol{\sigma}_{xl}^T & \boldsymbol{\sigma}_{yl}^T & \boldsymbol{\sigma}_{ll} \end{pmatrix}, \tag{5.31}$$

with $\boldsymbol{\sigma}_{xx}$, $\boldsymbol{\sigma}_{yy}$, $\boldsymbol{\sigma}_{ll}$, $\boldsymbol{\sigma}_{xy}$, $\boldsymbol{\sigma}_{xl}$ and $\boldsymbol{\sigma}_{yl}$ being 2×2-matrices, e.g.

$$\boldsymbol{\sigma}_{xx} = \begin{pmatrix} \langle x^2 \rangle & \langle xx' \rangle \\ \langle xx' \rangle & \langle x'^2 \rangle \end{pmatrix}. \tag{5.32}$$

Physical measurements typically provide discrete values in time or space rather than a continuous function. For example, an RMS beam size measurement requires the sum of discrete bins in space, where the first and second moments are defined by

$$\langle u \rangle = \frac{\sum_{i=1}^{N} \rho(u_i) u_i}{\sum_{i=1}^{N} \rho(u_i)} \tag{5.33}$$

and

$$u_{rms} = \sqrt{\langle u^2 \rangle} = \sqrt{\frac{\sum_{i=1}^{N} \rho(u_i)(u_i - \langle u \rangle)^2}{\sum_{i=1}^{N} \rho(u_i)}}. \tag{5.34}$$

This statistical definition is commonly used in electron accelerators and the following considerations are on the basis of it.

Transverse Beam Emittance

To fully characterise a particle beam, six-dimensional emittance $\epsilon^{nD} = \sqrt{\det\boldsymbol{\sigma}^{nD}}$ and Eq. 5.31 are required. In most cases only the transverse emittance, defined by

$$\sigma^{4D} = \begin{pmatrix} \boldsymbol{\sigma}_{xx} & \boldsymbol{\sigma}_{xy} \\ \boldsymbol{\sigma}_{xy}^{T} & \boldsymbol{\sigma}_{yy} \end{pmatrix}, \tag{5.35}$$

is experimentally accessible, as the transverse projection of a beam is being observable. This 4×4-matrix consists of the three 2×2-matrices $\boldsymbol{\sigma}_{xx}$, $\boldsymbol{\sigma}_{yy}$, and $\boldsymbol{\sigma}_{xy}$ and describes the transverse phase-space. When dispersion is present, an additional contribution expressing the energy dependence occurs within the second moments. The C-S parameters and emittance in this case do not describe pure betatron motion, but rather a superposition of all betatron motions and dispersion.

Defining $\epsilon_{rms}^{4D} = \sqrt{\det\boldsymbol{\sigma}^{4D}}$ as the effective projected four-dimensional transverse RMS emittance provides an important measure for the transverse beam dynamics. Normally, the two-dimensional emittance of one transverse plane is investigated separately, but there is the possibility of a coupling between the horizontal and vertical betatron oscillations. Then $\boldsymbol{\sigma}_{xy}$ describes this coupling and it vanishes when the beam is transversely uncoupled. Even for coupled planes, the projected two-dimensional emittances in horizontal and vertical directions are defined as

$$\epsilon_x = \sqrt{\det\boldsymbol{\sigma}_{xx}} \tag{5.36}$$

$$\epsilon_y = \sqrt{\det\boldsymbol{\sigma}_{yy}}. \tag{5.37}$$

This is often called the geometrical emittance, since it is defined with geometric coordinates. The geometrical emittance is preserved in the case of no coupling. However, only the statistical properties of a beam's projection onto a detector screen are accessible in an experiment, such as

- $\langle x \rangle$ - mean beam position
- $\langle x' \rangle$ - mean beam pointing
- $x_{rms} = \sqrt{\langle x^2 \rangle}$ - RMS beam size
- $x'_{rms} = \sqrt{\langle x'^2 \rangle}$ - RMS beam divergence
- $\langle x\, x' \rangle$ - correlation between transverse position and angle.

With Eq. 5.32, a clearer definition of the RMS phase-space emittance can be given as

$$\epsilon_x = \sqrt{\langle x^2 \rangle \langle x'^2 \rangle - \langle x\, x' \rangle^2}. \tag{5.38}$$

Analogous to Fig. 5.2, the emittance represents an ellipse with RMS-properties, containing a certain fraction of the particle distribution. The emittance defined by the RMS covers a fraction of 68 % of the particles in the case of spatial and angular Gaussian distributions. Unless otherwise stated, the term 'emittance' in this thesis refers to this definition of emittance.

All phase-space evolutions, resulting in changing beam sizes and divergences, are equivalent to ellipse transformations. Due to the conservation of the emittance, the phase-space volume is conserved. However, this is only true if there is no longitudinal momentum change and the energy variations are sufficiently small. In accelerating modules, the particles' longitudinal momentum increases while their transverse momentum remains constant. As a result, the angle between the direction of motion and the design orbit decreases, as does the emittance. This effect is known as adiabatic damping. Multiplying the geometrical emittance by p/m_0c results in the normalised emittance

$$\epsilon_N = \frac{p}{m_0 c}\epsilon = \beta_r \gamma_r \epsilon, \tag{5.39}$$

with γ_r being the relativistic Lorentz factor and $\beta_r = v/c$ the ratio of the velocity v to the speed of light. ϵ_N is conserved during acceleration. However, several effects in the experiment can cause emittance degradation. Section 6.2 discusses the relevant effects for this thesis.

6 ELECTRON BEAM TRANSPORT WITH AN ACTIVE PLASMA LENS

Electron beams generated by LPA, such as the experimentally demonstrated beams in Sec. 4, have large intrinsic divergences and energy spreads when compared to those in conventional accelerators. They suffer from significant chromatic emittance degradation in a free drift, proving them unsuitable for applications [108, 109]. To capture these beams as soon as possible, a compact and strong focusing element is required. APLs, which provide single-element capturing with symmetric strong focusing gradients, are one possible solution to this problem and were used in the experiments. Section 6.1 provides an introduction into the principles of APLs and how they perform as a focusing device. Aside from the chromatic emittance growth in a free drift, there are other sources of emittance degradation, some of which are caused by APLs. Section 6.2 discusses the sources that are relevant to this work. Finally, the APL's role in the beamline will be highlighted, resulting in a modified experimental setup. Section 6.3 presents the setup for performing slice emittance measurements and reconstructing the electron energy spectrum, which includes the APL.

6.1 ACTIVE PLASMA LENS PRINCIPLE

In advanced acceleration technologies, compact plasma-based acceleration units are being combined with conventional beamline elements. Plasma focusing is a modern approach for replacing conventional quadrupole magnets for capturing and focusing in plasma-based applications. These types of lenses are based on plasmas and require an igniting gas target in the beamline. Plasma focusing can occur by two mechanisms: (i) An electron bunch feels the transverse focusing force of a wakefield that can be driven by itself. However, the wakefield provides only linear focusing if driven by a leading laser- or particle beam in the non-linear regime. This type of lens is known as a passive plasma lens [113–116]. (ii) An azimuthal magnetic field is generated for focusing by using an externally driven axial current. This is the type of lensing accomplished by an APL. This thesis focuses on applications utilising active plasma lenses, and unless otherwise specified, the term plasma lens refers to the APL.

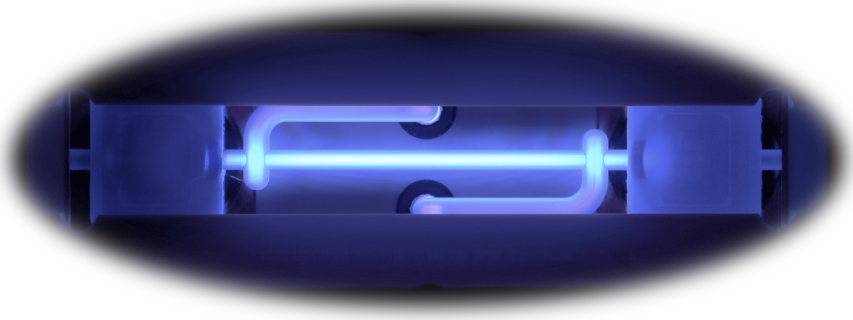

Figure 6.1: Picture of the plasma channel in an argon-filled APL during discharge.

Active plasma lenses were first recognised by Panofsky and Baker in 1950 [37], and were demonstrated on ion beams in 1991 [38]. They were proposed by Tilborg in 2015 for LPA electron beams [39] and have attracted more interest in modern particle acceleration owing to their unique advantages, which will be explained in Sec. 6.1.3. The author of this thesis contributed to several publications involving APLs [75, 76, 117, 118]. The basic setup consists of a gas-filled capillary in which a discharge current ignites a plasma. The plasma serves two functions: it transports current through the capillary and it allows the electron beam to pass through. The current in the plasma creates an azimuthal magnetic field, which allows for transverse focusing of passing charged particles such as electrons. Figure 6.1 shows a photograph of the plasma channel during a discharge in the APL used. The APL principle is presented in detail below, including its analytical derivation and focusing characteristics.

6.1.1 Analytic Derivation of the Magnetic Field

There is no symmetric focusing in a magnetic field $\mathbf{B}$ of a quadrupole magnet due to the vanishing of its curl: $\bigtriangledown \times \mathbf{B} = 0$, implying that focusing and defocusing contribute equally. A circular magnetic field, however, is required for focusing in both planes, and according to the time-independent Ampère's law

$$\nabla \times \mathbf{B} = \mu_0 \mathbf{J} \tag{6.1}$$

it can only be achieved with an axially-symmetric current density $\mathbf{J}$. In this case, the vector potential has an axially-symmetric behaviour described by $\mathbf{A} = A_r \mathbf{e}_r + A_z \mathbf{e}_z$ in cylindrical coordinates and induces the magnetic field

$$\mathbf{B} = \nabla \times \mathbf{A}. \tag{6.2}$$

The magnetic field's transverse and longitudinal components then vanish, i.e.

$$B_r = (\nabla \times \mathbf{A})_r = \frac{1}{r}\frac{\partial A_z}{\partial \varphi} - \frac{\partial A_\varphi}{\partial z} = 0 \tag{6.3}$$

and

$$B_z = (\nabla \times \mathbf{A})_z = \frac{1}{r}\left(\frac{\partial}{\partial r}(rA_\varphi) - \frac{\partial A_r}{\partial \varphi}\right) = 0. \tag{6.4}$$

Thus, the magnetic field of an axially-symmetric current $\mathbf{J}$ is composed exclusively of an azimuthal component B_φ. Using Stoke's theorem, Ampère's law from Eq. 6.1 can be transformed into an integral form given by

$$\oint \mathbf{B}\,\mathrm{d}\mathbf{s} = \mu_0 I_{\text{enclosed}}, \tag{6.5}$$

where I_{enclosed} is the current enclosed within the closed-curve integral $\oint \mathbf{B}\,\mathrm{d}\mathbf{s}$. This system is only dependent on the radial component due to the axial symmetry. Assuming a uniform current density in a conducting medium, such as a plasma, over a cylindrical volume with radius R, the enclosed current within a circular area with radius r is given by

$$I_{\text{enclosed}} = \begin{cases} \frac{\pi r^2}{\pi R^2} I_0, & \text{for } r \leqslant R \\ I_0, & \text{for } r > R, \end{cases} \tag{6.6}$$

where I_0 denotes the total current. The magnetic field inside the current flow ($r \leqslant R$) can then be calculated using

$$2\pi r B_\varphi = \oint \mathbf{B}\,\mathrm{d}\mathbf{s} = \mu_0 \frac{r^2}{R^2}, \tag{6.7}$$

and outside the current flow ($r > R$) it simplifies to

$$2\pi r B_\varphi = \oint \mathbf{B}\,\mathrm{d}\mathbf{s} = \mu_0 I_0. \tag{6.8}$$

Then the magnetic field yields

$$B_\varphi = \begin{cases} \frac{\mu_0 I_0}{2\pi}\frac{r}{R^2}, & \text{for } r \leqslant R \\ \frac{\mu_0 I_0}{2\pi r}, & \text{for } r > R. \end{cases} \tag{6.9}$$

The magnetic field's radial dependence is depicted qualitatively in Fig. 6.2. A linear increase up to $\mu_0 I_0/2\pi R$ arises within the uniform current distribution, similar to the focusing plane of a quadrupole magnet. The focusing capability of the APL is typically characterised by the constant magnetic field gradient

$$g_{ideal} = \frac{\partial B_\varphi}{\partial r} = \frac{\mu_0 I_0}{2\pi R^2} \tag{6.10}$$

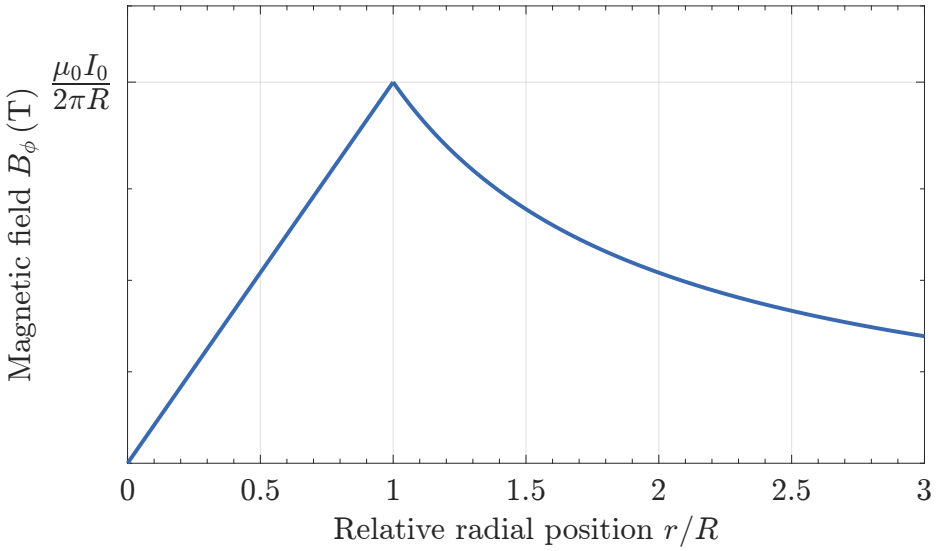

Figure 6.2: Magnetic field strength induced by a uniform current distribution confined in a capillary of radius R. Within the current flow the magnetic field increases linearly with radial position r, and outside it decreases with $\sim 1/r$.

within the current flow. An APL can provide field gradients on the kT/m-scale for sufficiently large discharge currents [39, 118]. The magnetic field drops with r^{-1} outside the current flow.

These basic formula for the magnetic field of a current-carrying medium, known as an ideal or linear plasma lens, is only valid for a perfectly uniform current density. The effects of a non-uniform current distribution are discussed in Sec. 6.2.5.

6.1.2 Capillary Discharge

The magnetic field within a uniform current distribution was derived in Sec. 6.1.1. In order for a passing electron to be influenced by this field, it needs to propagate along with the current flow. The use of a discharge through a gas-filled capillary creates a plasma to transport the current in a confined cross-section, allowing a particle beam to pass with minimal disturbances. A typical APL is composed of a few cm long, round, gas-filled capillary with a diameter of up to a couple of mm. To ionise the gas and form a current density, a **H**igh **V**oltage (HV) of up to tens of kV is applied to electrodes at both ends of the capillary for a Townsend discharge. The direction of the current flow is determined by the polarisation of the applied voltage.

The breakdown of a gas can be described by Townsend's theory [119]. Within the electric field formed by two electrodes, free electrons will be accelerated towards the anode. These electrons can collide with gas molecules, ionise them, and produce more

Table 6.1: Paschen's coefficients A and B are empirically determined constants of a specific gas species valid in a given range of the ratio of the electric field E to pressure p. Coefficients taken from [121].

GAS	A ($cm^{-1}Torr^{-1}$)	B ($V\,cm^{-1}Torr^{-1}$)	RANGE OF E/p ($V\,cm^{-1}Torr^{-1}$)
H_2	4.8	136	$15-600$
He	2.8	77	$30-250$
N_2	11.8	325	$100-600$
Ar	11.5	176	$100-600$

free electrons. Finally, an avalanche phenomenon occurs in which newly generated electrons scatter with additional gas molecules, resulting in more free electrons, until an electrically conducting pathway through the gas is established. The plasma channel is formed during the gas ionization process. The process is dictated by the strength of the electric field and the free path length of the electrons. The electrons scatter inelastically and further ionise the gas only if electrons receive enough energy from the electric field. Electrons will lose energy in many non-ionising collisions if the free path length is too short. On the other hand, if the free path length is too long, the electrons will arrive at the anode without colliding with a gas molecule.

Paschen's law [120] describes a gas's essential breakdown characteristics and can be used to estimate the capillary breakdown threshold. The breakdown voltage U_B is the voltage required to ionise the first ion and initiate the subsequent chain reaction. It is primarily determined by the gas species, gas pressure p and electrode separation d. The Paschen curve characterises the breakdown voltage based on experimentally measured data. It can be obtained for a given gas species by [121]

$$U_B(p\,d) = \frac{B}{\ln(A\,p\,d) - \ln(\ln(1+\gamma_{se}^{-1}))} p\,d. \tag{6.11}$$

The breakdown voltage U_B is a function of the product $p \cdot d$. A and B are gas specific coefficients, as shown in Tab. 6.1, and γ_{se} is the secondary emission coefficient for ions that depends on the electrode material.

Paschen's curves for the gas species hydrogen, helium, nitrogen and argon are depicted in Fig. 6.3. For large values of $p \cdot d$, the breakdown voltage increases essentially linearly. There is a limit below which a breakdown cannot occur, and each curve has a minimum at $(p \cdot d)_{min}$. In the region $p \cdot d < (p \cdot d)_{min}$, the product $p \cdot d$ is on the lower end. Owing to the mean free path length being inversely proportional to the pressure of the gas, a free electron travels a longer distance before colliding with an

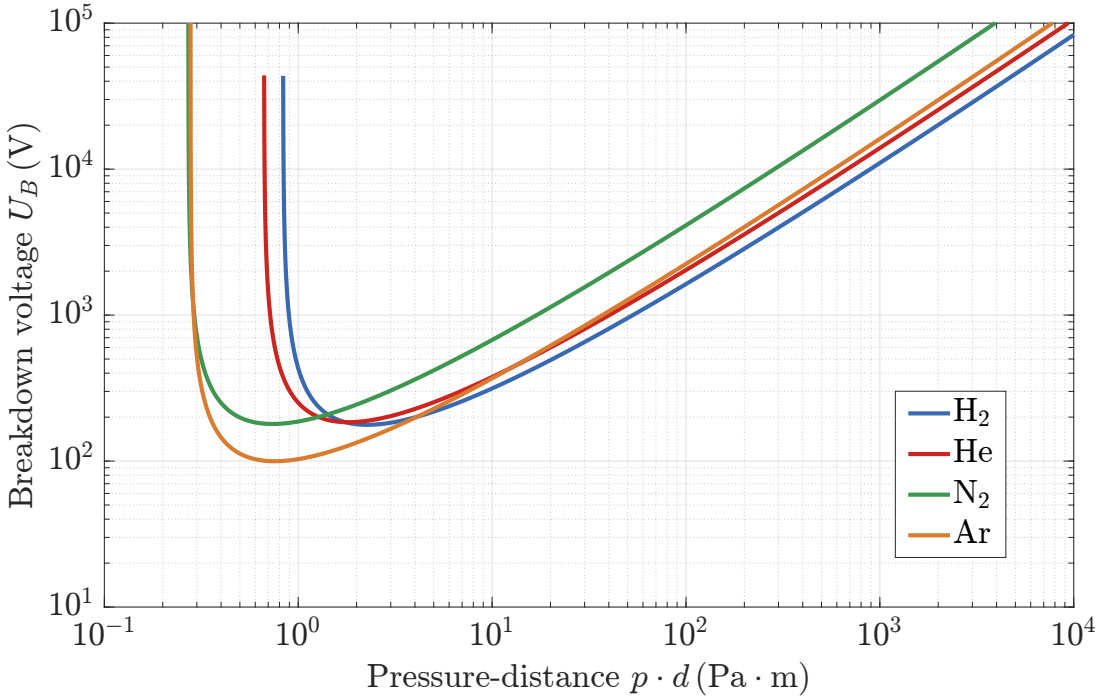

Figure 6.3: Paschen's curves for typical gas species. For hydrogen (H_2), helium (He), nitrogen (N_2), and argon (Ar), the breakdown voltage U_B evolves as a function of the product of gap distance d and pressure p. The example employs empirically determined coefficients from Tab. 6.1 as well as a common second emission coefficient of $\gamma_{se} = 0.1$.

ion as the pressure decreases. As a result, the electrons have fewer collisions. For the few collisions to cause a breakdown, a higher voltage is required. More collisions will occur when $p \cdot d > (pd)_{min}$. However, each collision reduces the energy of the free electron and makes it more difficult to ionise an ion. Therefore, a stronger electric field is required for electrons to gain enough energy to ionise ions.

Paschen's law does not cover the degree of ionization of a specific gas species. Hydrogen can often be approximated as a fully ionised gas. However, due to the greater complexity of the electron distribution in argon, the precise degree of its ionization is unknown. The degree of ionization determines the plasma density, but the radial current profile is decisive for the focusing properties of the APL. As long as the plasma is uniformly distributed, the degree of ionization has no influence on the current density. Paschen's law is only valid in an unconfined space. Then a confined capillary volume influences the breakdown behaviour and thus Paschen's law can only be considered as a rule of thumb for estimating the breakdown voltage for a capillary discharge.

6.1.3 Active Plasma Lenses for Focusing

As explained in Sec. 6.1.1, a uniform current distribution through a capillary produces an azimuthally oriented magnetic field which increases linearly with the radial position in the capillary. The principle of focusing an electron beam with an APL is illustrated in Fig. 6.4. The cylindrical volume is a gas-filled capillary with radius R and electrodes at both ends. A capillary discharge forms a plasma channel and transports the current. The flowing current creates the aforementioned magnetic field. When an electron beam passes through the plasma and therefore the magnetic field, the Lorentz force acts on it, directing it towards the capillary's centre. To achieve focusing, the technical current must be directed in the direction opposite to that of the electron beam. In the case of the other current direction, the electron beam will be defocused. Because the direction of the Lorentz force is determined by the sign of the traversing charge, an APL can also be used for positively charged beams. A current direction that defocuses electrons will focus positive charged particles, and vice versa.

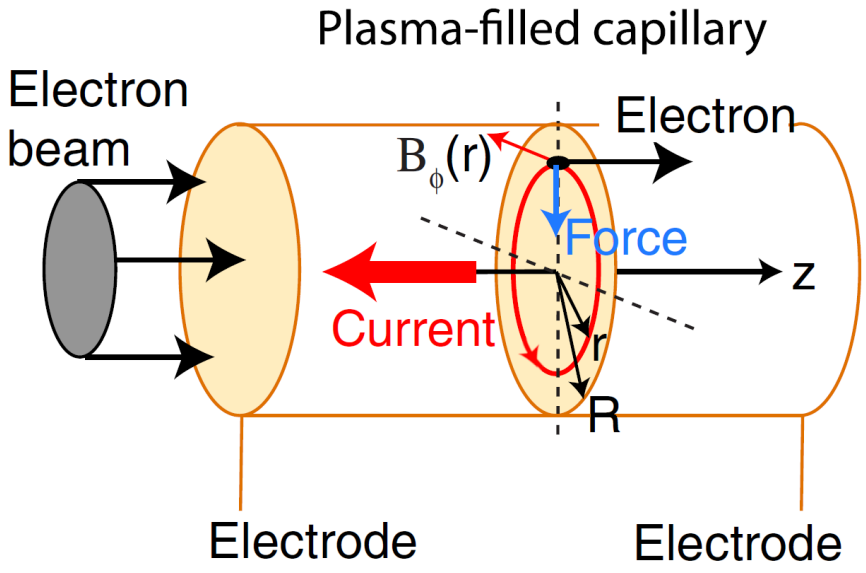

Figure 6.4: A schematic representation of a current-based plasma channel for symmetric electron beam focusing. A plasma channel is formed when a plasma ignites between two electrodes inside a gas-filled capillary. The flowing current creates a magnetic field, which acts with radial focusing properties on a passing electron beam. Image adapted from [39].

APLs have a few advantages over conventional focusing devices [39]. Because the focusing strength of solenoids scales with the relativistic Lorentz factor as $1/\gamma_r^2$, they only provide weak focusing for relativistic electrons. Stronger focusing with gradients on the order of 500 T/m can be achieved by quadrupole magnets due to their

strength scaling with $1/\gamma_r$ [122]. The requirement of using a combination of multiple quadrupole magnets with opposite strengths to achieve symmetric focusing, however, greatly reduces the effective field gradient. In order to minimise chromatic emittance growth (see Sec. 6.2.2), it is crucial to use an optical setup that reduces beam divergence as quickly as possible. However, quadrupole magnets first increase divergence in one dimension, whereas ideal APLs can produce the same emittance-preserving magnetic fields in both transverse planes simultaneously. Furthermore, when compared to solenoids and quadrupole triplets, APLs have much weaker chromatic dependence, i.e. the energy-dependent change in focal length [39]. By using Eq. 6.10 for a discharge current of 1000 A and a capillary radius of 0.25 mm, a field gradient of $> 3000\,\mathrm{T/m}$ is created, as has already been successfully demonstrated [118]. These substantial gradients can be fast and easily tuned with the discharge current and used to capture highly divergent electron beams from a plasma-wakefield accelerator, making them also a viable option for high-energy compact designs.

On the negative side, an APL involves the handling of a gas flow within the beamline, and that might not be compatible with the vacuum requirements of a conventional accelerator although it is commonly practised in plasma-based accelerators. Additionally, plasma lenses have yet to be thoroughly studied. That is critical if they are to be used on a regular basis. Exact field gradient measurements for various gas species and the associated emittance growth are still being carried out. The main causes of emittance degradation in APLs are discussed in Sec. 6.2. An intense electron beam might drive a wakefield in the plasma, and the real discharge current distribution can be non-uniform. Both effects result in non-linear focusing fields and, thus aberrations become apparent. Furthermore, beam scattering with gas molecules and plasma can cause an increase in emittance. For high discharge currents or repetition rates, a significant amount of energy is transferred to the capillary in the form of heat. This can eventually lead to ablation and the destruction of the capillary. New technologies, such as the use of different capillary materials or active cooling, are needed when scaling up the average power of the discharge. Within the framework of this thesis, no damage to the APL's capabilities was expected nor observed.

As a focusing element the ideal APL yields the same transport matrix as a quadrupole magnet, i.e.

$$\mathbf{R}_{\mathrm{APL}} = \begin{cases} \begin{pmatrix} \cos\left(\sqrt{k}L_{\mathrm{APL}}\right) & \frac{1}{\sqrt{k}}\sin\left(\sqrt{k}L_{\mathrm{APL}}\right) \\ -\sqrt{k}\sin\left(\sqrt{k}L_{\mathrm{APL}}\right) & \cos\left(\sqrt{k}L_{\mathrm{APL}}\right) \end{pmatrix} & \text{for } k > 0 \\ \begin{pmatrix} \cosh\left(\sqrt{|k|}L_{\mathrm{APL}}\right) & \frac{1}{\sqrt{|k|}}\sinh\left(\sqrt{|k|}L_{\mathrm{APL}}\right) \\ -\sqrt{|k|}\sinh\left(\sqrt{|k|}L_{\mathrm{APL}}\right) & \cosh\left(\sqrt{|k|}L_{\mathrm{APL}}\right) \end{pmatrix} & \text{for } k < 0. \end{cases} \tag{6.12}$$

However, in contrast to quadrupole magnets, the focusing strengths k_x and k_y are the same, i.e.

$$k_{\mathrm{APL}} = k_x = k_y \tag{6.13}$$

$$= \frac{e}{m_0\gamma_r c}\frac{\partial B_\varphi}{\partial r} \tag{6.14}$$

$$= \frac{ec}{E}\frac{\partial B_\varphi}{\partial r} \tag{6.15}$$

This enables symmetric focusing. A thin lens approximation ($k_{\mathrm{APL}}L_{\mathrm{APL}} \ll 1$) is often applicable. Then the focal length is given as $f \approx 1/(k_{\mathrm{APL}}L_{\mathrm{APL}})$.

6.1.4 Injection with Transverse Offset

The matrix elements derived for quadrupole magnets and plasma lenses, such as those in Eq. 6.12, are generally used for beams passing through the magnetic field's centre throughout the beam optic. If the electron beam is injected with a transverse offset with respect to the APL for example, an additional transverse motion is introduced. As a result, the beam's centroid is shifted transversely. It makes no difference whether the electron or the APL is shifted relative to the other. It is simply a shift of the beam axis. The effect of an additional transverse motion must be considered because it will have an impact on the beam transport. When scattering off the electron beam focus, for example, the focal position in the transverse plane can be shifted. A simplified model describing this centroid shift is presented below.

Assuming the thin lens approximation is valid, an electron passing through the plasma lens sees a constant magnetic field. If the electron is injected with a transverse offset Δr into the APL, it witnesses the magnetic field $B(\Delta r)$ along the entire length of the lens. The maximum offset is limited by the capillary radius. In this case, the plasma lens introduces a deflecting kick in addition to the focusing properties. This

discrete transverse kick changes the direction of the electron by the angle $\Delta x'$. The magnetic field acts on the election via the Lorentz force F_L from Eq. 5.1, resulting in the equation of motion

$$\gamma_r m_e \frac{d^2x}{dt^2} = F_L = ecB(\Delta r). \tag{6.16}$$

By transforming the derivative in time into a derivative in space for relativistic particles, the left side of equation 6.16 yields

$$\gamma_r m_e \frac{d^2x}{dt^2} = \gamma_r m_e c^2 \frac{d^2x}{ds^2} \tag{6.17}$$

$$= E\frac{d^2x}{ds^2}, \tag{6.18}$$

with the electron-energy relation $E = \gamma_r m_e c^2$. For a constant pointing angle $\Delta x'$, the derivative can be expressed as $\frac{d^2x}{ds^2} = \frac{\Delta x'}{\Delta s}$, where $\Delta s = L_{APL}$ is the effective length of the APL. The electron direction is then changed by the angle

$$\Delta x' = \frac{ec}{E} \cdot L_{APL} \cdot B(\Delta r), \tag{6.19}$$

and the transverse offset Δx relative to the beam axis at distance d is given by $\Delta x = \Delta x' \cdot d$, i.e.

$$\Delta x = \frac{ec}{E} \cdot d \cdot L_{APL} \cdot B(\Delta r). \tag{6.20}$$

Equation 6.20 correlates a particle's transverse offset in the APL to a transverse shift relative to its original trajectory at a distance d.

An additional transverse kick must be taken into account because it will affect beam transport. In fact, Eq. 6.20 also denotes a method for directly probing the magnetic field within the plasma lens. The magnetic field gradient can be calculated from it by moving the APL transversely relative to the electron beam and measuring the extent of the introduced shift at a fixed distance. This method requires accurate knowledge of the beam properties and the beam being small in comparison to the capillary size. A direct measurement of the focusing strength of an APL was first performed by J.-H. Röckemann *et al.* [75, 123].

Note that the transverse kick described by Eq. 6.20 is inversely proportional to the electron energy. However, in experiments where the focusing strength of the APL is adjusted to image different electron energies into the same position, the transverse motion stays the same. According to Eq. 6.14, the focusing strength scales linearly with the electron energy E. Thus, the extent of the transverse kick is energy-independent

for a fixed focal length. This becomes clear when the definition of the magnetic field from Eq. 6.9 and the focusing strength from Eq. 6.15 are inserted into Eq. 6.20, i.e.

$$\Delta x = \frac{ec}{E} \cdot d \cdot L_{APL} \cdot \frac{\partial B_\varphi}{\partial r} \cdot \Delta r \tag{6.21}$$

$$= \frac{ec}{E} \cdot d \cdot L_{APL} \cdot k_{APL} \frac{E}{ec} \cdot \Delta r \tag{6.22}$$

$$= d \cdot L_{APL} \cdot k_{APL} \cdot \Delta r \tag{6.23}$$

$$= \frac{d}{f} \cdot \Delta r. \tag{6.24}$$

The last line used the definition of the focal length $f = 1/(k_{APL} L_{APL})$. Note that Eq. 6.24 is no longer dependent on the electron energy as long as the focal length remains constant.

This has important implications for the X-ray source based on Thomson scattering presented in Pt. III where various electron energies are imaged. The spatial overlap position for the imaged electron energy is fixed when the focusing strength of the plasma lens is changed accordingly. Furthermore, a jitter in focusing strength only causes a jitter of electron energy in focus but no change of the spatial overlap position. However, a jitter in the transverse source position translates to a jitter of the transverse focal position. The transverse motions are primarily determined by the focusing geometry, and their extent can be reduced by increasing the focal length. An additional transverse motion also has consequences on the resolution of the emittance measurement in Sec. 7.1.3. Section 7.1.4 discusses the effects of offsets in beam position and beam direction for the dispersed focal spot with respect to the emittance measurement.

6.2 SOURCES OF EMITTANCE DEGRADATION

The beam emittance requirements for various accelerator applications vary. **F**ree-**e**lectron **L**asers (FELs) and linear colliders require very high beam quality, whereas medical applications and Compton scattering generally have more relaxed beam emittance requirements. One advantage of LPA electron beams is that they have intrinsic normalised emittances on the order of 1 mm mrad, or less [124]. In a single-pass accelerator, normalised emittance never decreases, but there are sources of emittance growth that cannot be avoided. To meet the application's requirements, these sources must be understood and minimised. The main sources of emittance degradation in advanced accelerators is summarised in [125].

The injection and acceleration will have an impact on the emittance of the generated electron beams. For example, beams injected via a down-ramp are expected to have a lower emittance than beams from ionisation injection [58]. However, this section focuses on emittance degradation during beam transport, specifically on the sources caused by APL.

6.2.1 Space Charge

Space charge forces are generated by the charge distribution within a bunch [126]. These forces originate from a collective effect in which particles are repelled by charged particles of the same charge sign in the bunch. Space charge effects in accelerators are often negligible. The exceptions are low energy beams with high charge density. Conventional accelerators typically have cavities of the order of hundreds of mm, whereas the accelerating structure of LPA is typically tens of µm long. Therefore, the accelerated bunch in LPA is significantly shorter, and this increases the charge density. This can lead to a high peak current, so that space charge effects cannot be neglected [127]. In general, space charge effects introduce an additional defocusing term K_{SC} into the radial envelope equation. It can be written as [128]

$$K_{SC} = -\frac{2r_e I}{ecr(\beta_r\gamma_r)^3}, \tag{6.25}$$

where r_e is the classical electron radius, and β_r and γ_r are the relativistic factors. r denotes the transverse size of the electron bunch and I is the beam current. The negative sign indicates that the space charge term adds a defocusing contribution to the envelope equation. It scales inversely with the beam radius r because smaller beam sizes have a higher charge density and are thus more affected. According to Eq. 6.25, the defocusing force scales with the beam current and is strongly suppressed at higher energies. This suppression can be understood by viewing the bunch from different reference frames. Higher energy causes more relativistic length contraction in the lab frame, implying a lower charge density and thus less space charge in the rest frame. In general, the space charge force increases emittance. Space charge effects can often be neglected during the LPA stage due to charge screening caused by the positively charged ion background. The used LPA source generates electron beams with energies above 30 MeV and total beam charges less than 10 pC. As particle tracking simulations with **A** **S**pace Charge **Tr**acking **A**lgorithm (ASTRA) [129] did not show any observable effect by space charge, they are excluded throughout this thesis.

6.2.2 Chromaticity

Emittance growth due to chromaticity is one of the biggest challenges in LPA, as it quickly makes them unusable for applications [108, 109]. Chromaticity refers to the energy-dependent dynamics of the electron beam within the beam transport. Such effects can be seen in both free drifts and basic focusing elements like the APL. As explained below, during beam transport, a chromatic contribution to the initial emittance $\epsilon_{n,0}$ is commonly represented by a quadratic sum, such that

$$\epsilon_n = \sqrt{\epsilon_{n,0}^2 + \epsilon_{n,chr}^2}, \tag{6.26}$$

where ϵ_n is the total normalised emittance and $\epsilon_{n,chr}$ is the contribution of chromatic emittance growth.

Unlike in conventional accelerators, the combination of high divergences and broadband energy spectra, as was the case for the LPA beams described in Sec. 4, results in a severe emittance growth in a free drift after the source. The following consideration follows the work of [108, 109]. Analogue to Eq. 5.39, the normalised emittance in the case of an electron bunch with finite energy spread can be written as $\epsilon_n = \langle \beta_r \gamma_r \rangle \epsilon$. However, this approximation does not hold for LPA electron beams with large beam divergences and energy spreads. Assuming relativistic electron beams ($\beta_r = 1$) and no correlation between energy and transverse position, the projected squared normalised beam emittance can in general be written as

$$\epsilon_n^2 = \langle \gamma_r^2 \rangle \langle x^2 \rangle \langle x'^2 \rangle - \langle \gamma_r \rangle^2 \langle x\, x' \rangle^2, \tag{6.27}$$

with the conventions from Sec. 5.3. By using the definition of the relative energy spread

$$\sigma_E^2 = \frac{\langle \gamma_r^2 \rangle - \langle \gamma_r \rangle^2}{\langle \gamma_r \rangle^2}, \tag{6.28}$$

Eq. 6.27 can be rewritten as

$$\begin{aligned} \epsilon_n^2 &= \langle \gamma_r \rangle^2 \sigma_E^2 \langle x^2 \rangle \langle x'^2 \rangle + \langle \gamma_r \rangle^2 \langle x^2 \rangle \langle x'^2 \rangle - \langle \gamma_r \rangle^2 \langle x\, x' \rangle^2 && (6.29)\\ &= \langle \gamma_r \rangle^2 (\sigma_E^2 \langle x^2 \rangle \langle x'^2 \rangle + \epsilon^2) && (6.30)\\ &= \langle \gamma_r \rangle^2 (\sigma_E^2 x_{rms}^2 x_{rms}'^2 + \epsilon^2), && (6.31) \end{aligned}$$

where ϵ is the geometric emittance from Eq. 5.38. The second term in Eq. 6.31 is the original squared normalised emittance, which is conserved during drift. The first term is the chromatic contribution $\epsilon_{n,chr}^2$ and describes the emittance growth during a drift depending on the energy spread σ_E, the beam size x_{rms} and the divergence x'_{rms}.

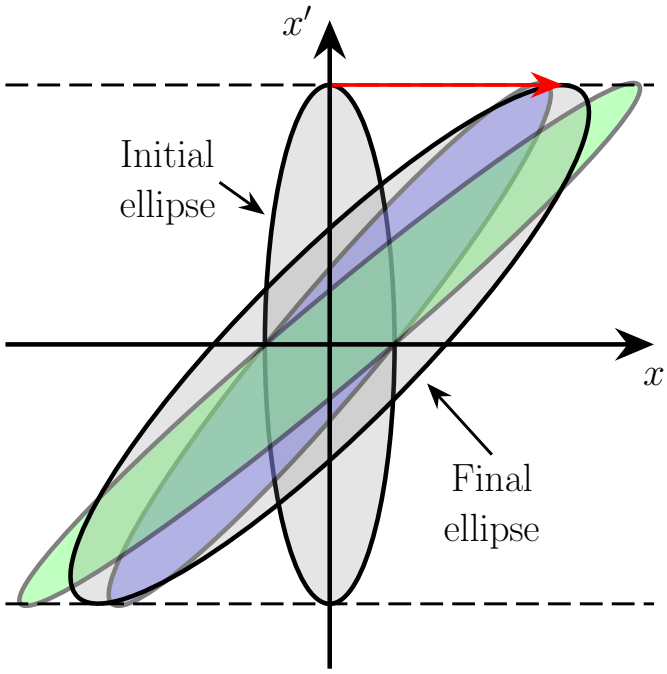

Figure 6.5: The principle of chromatic emittance growth in a free drift is depicted schematically. The initial ellipse is cut into various energy slices (depicted as a green and blue ellipses). In a free drift, the divergence x' remains constant while the beam size x grows, as shown by shearing the ellipse. The red arrow indicates the shearing in a free drift, but ellipses shear at a different speed depending on the energy. The sum of these ellipses can be approximated by a final ellipse that occupies a larger area in phase space, implying that the projected emittance has increased.

In beams with high divergence, the beam size is dominated by the divergence after a short drift s and can be written as $x_{rms} \approx x'_{rms} \cdot s$. Then Eq. 6.31 yields

$$\epsilon_n^2 \approx \langle \gamma_r \rangle^2 \, (\sigma_E^2 \cdot x'^4_{rms} \cdot s^2 + \epsilon^2). \tag{6.32}$$

In the case of low initial geometric emittance ϵ, such as beams from an LPA source, it can be simplified further to

$$\epsilon_n \approx \langle \gamma_r \rangle \cdot \sigma_E \cdot x'^2_{rms} \cdot s. \tag{6.33}$$

This estimate shows how the emittance can grow rapidly in a free drift of length s. The chromatic contribution grows linearly with increasing energy spread and quadratically with increasing divergence. Figure 6.5 depicts the principle of this effect. The phase-space ellipse is thought to be cut into various energy slices that overlap at beginning. These ellipses shear at different rates depending on their energy during

a free drift. When these single ellipses are added again after a drift, the resulting shape approximated by an ellipse occupies a larger volume in phase-space than the initial ellipse, implying that the projected emittance has increased. An electron beam with a central energy of 50 MeV ($\gamma_r \approx 98$), an energy spread of 50 %, and a beam divergence of 6 mrad, for example, results in a normalised emittance of approximately 176 mm mrad after a drift of 10 cm. That is an increase of 17600 % compared to typical normalised emittances of about 1 mm mrad. Strong focusing, such as with an APL, is required immediately behind the accelerating structure to minimise this chromatic contribution.

Note that Eq. 6.33 is only valid in the initial drift and does not apply inside or after a magnetic structure. Chromatic effects that result in emittance growth also exist in other beam elements, such as a focusing structure. The focusing chromaticity becomes more important due to small beta functions and strong focusing during the acceleration process [125, 130]. It describes the energy dependence of the focusing and the C-S parameters. This is exemplified in Sec. 9.2's Thomson scattering experiment, where the focusing APL serves as a chromatic filter for the electron beams. The chromatic amplitude is a measure of the chromatic error during beam transport and is quantified (to first order) in the horizontal plane x as [125]

$$W_x = \sqrt{\left(\frac{\partial \alpha_x}{\partial \delta} - \frac{\alpha_x}{\beta_x}\frac{\partial \beta_x}{\partial \delta}\right)^2 + \left(\frac{1}{\beta_x}\frac{\partial \beta_x}{\partial \delta}\right)^2}, \tag{6.34}$$

where δ is the the relative energy offset, and α_x and β_x are the C-S parameters. With this, the relative emittance growth can be expressed as [130]

$$\frac{\Delta(\epsilon_x^2)}{\epsilon_x^2} = W_x^2 \sigma_\delta^2 + \mathcal{O}(\sigma_\delta^4), \tag{6.35}$$

with ϵ_x being the initial emittance and σ_δ is the energy spread. Assuming a thin lens model in a beam optic with linear focusing, such as an ideal APL, and a focal length f, the chromatic amplitude grows by approximately $\Delta W_x = \beta_x / f$ [131]. Because in the thin lens model the beam size remains constant within the beam optic, β_x can be replaced by the constant $x_{rms} = \sqrt{\beta_x \epsilon_x}$. The relative emittance growth of an electron beam imaged to focus by an APL can then be estimated as

$$\frac{\Delta(\epsilon_x^2)}{\epsilon_x^2} \approx \frac{x_{rms}^4}{\epsilon_x^2 f^2} \sigma_\delta^2, \tag{6.36}$$

or as the absolute emittance growth

$$\Delta(\epsilon_x^2) \approx \frac{x_{rms}^4}{f^2} \sigma_\delta^2. \tag{6.37}$$

This implies that the combination of strong focusing (i.e. short focal length) and large beam size results in high chromaticity and thus high emittance growth. It should be noted that the emittance growth only applies to the projected beam. Within an energy slice, there is no emittance growth.

6.2.3 Multiple Coulomb Scattering

In contrast to conventional accelerators that operate in an ultra-high vacuum environment, LPA and the use of APLs rely on gas in the beamline to ionise plasma. Therefore, Coulomb collisions of beam particles with background plasma and gas atoms are unavoidable. These collisions cause either an elastic small-angle deflection or an inelastic collision with energy loss. Inelastic collisions occur less frequently. Multiple Coulomb scattering theory describes the longitudinal-averaged process, which is dominated by elastic scattering. As a result, the beam's divergence increases by [125, 132]

$$\frac{d\left\langle\theta^2\right\rangle}{ds} = \frac{k_p^2 r_e}{\gamma_r^2}\left[Z_i^2 \ln\left(\frac{\lambda_D}{R_a}\right) + 1.78\, Z(Z+1)\ln\left(\frac{287}{\sqrt{Z}}\right)\right], \tag{6.38}$$

where Z is the atomic number, Z_i describes the ion charge state, $R_a = 10^{-10}$ m is the atomic radius and r_e is the classical electron radius. For neutral plasma λ_D is the Debye length with k_p being the plasma wave number. The first term comes from ion scattering, while the second comes from neutral atom scattering. When assuming singly ionised plasmas, the ion scattering term can usually be neglected for heavy gases (Z>2). As can be seen in Eq. 6.38, the divergence is suppressed by higher beam energies γ_r and increases for higher plasma densities n_p due to $k_p \propto \sqrt{n_p}$. The normalised emittance growth in one transverse dimension due to the additional divergence contribution can be estimated by [125, 133, 134]

$$\frac{d\epsilon_{n,x}}{ds} = \frac{\beta_x \gamma_r}{2}\frac{d\left\langle\theta^2\right\rangle}{ds}. \tag{6.39}$$

where the C-S beta function β_x describes the horizontal transverse beam size in the plasma. This worsening in emittance occurs in both the LPA and the APL and can be reduced by using a lighter gas, such as hydrogen, or by decreasing the plasma density if the experiment allows it. The emittance growth due to scattering will be negligible inside the LPA stage for typical beam and plasma parameters, owing to the very small beta function. However, the beta function will be significantly larger during beam focusing with the APL, resulting in a larger scattering effect. In addition, the plasma for APLs is typically created by using heavier gas species such as argon with lengths of several centimetre.

Equations 6.38 and 6.39 can be used to approximate the emittance growth caused by multiple Coulomb scattering. However, this scattering regime is invalid when an electron beam does not experience multiple scattering events [135]. To investigate this, the number of collision events between an electron and the gas molecules can be calculated. For a neutral gas, the number of collision events in an APL with length L_{APL} is given by [126]

$$N_s = n_s \sigma_s L_{APL}, \tag{6.40}$$

where n_s is the atomic particle density of the gas molecules, and σ_s is the total scattering cross section. The total number of scattering events is less than 0.005 for an electron energy of 60 MeV and a 4 cm long APL filled with argon at a gas pressure of 0.1 mbar. Therefore, multiple scattering can be neglected under the experimental conditions. Although, it may become an effect to be considered for higher gas particle densities, larger scattering cross sections, or longer distances travelled through the gas.

6.2.4 Plasma Wakefields in Active Plasma Lenses

Passive plasma lenses take advantage of the strong fields within a wakefield to focus a particle beam. Although this method can provide strong focusing fields, it requires a leading laser beam with a laser strength parameter of $a_0 > 1$ or a particle beam to drive the plasma wake in a regime with linear focusing. A particle beam traversing an APL's plasma can also drive a wakefield that exhibits non-linear focusing behaviour. According to Liouville's theorem, a non-linear transformation of the phase-space increases emittance. These fields can have an impact on the driver bunch itself.

An analytic model to investigate whether wakefields cause significant non-linear aberrations in APLs was developed by [136] on the basis of a combination of linear and non-linear plasma wakefield theory. When non-linear aberrations are negligible, emittance growth is also negligible. Therefore, the requirement of emittance preservation is expressed as $g_{APL} \gg g_{wakefield}$, implying that the APL dominates the focusing over the non-linear focusing of wakefields. This has been reformulated to give a maximum acceptable focusing gradient of

$$g_{wakefield,max} \approx -\frac{\mu_0 c}{2} \min\left(e n_0, \frac{Q k_p^2 \sigma_z}{\pi \sigma_x \sigma_y \left(1 + \frac{k_p^2 \sigma_x \sigma_y}{2}\right)\left(1 + \sqrt{8\pi} k_p^2 \sigma_z^2\right)} \right), \tag{6.41}$$

where n_0 is the plasma density, k_p is the plasma wavenumber, Q is the beam charge. The longitudinal and radial RMS beam size inside the plasma lens are given by σ_z

and $\sigma_{x/y}$. The size of the wakefield is primarily determined by the peak current of the driver beam and the plasma density. A bunch with a high charge and small longitudinal and transverse dimensions is more likely to drive a significant wakefield. Placing an APL too close to a LPA source where σ_r did not diverge sufficiently to drive a wakefield may result in problems. Furthermore, it is advantageous to operate the plasma lens at a lower plasma density to reduce the extent of wakefields. Assuming that the beam size does not change inside the plasma lens, the corresponding absolute emittance growth in one transverse dimension can be approximated by [137]

$$\frac{d\epsilon_{n,x}}{ds} \approx \frac{\sqrt{7}\mu_0 e Q k_p^2 \sigma_z \sigma_x}{12\sqrt{2\pi}^3 m_e \sigma_y \left(1+\frac{k_p^2\sigma_x\sigma_y}{2}\right)\left(1+2\sqrt[4]{3}k_p^2\sigma_z^2\right)}. \tag{6.42}$$

Like the chromatic emittance growth, this term should be added quadratically to the initial emittance.

Equation 6.42 can be used to estimate the emittance growth caused by plasma wakefields. In the APL, the electron beam is assumed to have a total bunch charge of $Q = 4.5\,\mathrm{pC}$, a longitudinal beam size of $\sigma_z = 3\,\mu\mathrm{m}$, and a radial beam size of $\sigma_{x/y} = 1\,\mathrm{mm}$. When it passes through a 4 cm long APL with a plasma density of $10^{14}\,\mathrm{cm}^{-3}$, its normalised emittance increases by about 0.002 mm mrad. Because the experiments were carried out with a reduced bunch charge, lowest possible plasma density which still enables stable APL operation, and the electron beam filling almost the entire aperture of the plasma lens (due to the large beam divergence and the initial drift length), wakefields were estimated to be negligible.

6.2.5 Chromatic Aberrations in Active Plasma Lenses

A magnetic field gradient forms within the capillary depending on the current density. In Sec. 6.1.1 the constant gradient for an ideal APL with uniform density and temperature was derived, resulting in a uniform current density. However, this is not necessarily the case. The fundamental theory of non-uniform discharge currents is based on the work from [138, 139]. Because of the symmetry of the capillary design, no azimuthal dependency is taken into account, reducing the problem to a radial one. In a collisional model of plasma, the plasma conductivity σ_c depends on the plasma density n_e and the plasma temperature T_e via [43, 139]

$$\sigma_c = \frac{32\epsilon_0^2}{e^2 m_e^2}\frac{(k_B T_e)^{3/2}}{\ln(\Lambda)}, \tag{6.43}$$

with $\Lambda = n_e\lambda_D^3$, the Debye length $\lambda_D = \sqrt{\epsilon_0 k_B T_e/(n_e e^2)}$, ϵ_0 the vacuum permittivity, and k_b the Boltzmann constant. Since there is only a weak scaling with n_e, the plasma

temperature dominates the conductivity. The current density is then given by Ohm's law

$$J_z(r) = \sigma_c(r) E_z, \tag{6.44}$$

where E_z is a uniform electric field. Because the current density scales with $J_z(r) \propto T_e(r)^{3/2}$, this model is referred to as $J \sim T^{3/2}$-model. Typical plasma temperatures exceed 1 eV, while a capillary wall temperatures are around 0.3 eV. The exchange between Ohmic heating from the applied current and heat loss to the capillary wall determines the plasma conditions inside the capillary. The formation of the temperature gradient can be divided into four steps [137, 140]:

1. The plasma is ionised.
2. Electrons are Ohmic heated by the current.
3. Because the wall material is an electrical isolator, a virtually electron-free sheath near the wall forms. The hot electrons only transfer their heat to the ions because the electron-free sheath prevents them from directly heating the wall.
4. Ions then transfer heat to the wall, predominantly cooling the plasma near the wall. As a result, a temperature gradient is formed.

Any temperature gradient in the plasma will result in non-uniform current distribution and, as a consequence, a non-uniform focusing gradient, which is a source of emittance growth.

The magnetic field's radial dependence is depicted in Fig. 6.6, which was obtained from **m**agneto-**h**ydro**d**ynamics (MHD) simulations of temperature and current distributions in a discharged capillary. A wall temperature of 0.3 eV is assumed and the results of the simulations are analytically approximated by the simplified $J \sim T^{3/2}$-model. The magnetic field from a uniform and non-uniform current distribution have to agree at two points in this consideration. In both cases, there is no magnetic field on-axis ($r = 0$). Furthermore, all current is enclosed at the capillary wall, and the magnetic fields have to be the same. A non-uniform current distribution produces a stronger magnetic gradient near the axis and a weaker gradient near the wall when compared to a uniform current distribution. Figure 6.6 shows a gradient enhancement of approximately 35 %. However, in the $J \sim T^{3/2}$-model, the assumed wall temperature has a significant influence on the enhancement, and the theoretical upper limit 48 % is achieved by assuming a cold wall of 0 eV, i.e.

$$\left(\frac{\partial B_\varphi}{\partial r}\right)_{r=0,\max} \hat{=} 1.48 \cdot g_{ideal}. \tag{6.45}$$

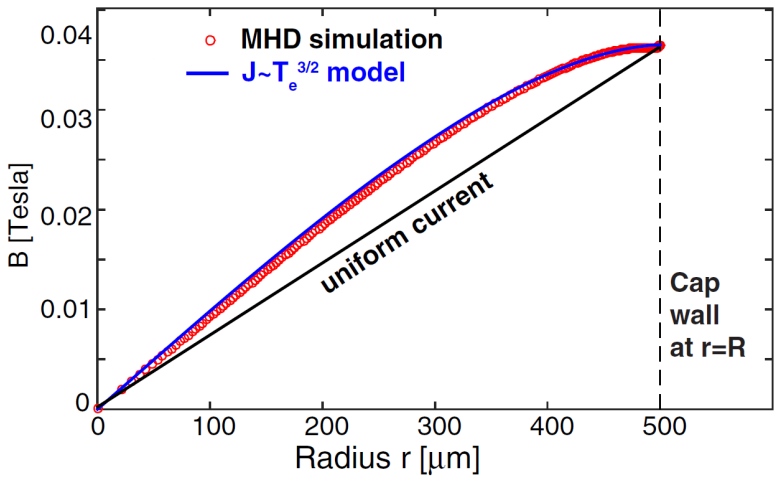

Figure 6.6: Radial dependence of the magnetic field in a discharge capillary for a wall temperature of 0.3 eV according to MHD simulations and the $J \sim T^{3/2}$-model. Here, an approximately 35 % enhancement in near-axis magnetic field was observed. Image taken from [139].

The $J \sim T^{3/2}$-model has limitations in that it does not account for different gas species and treats it as a time-independent problem. Choosing a gas species with a high thermal conductivity in comparison to its electric conductivity allows the plasma to transport heat more efficiently. The on-axis gradient increase ranges from 1 to 1.5 and is strongly influenced by current, time of measurement after discharge initiation, capillary wall temperature, and gas species [141]. Non-uniformity is expected to increase over time, reaching a plateau in the equilibrium state. The difference between different gas species is expressed in the time scales at which equilibrium is reached. In an experiment, it was directly measured that helium can have a 34 % enhancement, whereas argon can have no enhancement [117]. Based on this result, emittance preservation for an electron beam focused by an argon-filled APL is expected if operated under the right conditions.

6.3 SETUP WITH AN INTEGRATED ACTIVE PLASMA LENS

Including an APL into a setup based on LPA has several advantages. Capturing and imaging divergent electron beams is required for reducing chromatic emittance growth, but it is also a critical component for many applications. The main objective of this compact imaging device for this thesis experiment is to scatter an additional laser beam off the chromatic electron focal spot in order to realise a Thomson X-ray source. Furthermore, the APL allows the electron spectrometer to be used with

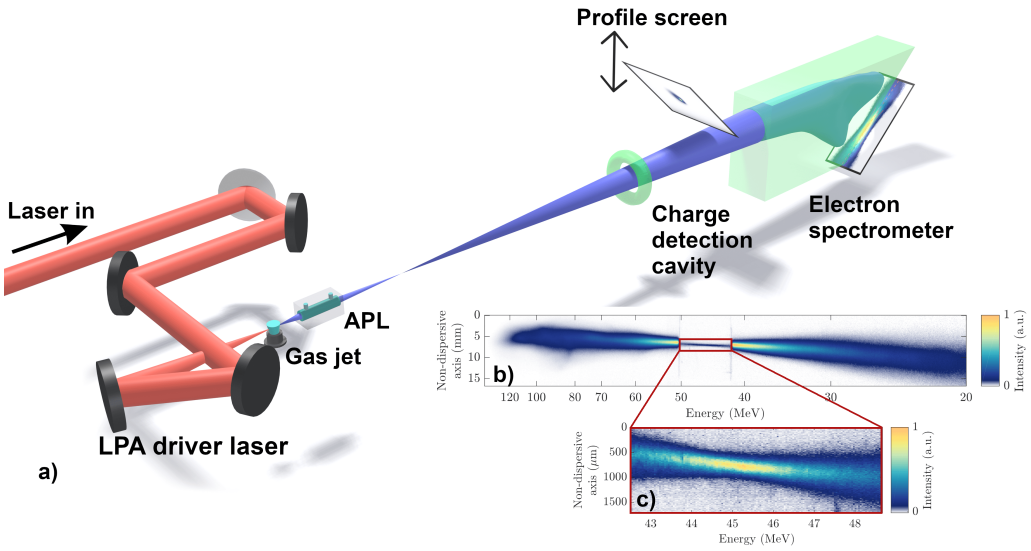

Figure 6.7: (a) The setup for characterising LPA generated electron beams is depicted schematically. To drive a laser-wakefield electron beam source, the incoming laser beam (red) is transported and focused onto a gas jet. Electrons are injected via ionisation injection and then accelerated. The generated electron beam (blue) is pointing in the same direction as the incoming LPA driver laser beam. It passes through a charge detection cavity to measure beam charge, and a profile screen can be driven into the beam axis to characterise the beam profile. An APL can capture the electron beam and image it in the LPA chamber or on the electron energy spectrometer. (b) shows the imaged electron beam profile on the electron spectrometer and to resolve the focused electron energy a high resolution screen is embedded within the lower resolution screen, as shown in (c).

imaging capabilities while also providing a tool for characterising the slice emittance. Figure 6.7a depicts the schematic setup with an APL. To inject charge via ionisation injection and accelerate the electron beam based on LPA, the LPA driver laser beam is focused onto a gas jet. The electron and laser diagnostics are identical to those described in Section 3.3. The difference is that the APL can focus the electron beam inside the LPA chamber or onto the electron spectrometer. By imaging onto the electron spectrometer the electron focal spot is dispersed in energy, as shown in Figs. 6.7b and 6.7c. Because of the chromaticity of the APL, higher energies are not yet focused, while lower energies are over focused. Section 3.3.2.3 describes the imaging systems shown in Figs. 6.7b and 6.7c (higher resolution to resolve the focal spot). In order to integrate an APL into a setup, various conditions must be fulfilled and the experiment must be designed accordingly. Section 6.3.1 explains the key considerations that must be met, while Sec. 6.3.2 presents the design of the used APL.

6.3.1 Requirements on the Imaging Setup

The schematic in Fig. 6.7a marks a starting point to design the beamline. The APL should primarily be capable of imaging the whole spectral range of the electron bunches (about 20 MeV – 100 MeV) inside the LPA chamber for Thomson scattering experiments and onto the electron spectrometer. Advantageously, the strength of the APL can be directly adjusted via the applied discharge current. Nevertheless, there are currents that are more convenient to apply. The minimum current is given by the total resistance of the discharge system combined with the discharge voltage at which the APL remains stable. This is approximately 150 A in the discharge setup used. The maximum applicable current is limited by the current density at which ablation occurs in the capillary. Experiments have shown that a discharge current of 1200 A in a capillary with a radius of 150 µm will only sustain a few discharges before melting the sapphire capillary. Since current density decreases with cross section, a larger capillary radius can prevent current densities from becoming too high at the cost of focusing strength. In this case, the reduced focusing gradient must be compensated for by increasing capillary length. Furthermore, the tuning range of the discharge current is limited by the applied discharge voltage range. To achieve a different discharge current, the experiment may need to be paused to change the total resistance of the HV system. Section 6.3.2.1 contains more information on the discharge setup.

A disadvantage of using plasma lenses is the additional gas load in the vacuum chamber and on the beam axis. The gas pressure should be kept as low as possible while operating the APL in a stable regime. During the design process, Paschen's law from Sec. 6.1.2 can be used to evaluate the required breakdown voltage for various gas species, gas pressures, and plasma lens lengths, but the optimal working pressure must be determined experimentally. Lower gas pressures also help to reduce emittance growth caused by beam scattering and wakefields in the plasma. Since the laser system and the LPA can operate at up to 10 Hz, the APL should be able to as well. The APL, like the gas jet, uses a differential pumping system to reduce the gas load into the vacuum chamber. It allows the APL to run with a constant gas flow, enabling it to be unconstrained by any system's repetition rate. Sec 3.2 describes the designed differential pumping system.

The position of the APL behind the electron beam source must be taken into account as it determines several aspects of the geometry. Aspects such as imaging magnification, electron beam size at the plasma lens entry, and high laser intensities must be weighed. Because electron beams from LPA are prone to severe chromatic

emittance growth in a free drift, it is beneficial to capture the beam as soon as possible. Furthermore, an APL with a fixed aperture closer to the source can capture beams with higher divergences or pointing jitter. Otherwise, the particle beam could clip at the APL capillary, resulting in loss of beam charge and creation of a Bremsstrahlung background. On the other hand, high laser intensity limits the minimum distance between the LPA source and the APL. The laser beam could drive a wakefield in the plasma lens or damage the APL itself. For long distances z compared to the Rayleigh length, the laser intensity I after its focal spot scales as

$$I(z) = I_0 \left(\frac{d(z)}{d_0}\right)^2 \tag{6.46}$$

$$= I_0 \left(\frac{2f^2\lambda}{D^2}\frac{1}{z}\right)^2, \tag{6.47}$$

where I_0 is the intensity in focus, f is the focal length of the focusing optic and the laser beam has a diameter D. The laser beam diameter is geometrically estimated using the relation $d(z) = Dz/f$ and is given in focus as $d_0 = 2f\lambda/D$, where $\lambda = 800\,\text{nm}$ is the wavelength of the laser [71]. According to Eq. 6.47, if a laser pulse focused with a focal length of 500 mm has an intensity of $I_0 = 5 \cdot 10^{18}\,\text{W cm}^{-2}$ in focus, the intensity decreases to about $8 \cdot 10^{13}\,\text{W cm}^{-2}$ at a distance of 5 cm and to about $2 \cdot 10^{13}\,\text{W cm}^{-2}$ at a distance of 10 cm. This level of intensity is insufficient to generate a wakefield in the APL with non-linear focusing effects, but it could damage the plasma lens holder made of **P**oly**e**ther**e**ther**k**etone (PEEK). Therefore, a ceramic plate with a hole larger than the APL aperture is placed on the APL's entry side. In our case, this prevented the laser beam from causing any visible damage to the APL, but it can cause issues for laser systems with higher average powers. To deflect the laser beam and prevent it from reaching the plasma lens, a plasma mirror, such as one consisting of a tape drive, can be used [142, 143]. However, the electron beam passes through the plasma mirror, causing emittance growth due to scattering processes.

Another constraint on the APL's position is the limited space between the gas jet and the APL. Differential pumping is used in both systems to reduce the gas load into the vacuum chamber, which takes up space. Furthermore, the magnification of the imaged electron beam is determined by the drift lengths before and after the APL. In the case of an imaging system with a single thin lens, it can be estimated as

$$M = \frac{d_1}{d_2}, \tag{6.48}$$

with d_1 being the distance from source to the lens and d_2 being the distance from the lens to the imaged plane. When imaging the beam onto the electron spectrometer at a fixed position, a shorter d_1 distance increases magnification and results in a more

Table 6.2: APL imaging parameters for the Thomson interaction point and the electron spectrometer retrieved from beam tracking simulations assuming a 4 cm long APL positioned 7.4 cm after the electron beam source. The distance to the respective focal plane is displayed along with the required focusing strength. The focal length is estimated using the thin lens model, and the required APL current is calculated using an APL with a radius of 1 mm and an imaged electron energy of 50 MeV. While the electron beam source size in the Thomson interaction point at a distance of 23 cm is magnified by a factor of 2.6, the magnification in the electron spectrometer at a distance of 259 cm is 27.5.

	THOMSON INTERACTION POINT	ELECTRON SPECTROMETER
Distance	23 cm	259 cm
Focusing strength	404 m^{-2}	296 m^{-2}
APL current (for 50 MeV)	337 A	247 A
Focal length	6.2 cm	8.5 cm
Magnification	2.6	27.5

easily resolvable focal spot. It reduces the demands on the imaging system for the slice emittance measurement, but selecting the correct focusing geometry is more important for the Thomson scattering experiment. For maximal photon yield the electron focal spot should be matched to the focal spot of the scattering laser beam. Therefore, the electron slice focal spot was experimentally matched to the scattering laser beam focal spot, which was predetermined to be about 10 µm by its focusing **O**ff-**A**xis **P**arabolic mirror (OAP). For more details on the spatial overlap between the electron beams and the scattering laser beam refer to Sec. 9.3.1. Due to the imaging requirements and the available space, the drift length from the source to the plasma lens was 7.4 cm.

To design an APL with the required geometrical boundary conditions, particle tracking simulations based on the transfer matrix formalism from Sec. 5.1 were performed. In addition, electron trajectories through a lattice of various beam elements were simulated using the program *elegant* [144]. It covers six-dimensional tracking with arbitrary beamline transfer matrices and electron density distributions. *elegant*'s capabilities include the ability to simulate random errors and coherent synchrotron radiation effects. Several simulations were run for various APL geometries and drift lengths. Furthermore, different electron beam parameters with different central energies and energy spreads were taken into account in the beam transport for imaging effects

and transporting as much charge as possible. Table 6.2 shows the results for imaging the electron beam into the Thomson interaction point at a distance of 23 cm and into the electron spectrometer at a distance of 259 cm. For the given circumstances, an APL with a length of 4 cm and a radius of 1 mm was found to be a good fit. Such an APL requires a focusing strength of 404 m^{-2} to image the electron beam into the Thomson interaction point, and a focusing strength of 296 m^{-2} to image it into the electron spectrometer. Using the thin lens approximation, this translates to 6.2 cm and 8.5 cm focal lengths, respectively. A discharge current of 337 A or 247 A is required for such an APL to focus an electron energy of 50 MeV. While the electron beam source size is magnified by a factor of about 2.6 in the Thomson interaction point, the magnification in the electron spectrometer is about 27.5. For a 1 mm APL radius, there is an exit aperture of 7.8 mrad. In the case of neglected electron beam pointing, it is capable of capturing nearly all of the charge of the generated electron beam (see Sec. 4). Increasing the aperture would imply that either the APL radius needs to be increased or the APL should be moved closer to the electron beam source. The decreased focusing strength of a bigger APL radius must be compensated for by either a longer APL or higher discharge currents. Without additional APL characterisations, neither option appears feasible. In addition, moving the APL closer to the gas jet's differential pumping cube is difficult because it increases the likelihood of a discharge from the electrode to the cube rather than through the capillary.

6.3.2 Active Plasma Lens Design

This section presents the experimental design of the APL used to investigate the slice emittance from an LPA electron beam source and to serve as a key component in the Thomson scattering experiment that follows. Figure 6.8 shows a photograph of the APL, with all parts designed to meet the requirements outlined in Sec. 6.3.1. First, the method for creating a HV discharge in a capillary is described below. The plasma lens capillary design report, including its holder, gas supply, and differential pumping system, is then shown. Finally, the APL alignment process is explained.

6.3.2.1 *Discharge Setup*

To drive the plasma discharge and supply current to the APL, a modified HV pulser setup originally designed to drive kicker magnets is used. This configuration was optimised for capillary discharges [145] and is shown in Fig 6.9 as a circuit diagram. A HV power supply applies DC voltages of up to 25 kV to the capacitors of a **P**ulse-

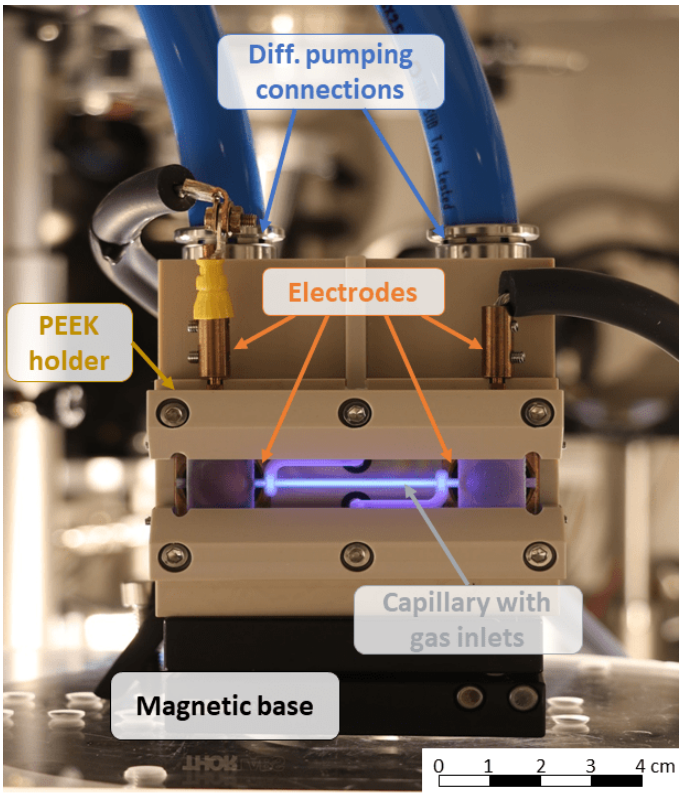

Figure 6.8: Photograph of the designed APL during a discharge. The capillary with the gas inlets is highlighted, and the blue plasma glow is typical of ionised argon. The holder for mounting the sapphire slabs with the milled capillary is made of PEEK and is installed on a magnetic base to maintain its position when working at the APL.

Forming **N**etwork (PFN) [146, 147]. The capacitors are made up of up to four 50 Ω impedance coaxial cables[1] connected in parallel. Currents of up to 1000 A can be delivered depending on the number of cables used as capacitors. Longer cables have longer discharge times due to higher capacity, resulting in longer discharge profiles. A 400 V HV trigger releases the stored energy through a hydrogen-based thyratron switch[2]. The supplied voltage is half the charging voltage due to the PFN principle. The current is then delivered to the capillary via parallel coaxial cables with the same impedance as before. Before the discharge is initiated, the resistance of the gas-filled capillary is nearly infinite. Therefore, impedance matching to the coaxial cables is required, which is accomplished by using DC resistors with the same resistance as the coaxial cables' impedance, so that $R_M = 50\,\Omega/N$, where N is the number of cables used. Following the resistors, single-wire cables are used to transport the current to

1 Philips HF-Impulskabel 4,9/17,3 FRNC-Mtl.; C ~ 101 pF/m, wave resistance 50 Ω ± 2 %
2 E2V Technologies CX1154

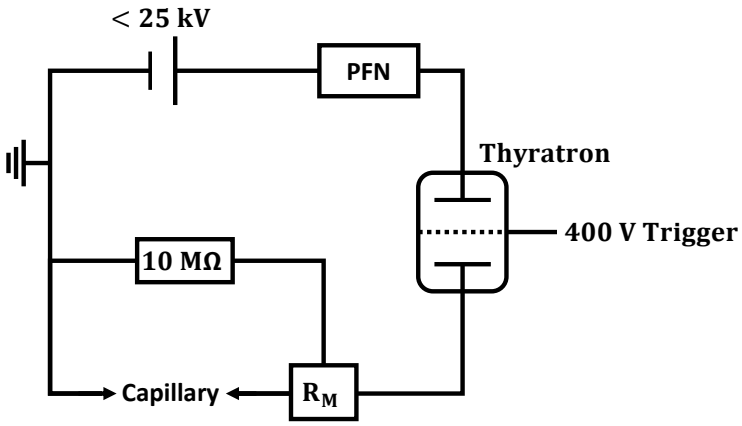

Figure 6.9: Circuit diagram of a < 25 kV DC charging a PFN via a bypass current limiting resistor of 10 MΩ. A 400 V trigger voltage applied to the thyratron relays half of the potential difference to the capillary, resulting in HV breakdown. The resistance R_M is used to match the impedance between the PFN and the capillary.

the electrodes at the capillary, which contributes an additional resistance of about 4 Ω during discharge. All of the experiments for this thesis used two coaxial cables as capacitors in the PFN ($N = 2$) and a resistance of $R_M = 21.6\,\Omega$ to match the impedance. An extra bypass-resistance of 10 MΩ is installed to prevent a potential build up that could cause the discharge to spontaneously ignite. A second hydrogen thyratron can be used to terminate the current throughput and direct it towards ground. This feature allows the discharge pulse to be shortened but was not used.

The current through the plasma lens is measured via an inductive coil [3] on the ground side of the capillary with an output of 0.5 V/A. The electrical signal is attenuated by 10 dB directly at the coil and by another 40 dB just before it is converted in an **A**nalog-to-**D**igital **c**onverter (ADC). This was required because the ADC can only read a voltage range of ±1 V. Figure 6.10a shows 500 consecutive discharge profiles with its average profile depicted in Fig. 6.10b. A charging voltage of 20 kV results in a stable current plateau at about 420 A. However, it was tuned between 11 kV and 24 kV during the experiment to image different electron energies with the APL. Because the breakdown voltage was too low for charging voltages less than 10 kV, the discharge would have became unstable. The current plateau has a duration of about 300 ns and a rise time of about 20 ns. Due to the capillary's high resistance before discharging, a reflection of the actual pulse appears as a secondary pulse. To obtain the current seen by the electron beam, it is assumed that the electron beam's timing is the same as

3 Pearson Current Monitor 6595; max. 1000 A, 2.5 ns rise time

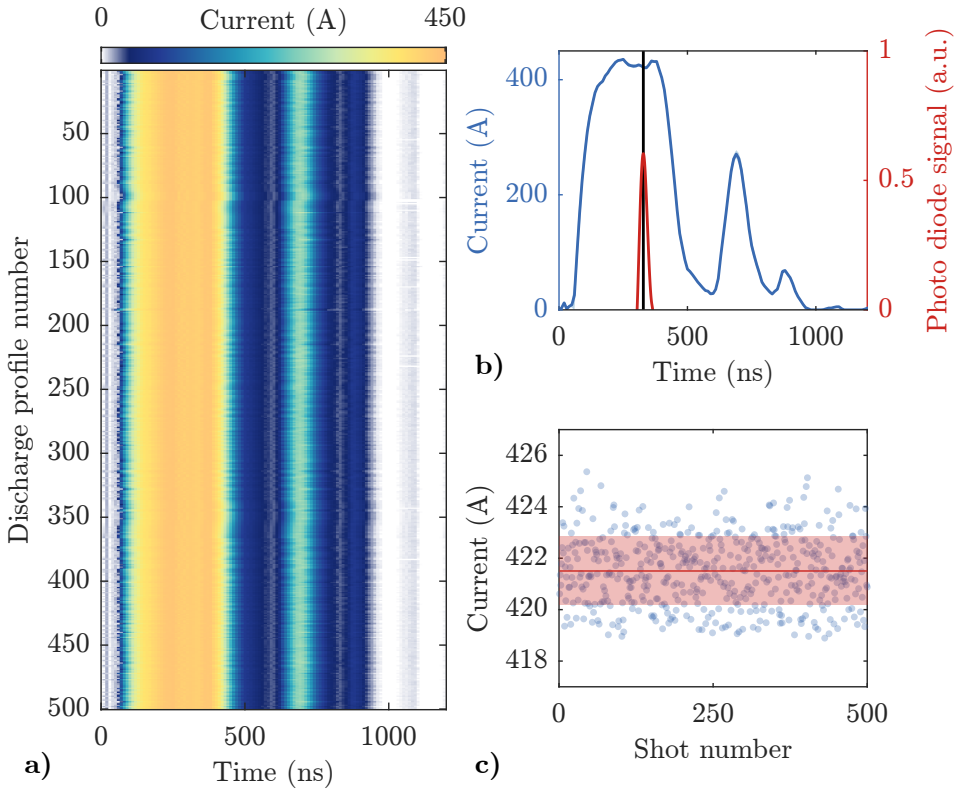

Figure 6.10: Measurement of the discharge current going through the APL at a charging voltage of 20 kV. (a) depicts a waterfall plot of 500 consecutive shots, with its average profile shown in in (b). Besides that, (b) depicts the signal of a photo diode used to evaluate the laser beam timing, i.e. the timing of the electron beam with respect to the discharge current. The diode signal's peak (vertical black line) determines when the electron beam passes through the discharge and thus what discharge current it perceives. The individual currents from the 500 shots are plotted in (c), yielding a mean current of 421.5 A with a standard deviation of 1.3 A (1.3 %).

the laser beam timing. Thus, the laser beam timing relative to the discharge profile is determined using a photo diode and sent to the same ADC, as can be seen in Fig. 6.10b. The arrangement with the photo diode is explained in Sec. 3.3.1.1. Since the electron bunch length is on the order of few femtoseconds and thus short in comparison to the discharge profile, each shot can be assigned a constant current value. The magnetic field and hence the focusing strength of the APL can be calculated from this current value. The individual currents from the 500 consecutive shots are illustrated in Fig. 6.10c, yielding a mean current of (421.5 ± 0.3) A.

6.3.2.2 *Capillary and Gas Supply*

The beamline simulations in Sec. 6.3.1 decided the focusing strength of a single focusing element required to image the electron beam into the Thomson interaction point and into the electron spectrometer. In addition, the requirements for this specific experiment were discussed. The APL must meet these requirements, resulting in a capillary length of 4 cm and a radius of 1 mm. This means that the central part of the electron spectrum ranging from about 40 MeV to about 90 MeV can be imaged on the electron spectrometer with the available tuning range of the discharge current. Changing the number of capacitors in the PFN allows for stronger and weaker focusing. Figure 6.11 shows a schematic of the plasma lens capillary design with the connected electrodes. The capillary is formed by two sapphire slabs measuring 70 mm x 20 mm x 4 mm, each with a half-cylindrical channel machined into the surface. The machining process of such sapphire crystals is described in detail in [148]. Two round inlets, one from the top and one from the bottom, are connected to the gas supply and transport gas to the capillary. The gas supply channels are 0.5 mm larger in diameter than the capillary diameter, ensuring that the gas flow is distributed uniformly. Having gas inlets on opposite sides reduces the possibility of the discharge passing through them rather than the actual capillary. Extra recesses are provided where the gas supply lines meet the capillary to ensure symmetric current flow along the capillary. The sapphire slab is longer than the capillary because it has a 13 mm diameter pocket at each end with an open backside where a copper electrode with a hole is embedded. The electrodes are connected to each end of the capillary with a 2.5 mm aperture to allow the electron beam to pass through while transporting the discharge current through the capillary. The discharge setup generates a positive pulse with a voltage of up to 25 kV that is connected to the anode downstream of the beamline. The upstream electrode is connected to ground. This kind of polarity allows for negative particles to be focused.

To connect the gas supply line and the HV to the capillary, as well as to align the sapphire plates, a holder is required. PEEK, a semicrystalline thermoplastic with excellent mechanical and chemical resistance properties, was used to build the holder. It can maintain stiffness at high temperatures and is electrically isolating. Two clamps secure the two sapphire plates to the holder, and four setscrews at each corner allow for precise capillary adjustment. O-rings seal the gas lines between the main body and the sapphire crystal at the gas inlets and on both sides of the electrodes. The APL is placed on a magnetic base, as shown in Fig. 6.8, so that its position can be maintained when work is done at the APL. Everything is mounted on a vacuum-compatible

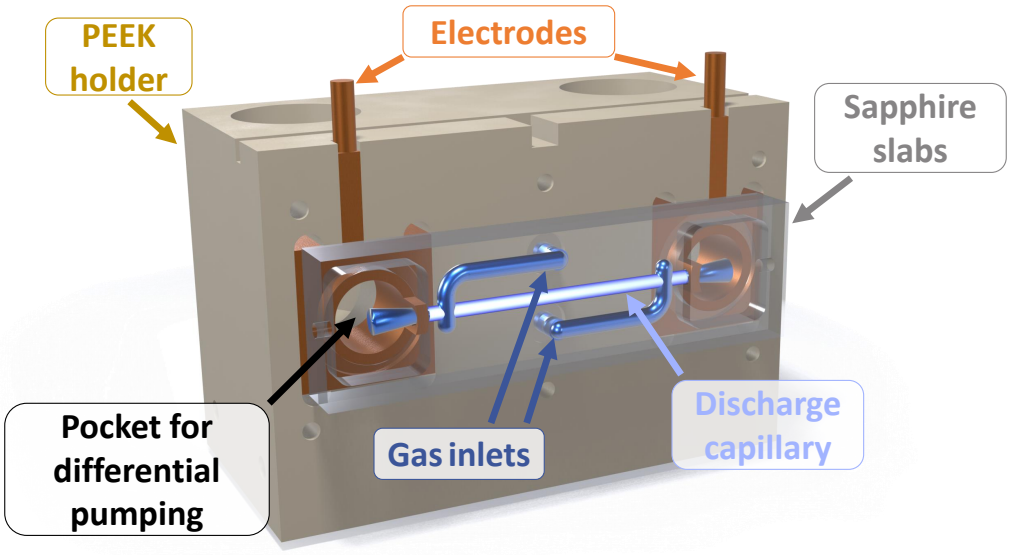

Figure 6.11: The APL design schematic shows the discharge capillary as well as the electrodes used to conduct the discharge. A pair of sapphire slabs is milled with a capillary connected to two gas inlets and pockets at both ends for differential pumping. The gas inlets fill the capillary with gas (blue). To ignite the gas into plasma (white), electrodes are located in each pocket and connected to each end of the capillary. The gas exits the sapphire structure via a pocket that can be differentially pumped through the electrode and the PEEK holder.

hexapod[4] in order to align the capillary with µm- and µrad-precision, and drive the APL out of the beamline. The APL is isolated from the metallic hexapod by an acrylic glass plate, preventing a discharge into the hexapod. The laser pulse causes no apparent damage to the capillary at 5 cm after its focal spot, as discussed in Sec. 6.3.1. To prevent the laser beam from damaging the PEEK holder and potentially coating optics in vacuum, a ceramic aperture was placed in front of the APL to dump the laser beam. The aperture has a diameter of 3 mm, which is larger than the diameter of the capillary to allow the electron beam to pass through.

Argon is used to ignite the plasma and carry the current through the confined channel. As discussed in Sec. 6.2.5, argon is the only gas species with a confirmed linear focusing field that conserves emittance. Compared to hydrogen, it is easier to ignite a plasma (see Sec. 6.1.2), and its higher mass makes it easier to pump out of a vacuum. The higher mass, on the other hand, results in principle in a more severe emittance growth due to beam scattering, but beam scattering was shown in Sec. 6.2.3 to be negligible under the experimental conditions. Because the APL must be able to

4 H-824 6-Axis Hexapod; Min. incremental motion of 0.3 µm; Repeatability of ±0.1 µm/±2 µrad.

run at least at the laser system's repetition rate of 10 Hz, the gas is supplied with a steady flow rather than from a pulsed gas supply. The gas system consists of a 2.5 L buffer volume filled with argon by a mass flow controller. It is then transported to the APL via a 10 mm inner-diameter pipe. Only then is the cross section of the gas line reduced to approximately the size of the capillary. As a result, the system's pressure drop is kept low, and the pressure in the buffer volume is similar to the pressure in the capillary. Because a constant gas flow increases the gas load into vacuum, the gas after the discharge capillary must pass through a pocket in the sapphire before exiting the APL through a 2 mm aperture. It can be differentially pumped through the electrode and holder into the same pumping system that is used to differentially pump the LPA source. The APL's closed design has the added benefit of preventing discharges outside the capillary, allowing it to operate at lower backing pressures. During the experiment, stable discharges were achieved with a pressure in the buffer volume of less than 0.1 mbar (measurement limited by the resolution of the pressure gauge at the buffer volume). With a assumed plasma temperature of 3 eV, the plasma density in equilibrium is less than $10^{14}\,\mathrm{cm}^{-3}$. As shown in Sec. 3.2, this pumping system allows the electron beam source to operate at its maximum repetition rate of 10 Hz while also using the APL with a continuous gas flow, i.e. the system's repetition is not limited by the gas load.

6.3.3 Alignment Procedure

To avoid additional transversal electron motion introduced by the APL, it is crucial to enter a centred plasma lens. Furthermore, for the Thomson scattering experiment, the electron beam must be imaged on-axis because it determines the direction of the generated X-ray beams. Because the LPA driver laser beam defines the beam axis, the laser light passing through the APL was examined in a far field. The light throughput was maximised by moving and rotating the plasma lens transversely while ensuring that the laser light was central. Similarly, the on-axis position is marked on the image of the profile screen. The APL is driven out of the beamline with the hexapod before an experiment begins. The electron beams are optimised for the experiment's demands while pointing centred on the profile screen. The APL is then moved into the beamline and the electron beams are focused on the profile screen. Small adjustments to the APL's position were made to fix the electron beam focus on the marked position on the profile screen image. The electrons, and thus the X-rays, travel along the beam axis, ensuring that the electrons enter the electron spectrometer centrally and the X-rays reach the X-ray detector.

7 IMAGING AND EMITTANCE MEASUREMENTS

The initial phase-space, including emittance, are important parameters for describing an electron beam, and quantifying them is critical for LPA-based accelerator applications. Compact FELs, for example, require normalised emittances of 1 mm mrad or less. However, this is a requirement for the slice emittance, and in certain cases, the projected emittance can be higher [149]. The energy spread in a Thomson scattering process can be effectively reduced by chromatic filtering in an APL [40, 41], making the slice emittance a more decisive quantity. Furthermore, to reconstruct and understand the scattering process in simulations, the designed Thomson X-ray source necessitates knowledge of the electron energy spectrum and the initial phase-space.

Due to the nature of beams from LPA, conventional emittance measurement methods are challenging, and only a few direct measurements were performed. The pepper-pot technique is one option for measuring direct emittance, but chromatic aberrations and high beam energies limit its resolution to 1.1 mm mrad [150, 151]. Multi-shot scanning techniques, such as a conventional quadrupole scan, can fail in the presence of shot-to-shot fluctuations and large energy spreads. Several indirect measurements were performed, such as spectral analysis of X-ray betatron or Compton radiation, but these techniques rely on various assumptions and simulations [124, 152, 153].

A single-shot method for directly measuring slice emittance [107] is enabled by using an APL for beam imaging. Furthermore, the plasma lens makes it possible to measure an electron energy spectrum from an imaging electron spectrometer that is less distorted by beam divergence and electron energy spread. Section 7.1 describes this method, and Sec. 7.2 shows the experimental results of the reconstructed initial beam properties and electron spectrum.

7.1 EMITTANCE MEASUREMENT METHOD

This section describes the method used to measure the slice emittances of the electron beam used in the Thomson scattering experiment. The setup's beam transport matrix is shown in Sec. 7.1.1 and is required for emittance measurements using a quadrupole-scan or the single-shot method, introduced in Sec. 7.1.3 with an example shot. Section 7.1.4 discusses the reconstruction errors due to imaging and detection effects.

7.1.1 Definition of the Beam Transport

A transport matrix R, as introduced in Sec. 5, can be used to express a particle's motion through a beamline with linear beam dynamics. Since the motion is assumed to be transversely decoupled, each transverse mean position and mean direction at any position s can be calculated as

$$\langle x_s \rangle = R_{11} \langle x_{s_0} \rangle + R_{12} \langle x'_{s_0} \rangle \tag{7.1}$$

and

$$\langle x'_s \rangle = R_{21} \langle x_{s_0} \rangle + R_{22} \langle x'_{s_0} \rangle , \tag{7.2}$$

where $\langle x_{s_0} \rangle$ and $\langle x'_{s_0} \rangle$ are the mean position and mean direction at the initial position s_0, respectively. In this case, s_0 denotes the end of the plasma target where the beam is accelerated and R_{ij} with $i, j \in 1, 2$ are the elements in the transport matrix given by the optical elements. It should be noted that the matrix elements depend on the electron energy E. The beam size, divergence and correlation are determined by the second central moments

$$\langle x_s^2 \rangle = R_{11}^2 \langle x_{s_0}^2 \rangle - 2R_{11}R_{12} \langle x_{s_0} x'_{s_0} \rangle + R_{12}^2 \langle x'^2_{s_0} \rangle , \tag{7.3}$$

$$\langle x'^2_s \rangle = R_{21}^2 \langle x_{s_0}^2 \rangle + 2R_{21}R_{22} \langle x_{s_0} x'_{s_0} \rangle + R_{22}^2 \langle x'^2_{s_0} \rangle \tag{7.4}$$

and

$$\langle x_s \, x'_s \rangle = R_{11}R_{21} \langle x_{s_0}^2 \rangle + (R_{11}R_{22} + R_{12}R_{21}) \langle x_{s_0} x'_{s_0} \rangle + R_{12}R_{22} \langle x'^2_{s_0} \rangle . \tag{7.5}$$

Then the RMS beam size and divergence, measured on a scintillating screen at a position s, are given by $x_{\mathrm{rms},s} = \sqrt{\langle x_s^2 \rangle}$ and $x'_{\mathrm{rms},s} = \sqrt{\langle x'^2_s \rangle}$. Therefore, the beam size at any given position correlates to the initial beam properties and thus to the conserved geometrical beam emittance (see. Eq. 5.38). The initial beam parameters, including the emittance, can be found by measuring the beam size for varied transfer matrices.

The total transfer matrix is the product of all single beamline elements, i.e.

$$\mathbf{R}(E) = \mathbf{R}_{\mathrm{drift}}(d_m(E)) \cdot \mathbf{R}_{\mathrm{drift}}(d_2) \cdot \mathbf{R}_{\mathrm{APL}}(k(E)) \cdot \mathbf{R}_{\mathrm{drift}}(d_1). \tag{7.6}$$

In the experiment, there is a drift of length $d_1 = 7.4\,\mathrm{cm}$ from the electron beam source to the APL. The electron beam is then captured by an APL with a length $L_{\mathrm{APL}} = 4\,\mathrm{cm}$

and an energy-dependent focusing strength $k(E)$. Another fixed drift specifies the distance between the APL's exit and 50 cm before the dipole magnet of the electron spectrometer. Finally, $d_m(E)$ represents the energy-dependent path length 50 cm before and inside the electron spectrometer, as determined by tracking simulations for the applied magnet current. The final transport matrix reads as

$$\begin{aligned}\begin{pmatrix} R_{11}(E) & R_{12}(E) \\ R_{21}(E) & R_{22}(E) \end{pmatrix} = &\begin{pmatrix} 1 & d_m(E) \\ 0 & 1 \end{pmatrix} \cdot \begin{pmatrix} 1 & d_2 \\ 0 & 1 \end{pmatrix} \\ &\cdot \begin{pmatrix} \cos\left(\sqrt{k(E)}L_{APL}\right) & \frac{1}{\sqrt{k(E)}}\sin\left(\sqrt{k(E)}L_{APL}\right) \\ -\sqrt{k(E)}\sin\left(\sqrt{k(E)}L_{APL}\right) & \cos\left(\sqrt{k(E)}L_{APL}\right) \end{pmatrix} \\ &\cdot \begin{pmatrix} 1 & d_1 \\ 0 & 1 \end{pmatrix}. \end{aligned} \tag{7.7}$$

7.1.2 Quadrupole-Scan Method

The conventional quadrupole scan technique is useful in accelerators for calculating transverse beam emittance and characterising beam phase space parameters. By expressing the initial beam parameters in Eq. 7.3 with the C-S parameters α_0, β_0, γ_0, and the geometrical emittance ϵ, the equation yields

$$x_{rms}^2 = R_{11}^2 \cdot \beta_0 \epsilon - 2R_{11}R_{12} \cdot \alpha_0 \epsilon + R_{12}^2 \cdot \gamma_0 \epsilon. \tag{7.8}$$

The initial beam parameters and the emittance are reconstructed by varying the transfer matrix R while measuring the transverse beam size x_{rms}. The tracking software *elegant* was used to simulate a theoretical quadrupole scan using the APL and the profile screen. The transfer matrix is given by Eq. 7.7 with $d_m = 0\,\text{m}$ and $d_2 = 1.36\,\text{m}$. The focusing gradient dB/dr of the APL was set to focus it on the profile screen, assuming an electron bunch with a central energy of 50 MeV, a normalised emittance of 1 mm mrad, a source size of 1 µm and no energy spread $\sigma_E = 0\,\%$. The focused spot size is approximately 18 µm. When the gradient is tuned in both directions, the measured beam size on the screen increases, as can be seen in Fig. 7.1a. By scanning through a beam waist and fitting it with Eq. 7.8, the initial beam parameters are reconstructed within the error. However, when the energy spread is not negligible, the beam size increases dramatically because the beam sizes for non-focused electron energies overlap at the focus. For an energy spread of $\sigma_E = 5\,\%$, the measured beam waist is at about 1 mm and the quadrupole scan results in a fitted emittance of almost 100 mm mrad. Figure 7.1b depicts the beam waist and fitted normalised emittance

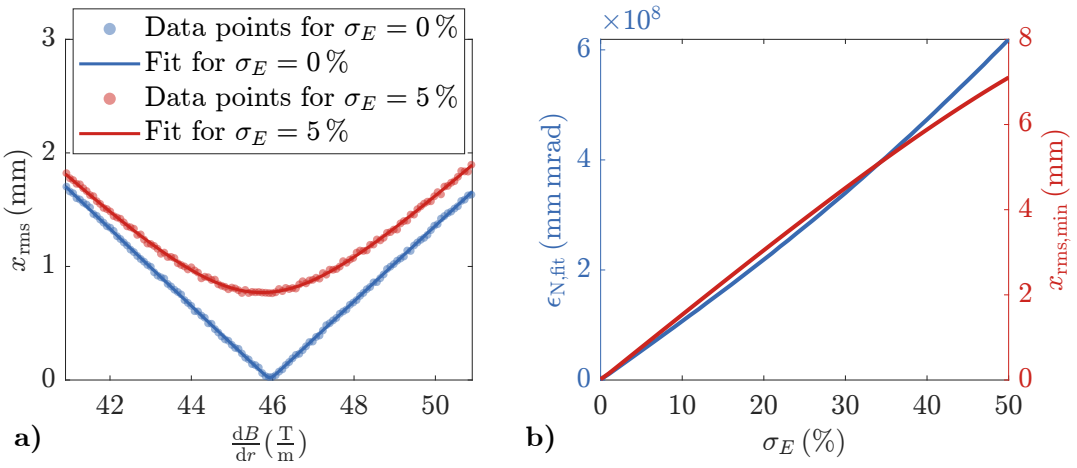

Figure 7.1: Quadrupole scan simulated with *elegant* using the APL instead of quadrupole magnets to image the electron beam. An electron bunch with a central energy of 50 MeV, a normalised emittance of 1 mm mrad and a source size of 1 µm is imaged onto the profile screen and scanned through the beam waist for an energy spread of 0 % and 5 % (a). The beam size is measured with a resolution of 10 µm and a fit is performed to calculate the projected emittance in the horizontal plane. For various beam energy spreads, the observed minimal focal spot $x_{\mathrm{rms,min}}$ and reconstructed normalised emittance $\epsilon_{\mathrm{N,fit}}$ are shown in (b).

for various energy spreads. The measured emittance quickly increases hundredfold for energy spreads of a few tens of percent. Since a quadrupole scan only measures projected emittance, the decisive emittance from a single energy slice cannot be resolved in this way. Furthermore, because it is a scanning technique, it relies on multiple shots with constant beam parameter. As a result, with its broadband spectra and shot-to-shot fluctuations, this method is often inapplicable for electrons from an LPA source. However, if the electron beam source is stable, the quadrupole scan can be performed in a dispersive section, such as an electron spectrometer. There, the measurement can be done individually for each energy slice. The slice emittance in the non-dispersive axis can then be calculated [107, 154].

7.1.3 Single-Shot Method

In the presence of percent-level energy spread, the standard quadrupole scan fails to measure dispersion-free emittance. Furthermore, because it relies on a scanning procedure, it is assumed that the beam properties remain constant throughout the scan. For an electron beam with a large energy spread and shot-to-shot fluctuations, an energy-resolved single-shot measurement is required. Weingartner *et al.* [107] developed such a technique for characterising electron beams from a plasma-based accelerator.

As in a quadrulpole scan, the transverse planes are assumed to have no correlation and are treated separately. The key components are a focusing structure and a magnetic spectrometer. An APL is used to achieve symmetric focusing in this thesis. The idea is to focus an electron beam behind the magnetic spectrometer in order to introduce an energy-dependent component to the beam transport. While one energy is in focus, the others are either under or over focused and propagate along different paths. Instead of scanning multiple linear transformations of R, such as in the quadrupole scan, the beam transport is examined for various energies in a single shot. The transport matrix is kept unchanged but is regarded as energy-dependent. As in Eq. 7.8, the expression for calculating the emittance is

$$x_{\mathrm{rms}}^2(E) = R_{11}(E)^2 \cdot \beta_0 \epsilon - 2R_{11}(E)R_{12}(E) \cdot \alpha_0 \epsilon + R_{12}(E)^2 \cdot \gamma_0 \epsilon. \tag{7.9}$$

This technique requires a multi-percent energy spread because the beam sizes of the various energy slices are detected simultaneously for measuring the emittance in a single shot. However, the single-shot method assumes that the initial beam properties are the same within the energy range required for fitting. Conclusions about the initial beam parameters for an energy slice can be drawn as a result of an energy-dependent consideration of the beamline and simultaneous measurement of the energy-dependent beam size. To retrieve the beam properties for all electron energies, the focused energy must be changed. To accomplish this, the APL focusing strength can be adjusted. However, this single-shot method can only determine the emittance for one energy slice along the non-dispersive axis. Previously, it was primarily used for electron beams from an LPA source [76, 107, 154–156].

An example of an emittance analysis for the following Sec. 7.2 is depicted in Fig. 7.2. Figure 7.2a shows a camera image of an energy-dispersed electron focal spot on the high resolution screen in the electron spectrometer. The spectrometer's magnet current was set to 171 A to centre the minimum beam waist at about 74.9 MeV on the imaging system and the intensity distribution was integrated in bins of 0.17 MeV width. Instead of using the measured discharge current to determine the APL's focusing strength, the observed electron focal spot was used. For this a matched electron beam, i.e. $\langle x_{s_0} x'_{s_0} \rangle = 0$, is assumed because it affects the position of the focused energy in the electron spectrometer (see Sec. 7.1.4.1). Because at the end of the LPA stage the beam is released into vacuum via a naturally formed soft transition, the assumption of a matched electron beam is generally justified [157, 158]. However, this uncertainty is taken into account in the total error of the obtained focusing strength. This enables the APL to have the correct focus strength for the observed imaging and avoids the errors resulting from converting the measured discharge current to its focusing strength.

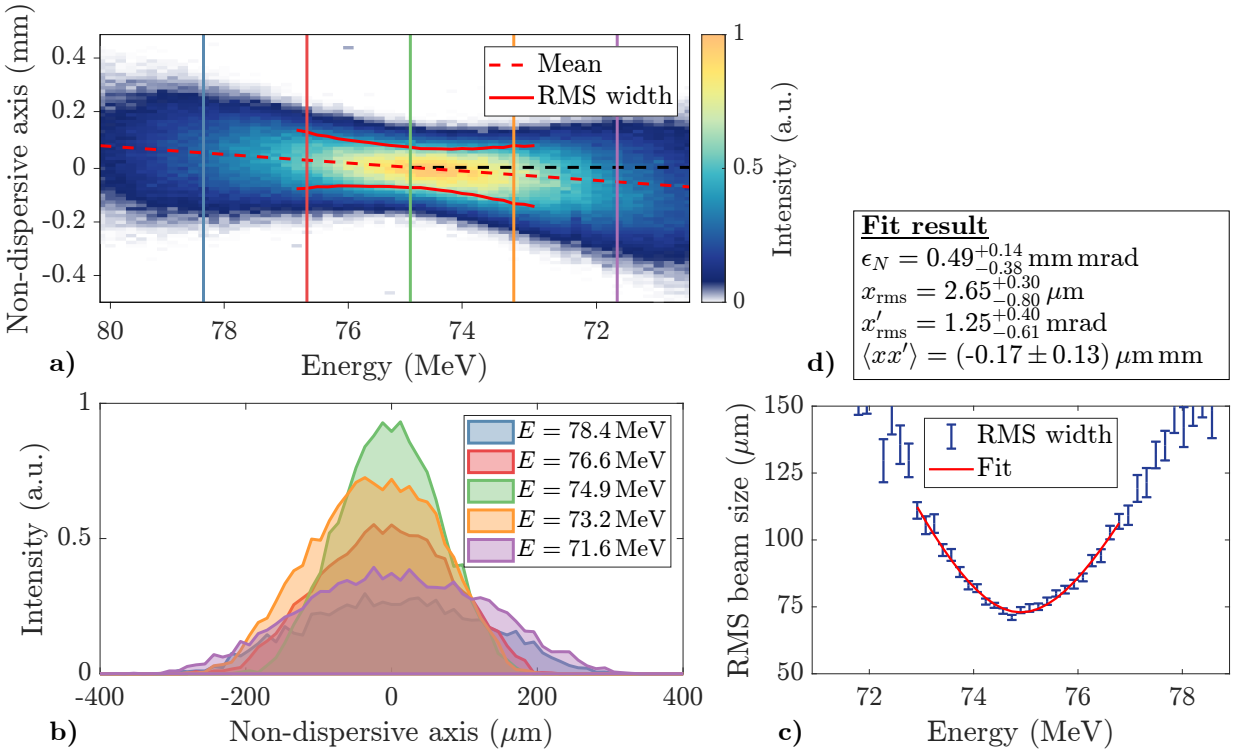

Figure 7.2: An example of a single-shot emittance measurement analysis. In the electron spectrometer, an energy-dispersed electron beam in focus is recorded on a high resolution screen. Selected non-dispersive axis intensity distributions for various energy slices are highlighted in (a) and explicitly shown in (b). In (c), the individual RMS beam sizes of each energy slice are plotted with their best fit using Eq. 7.9. The fit parameters describe the initial beam properties and correspond to the quantities listed in (d).

Due to current loss or altered focusing fields, the actual focusing strength may differ from the expected value. While non-linear focusing fields were calculated to not be an issue, the gas inlets may have an effect on the geometry of the APL, resulting in an effective length and radius, for example.

As previously stated, the RMS beam size is calculated for each energy slice individually. Figure 7.2b depicts five lineouts of different energy slices, which are also highlighted in Fig. 7.2a. Gaussian fits were used to calculate the RMS beam widths in the non-dispersive axis for each energy slice individually. An alternative to gaussian fitting to suppress the influence of camera noise and obtain the real RMS width is to calculate the direct RMS beam size of the distribution where the wings of the distribution are excluded, as done in [154]. Figure 7.2c shows the calculated beam sizes along with the errors given by the fitting routine and the imaging resolution. To reconstruct the initial beam parameters, Eq. 7.9 is used to fit the widths in a range

of ± 2 MeV around the beam waist. The dispersed electron focal spot in Fig. 7.2a results in a normalised slice emittance of $0.49^{+0.14}_{-0.38}$ mm mrad, an initial beam size of $2.65^{+0.30}_{-0.80}$ µm and an initial beam divergence of $1.25^{+0.40}_{-0.61}$ mrad for the central energy 74.9 MeV, as summarised in Fig. 7.2d. In addition to the fitting uncertainty, the errors include screen imaging resolution, electron spectrometer errors, APL focusing strength errors and errors in the focusing geometry. Furthermore, the imaging and detection effects caused by electron beam transport are taken into account. Figure 7.2a depicts the mean position of the beam in each energy bin. The beam shape appears sheared along the non-dispersive direction due the electron beam's angle with respect to the designed propagation axis. Section 7.1.4 discusses in more detail about the imaging and detection effects that occur.

7.1.4 Imaging and Detection Effects

The initial beam properties and deviations from the designed propagation axis have an impact on the image of the electron focal spot. Accurate imaging in both transverse directions is essential for accurate emittance measurements. Even small deviations in the imaging can result in large errors in the reconstructed beam properties due to the large magnifications of the electron beam. The main factors affecting the emittance measurement are discussed below in order to estimate the limits of the single shot emittance measurement. Particle tracking simulations are performed to track electron distributions from the source through the APL and onto the high resolution screen in the electron spectrometer in order to generate generic camera images. These are analysed using the same tools as for the measured data to estimate the errors in beam emittance, beam size, beam divergence, and beam correlation. Most of these considerations follow the work from [154].

7.1.4.1 *Initial Phase-Space Effects*

The effects of the initial phase-space distribution on the shape of the dispersed focal spot are discussed first. Equation 5.38 exactly defines the beam emittance in relation to the RMS beam size x_{rms}, divergence x'_{rms}, and correlation $\langle xx' \rangle$. As a result, the shape of the energy-dispersed focal spot is directly affected by these parameters. Figure 7.3 depicts the dependence of the initial beam parameters on the RMS beam widths in focus according to Eq. 7.9.

The focused electron energy is set to 45 MeV without restriction of generality, with the beam waist being primarily determined by the initial source beam size (see Fig.

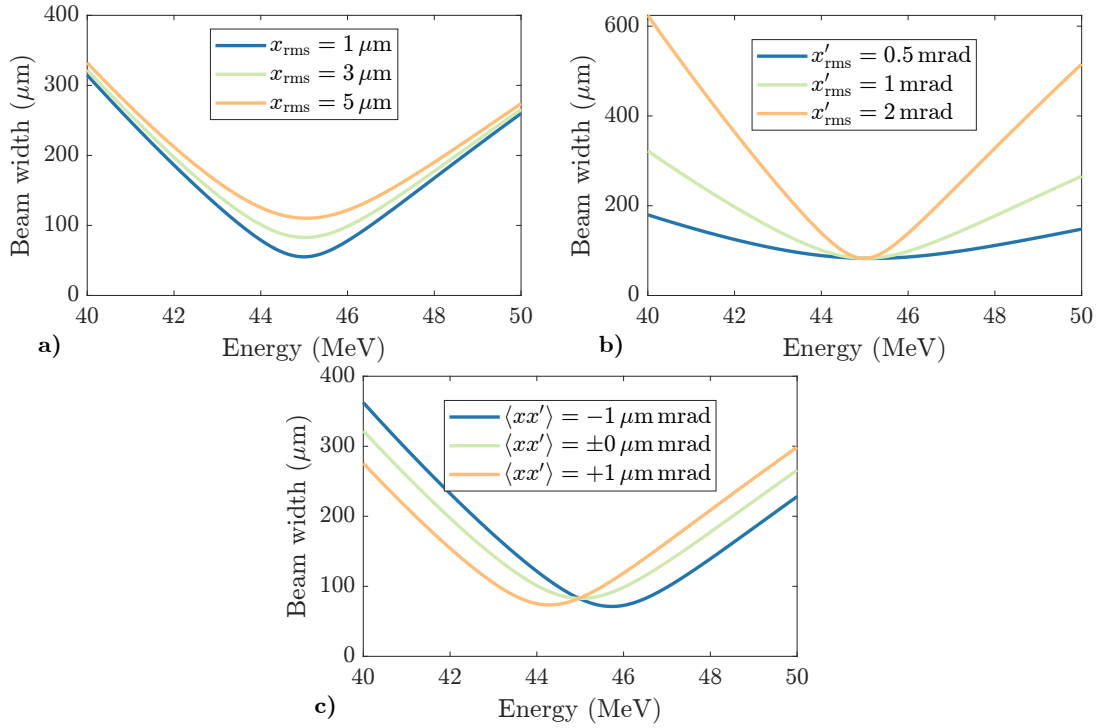

Figure 7.3: Influence of the initial phase-space distribution on the measured beam profile focused in the electron spectrometer. An electron beam focused at 45 MeV with an initial beam size of 3 µm, a divergence of 1 mrad, and no correlation is used as the starting point. The change in dispersed RMS beam shape is observed respectively as a consequence of (a) varying beam sizes, (b) divergences (b), and (c) correlations.

7.3a). The observed minimum beam size is the result of the imaging geometry's magnification. While the minimum beam size is fixed, the rate of increase for off-focus energies is mainly determined by beam divergence, as shown in Fig. 7.3b. Only the presence of a correlation in transverse phase-space causes the focused energy to shift, according to Fig. 7.3c. It should be noted that the emittance is always influenced by changing each parameter separately. When there is a non-zero correlation, the emittance decreases, leading to a reduced beam size in addition to the energy shift. Because the focused energy is assumed to be correct in the single shot method, no correlation is used as the fit function's starting value.

This emittance measurement method reconstructs the beam parameter after acceleration, but a shift in the virtual electron beam source position may occur due to the plasma-to-vacuum transition. A change in the initial drift length produces a different electron energy image and influences the shape of the final beam profile. This mismatch is equivalent to a correlation in transverse phase-space due to the additional or missing drift between the source and image plane. The measurement error of the drift length is assumed to be within 2 mm.

7.1.4.2 *Alignment Effects*

Transverse misalignment between the source position and the APL alters the electron image (see Sec. 6.1.4) and causes errors in the emittance reconstruction method. This deviation can be caused by a misplaced APL as well as the source's transverse positional jitter. The positional source jitter in the case of the demonstrated LPA source is assumed to be given by the focal spot jitter of the LPA driver laser beam, which was measured to be about 0.5 µm. The effects are the same if the source is stationary and the APL is misaligned or vice versa. A shift in the coordinate system is all that is required to describe it mathematically.

Using the simulation code *elegant*, electron beam distributions were tracked from the electron beam source through the APL and onto a screen in the electron spectrometer to produce generic images. Because the errors in the single shot method are influenced by the parameters to be resolved, the average experimentally measured values are used to define the electron bunch (see Sec. 7.2.2). A normalised emittance of 0.3 mm mrad, a beam size of 3.2 µm, and a divergence of 1.3 mrad characterise the initial phase-space. The same analysis is carried out on the generic data as on the measured data, with the assumption that there is no correlation. Figure 7.4 summarises the errors in the initial phase-space reconstruction originating from a transverse misalignment.

Figure 7.4a depicts the electron beam profile on the spectrometer screen for perfect alignment. The focused energy is set to 45 MeV, and the mean beam position (dashed red line) and the beam width (solid red line) are indicated. In the case of a horizontal position offset of $\langle x \rangle = \pm 3\,\mu m$, i.e. along the non-dispersive axis, the beam image is shown in Fig. 7.4b and Fig. 7.4d, respectively. Due to entering the APL with a transverse offset, the beam receives a dipole kick and is shifted along the non-dispersive axis by a few micrometers. Figure 7.4f displays the RMS beam widths of the single energy slices required for the emittance fit. Because the beam profile shift is along the axis where the beam width is measured, the result is quasi-unaffected by the initial offset. The error in the reconstruction of the beam emittance, beam size and divergence for a horizontal offset is shown in Fig. 7.4h. While the divergence is primarily determined by the slopes of the beam waist and exhibits no real deviation, the beam size and thus the emittance have an error of about 0.1 %. The dipole kick caused by a few micrometers of offset plays no significant role, but it is an energy-dependent effect that shears the beam profile. Following the shearing, the minimal focal spot changes, and the reconstructed beam size is incorrect.

Figure 7.4c illustrates the beam profile on the spectrometer screen for a vertical source offset of $\langle y \rangle = +3\,\mu m$, and the energy-dependent beam size is shown in Fig. 7.4e. Due to an energy-dependent dipole kick along the dispersive axis, the focused

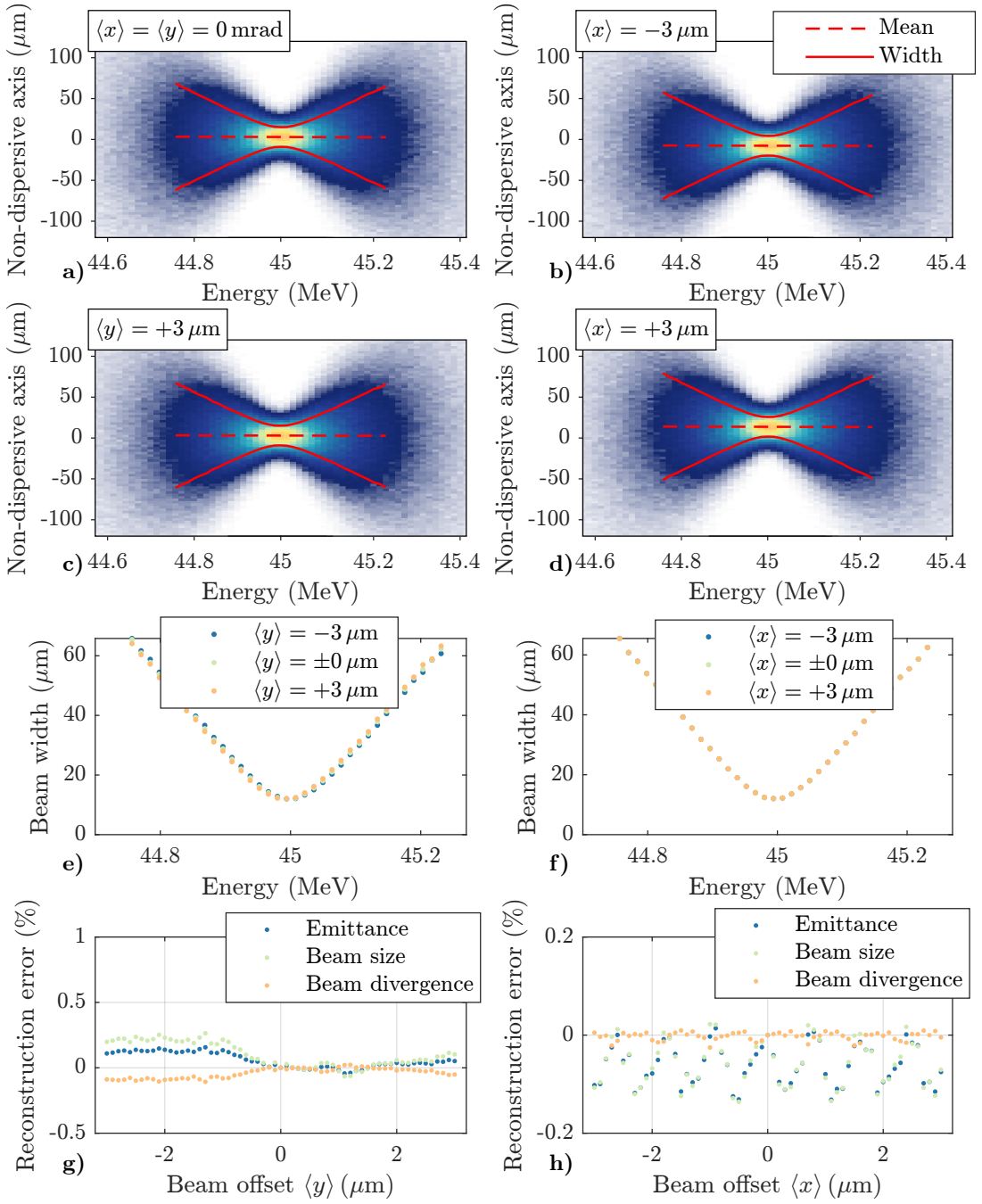

Figure 7.4: Summary of the emittance reconstruction errors originating from a transverse misalignment. Generic images were generated by tracking electron beams with a normalised emittance of 0.3 mm mrad, a beam size of 3.2 µm, and a divergence of 1.3 mrad. The simulations were performed for various transverse source offsets, such as no offset (a), a horizontal offset of −3 µm (b) and +3 µm (d), and a vertical offset of +3 µm (c). A horizontal offset causes a shift and shearing of the beam profile in the non-dispersive axis, while a vertical offset shifts the beam waist in the dispersive axis in combination with a stretching or squeezing. However, for offsets up to ±3 µm, the effects are not pronounced and thus hardly noticeable. The beam widths of the respective energy slices are shown in (e) and (f), and the reconstruction errors of the single shot emittance measurement are depicted in (g) and (h).

Table 7.1: Relative reconstruction error based on of experimentally determined mean source offset and pointing. Because the reconstruction error is directional, take note of the plus/minus signs of the errors shown.

	REL. RECONSTRUCTION ERROR		
	$\sigma(\epsilon_0)$ (%)	$\sigma(x_{rms,0})$ (%)	$\sigma\left(x'_{rms,0}\right)$ (%)
SOURCE OFFSET			
$\langle x \rangle = +0.5\,\mu m$	−0.07	0.07	< 0.01
$\langle x \rangle = -0.5\,\mu m$	−0.13	0.14	< 0.01
$\langle y \rangle = +0.6\,\mu m$	−0.01	< 0.01	−0.01
$\langle y \rangle = -0.6\,\mu m$	0.06	0.10	0.04
SOURCE POINTING			
$\langle x' \rangle = +2.4\,mrad$	26.7	24.4	1.9
$\langle x' \rangle = -2.4\,mrad$	26.0	24.0	1.6
$\langle y' \rangle = +4.4\,mrad$	−24.5	2.7	−26.7
$\langle y' \rangle = -4.4\,mrad$	51.1	5.0	44.3

energy is either shifted to higher energies with the profile shape being stretched or shifted to lower energies with the profile being squeezed. Experimentally, the shift along the energy axis cannot be distinguished from a change in imaged energy. For the source offset jitter of about 0.6 µm present in the experiment, the reconstruction errors are summarised in Tab. 7.1. This effect is barely noticeable and the errors in the emittance reconstruction are less than 0.3 %, as can be seen in Fig. 7.4g.

7.1.4.3 *Pointing Effects*

The direction of the electron beam will also affect the beam profile, just as for the deformation of the dispersed electron focal spot due to beam misalignment. The same tracking simulations as in Sec. 7.1.4.2 were run, but instead of varying the transverse source position, the pointing from the source was taken into account. Due to the electron pointing in combination with the initial drift length, the beam enters the APL with a greater offset than previously considered. The dipole kick of the APL will be more pronounced, impacting the imaged beam more. The errors in the initial phase-space reconstruction caused by an initial pointing angle are summarised in Fig. 7.5.

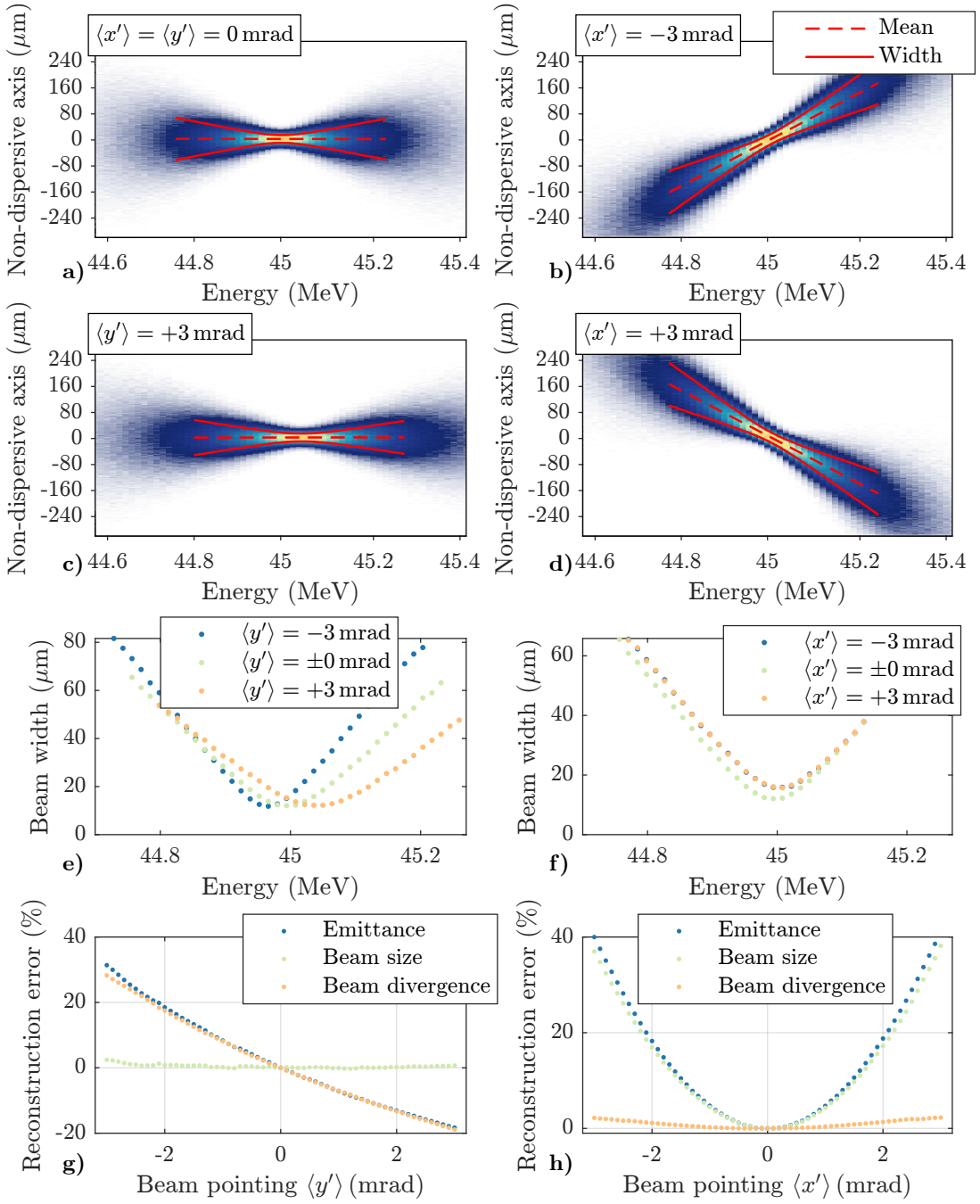

Figure 7.5: Summary of the emittance reconstruction errors originating from a pointing angle. Generic images were generated by tracking electron beams with a normalised emittance of 0.3 mm mrad, a beam size of 3.2 µm, and a divergence of 1.3 mrad. The simulations were performed for various pointing angles, such as no angle (a), a horizontal angle of −3 mrad (b) and +3 mrad (d), and a vertical angle of +3 mrad (b). In general, a pointing angle causes the beam to enter the APL with an offset, resulting in an energy-dependent dipole kick. In the horizontal it results in a shift and shearing of the beam profile in the non-dispersive axis, while in the vertical the beam waist is shifted in the dispersive axis in combination with a stretching or squeezing. The beam widths of the respective energy slices are shown in (e) and (f), and the reconstruction errors of the single shot emittance measurement are depicted in (g) and (h).

Figure 7.5a depicts the spectrometer screen's beam profile for an electron beam pointing on axis. In the case of an horizontal pointing of $\langle x' \rangle = \pm 3\,\mathrm{mrad}$, the electron beam receives an energy-dependent dipole kick in the non-dispersive axis in the APL, resulting in the beam image shown in Fig. 7.5b und Fig. 7.5c, respectively. There is noticeable shearing, with the shearing direction given by the sign of the pointing direction. The shearing angle correlates with the initial horizontal pointing and can be measured experimentally to determine the pointing with a single shot. Figure 7.5f illustrates the beam width for the various energy slices. Because width is measured along the non-dispersive axis, there is no difference between both shearing directions. However, due to shearing, electrons of different energies overlap in a given energy bin, resulting in a larger RMS beam width. Furthermore, as a result of the pointing, the beam travels on a longer path length than the design orbit, shifting the focused energy to a higher value. The deformation of the beam waist causes an error in the reconstructed beam divergence, as shown in Fig. 7.5h. The observed minimum beam width increases quadratically with the horizontal pointing angle, resulting in a quadratic deviation of the initial beam size and emittance.

Figure 7.5c shows the spectrometer image for an electron beam with a vertical pointing angle of $\langle y' \rangle = +3\,\mathrm{mrad}$. Since the electron spectrometer's dispersion axis is in the vertical, the additional dispersion from the APL's dipole kick must be added to it. A positive angle causes the beam waist to be shifted to higher energies and be stretched along the energy axis. The opposite pointing direction results in a shift to lower energies and squeezes the beam along the energy axis, as shown in Fig. 7.5e. Unless the dispersive beam profile is severely compressed or large energy bins are used, the minimum beam size remains constant. Therefore, the error on the reconstructed beam size can be neglected, as shown in Fig. 7.5g. However, the fit result will be assigned to a different energy slice, which cannot be distinguished experimentally from focusing a different electron energy. Due to the deformation of the beam waist slopes, the beam divergence is reconstructed incorrectly. Its error increases approximately linearly with the vertical beam pointing, as does the emittance error. It is worth noting that the errors from electron beam pointing are asymmetric in nature. While an additional pointing angle in the non-dispersive axis causes the reconstructed parameter to be overestimated, the direction of the pointing in the dispersive-axis determines the sign of the error.

For both, a misaligned electron beam and an electron beam with a pointing angle, the reconstruction errors in the measurement method are more severe for smaller beam divergences. Because a smaller divergence appears as a broader beam waist in focus, a larger energy range is required for the fit, making it more sensitive to

divergence deviations. As the errors caused by the source's positional jitter are small in comparison to the errors caused by pointing jitter, only the latter were taken into account for the measured data. While the shearing angle can be used to assign a specific error to beams with horizontal pointing, the average error for the mean vertical pointing jitter was used. The mean RMS pointing angles of the electron beam source were measured to be 2.4 mrad in the horizontal and 4.4 mrad in the vertical. This results in reconstruction errors of tens of percent, as presented in Tab. 7.1, dominating the total errors.

7.2 ELECTRON BEAM CHARACTERISATION

This section presents the experimental results of the reconstructed energy spectrum and slice emittances of the generated electron beam. Following the electron beam analysis from Sec. 4, it serves as a further beam characterisation. As such, the data presented here was collected following these measurements and prior to the Thomson scattering experiment from Pt. III. It should be noted that the reconstruction describes the electron beam at the source position, but only the charge transmitted by the APL can be taken into account. As a result, they do not necessarily describe the entire electron beam after the LPA stage, but rather the beam behind the APL. Both the electron energy spectrum reconstruction and the emittance measurements use the same data set. Section 7.2.1 presents the measurement procedure and the reconstruction of the electron energy spectrum. The experimentally determined slice emittances are shown in Sec. 7.2.2.

7.2.1 Electron Energy Spectrum

Various electron energies can be imaged onto the electron spectrometer to reconstruct the electron spectrum by tuning the focusing strength of the plasma lens [159]. To maintain constant detection conditions, the respective focused energies were observed on the same high resolution screen (see Sec. 3.3.2.3) by adjusting the dipole magnet current. This has the advantage of allowing the emittance measurement analysis to be performed on the same data set and thus to look for correlations. However, because the screen has a lower sensitivity than the surrounding phosphor screen, camera images with more noise are expected. Each camera image resembles the one shown in Fig. 7.2a.

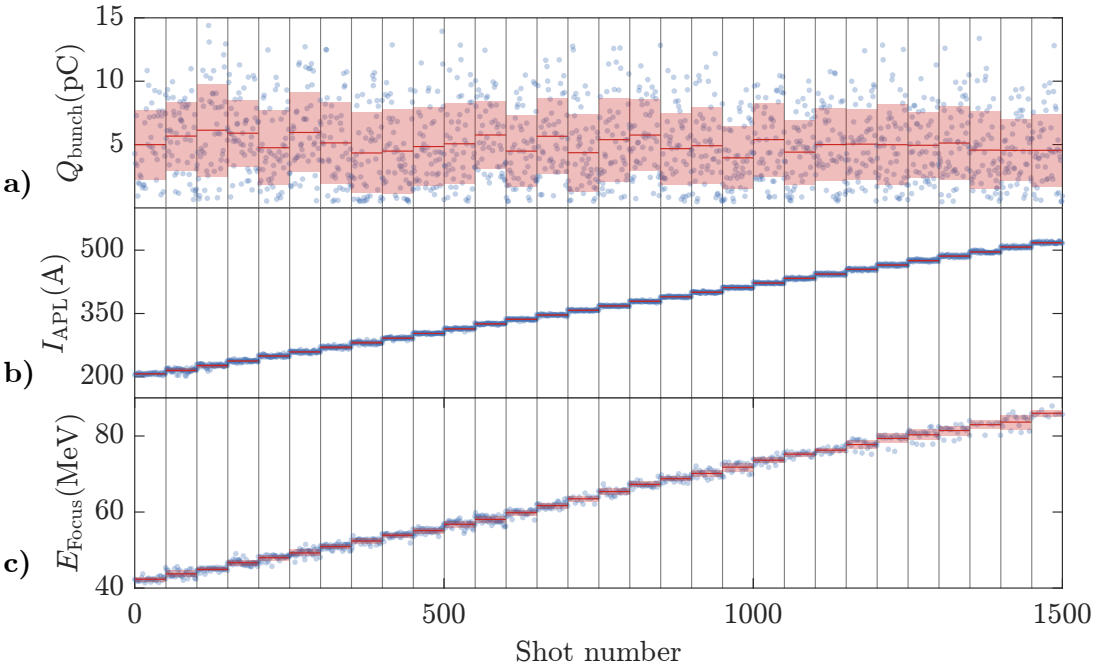

Figure 7.6: Scanning the focused electron energy on the electron spectrometer with an APL to measure the slice emittance and the electron spectrum. The beam charge of each shot is shown in (a), yielding an average beam charge of (5.0 ± 2.9) pC after the APL. The APL discharge current I_{APL} was tuned between 210 A and 520 A (b) to image various electron energies E_{Focus} onto the high resolution screen in the electron spectrometer (c).

Because a shot-to-shot jitter with varying beam charges is expected, multiple shots are required for a meaningful measurement. Figure 7.6a illustrates the beam charges during the measurement, which consists of 1500 shots and resulted in an average beam charge of (5.0 ± 2.9) pC after the APL. To reconstruct the central part of the electron spectrum piecewise, the APL current was set to about 210 A to image an electron energy of about 42 MeV, then gradually increased to 520 A to image an electron energy of about 85 MeV. The discharge setup would need to be changed to image a different energy range on the electron spectrometer. To observe the focused energy in the centre of the high resolution screen, the dipole magnet current was adjusted for each fixed plasma lens current, and 50 focused spectra were summed up. Figures 7.6b and 7.6c show the measured APL current and focused electron energy for each shot, respectively. The mean standard deviation of all APL currents yields 1.97 A (0.4 % – 1 % relative jitter depending on the applied discharge current), indicating stable beam imaging conditions. The observed electron focal spot has a standard deviation of 0.85 MeV on the electron energy spectrometer, which is primarily caused by electron beam pointing jitter along the dispersive axis.

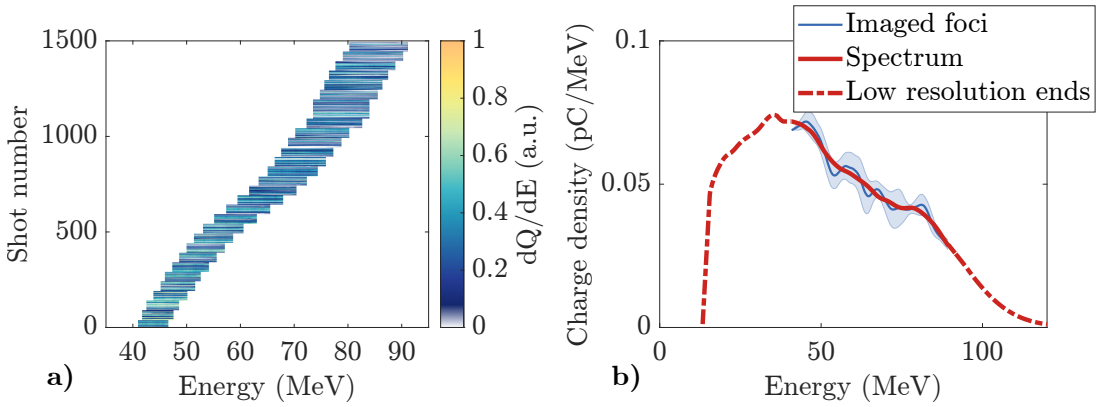

Figure 7.7: Reconstructed average electron energy spectrum from the imaging electron spectrometer. (a) depicts all focused electron energies as a waterfall plot, and the central part of the electron spectrum (blue line) was reconstructed by piecewise combining them, as shown in (b). The final spectrum (red line) was smoothed using a moving average filter compared to the spectrum of the imaged foci. The left and right ends of the spectrum (dashed red line) are both estimated from unfocused energies. As a result, at the high energy end, there is a long decay caused by beam divergence and low screen resolution.

Each focused spectrum is shown as a waterfall plot in Fig. 7.7a. Background subtraction was performed after summing up the camera images from the same imaging setting. The recorded electron energies of the various settings overlap, as shown in Fig. 7.7a. To piecewise combine them, a triangular weighting around the observed energy in focus was used. The weight of the energy in focus was set to one, and it decreases linearly to zero for ± 3 MeV off focus. As a result, each setting has a 6 MeV energy range that overlaps with adjacent settings.

The piecewise combination of all settings is shown in Fig. 7.7a as the solid blue line with the filled area indicating its weighted uncertainty. There are wiggles in the measured charge density distribution. They are a hint of variable charge injection during the LPA stage using ionisation injection, as previously observed in simulations [100]. The observed charge jitter is predicted to be caused primarily by changes in the laser beam spot size during the injection process. In the simulations that follow in Pt. III, a smoothed distribution using a moving average filter is used in this energy range. The red line shows the final electron spectrum, which includes a smoothed version of the imaged foci (solid line) as well as the low resolution ends (dashed line). Both energy ends had to be estimated by the non-focused energies on the surrounding screen because they could not be imaged onto the electron spectrometer without changing the discharge setup of the APL. As a result of beam divergence and a lower screen resolution, a broadened decrease is present at the high energy

end. Only the central electron spectrum obtained through imaging was used for the Thomson scattering experiment. However, the charge density for the entire spectrum was calculated by monitoring the full beam charge on the electron spectrometer.

7.2.2 Slice Emittance Measurement

The horizontal slice phase-space, including its emittance, was reconstructed using the single shot method described in Sec. 7.1.3. In addition to the data set in Sec. 7.2.1, the same scan was redone at the end of the day for more statistics. There was no discernible difference in the reconstructed properties. However, the usable shots in the data had to be selected further. Only shots with sufficient charge density (approximately $> 15\,\mathrm{fC/MeV}$) produced a distinctive beam waist along the dispersive axis that could be measured. Furthermore, to perform the emittance fit, an energy range of $\pm 2\,\mathrm{MeV}$ around the focused energy is required, as such shots with the focused energy close to the screen edge are excluded. Consequently, roughly only half of the total shots could be evaluated. Fewer outliers of electron beams with very low beam charges and smaller pointing angles along the dispersive axis would improve the number of measurable shots significantly. Besides that, a scintillator with a higher light yield can increase the number of resolvable beam waists. Yet, the resolution of scintillators with high light yield is often low. In this case, the magnification of the electron beam imaging would need to be increased, presumably through the use of a different focusing geometry or multiple APLs.

The reconstructed horizontal slice phase-space at the electron beam source position is summarised in Fig. 7.8. Each single data point represents a fit parameter from the single shot method, namely the normalised emittance, the RMS beam size, the RMS divergence and the correlation. The red line represents the weighted average of all data points within a 1 MeV bin, and the red area indicates its error. When each measurement is weighted with its error, the outliers have a lower weight due to their larger fit error. It is worth noting that the systematic errors are dominated by electron beam pointing, and because of their asymmetric nature, the fit parameters are rather overestimated.

The reconstructed normalised slice emittance in the horizontal is shown in Fig. 7.8a. The average emittance is $0.43^{+0.12}_{-0.33}\,\mathrm{mm\,mrad}$, in which a small increase of about $0.006\,\mathrm{mm\,mrad/MeV}$ is present. Simulations did not show any observable emittance growth due to the space charge effect. Because the contribution of space charge scales inversely with energy to the power of three (see Sec. 6.2.1), the emittance would have to decrease for higher energies, if at all. Furthermore, the emittance growth

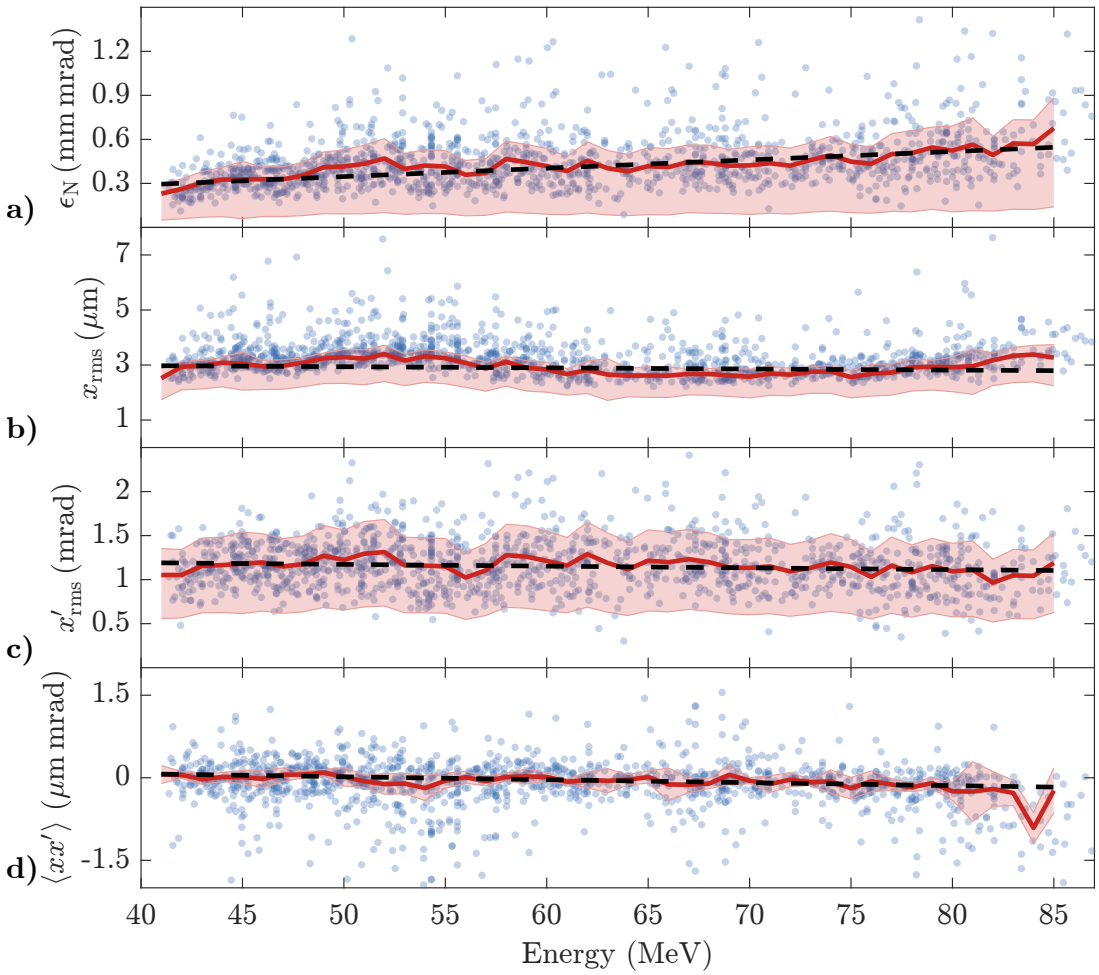

Figure 7.8: Horizontal phase-space reconstruction at the electron beam source position for various electron energies. The normalised emittance ϵ_N (a), beam size x_{rms} (b), beam divergence x'_{rms} (c) and correlation $\langle xx' \rangle$ (d) were calculated for various energy slices. Each shot's results are represented by the respective blue data points. The red line is the weighted average for each 1 MeV energy bin, and the error band describes its uncertainty. The linear trend of the average values is highlighted by the black dashed line.

should scale linearly with charge, but the measured charge density decreases within the observed energy interval. Emittance growth due to beam scattering during the acceleration process could potentially explain this trend. Because ionisation injection is a continuous process, electrons injected first achieve the highest energies as they are accelerated the longest. Electrons injected at the end of the acceleration process, on the other hand, have less time to be accelerated, resulting in a lower final energy. Since higher energetic electrons were accelerated for a longer period of time, they had more time to Coulomb-scatter with the background plasma and suffer emittance growth. Nevertheless, as explained in Sec. 6.2.3) emittance growth due to multiple scattering can be neglected under the conditions from the experiments. The increase in average normalised emittance is on the order of measurement uncertainty and could be the result of the measurement error or too few statistic.

Figure 7.8b depicts the reconstructed initial RMS beam size. It is approximately constant for the various electron energies and averages to $2.92^{+0.28}_{-0.86}$ µm. This value is consistent with the calculated magnification and observed beam size in focus. The RMS beam divergence is illustrated in Fig. 7.8c and yields an average of $1.16^{+0.32}_{-0.86}$ mrad. On the profile screen, the **F**ull **W**idth at **H**alf **M**aximum (FWHM) divergence of the entire electron beam was measured 3.8 ± 0.7 mrad in this axis. On the one hand, this difference can originate from an electron beam clipping in the plasma lens. The reconstructed divergence, on the other hand, is only valid for a specific energy slice. When different electron energies exit the acceleration stage at different betatron phases, their pointing angles could differ slightly. As a result, the slice divergence is smaller than the projected divergence of all energies.

Figure 7.8d shows the reconstructed initial phase-space correlation. The average correlation is -0.08 ± 0.15 µm mrad, which is close to zero as it had to be assumed. A non-zero correlation could be caused by a distance mismatch between the imaged planes and the virtual source plane. Its fluctuations could be caused by changes in the plasma-to-vacuum transition. However, in order to calculate the APL focusing strength, the correlation was initially assumed to be zero in the beginning. Then, deviations in the correlation can be explained by imaging and detection effects in the electron spectrometer that shift the focused energy (see Sec. 7.1.4).

The total beam charge after the plasma lens is distributed according to Fig. 7.7b and was measured for each separate shot during the emittance measurement. The correlation between the reconstructed normalised emittance and the total beam charge is depicted in Fig. 7.9a, indicating a small positive correlation. When the emittance is correlated with the observed charge within ± 0.5 MeV of the focused energy, the correlation becomes slightly stronger. On average, a higher charge density results in a

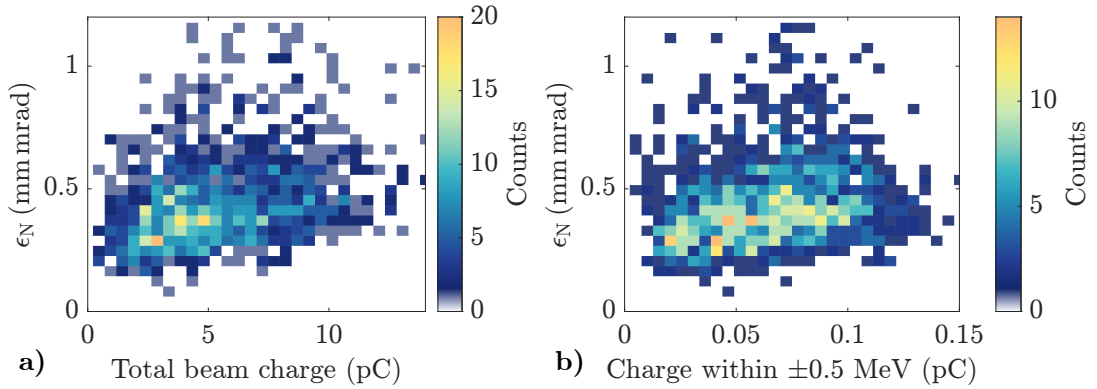

Figure 7.9: (a) Correlation between the total electron beam charge after the APL and the normalised slice emittance. (b) Correlation between the observed charge within ±0.5 MeV of the focused energy and the normalised emittance.

higher normalised emittance [156]. The effects of space charge during beam transport are one possible explanation, but they were previously excluded. However, it could also be that these quantities are not directly correlated. For example, a higher laser pulse energy typically causes more charge to be injected in the LPA stage. At the same time, the more intense laser pulse creates a larger phase-space volume into which charge can be injected, resulting in increased emittance [47, 154]. Furthermore, **P**article-**i**n-**c**ell (PIC) simulations could demonstrate that fluctuations in plasma density cause a correlation between beam emittance and beam charge [100]. Higher plasma densities result in stronger plasma focusing, which increases the ionised charge as well as the emittance of the beam.

The slice parameters presented here can only be reconstructed along the electron spectrometer's non-dispersive axis, which is the horizontal axis of the beamline. Because the LPA driver laser beam is vertically polarised, elliptic electron beam profiles are generated that are elongated along the polarisation axis, resulting in larger emittances. Electrons passing the driver laser beam during laser ionisation experience an additional transverse ponderomotive kick along the polarisation axis, as explained in Sec. 2.3. The vertical emittance can be estimated under the assumption that this effect only alters the beam divergence and that the beam size is the same along both axes. As shown in Sec. 4, the ellipticity of the beam profile is approximately 2, resulting in a twice-as-large slice divergence along the polarisation axis. Therefore, the slice emittance in the vertical is at least twice that of the emittance in the horizontal for a beam size unaffected by laser polarisation.

Part III

LOW BANDWIDTH TUNABLE THOMSON SOURCE

Many medical and biomedical applications rely on X-ray sources that must meet stringent photon flux, spatial resolution, and spectral bandwidth requirements. The non-invasive method of **X**-ray **F**luorescence **I**maging (XFI) [9, 10, 13, 16, 160] is one example. Small amounts of chemical elements can be detected in the human body by observing the emitted characteristic X-ray photons after being excited with the correct incident photon energy. Because there are no elements with high atomic-numbers in the human body, one option with several advantages is to use **g**old **n**ano**p**articles (GNPs) as tracers for cells of interest [14–16]. To excite the gold fluorescence with GNPs, an incident X-ray energy of 90 keV with a relative **F**ull **W**idth at **H**alf **M**aximum (FWHM) spectral bandwidth of less than 15 % is required. Furthermore, because it is a scanning imaging technique, a pencil-beam with a high photon flux and a high spatial resolution of about 1 mm is required. By functionalising GNPs, *in-vivo* usage for early cancer diagnostics and pharmokinetic studies becomes possible.

Radiation therapy [4], crystallographical applications [5], and advanced imaging modalities such as X-ray absorptiometry [6], fluorescence tomography [7], and K-edge imaging [8] are other examples of novel applications for bright X-ray beams that require or benefit greatly from a narrow spectral bandwidth and tunable energies. In the case of medical imaging using K-edge subtraction [161, 162], a percent-level bandwidth is required, as well as precisely tuned X-ray energy above and below a K-edge, which is 80.7 keV for gold.

While conventional X-ray tubes cannot provide the narrow bandwidths needed for such applications, high-brilliance synchrotrons are nowadays able to achieve that while tuning their incident radiation with high precision. However, because they span hundreds of meters in circumference, these expensive machines are unsuitable for use in a medical environment. To implement a medical-imaging technique, such as the aforementioned XFI application, in a hospital, the source device must be significantly reduced in size. Scattering laser light off relativistic electrons is a promising method for producing X- and γ-ray photons in a compact manner. In the future, this so-called **T**homson **S**cattering (TS) scheme, in combination with a likewise compact **L**aser-**P**lasma **A**cceleration (LPA) electron source, as discussed in Pt. I, could provide the means to apply novel imaging techniques into hospitals [14, 40, 41, 163]. Even though such sources have been demonstrated before [23–28], in the context of this thesis an **A**ctive **P**lasma **L**ens (APL) will be implemented as a proof-of-principle experiment to gain control over the radiated energies, further reduce its spectral bandwidth and relax the requirements on the electron bunch parameter.

In the following, the theoretical foundations of scattering an electron bunch with a laser beam are presented in Sec. 8. Then Sec. 9 describes the TS source with the APL as a central element and explains the benefits of its usage. Finally, the acquired data is analysed and compared to simulations in Sec. 10. The next steps for further optimisation and an outlook is discussed in Sec. 10.3.

8 CHARACTERISTICS OF THOMSON SCATTERING RADIATION

Following the earlier explanations, X-ray and γ-ray radiation can be produced by scattering photons from highly energetic electrons. This scheme, known as inverse Compton scattering or TS, was first proposed and demonstrated after the experimental realisation of laser light in the 1960s [17–19]. TS describes the low-energy limit, where the electron recoil can be neglected. In the context of this thesis the electron recoil can also be neglected, which is why the term TS will be used throughout this work.

Unless otherwise stated the following theoretical basics on TS follow [164, 165], where Sec. 8.1 introduces the interaction between a single electron and a single photon in the case of TS. Section 8.2 then covers the more practical approach of scattering an electron bunch with a laser beam.

8.1 SCATTERING OF AN ELECTRON AND A PHOTON

When considering the scattering of a single electron and a single photon in the TS regime, two assumptions about the electron energy are made at the beginning. On the one hand, the electron energy must be low enough so that no quantum effects occur during the scattering process. In addition, the energy of the scattering photons is much lower than the electron rest mass, allowing the electron recoil to be neglected. Then, in the classical picture, TS can be considered as the optical equivalent of undulator radiation, where the laser fields act as the undulator. A relativistic electron is exposed to the Lorentz force in the electromagnetic field of a laser photon and begins to oscillate. Due to this acceleration it starts to emit radiation into the forward direction. In the mean rest frame of the electron, its motion can be described as a Hertzian dipole and the emission angle in the forward direction is Lorentz contracted. It is analogous to the synchrotron angle $\theta_S \propto 1/\gamma_e$. For a laser beam, the extent of this oscillation can be described by its laser strength parameter [166]

$$a_0 = q_e E_0/\omega m_e c \propto \sqrt{I_0}, \tag{8.1}$$

which is also used to quantify the laser intensity I_0. Here, q_e and m_e are the electron charge and mass, c is the speed of light, ω is the laser frequency and E_0 is the electric

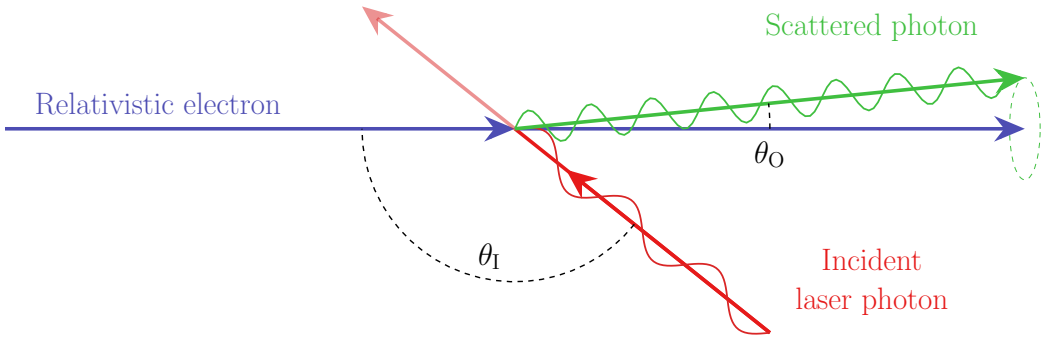

Figure 8.1: The geometry of the TS process of an electron and a laser photon. An incident electron interacts with a laser photon under an angle θ_I and as a result transfers energy to the photon, which is given by Eq. 8.2. The photon is scattered at an observation angle θ_O relative to the electrons undisturbed trajectory.

field amplitude. During this process an electron with the velocity $\beta_e = v/c$ and Lorentz factor $\gamma_e = (1-\beta_e^2)^{-1/2}$ emits a photon with an energy of [164, 167]

$$E_\gamma = \frac{2\gamma_e^2(1-\beta_e\cos\theta_I)}{1+\gamma_e^2\theta_O^2+a_0^2/2}\,E_L. \tag{8.2}$$

Figure 8.1 depicts this process in the particle picture. The laser photon with wavelength λ scatters with the electron under the interaction angle θ_I and has a initial energy of $E_L = hc/\lambda$, with h being the Planck constant. θ_O represents the observation angle. In this particle picture the photon gains energy from the electron, resulting in a reduction of the photon's wavelength. As shown in Eq. 8.2 the total energy transfer depends on the laser strength parameter a_0. While the highest accelerating field for LPA can be obtained for high peak intensities with an $a_0 \gtrsim 1$, such field strengths in the TS interaction result in larger transverse oscillations of the electron. This leads to a reduced longitudinal electron velocity, i.e. a decreased γ_e-factor in the interaction. Therefore, the maximum photon energy can be achieved for weak laser strengths ($a_0 \cong 0$) together with a head-on collision ($\theta_I = \pi$) and the photon being scattered into the direction of the electron ($\theta_O = 0$). Then, the maximum photon energy is

$$E_{\gamma,\max} \approx 4\gamma_e^2 E_L. \tag{8.3}$$

As illustrated in Fig. 8.2, the maximum energy a secondary photon can have by scattering a primary photon with a wavelength of 800 nm with a 60 MeV electron is about 85 keV.

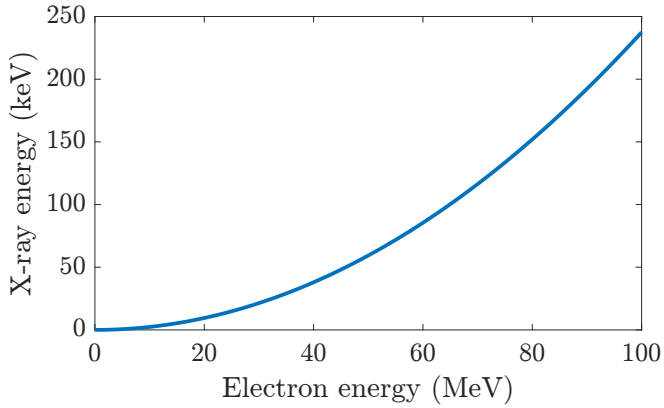

Figure 8.2: Maximum energy of a TS photon from the scattering process between a photon with a wavelength of 800 nm and an electron with energies up to 100 MeV.

8.2 SCATTERING OF AN ELECTRON BUNCH WITH A LASER BEAM

The energy of a Thomson photon depends on several parameters, including the electron energy γ_e, the laser amplitude a_0, the laser pulse energy E_L, and the interaction angle θ_I. However, realistic electron bunches are collections of large numbers of electrons with various energies travelling in different directions, resulting in an electron bunch energy spread and a beam divergence. In the same way, a laser pulse consists of many photons with a spectrum of several wavelengths and potentially curved phase fronts. Therefore, these parameters are not fixed when scattering an electron bunch with a laser beam, and several effects have to be taken into account. Scattered X-ray photons form a Thomson spectrum, whose bandwidth is difficult to describe analytically. In the following, a theory of the FWHM Thomson bandwidth on the basis of [164, 165] is presented. If not stated otherwise, the following considerations are only valid for $a_0 < 1$.

8.2.1 Effects of Electron Bunch Divergence

The FWHM electron beam divergence $\sigma_{\theta,\mathrm{FWHM}}$ describes the fact that electrons within a bunch propagate with various angles θ relative to the main electron axis. During the scattering process, these electrons can still emit a photon onto the main axis with an energy reduced by a factor of $1/(1+\theta^2\gamma_e^2)$, according to Eq. 8.2. As a result, a detector will detect photons of different energies emitted from electrons of various pointing angles. Assuming a circularly polarised laser beam and no electron energy

spread, the contribution of electron beam divergence to the on-axis FWHM bandwidth can be calculated as [164]

$$\left(\frac{\Delta\omega}{\omega}\right)_{\sigma_\theta} = \frac{\gamma_e^2 \sigma_{\theta,\mathrm{FWHM}}^2}{4}. \tag{8.4}$$

Note that the laser beam polarisation determines the polarisation of the X-ray radiation but not the total photon number or its spectral bandwidth. This quadratic dependency of the bandwidth with the beam divergence is often the dominant factor of conventional accelerators and has also a significant impact in the case of electron beams from an LPA source.

8.2.2 Effects of Electron Bunch Energy Spread

The next largest contribution to the spectral broadening when using LPA electron beams is often the electron bunch energy spread. According to Eq. 8.2, an electron with a different energy γ_e will generate an X-ray photon with a different energy. Assuming a Gaussian energy distribution for an electron beam with no divergence, the contribution of the electron energy spread to the bandwidth can be estimated as [164]

$$\left(\frac{\Delta\omega}{\omega}\right)_{\gamma_e} = 2\frac{\Delta\gamma_e}{\gamma_e}. \tag{8.5}$$

For example, an electron bunch with a 10 % FWHM energy spread will result in a photon source of at least 20 % FWHM bandwidth. Thus, the electron energy spread in the TS interaction must be kept as low as possible.

8.2.3 Effects of Laser Pulses

In the interaction between an electron bunch and a laser pulse, the laser pulse has several effects on the Thomson spectrum, especially for focused laser beams. As both beams intersect each other, the electrons interact with regions of the pulse with various intensities. Thus, the spectrum will be broadened, even for a monochromatic electron beam. In addition, the X-ray spectrum inherits the initial bandwidth of the laser beam, and this contribution can be written as

$$\left(\frac{\Delta\omega}{\omega}\right)_{\omega_{\mathrm{Laser}}} = \frac{\Delta\omega_{\mathrm{Laser}}}{\omega_{\mathrm{Laser}}}. \tag{8.6}$$

Large spectral widths are typically required for an intense laser pulse with a short pulse duration, as specified in Sec. 3.1. This means that the bandwidth is typically of the order of 10 % for a laser pulse duration of tens of femtoseconds.

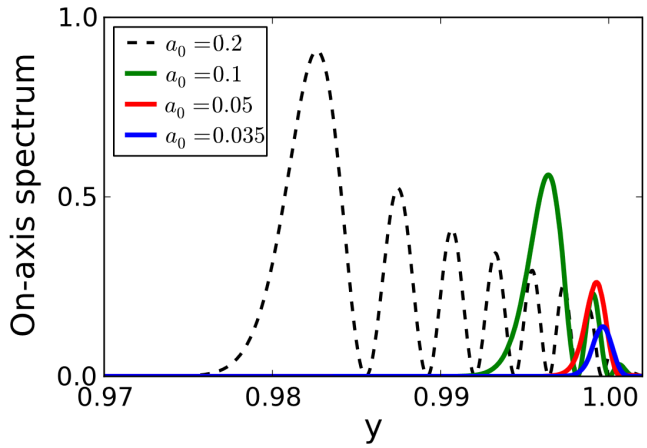

Figure 8.3: Normalised on-axis X-ray spectrum as a function of normalised laser photon energy $y = E_\gamma/E_{\gamma,max}$ for the different laser pulse amplitudes $a_0 = 0.035$ (blue line), $a_0 = 0.05$ (red line), $a_0 = 0.1$ (green line) and $a_0 = 0.2$ (black dashed line). Plot taken from [164].

The phase-front curvature of a laser pulse causes individual laser photons to scatter at different interaction angles, resulting in a broadening of the X-ray spectrum. However, because the effect is small in comparison to other broadening effects, it is typically neglected in the literature by assuming a flat phase-front and will also not be considered throughout this thesis.

In order to increase the photon yield, the laser intensity and therefore the a_0 can be increased. However, this also causes undesirable effects that lead to broadening, such as the appearance of sub-structures in the spectrum [168]. For large a_0, the commonly used Eq. 8.2 looses its validity and some of the laser photons generate higher harmonics in the X-ray spectrum. Figure 8.3 depicts the influence of the laser pulse amplitude on the resulting photon spectrum. The spectra were calculated with the numerical code VDSR [169] for a single electron interacting with a Gaussian plane wave with a FWHM duration of 800 fs [164]. Increasing the laser pulse amplitude from $a_0 = 0.035$ to $a_0 = 0.05$ means that the number of laser photons is doubled. In this case, the spectral shape does not change much, and the number of X-ray photons is doubled. If a_0 is increased from 0.05 to 0.1, the number of laser photons quadruples, but the amplitude only approximately doubles. The further the a_0 is increased, the more broadening and sidebands occur. In general, this contribution to the FWHM bandwidth of the spectrum is estimated to be

$$\left(\frac{\Delta\omega}{\omega}\right)_{a_0} = \frac{a_0^2}{2}. \tag{8.7}$$

In an experiment, it is often advisable to use moderate values of a_0 and to compromise between the needs of the photon flux and the bandwidth. One way to compensate for the broadening of an excessive a_0 without significantly reducing the photon flux can be the use of dispersive devices, such as chirped mirrors, to stretch the laser pulse in time and effectively reduce the a_0 [170].

8.2.4 Effective Quantities of the Scattering Process

The scaling laws of the broadening effects presented so far do not take the interaction geometry into account. In reality, the shape and size of both the electron beam and the scattering laser beam influence the spectral distribution of the X-ray photons generated. This effect was investigated in depth using a linear accelerator, which enabled stable control of both beams independently [165]. In these experiments, the divergence in the interaction volume was varied by altering the final focusing of the electron beam, and the laser strength parameter of the scattering laser beam was varied by changing its intensity. The agreement between an analytical model and experimental results was demonstrated by properly incorporating the interaction volume into the model. As a result, an effective beam divergence and an effective laser strength parameter are introduced as a way to adequately describe the spectral dependence.

During the Thomson interaction process, electrons oscillate in the local laser field. Because the laser beam is pulsed, the longitudinal laser strength varies with its peak value given by the laser strength parameter a_0. Therefore, electrons emit radiation of lower intensity at the beginning and end of the interaction region. Furthermore, depending on the local field, they emit radiation with different energies, increasing the bandwidth of the Thomson spectrum. In the work of [165], the use of an effective laser strength parameter $a_{0,\mathrm{eff}}$ is proposed by weighting the local laser field with the number of scattered photons. The calculation assumes a head-on collision of a 3D Gaussian distribution of the laser field with its peak defined by a_0 and a transverse electron charge density. This results is an effective laser strength of

$$a_{0,\mathrm{eff}} = \begin{cases} 54.4\,\% \cdot a_0 & \text{for } \sigma_e \gg \sigma_L \\ 61.2\,\% \cdot a_0 & \text{for } \sigma_e = \sigma_L \\ 81.6\,\% \cdot a_0 & \text{for } \sigma_e \ll \sigma_L. \end{cases} \tag{8.8}$$

The spatial overlap is affected by the electron beam size σ_e relative to the laser size σ_L, which influences the effective laser strength. This definition takes into account the

shape of the laser pulse and the interaction volume, but assumes a constant transverse electron distribution. The effective beam divergence $\sigma_{\theta,\mathrm{eff}}$ is defined in the same way. It is defined as the weighted mean of the scattering angle caused by electron beam divergence. As a result and by using Eq. 8.2, the mean scattered energy on-axis can be written as

$$E_\gamma = \frac{2\gamma_e^2(1-\beta_e\cos\theta_I)}{1+\gamma_e^2\sigma_{\theta,\mathrm{eff}}^2+a_{0,\mathrm{eff}}^2/2}\,E_L. \tag{8.9}$$

Using Eq. 8.9 with the effective quantities for the electron beam divergence and the laser strength, the FWHM spectral broadening contributions are recalculated as [165][1]

$$\left(\frac{\Delta\omega}{\omega}\right)_{\sigma_{\theta,\mathrm{eff}}} = \frac{2.47\gamma_e^2\sigma_{\theta,\mathrm{eff,rms}}^2}{1+\gamma_e^2\sigma_{\theta,\mathrm{eff,rms}}^2} \tag{8.10}$$

and

$$\left(\frac{\Delta\omega}{\omega}\right)_{a_{0,\mathrm{eff}}} = \frac{c_{\mathrm{overlap}}a_{0,\mathrm{eff}}^2}{2+a_{0,\mathrm{eff}}^2}. \tag{8.11}$$

In Eq. 8.11, the contribution due to effective laser strength is again determined by the spatial overlap of the laser beam and electron beam. The spatial overlap factor is

$$c_{\mathrm{overlap}} = \begin{cases} 2.07 & \text{for } \sigma_e \gg \sigma_L \\ 1.70 & \text{for } \sigma_e = \sigma_L \\ 1.17 & \text{for } \sigma_e \ll \sigma_L. \end{cases} \tag{8.12}$$

8.2.5 Estimation of Total Bandwidth

So far, only the main effects leading to the broadening of the on-axis spectrum have been presented. The estimation of the total FWHM broadening is obtained from the sum of squares of the individual contributions. For this one, it employs Eq. 8.4, Eq. 8.5, Eq. 8.6 and Eq. 8.7. It results in [164]

$$\frac{\Delta\omega}{\omega} = \sqrt{\left(\frac{\gamma_e^2\sigma_{\theta,\mathrm{FWHM}}^2}{4}\right)^2+\left(2\frac{\Delta\gamma_e}{\gamma_e}\right)^2+\left(\frac{\Delta\omega_{\mathrm{Laser}}}{\omega_{\mathrm{Laser}}}\right)^2+\left(\frac{a_0^2}{2}\right)^2}, \tag{8.13}$$

and is useful in inspecting the scaling laws. As shown in Sec. 8.2.4, a more precise description includes the interaction volume and defines the effective properties of the

1 It should be noted that, in contrast to [165], an additional factor $2\sqrt{2\ln(2)}$ was included to convert the standard deviation contribution to the FWHM contribution.

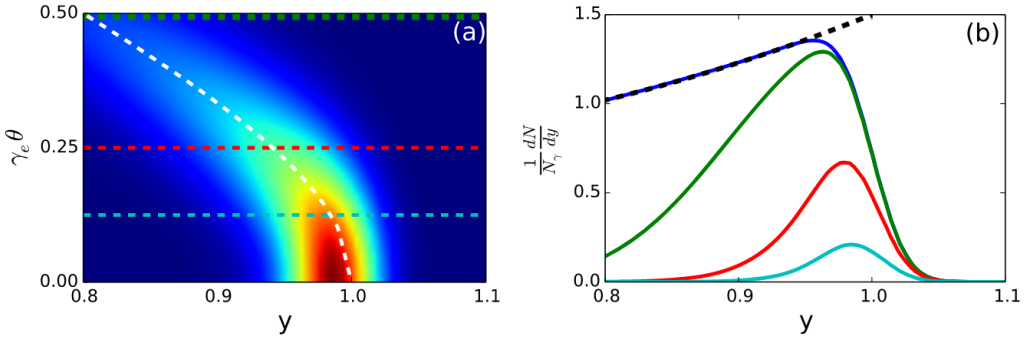

Figure 8.4: Typical energy-angular TS spectrum (a) with the corresponding angular integrated spectra (b) as a function of the normalised laser photon energy $y = E_\gamma/E_{\gamma,max}$. (a) shows the photon distribution for various observation angles $\gamma_e\theta$, where $\theta = 0$ is the main axis of the X-ray radiation. The white line depicts the angular dependency according to Eq. 8.2. The spectra in (b) are obtained by integrating the distribution in (a) from 0 to the collimation angle θ_c marked with the dashed line in the same colour. The dark blue line represents the uncollimated case. Image taken from [164].

laser strength and electron beam divergence. For an electron-beam size much larger than the laser-beam size, the total FWHM broadening is estimated to be

$$\left(\frac{\Delta\omega}{\omega}\right)_{\text{eff}} = \sqrt{\left(\frac{2.47\gamma_e^2\sigma^2_{\theta,\text{eff,rms}}}{1+\gamma_e^2\sigma^2_{\theta,\text{eff,rms}}}\right)^2 + \left(2\frac{\Delta\gamma_e}{\gamma_e}\right)^2 + \left(\frac{\Delta\omega_{\text{Laser}}}{\omega_{\text{Laser}}}\right)^2 + \left(\frac{2.07a_{0,\text{eff}}^2}{2+a_{0,\text{eff}}^2}\right)^2}. \tag{8.14}$$

Rather than registering just the on-axis spectrum, an X-ray detector will register the bandwidth within a defined area. Also, a TS spectrum has an intrinsic energy-angle and intensity-angle relation. Figure 8.4a shows a typical TS spectrum resolved with regards to its angular component. Both the photon energy and the photon number are maximum on-axis and decrease with larger observation angle. The bandwidth contribution from the collimation angle $\pm\theta_c$ is given by $\gamma_e^2\theta_c^2/(1+\gamma_e^2\theta_c^2)$ [164], and thus the total bandwidth within the defined cone is

$$\left(\frac{\Delta\omega}{\omega}\right)_{\theta_c} = \sqrt{\left(\frac{\Delta\omega}{\omega}\right)^2_{\text{eff}} + \left(\frac{\gamma_e^2\theta_c^2}{1+\gamma_e^2\theta_c}\right)^2}. \tag{8.15}$$

For electron beams from LPA, the X-ray bandwidth is dominated by the electron energy spread and divergence at moderate $a_0 < 1$. This is due to the typically high intrinsic energy spread at the percent level and a divergence of the order of a couple mrad (see Sec. 2.3). For the data presented in this thesis, the electron source has an energy spread of over 100 % FWHM with a mean divergence of about 6 mrad FWHM.

In addition, the measured spectral width of the scattering laser beam is about 8.8 %. Neglecting the effect of the laser amplitude a_0, this results theoretically in a highly broadband X-ray beam. The main reason is the energy spread, but the contribution of the divergence and the laser beam bandwidth also counts for a few percent. Such bandwidths are not usable for most dedicated applications where narrowband X-ray sources are required.

However, this theoretical approach overestimates the resulting bandwidth. The model assumes that a confined cone cuts equivalent parts of the single electron spectra, but several bandwidth contributions are asymmetrical. For example, it neglects that for increasing divergences or larger opening angles, the spectrum only broadens in the direction of lower energies. Therefore, the peak of a spectrum shifts to the left in Fig. 8.4b for increasing collimation angles. The spectral profile depends on the shapes of the electron bunch and the laser beam and can rarely be assumed to follow a Gaussian distribution due to its asymmetric contributions. Therefore, this theory cannot predict exact information on the spectral profile, and numerical simulations are indispensable for interpreting an experiment. Nevertheless, the model provides a powerful tool for understanding the dependencies and scaling effects.

8.3 PHOTON-YIELD ESTIMATION

Section 8.2 investigated the influences of electron bunches and laser beams on the spectral bandwidth of the X-ray beam generated. However, optimising a Thomson source purely on the basis of bandwidth is insufficient. Furthermore, a total number of photons is required for a specific application. This is also determined by the properties of the beams. To understand the fundamental relationship between spectral bandwidth and photon yield, an estimate of photon yield will be presented on the basis of [164]. The ideal case will be described first, followed by total photon yield calculations for non-ideal beams.

Ideal case

In an ideal case, an electron beam without divergence or energy spread interacts in vacuum with a plane-wave laser pulse. The laser pulse is assumed to have an infinitely narrow bandwidth, a constant laser strength parameter a_0, and result in a

large number of electron oscillations in the laser field ($N_0 \gg 1$). The total number of photons emitted in a $1/\gamma_e$-cone is given by

$$N_\gamma = \frac{2\pi}{3}\alpha_f N_e N_0 a_0^2, \tag{8.16}$$

where $\alpha_f \approx 1/137$ is the fine structure constant and N_e is the number of electrons in the bunch. In this case, the photon number scales linearly with the number of electrons and oscillations, but quadratically with the laser strength parameter. As with Eq. 8.15, a bandwidth κ from a collimation angle θ_c is described by

$$\kappa = \frac{\gamma_e^2\theta_c^2}{1+\gamma_e^2\theta_c^2}. \tag{8.17}$$

Then, the photon yield in a confined angle $\theta_c < \theta_S$ is given by

$$N_{\gamma,\theta_c} = N_\gamma \sigma(\kappa) \tag{8.18}$$

with $\sigma(\kappa)$ denoting the percentage of photons within θ_c. This is given by

$$\sigma(\kappa) = \kappa\left(\kappa^2 - \frac{3}{2}\kappa + \frac{3}{2}\right). \tag{8.19}$$

Therefore, a bandwidth requirement for the application limits the number of photons usable in this ideal case. According to Eq. 8.18, 19.5 % of all photons are included within a 15 % FWHM bandwidth, indicating that for small angular ranges, the majority of the photons generated have energies that lie outside the collimation angle.

Estimation of Total Yield

The total photon yield can be calculated using the cross-section formalism. As the the recoil effect on the electrons can be neglected in TS, the Thomson cross-section is given by $\sigma_T = 8\pi r_e^2/3$ with the classical electron radius r_e. The total number of generated photons is then defined by

$$N_\gamma = \sigma_T \int_{-\infty}^{+\infty} v_{rel} n_e(t,\mathbf{r}) n_p(t,\mathbf{r})\, d^2\mathbf{r}dt, \tag{8.20}$$

where n_e and n_p denote the time- and space-dependent densities of the electrons and laser photons, respectively, and the relative velocity of electrons and laser photons is $v_{rel} \approx 2c$. In general, the integral in Eq. 8.20 can only be evaluated numerically. However, several analytical solutions exist for specific cases. In the case of a head-on collision of a Gaussian laser pulse with an electron beam in vacuum with no relative longitudinal, transverse, or temporal displacements, the integral yields

$$N_\gamma = \frac{\sigma_T N_e N_p F(x)}{\sqrt{2\pi}\sigma_l\sqrt{\sigma_{e,o}^2+\sigma_{p,o}^2}} \frac{1}{\sqrt{\frac{\sigma_{e,o}^2}{\beta_e^{*2}}+\frac{\sigma_{p,o}^2}{\beta_p^{*2}}}} \tag{8.21}$$

with

$$F(x) = e^{x^2}\left[1 - \mathrm{erf}(x)\right], \tag{8.22}$$

$$x = \frac{\sqrt{2}}{\sigma_l}\sqrt{\frac{\sigma_{e,o}^2 + \sigma_{p,o}^2}{\frac{\sigma_{e,o}^2}{\beta_e^{*2}} + \frac{\sigma_{p,o}^2}{\beta_p^{*2}}}}, \tag{8.23}$$

and

$$\sigma_l = \sqrt{\sigma_{l,e}^2 + \sigma_{l,p}^2}, \tag{8.24}$$

where N_e and N_p describe the number of electrons and photons in the interaction, respectively. Different beam sizes in focus ($\sigma_{e,o}$ and $\sigma_{p,o}$), beta functions (β_e^* and β_p^*) and longitudinal sizes ($\sigma_{l,e}$ and $\sigma_{l,p}$) for the electrons and photons are taken into account. The subscripts 'e' and 'p' signify whether the parameter describes electrons or photons. The electron's beta function is given by $\beta_p^* = \sigma_{e,o}^2/\epsilon_t$ with the transverse geometrical beam emittance ϵ_t, and the laser beam's beta function defined by its Rayleigh length. As a given laser beam is focused more tightly, the photon yield increases. However, as shown in Sec. 8.2.3, increasing the laser's amplitude also broadens the spectrum. Therefore, the desired source bandwidth for an application limits the laser amplitude.

8.4 OPTIMUM BEAM PARAMETERS

A TS source is typically optimised for a particular application or set of parameters. Previous theoretical optimisations of TS processes have focused on maximising the photon production [164], decreasing the spectral bandwidth [171, 172], or increasing the photon number within a bandwidth and opening angle defined by a specific application [40].

Optimum Laser Waist and Duration

Using Eq. 8.16, the maximum photon number is obtained for the ideal case by maximising the number of electrons in the bunch N_e, the number of electron oscillations N_0, and the laser strength parameter a_0. However, this is only valid for laser pulses with constant a_0, and in order to further increase photon production, the laser pulse

duration must be increased. When a laser pulse with a given pulse energy is elongated, the laser strength parameter decreases. To compensate for the lower a_0, stronger laser beam focusing is required to achieve a smaller focal waist w_0. For every laser pulse energy there is an optimal laser pulse spot size and duration. The interaction length of the TS process is given by [173]

$$L_{int} = \frac{(\tau_{laser} + \tau_{bunch})c}{2} \approx \frac{\tau_{laser} c}{2}, \tag{8.25}$$

which is often dominated by the laser pulse length τ_{laser}, because the laser pulse duration is typically much larger than the electron bunch duration τ_{bunch}. It is required that this interaction length lies within the Rayleigh length $z_R = \pi w_0^2/\lambda$ ($L_{int} \leqslant z_R$) [164], yielding an optimum laser pulse duration of

$$\tau_{laser}(w_0) = \frac{2\pi w_0^2}{c\lambda} - \tau_{bunch} \tag{8.26}$$

$$\approx \frac{2\pi w_0^2}{c\lambda} \tag{8.27}$$

$$= \frac{2z_R}{c}. \tag{8.28}$$

To put it differently, the optimum laser pulse length is twice the Rayleigh length. The laser strength parameter of a Gaussian laser pulse is determined by the pulse energy E_p, laser pulse duration, and focal waist as [40]

$$a_0 = \frac{e}{2\pi m_e c^2} \sqrt{\frac{4E_p}{c\epsilon_0 \tau_{laser} \pi}} \frac{\lambda}{w_0}. \tag{8.29}$$

Equations 8.27 and 8.29 yield the optimum laser beam waist size for a fixed a_0 as

$$w_0 \approx 0.217 \frac{E_p^{1/4} \lambda^{3/4}}{\sqrt{a_0}}. \tag{8.30}$$

Optimum Electron Bunch Waist

Because the Thomson spectrum is sensitive on the overlap between the electron bunch and the laser pulse, there is also an optimum electron beam size. The electron beam size

$$\sigma_{x,y} \leqslant w_0/2 \tag{8.31}$$

provides the highest photon yield with the best overlap at moderate laser intensities and for a head-on collision [163, 173]. This requirement describes an electron beam size matched to that of the laser beam's focal spot. For a larger electron beam size,

there will be charge outside the laser beam that is not participating in the scattering process. This approach ignores the fact that more photons are emitted in higher laser fields, such as the centre of a Gaussian pulse. Moreover, the evolution of the laser pulse and electron bunch sizes during the interaction are neglected. In principle, the three-dimensional overlap must be optimised.

9 DESIGN OF THE THOMSON SOURCE

This section describes the experimental setup and principles of the all-optical tunable Thomson source based on a laser-plasma accelerator that was built. One challenge of such X-ray sources is that the bandwidths of the generated photon spectra are on the order of many tens of percent [23–28]. As described in Sec. 8.2.5, the bandwidth of the generated X-ray beam increases with electron bunch divergence and scales linearly with electron energy spread. As a result, in the case of LPA-electron beams, the bandwidth is dominated by the intrinsic energy spread on the percent-level and a divergence of a couple of milliradians. For example, the electron spectrum described in Sec. 8.2.2 of the generated electron beams has a relative energy spread of over 100 %, resulting in a theoretical X-ray beam broadening of 200 %.

Furthermore, to obtain a high photon yield from TS, these sources require either higher electron beam currents, more intense scattering laser beams, or other novel solutions to increase the effectiveness [164]. In the case of high beam currents, the demands on the shielding of the background radiation increase dramatically. While a scattering laser beam with higher a_0 increases the total photon yield, it also broadens the X-ray spectrum significantly. Therefore, it is beneficial to increase the process's efficacy by scattering the laser beam off a focused electron beam where both beam foci are matched in size to maximise the photon yield per electron.

While Thomson sources in combination with LPA-electron sources have been demonstrated before [23–28], in the context of this thesis an APL is used in a proof-of-principle experiment on the basis of previous theoretical work [40, 41, 163]. By chromatically focusing the electron bunches with an APL, both the photon yield per electron and the spectral bandwidth can be improved. In addition, the requirements on the electron bunch parameters are relaxed, and control over the radiated photon energies is gained.

Figure 9.1 depicts a schematic overview of the tunable Thomson source based on a laser-plasma accelerator. A more detailed sketch of the setup inside the vacuum chamber is shown in Fig. 3.2. The incoming laser beam was split into the LPA driver laser beam and the scattering laser beam using a beam splitter. To enable femtosecond temporal alignment of both laser arms, the beam splitter with an additional mirror was installed on a delay stage. As discussed in Sec. 4, the LPA driver laser beam

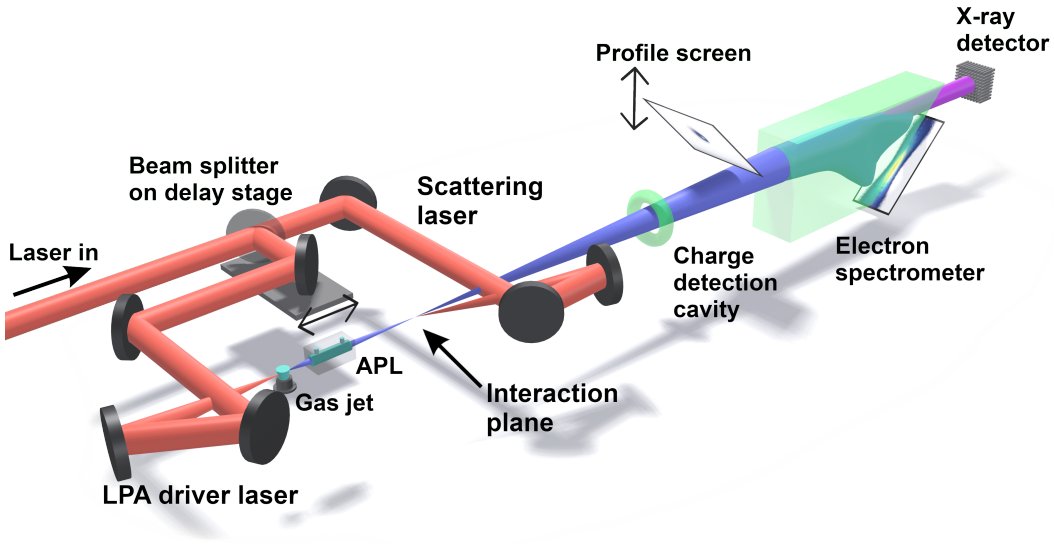

Figure 9.1: Schematic overview of the tunable Thomson source based on a laser-plasma accelerator. The incoming laser beam is divided into two parts: an LPA driver laser beam and a scattering laser beam. The LPA driver laser beam is focused into a gas jet, generating and accelerating an electron bunch. This bunch is captured by an APL and imaged chromatically into the interaction plane, where it interacts with the focused scattering laser beam. X-ray photons are being generated via TS that point into the same direction as the electron bunch. In the electron energy spectrometer, the electron bunch is deflected, while the X-ray beam travels forward onto an X-ray detector.

is focused into a gas jet to generate and accelerate an electron bunch. The APL can focus the bunch into the interaction plane, where it scatters with the focused scattering laser beam. The focusing is chromatic, and the imaged electron beam is an overlap of various energy slices with differing beam sizes. By imaging the electron beam, the beam divergence is reduced and the APL acts as a chromatic filter for the electron bunch, reducing the effective electron energy spread, that contributes to TS process. After the Thomson interaction, the generated X-ray photons point in the same direction as the electron bunch. While the electron bunch is deflected in the electron energy spectrometer before being dumped into lead bricks, the X-ray photons travel further and can be detected using an X-ray detector.

Details on the scattering laser beam and the electron beam control are described in Sec. 9.1 and Sec. 9.2, respectively. Section 9.3 explains the procedures used to align and optimise the X-ray spectra. Finally, Sec. 9.4 specifies how the X-ray spectra were measured and reconstructed.

9.1 SCATTERING LASER BEAM

The scattering laser beam, also known as Thomson laser beam, determines essential aspects of the Thomson interaction. To increase X-ray photon production, the longitudinal interaction duration must be maximised, which requires a long pulse duration and Rayleigh length while maintaining the overlap of the laser beam and electron beam.

The longitudinal overlap and photon production benefit from the head-on scattering geometry. Techniques, such as using a plasma mirror [23] or a focusing optic on-axis with a hole to allow the electron and X-ray beams to pass, can be used to realise head-on scattering. However, when the back-reflected LPA driver laser beam from a plasma mirror is used as the scattering laser beam, there is no separate control of the scattering laser beam properties, and the setup is incompatible with the use of an APL. While an on-axis focusing optic may be a solution, it is also a source of on-axis bremsstrahlung, particularly when using a chromatic electron beam imaging. Therefore, a focusing optic with the smallest incident angle into the TS interaction, where the electron particles do not hit the optic, is preferred.

Methods based on Traveling-Wave TS [174–176] or plasma channels to guide the scattering laser beam [164, 177, 178] are two examples of methods for increasing the interaction duration. However, these techniques necessitate high laser pulse energies, such as those produced by a petawatt laser system. The laser pulse energy is limited in the proposed setup, because a single 25 TW laser system drives both the LPA stage and the scattering interaction. In that case, photon production is limited by the number of available laser photons rather than the Rayleigh length. The laser pulse can be stretched in time to lengthen the interaction duration and increase the photon production [40].

In the proposed setup, the LPA driver laser beam and Thomson laser beam are driven by a single laser system, resulting in a pump-probe setup with intrinsic synchronisation of the Thomson laser beam and the electron beam. A 5 mm thick magnesiumfluorid beam splitter divides the incoming laser pulse, with two-thirds of the laser power reflected into the LPA driver laser beam and one-third transmitted into the scattering laser beam. During the Thomson spectra measurements, an average laser pulse energy of (50.8 ± 2.2) mJ was measured using the calibrated diagnostic described in Sec. 3.3.1.1. Analogue to the pulse duration measurement of the LPA driver laser beam (compare Sec. 3.3.1.2), an additional mirror before the focusing optic was used to transport the Thomson laser beam through a 1 mm vacuum window into the Wizzler for pulse duration measurement. The FWHM pulse duration was

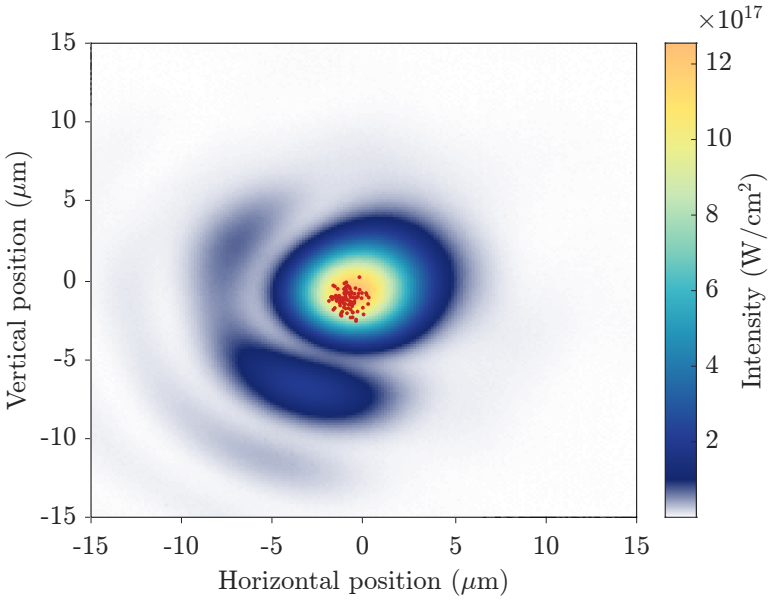

Figure 9.2: Average focal spot of the TS laser beam for 100 consecutive laser pulses. The intensity distribution is calculated for a laser pulse with a pulse duration of 32 fs, a pulse energy of 50.8 mJ and a wavelength of 800 nm. The red points represent the centre of mass for each shot, resulting in a pointing stability of 0.8 µrad in the horizontal axis and 0.9 µrad in the vertical axis. It is worth noting that the additional intensity outside the central distribution shifts the centre of mass.

measured to be (32.2 ± 0.3) fs. Furthermore, the spectral FWHM bandwidth of the laser pulse was measured with a spectrometer to be 8.8 %.

To focus the Thomson laser beam for the proof-of-principle experiment, an available 500 mm f/11 **O**ff-**A**xis **P**arabolic mirror (OAP) was used. The average focal spot and the pointing stability of 100 consecutive laser beam shots is shown in Fig. 9.2. The intensity distribution is shown assuming a laser pulse with a pulse duration of 32 fs, a pulse energy of 50.8 mJ and a wavelength of 800 nm, resulting in a normalised vector potential of $a_0 = 0.81 \pm 0.02$. Using pico motors, the OAP and the two mirrors before it could be controlled in the horizontal and vertical planes, allowing full control of the laser beam and optimising the focal spot. The $1/e^2$ beam width was measured to be (9.5 ± 0.1) µm in the horizontal and (7.8 ± 0.1) µm in the vertical, with a pointing stability of 0.8 µrad and 0.9 µrad, respectively. Take note of the additional intensity outside of the central intensity distribution, that has a normalised vector potential of up to $a_0 = 0.3$ and can contribute in the TS process. This, combined with the ellipticity of the focal spot, makes simulating the Thomson laser beam with a simple analytical function difficult (see Sec. 10.1.2).

Due to the limited space in the LPA chamber, the focusing laser beam was reflected into the interaction plane using a folding mirror, as shown in Fig. 3.2. Stepper motors are used to optimise the transverse focal spot position in a reproducible manner while maintaining the focal spot quality. Without the folding mirror being in the path of the electron beam, the incident angle of the Thomson laser beam into the interaction point is approximately 10°. Furthermore, each laser arm could be blocked independently to enable alignment.

9.2 ELECTRON BEAM CONTROL

Large X-ray beam bandwidths are a common issue of X-ray sources based on TS and electron bunches from an LPA-electron source. When only the electron bunch properties of milliradian beam divergence and $< 10\,\%$ relative energy spread are considered, an X-ray bandwidth of tens of percent is generated [23–28]. An APL with chromatic focusing can be used to overcome the problem caused by the initial electron beam properties while improving the photon production per electron.

The TS process occurs at a fixed electron focal position using an APL, which relaxes the quality requirements on the electron beam source. In addition, beam imaging enables electron beam magnification to match the focal waist of the scattering laser beam and reduces the beam divergence for the imaged electron energy. Matching the laser beam and electron beam sizes results in a maximum photon yield per scattered electron, and a reduced beam divergence has a positive effect on the X-ray beam bandwidth, as explained in Sec. 8.2. In the case of polychromatic electron beams, the APL acts as a chromatic filter, reducing the effective electron energy spread. Furthermore, the APL's focusing strength is directly tunable via the applied discharge current, allowing easy control of the electron energy in focus that contributes to the TS interaction. As a result, the mean X-ray beam energy can be precisely adjusted according to the application's requirements within seconds without changing the electron bunch properties. Only the spectral width of the electron beam and the applicable APL discharge current limit the tuning range.

Aside from the disadvantages of APLs discussed in Sec. 6.1.3, there are additional drawbacks of chromatic focusing. While APLs are compact devices with short focal lengths, the imaging and the device itself still takes up space. Particularly in focusing geometries with large focal lengths, the required space can become considerable. Therefore, the Thomson source must be optimised by taking into account both the design of electron beam imaging and laser beam imaging. When the electron

beam is chromatically focused, the electron energies surrounding the focused energy contribute primarily to the TS interaction. While this effectively reduces the electron energy spread, it also reduces the effective bunch charge. Furthermore, unfocused electrons are more likely to scatter from elements near the beamline and produce on-axis bremsstrahlung, which overlaps with the generated X-ray photons. Even the APL is on-axis and is a potential source of bremsstrahlung.

Figures 9.3a-9.3c visualise the chromatic beam transport in the designed TS source. The TS interaction plane, which coincides with the electron focal plane, was set to 23 cm after the APL exit. An APL with a magnetic gradient of about 67 T/m focuses electrons with an energy of 50 MeV into the interaction plane (highlighted by the red line). Higher electron energies are focused downstream, while lower energies are focused upstream. Due to the beam imaging into focus, the electron slice beam size is magnified by a factor 2.6 and the slice divergence is reduced by 62 %. Figures 9.3d and 9.3e show the evolution of beam divergence in this setup for various electron energies.

Because focused energies dominate X-ray photon production, the effective energy spread is smaller than the electron beam's total spectral width. In the case of the assembled focusing geometry, Fig. 9.4 depicts an analytical estimation of the effective electron energy spread in the TS interaction for various APL currents, i.e. different electron energies in focus. The calculation is on the basis of previous work [40, 41] and was performed in the case of a head-on collision between a Gaussian laser pulse and an electron beam. A laser pulse with a pulse energy of 50.8 mJ, a pulse duration of 32 fs, and a laser strength parameter of $a_0 = 0.81$ is assumed. The electron beam is assumed to have a normalised emittance of 0.43 µm mrad, a source size of 3.3 µm, and a flat energy spectrum. Depending on the focused energy, the effective energy spread ranges between 2.5 % and 10 %. However, this is independent of the initial electron energy spread and more than an order of magnitude smaller than the experimentally measured electron spectral width of 100 %. As the imaging chromaticity of the APL increases with increasing electron energy, so does the effective energy spread. Lower effective energy spreads at higher energies require a different focusing geometry or different initial beam properties. Equation 8.5 describes the linear dependence of the bandwidth of the produced Thomson spectrum on the electron energy spread. This correlation is also shown in Fig. 9.4.

While the measured initial beam size and divergence can be assumed to be constant across various energy slices, a 0.006 µm mrad/MeV, i.e. 1.4 %/MeV, increase in normalised emittance was measured (see Sec. 7.2.2). Figure 9.3i depicts the effect of the initial normalised emittance on beam size and beam divergence in focus to

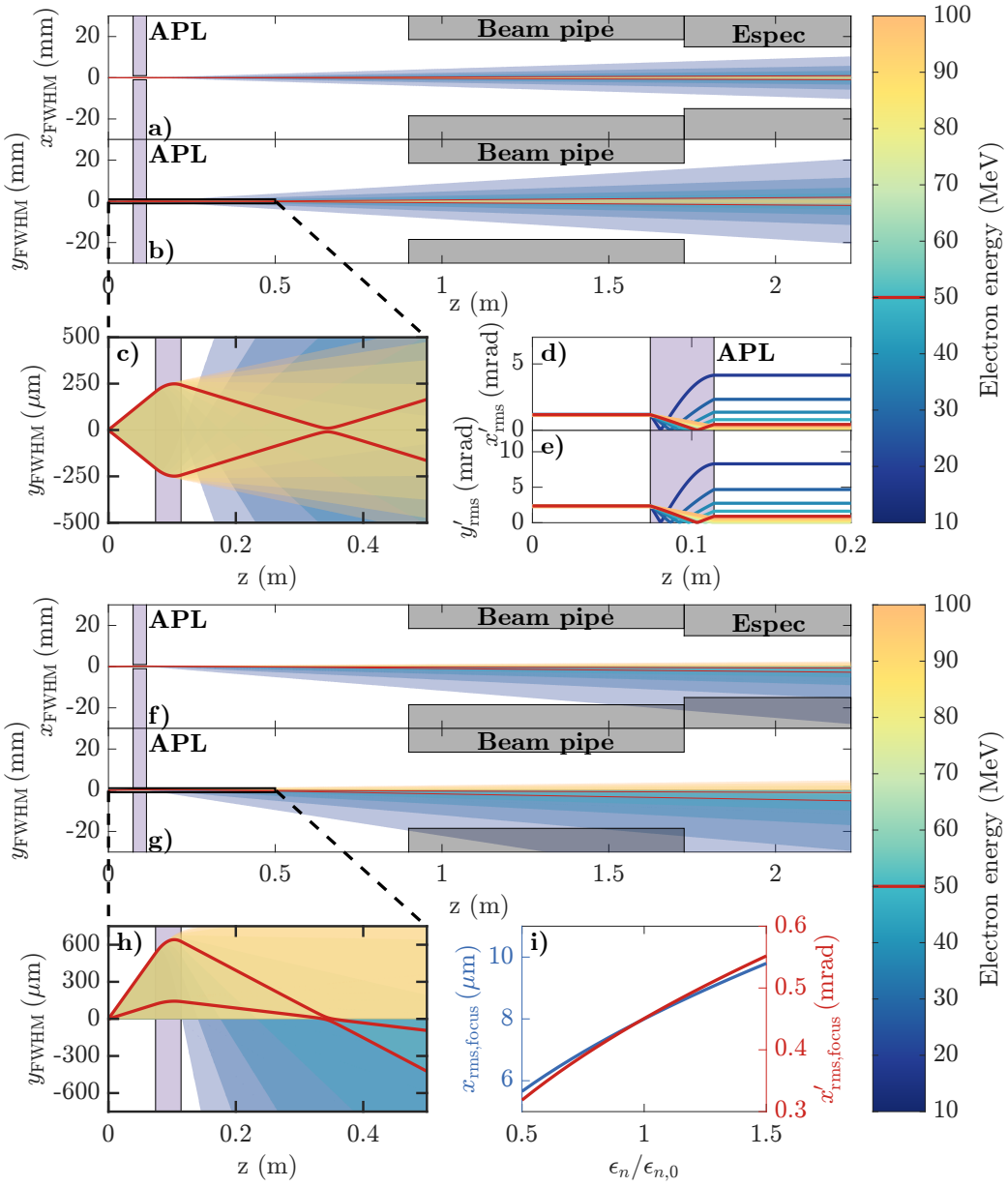

Figure 9.3: Chromatic focusing of electron energies between 10 MeV and 100 MeV into the Thomson interaction point using an APL. The APL current was set to about 340 A, yielding a focusing gradient of about 67 T/m, to focus an electron energy of 50 MeV into the interaction plane (highlighted as red line). The measured beam parameters discussed in Sec. 7.2.2 provide the electron beam source properties. The chromatic beam size evolutions in the horizontal (a) and vertical (b) are depicted, with the zoomed-in representation of the vertical plane (c). The evolution of the RMS divergence for both planes is shown in (d) and (e), respectively.
In analogy to the beam tracking in (a)-(c), (f)-(h) depict the FWHM beam evolution in the case of an initial beam pointing of 2.4 mrad in the horizontal and 4.4 mrad in the vertical. The evolution of beam divergence is independent of the initial beam pointing. The influence of the normalised emittance on the electron beam size and divergence in focus is shown in (i).

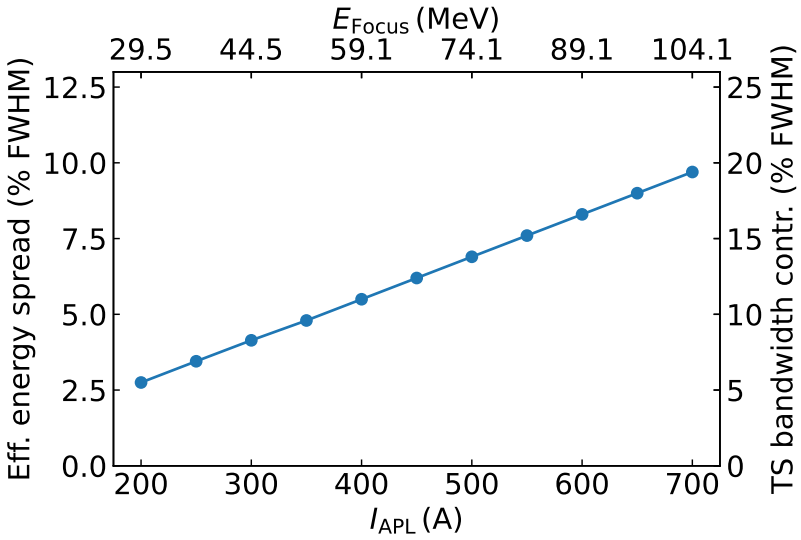

Figure 9.4: Effective electron energy spread in the TS interaction of a chromatically focused electron beam with a Gaussian laser pulse. The electron beam was assumed to have a normalised emittance of 0.43 µm mrad, a source size of 3.3 µm, and a flat energy spectrum. It interacts with a laser pulse with a pulse energy of 50.8 mJ, a pulse duration of 32 fs, and a laser strength parameter of $a_0 = 0.81$. The theoretical contribution to the Thomson spectrum bandwidth is given by Eq. 8.5. The analytical model is on the basis of the work from [40, 41].

understand its influence on the produced Thomson photons. When only the emittance is changed while the initial beam size and divergence remain constant, an effect on the properties in focus becomes apparent. A higher emittance increases the beam size and beam divergence in focus, whereas a lower emittance reduces beam size and divergence.

An increased electron focal spot size influences primarily the spatial overlap between the electron beam and the scattering laser beam. The photon yield is maximised when both beams are of the same size. With increasing and decreasing beam size, the photon yield decreases. Furthermore, a smaller electron focal spot generally results in a smaller effective energy spread because the focused electrons contribute more to scattering.

A change in beam divergence in focus has two main effects on the bandwidth of the produced X-ray spectrum. On the one hand, higher beam divergence results in a more defined energy-dispersed focal waist (compare Fig. 7.3b). The beam sizes of unfocused electron energies grow faster, reducing the effective energy spread and thus the X-ray beam bandwidth. On the other hand, as discussed in Sec. 8.2.1, the beam divergence increases the X-ray beam bandwidth directly. The X-ray beam bandwidth can rise or

fall depending on which effect is dominant. It should be noted that this reduction of the effective energy spread is only a consequence of the beam divergence. The beam divergence, however, has a direct impact on the bandwidth with a quadratic scaling. In general, it is more likely that as beam divergence increases, so will the bandwidth.

To understand the imaging stability and measure the focal spot size of a single energy slice, a high-resolution lutetium-yttrium oxyorthosilicate (LySo) scintillator in combination with a 1 T permanent dipole magnet was installed at the position of the Thomson interaction plane to observe the energy-dispersed electron focal waist. Section 3.3.2.3 describes the LySo scintillator, which is of the same type as that used for emittance measurements. To prevent the laser beam from reaching the screen, a 50 µm thick aluminium foil was installed directly at the scintillator facing upstream. This test was carried out while the scattering laser arm has yet to be assembled, hence the electron beam properties may differ from those presented elsewhere in this thesis. Figure 9.5 summarises the beam stability and beam waist in focus measurements for 100 consecutive shots. Figure 9.5a depicts an example of a dispersed beam profile, with its **R**oot **M**ean **S**quare (RMS) beam widths along the dispersive axis shown in Fig. 9.5b. Because no beam tracking was performed through the dipole magnet, the dispersive axis correlates to bins of unknown energies. However, by adjusting the APL's focusing strength, the focused energy was set to around 60 MeV. The minimum RMS beam widths for each shot are shown in Fig. 9.5c, yielding an average RMS focal spot size of (11.4 ± 0.6) µm. The positional jitter of the focused electron energy were measured in both planes. First, the focal position in the dispersive axis, i.e. the horizontal axis, was defined by the minimum beam width. The mean position of the intensity distribution in this energy slice was then used to define the focal position in the non-dispersive axis, i.e. the vertical axis. Figures 9.5d and 9.5e show the focal spot positions in the vertical and horizontal axis, respectively. The vertical position jitter was measured to be 4.5 µm, while the horizontal position jitter was 3.4 µm. It is worth noting that the dipole magnet's edge focusing reduces vertical position jitter. Even then, the vertical jitter is larger because the initial electron beam pointing jitter is larger in the vertical than in the horizontal (see Sec. 4). Position jitter is approximately one-third of the measured RMS beam waist, and the TS laser beam focal spot has a mean $1/e^2$ beam radius of about 8.7 µm. Perfect spatial overlap between the focused electrons and the laser beam cannot be achieved for every shot. This decreases photon production, which needs to be compensated by a prolonged measuring time.

One challenge with LPA-based X-ray sources is the underlying photon background, such as from bremsstrahlung. The beam transport depicted in Figs. 9.3a and 9.3b is undisturbed by the surrounding beamline structures, which are indicated as grey

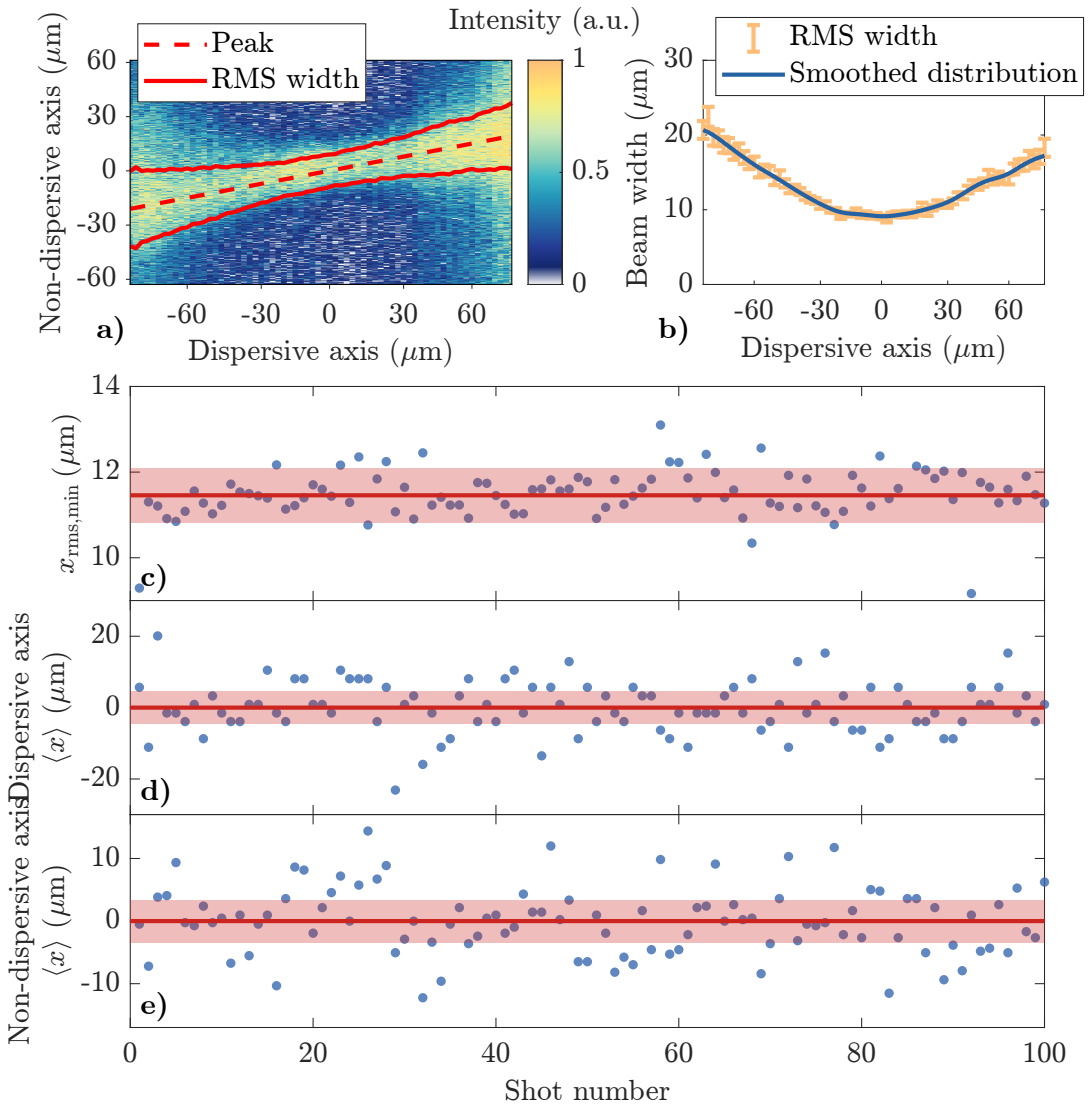

Figure 9.5: Measurement of the beam widths and position jitter of the focused electrons in the interaction plane for 100 consecutive shots. (a) depicts an example energy-dispersed beam profile with its RMS beam widths along the dispersed axis shown in (b). The minimum beam size is shown in (c) for each shot, yielding an average RMS focal spot size of (11.4 ± 0.6) µm. The mean position of the focused electron energy is summarised for both axes in (d) and (e), resulting in a position jitter of 4.5 µm in the dispersive axis and 3.4 µm in the non-dispersive axis.

areas for the beam pipe and electron spectrometer openings. This is not the case for electron beams with an initial pointing error. The average pointing angle of the electron beam was determined to be 2.4 mrad in the horizontal and 4.4 mrad in the vertical. Figures 9.3f and 9.3g show the beam trajectories of various energy slices in the case of an initial pointing error. Figure 9.3h depicts a zoomed-in representation of the beam transport, with the beam trajectory bent before approximately reaching the same interaction plane. Only the difference in total path lengths causes a relatively insignificant shift in the focal position. In the example presented, an energy of 50 MeV was focused into the interaction plane. Smaller energies will be over-focused and their beam sizes will increase rapidly along the beamline. Energies lower than 20 MeV will clip at the surrounding structures, resulting in on-axis bremsstrahlung. When higher energies are focused into the interaction plane, this effect becomes more significant.

9.3 ALIGNMENT FOR THOMSON RADIATION

To generate Thomson radiation, the focused electron beam and the TS laser beam must be precisely overlapped in both space and time. Spatial overlap on the order of a few micrometres is required, as well as femtosecond-level temporal overlap. Only after the first X-ray signal is detected, can it be further optimised. The methods used to overlap the electron and laser beams in space and time are described in the following.

9.3.1 Spatial Overlap

A separate overlap diagnostic system was designed to ensure overlap of the focal spot of the Thomson laser beam and the electron energy in focus. Figure 3.2 depicts the overlap system as a breadboard with the **C**harged-**C**oupled **D**evice (CCD) camera 'Cam3' mounted on it. The system is motorised in all three directions, and the vacuum-compatible camera can be moved longitudinally to image the correct plane. The diagnostic system consists of a DRZ-High phosphor screen (compare Sec. 3.3.2.1) angled at 45 degrees relative to the beam axis, which is observed by the camera. When driven into the beam axis, it measures the position of the electron beam focal spot. The LPA driver laser beam, which travels on the same axis as the electron beam, is blocked by a 50 µm thick aluminium layer in front of the scintillator. After the LPA driver laser beam is blocked, scattered light from the attenuated Thomson laser beam can be observed at the back of the screen, that is directly imaged by the camera.

Because, unlike the polychromatic electron focal spot, the TS laser beam focal spot is fixed longitudinally, it defines the longitudinal interaction position. A shift in longitudinal position corresponds to a change in electron energy in focus. As a result, the screen's position was first scanned to ensure that it was located within the laser beam focal spot. Since the electron beam focal spot is described by an overlap of several beam sizes with different electron energies, the focused energy was defined by the position of highest intensity. Because the initial beam pointing influences the beam profile in focus but not its position of the focused energy, summing several camera images makes the electron focal position more pronounced. Moving the APL changes the transverse position of the electron beam on the screen. However, the electron beam is aligned on-axis, which was predefined by the axis of the LPA driver laser, to ensure that the X-ray radiation is also on-axis and reaches the X-ray detector centrally. Therefore, the TS laser beam focal spot was moved transversely to the same position as the focused electron energy, using the folding mirror. The longitudinal position of the laser beam focal spot was then checked once more. This process was done iteratively until the longitudinal TS laser beam focal spot was located on the screen and it overlapped transversally with the electron focal spot.

9.3.2 Temporal Overlap

Attaining temporal overlap of the scattering laser beam and the electron beam is very challenging as it must be done with resolution of the order of the laser pulse duration. Because the electron beam and the LPA driver laser beam are separated in time by a few femtoseconds, it is sufficient to overlap both laser arms in time at the interaction plane for a start. As shown in Fig. 9.1, the beam splitter that divides the incoming laser beam into LPA driver beam and scattering laser beam is mounted on a delay stage. The relative timing between both laser beams can be adjusted with femtosecond precision by moving this delay stage.

The relative timing of both laser arms at the interaction plane was ensured to be within a nanosecond during the setup of the scattering arm using a photo diode, thus a precise timing within the range of motion of the delay stage was possible. After defining the interaction plane and completing the spatial overlap, both laser pulses were spatially overlapped using a pellicle beam splitter, allowing temporal alignment by spatial interferometry on the order of tens of femtoseconds. A 0.5" diameter uncoated pellicle beam splitter with 8% reflectivity and 92% transmission was mounted on the overlap diagnostic system and it could be moved into the same location as the phosphor screen. The beam splitter angle was adjusted so that the

reflected LPA driver laser beam and transmitted scattering laser beam overlapped spatially. Outside the vacuum, the overlapping laser beams were observed on a CCD camera to observe spatial interference. For the best contrast, the laser intensities of both beams on the camera must be similar. While the LPA driver laser beam has twice the laser energy of the TS laser beam, the pellicle beam splitter is 34.4 cm behind the laser's focal spot, resulting in a lower intensity on the pellicle. In contrast, the TS laser beam is in focus at the beam splitter. Therefore, both laser beams were attenuated to avoid damaging the beam splitter, and the laser intensity in the TS beam was reduced relative to the intensity of the LPA driver laser beam at the beam splitter by closing a motorised aperture. While a smaller beam diameter increases the size of the laser beam focal spot, the temporal properties remain unchanged. The delay stage was then scanned until spatial fringes were found to verify temporal overlap of both beams at the interaction plane. A downside of spatial interferometry is that the interference pattern is only visible when the two beams overlap within their coherence lengths, thus resulting in the need to scan the relative delay. An alternative would be to use spectral interference to directly measure the temporal delay between two beams, as proposed in [179].

9.4 MEASUREMENT OF THOMSON RADIATION

When the electron beam and the scattering laser beam are properly overlapped in space and time, TS results in X-ray photon emission. To understand and evaluate the Thomson source, the X-ray spectrum must be measured using an X-ray detector. The detector should be able to measure Thomson radiation at energies of up to 150 keV with sufficient resolution to reconstruct spectral properties such as peak energy and bandwidth. Ideally, the total photon yield is obtained as well. For this a **H**igh **E**nergy **X**-ray **I**maging **Tec**nology (HEXITEC) detector was used to observe the Thomson radiation beams. It is based on the room-temperature compound semiconductor **c**admium **t**elluride (CdTe), which allows it to measure X-ray energies up to 200 keV with a resolution of < 1 keV [180].

The following section describes the fundamentals of X-ray detectors, including X-ray spectrum measurements and corrections. Section 9.4.1 describes the methods of X-ray detection in detail. Then, Sec. 9.4.2 presents the HEXITEC detector, as well as its layout and detector effects. Finally, Monte Carlo simulations were performed to estimate the effects of X-ray detection and attenuation on the measured spectrum, as discussed in Sec. 9.4.3.

9.4.1 X-Ray Detection

Since photons are not charged, they can be separated from the electron beam in the experiment by using a dipole magnet. The electrons are dumped into lead bricks after the electron energy spectrometer, while the Thomson radiation travels unaffected by the dipole's magnetic field. However, because X-ray beams are not charged and have sufficiently short wavelengths, they can also pass through matter with little or no interaction. While this property explains why X-ray beams were first used in medicine to generate images of tissues and structures inside the human body, it also makes them difficult to detect. During their passage through matter, they lose energy due to interactions with orbital electrons or the absorber atom's nucleus. In one or multiple individual interactions, photons may lose all or a portion of their energy. Three mechanisms describe the X-ray interaction with the absorber atom: photoelectric effect, Compton scattering, and pair production. An X-ray detector, such as the HEXITEC detector, measures the deposited energy in an absorber material in the form of secondary particles rather than the X-ray photons themselves. All secondary particles must be measured and assigned to the correct initial photon in order to reconstruct an X-ray beam. The measurement depends on statistical events because only individual photons of an X-ray beam can be probed in the absorber material. This section describes the effects of the X-ray detection process following [181].

Photoelectric effect

The photoelectric effect is one kind of interaction between an X-ray photon and an atom. In absorber materials with a high atomic number Z, it is the dominant process for X-ray energies from the Thomson source described here. Figure 9.6 depicts a schematic of the photoelectric effect in an atom. In this example, all of the energy from the incident X-ray photon is transferred to a bound electron in the K-shell, but other shells are also possible. The electron is ejected from its bound state with a kinetic energy equal to the difference between the incident photon energy and its binding energy. For this effect to occur, the incident photon must have a higher energy than the electron's binding energy.

The vacancy left by the ejection of an orbital electron is filled by the transition of an electron from an upper energy shell. This is then followed by the emission of fluorescence radiation, which is characteristic for the absorber material used. Generally, fluorescence radiation also deposits its energy in the absorber material, contributing to the reconstruction of the incident photon energy. If the energy from the fluorescence radiation is caused by background radiation or was incorrectly assigned,

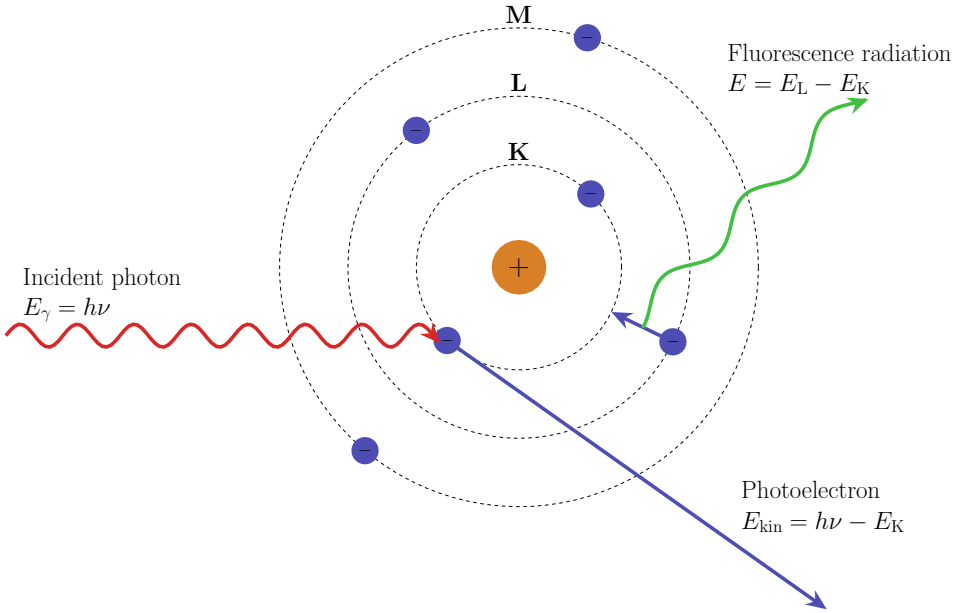

Figure 9.6: Schematic of the photoelectric effect in an atom. An incident photon with an energy of $E_\gamma = h\nu$ is completely absorbed by an inner-shell electron and an photoelectron is ejected from the atom. The kinetic energy of the photoelectron is equal to the initial photon energy E_γ minus the binding energy of the electron E_K. As outer shell electrons transition to fill vacancies in inner-shells, excess energy is released in the form of X-ray photons or additional electrons.

the X-ray detector measures its own fluorescence emission lines. However, if the fluorescence radiation escapes the absorber material, the incident photon energy is incorrectly reconstructed, i.e. shifted to lower energies by the amount of the escaped energy. When measuring a defined X-ray peak, an additional peak known as the escape peak often appears. In the case of a detector based on CdTe, the characteristic lines are located at 23 keV and 27 keV. This means that the measured X-ray spectrum will have a detector fluorescence line around 25 keV and an escape peak 25 keV lower than the actual incoming X-ray spectrum.

Compton scattering

While the photoelectric effect dominates at lower photon energies, Compton scattering contributes primarily at photon energies higher than 100 keV and is almost independent on the atomic-number of the absorber material. In Compton scattering, the incident X-ray photon transfers only a fraction of its energy to an electron in the absorber atom's outer shell, and the electron is ejected. Figure 9.7 shows a schematic of the Compton scattering process. Because the incident photon has a higher energy

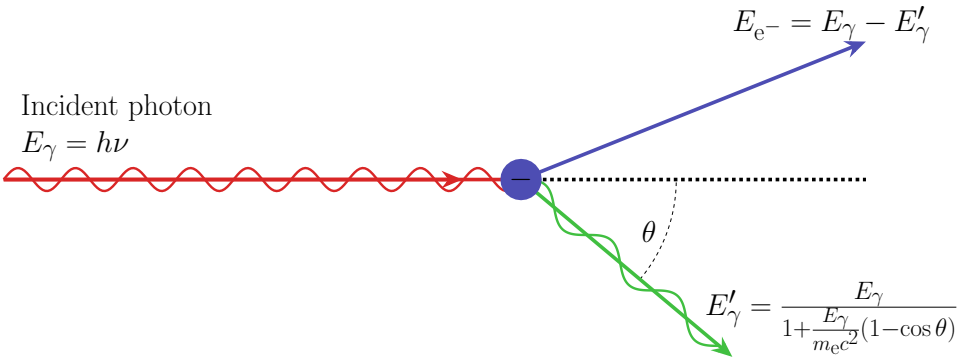

Figure 9.7: Schematic of the Compton scattering process. An incident photon with an energy of $E_\gamma = h\nu$ scatters with a quasi-free electron. The interaction reduces the photon's energy by transferring some of the photon's energy to the recoiling electron.

than in the photoelectric effect, the electron's binding energy can be neglected, and the electron is considered quasi-free. Therefore, Compton scattering is often referred to as an elastic scattering process. After scattering, the photon has a reduced energy and is deflected from its original direction. The less energetic photon may undergo further Compton scattering or it can be absorbed via the photoelectric effect. At higher X-ray energies, Compton scattering becomes dominant. Therefore, it is less important for the Thomson spectrum measurement in this thesis. However, X-ray photons with energies greater than 200 keV, that occur in the broad Bremsstrahlung background, can scatter elastically and then leave the absorber material. The scattered electron is detected and contributes to a broad background of the spectrum, which mainly affects the noise level of a measurement.

Pair production

For pair production to occur, an incident X-ray photon must have a minimum energy of 1022 keV, which corresponds to twice the electron rest mass. The photon is unlikely to interact with orbital electrons due to its high energy. Instead, the photon interacts with the nucleus' electric field as it passes through the absorber, converting into an electron-positron pair. The energy of each particle is half that of the original X-ray photon. Because pair production is more likely to happen in strong electric fields, the effect is predominant in high-Z materials. The particles continue to interact with the absorber material. The positron scatters and loses energy until it annihilates with another electron, resulting in two 511 keV photons emitted in opposite directions. Figure 9.8 depicts a schematic of pair production in an atom. Since pair production can occur only at energies greater than 1022 keV, it is not directly relevant for detecting the X-ray spectrum in this thesis. Only the resulting electrons may contribute to the overall X-ray background.

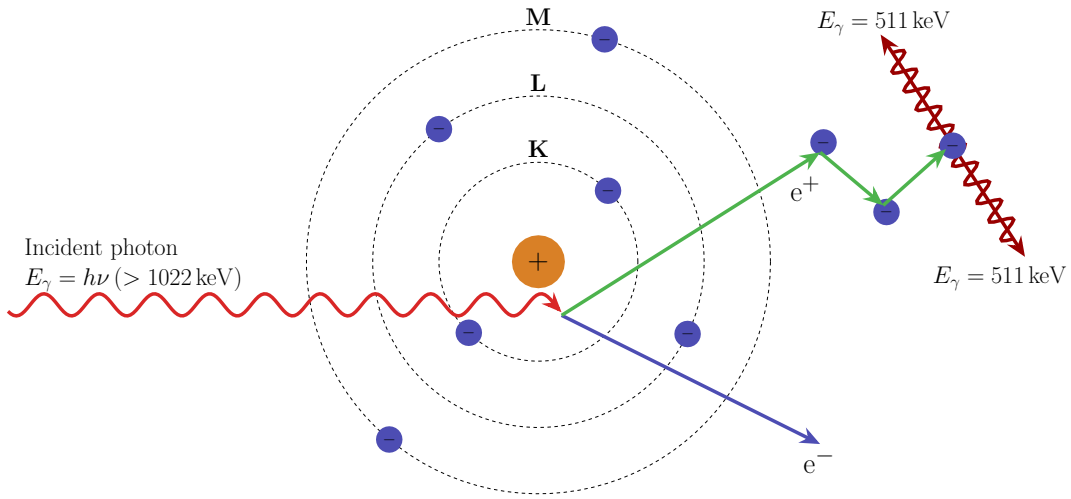

Figure 9.8: Schematic of pair production in an atom. An incident photon with an energy of $E_\gamma > 1022\,\mathrm{keV}$ interacts with a nucleus' electric field and converts into an electron and a positron. Each particle possesses half the energy of the incident photon, i.e. at least 511 keV. The positron interacts with other electrons until it annihilates with a free electron, and emits two photons with energies of 511 keV.

Semiconductor detectors

In order to measure the energy of an incoming X-ray photon, its secondary particles must be registered and assigned to the correct photon. Semiconductor detectors or solid-state detectors are used to reconstruct the energy of all secondary particles. Common semiconductor materials are silicon, germanium, and CdTe. These detectors, as in gas-filled detectors, are based on the ionisation of atoms via the mechanisms described above. Ionisations produced in the detector are collected as current and converted to voltage pulses by applying a voltage through a resistor. The pulse size is proportional to the amount of radiation energy absorbed by the detector. Because semiconductors are denser than gases, they are more efficient for X-ray detection.

Different detector materials have different efficacy in detecting X-ray photons. This is represented by the X-ray attenuation in the respective material, as shown in Fig. 9.9 for 1 mm thick silicon, germanium and CdTe. While silicon detectors are the most affordable and commonly used, they have a low attenuation for X-ray energies higher than 50 keV. On the other hand, germanium detectors have a higher resolution but are more expensive and require liquid nitrogen cooling. CdTe detectors have the highest efficacy of the three absorber materials for high X-ray energies and can operate at room temperature. Therefore, the HEXITEC detector system based on CdTe material was chosen for the experiments.

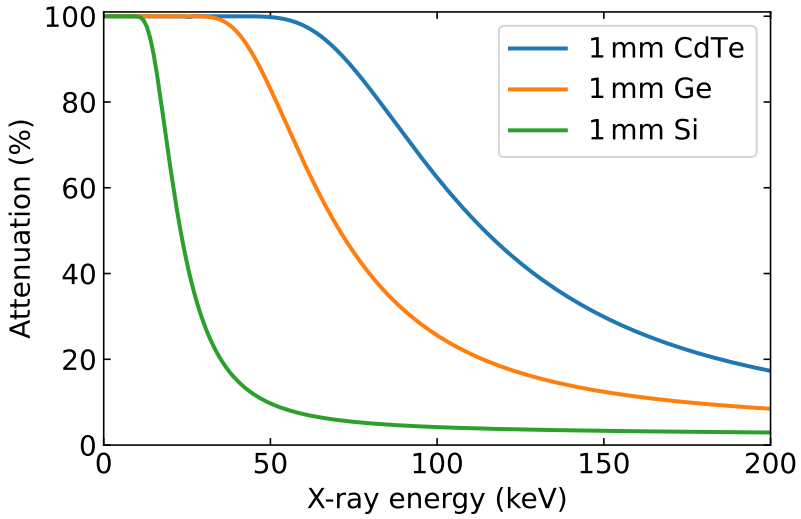

Figure 9.9: Attenuation of X-ray radiation in 1 mm thick silicon (Si), germanium (Ge) and CdTe. The plot is based on the database from [182].

9.4.2 The HEXITEC Detector System

X-ray beams from TS based on an LPA electron bunch have pulse durations of the order of femtoseconds due to the intrinsically short electron bunches. A single detector crystal cannot read out multiple photons at the same time. So a detector with multiple semiconductor crystals is required. The HEXITEC [180] detector is a pixelated detector based on the room temperature compound semiconductor CdTe and is made up of 6400 single crystals laid out in an 80×80 grid. Each pixel measures 250 µm by 250 µm and has a thickness of 1 mm, resulting in a chip area of 2 cm by 2 cm. In most cases, the pixel size allows the full energy of an incoming X-ray photon to be deposited in just one pixel. The detector is able to measure X-ray spectra up to energies of 200 keV with an energy resolution of < 1 keV. A photograph of the detector system is shown in Fig. 9.10. It depicts the housing, which measures $22\,\text{cm} \times 6\,\text{cm} \times 6\,\text{cm}$ and houses the detector chip and electronics. It was placed in air, on the axis of the generated X-ray beam, 7.47 m behind the Thomson interaction plane. As a result, the opening cone of the detector chip has a radius of about 1.61 mrad.

The HEXITEC detector records an X-ray spectrum in every pixel at a readout rate of 10 kHz. To remove or recover energy deposited by charge sharing events, various correction algorithms can be used. A charge-sharing event occurs when multiple events occur in neighbouring detector pixels. In the case of some signal in the neighbouring pixels, an event is removed using a mode known as charge-sharing discrimination. This improves the measurement's signal-to-noise ratio. Because a

Figure 9.10: Photograph on the HEXITEC detector system. On the right side of the image, the pixelated semiconductor chip is visible. The remainder is mostly made up of electronics. The detector chip was covered by a 1.5 mm thick aluminium plate during the X-ray spectrum measurements to further attenuate the X-ray flux. Photograph taken from [180].

large photon flux quickly saturates the detector, the number of photons from the Thomson source and from Bremsstrahlung must be reduced. Since Bremsstrahlung is predominant and caused by electrons interacting with matter, the electron bunch charge was lowered to avoid detector saturation.

To ensure that the correct X-ray spectrum is reconstructed, each individual detector pixel must be calibrated separately. Because detector performance varies over time, this was redone days after the Thomson radiation data was collected. The pixels were calibrated by fitting the spectra of known radioactive sources. As radioactive emitters, ^{241}Am and ^{57}Co were used, both of which have known emission lines at 59.54 keV and 122.06 keV, respectively. In addition, the detector's fluorescence lines were used, specifically the ~ 23 keV (cadmium) emission line and the ~ 27 keV (telluride) emission line. The calibration process is the same as previously done in [14, 92]. Calibration also resulted in the detection of dead pixels, which exhibit a high level of noise and are thus excluded from the analysis of the recorded X-ray spectra.

9.4.3 X-Ray Spectrum Corrections

Radioactive isotopes are well-suited for detector calibration due to the narrow bandwidth of their radiation. However, when resolving a spectrum with a bandwidth of tens of keV, several detector effects cause the measured spectrum to be distorted. The efficacy of a CdTe detector is non-uniform, as illustrated in Fig. 9.10, and different photon energies contribute with different cross sections. As the efficacy of higher X-ray energies decreases, the peak value of a broad spectrum is lower than it should be. These effects must be understood in order to reconstruct the correct X-ray spectra. Therefore, the detector and the X-ray beam path was modelled in Geant4 [183–185]. Geant4 is a Monte-Carlo-based tool kit for simulating particle passage through matter. Its capabilities allow for the simulation of X-ray beam attenuation and the investigation of detector reconstruction behaviour.

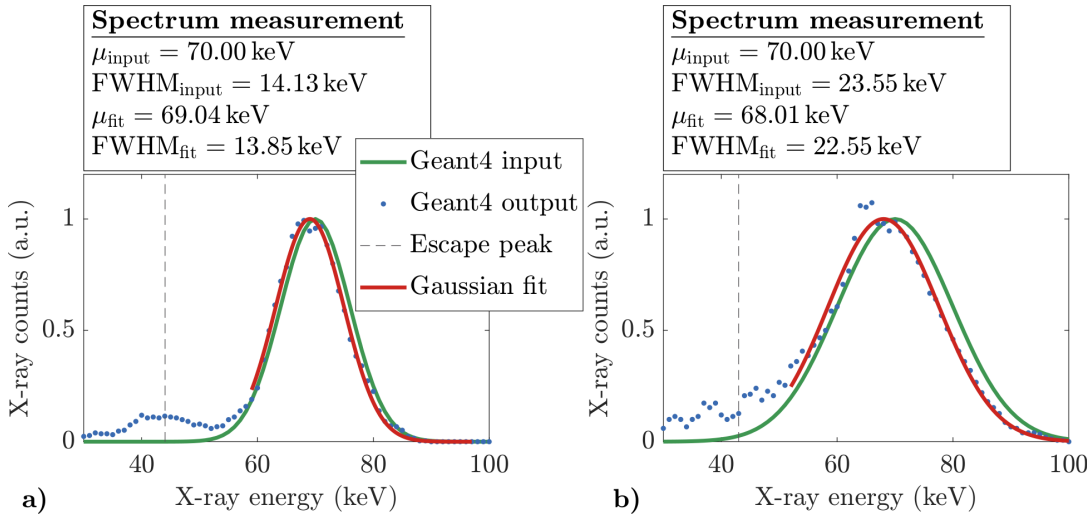

Figure 9.11: A comparison of the Gaussian input spectrum (green) and the output spectrum (blue) measured by the X-ray detector in a Geant4 simulation. The input spectrum is described by a mean value at 70 keV with a FWHM bandwidth of 14.13 keV (a) or 23.55 keV (b). The output spectrum is fitted with a Gaussian function and compared with the simulation input. Due to the fluorescence of CdTe, the measured spectrum is replicated as an escape peak at a lower energy of about 25 keV, as indicated by the dotted black curve.

In addition to the attenuation in the absorber material of the detector, other materials can attenuate the X-ray beam. The detector is located 7.47 m after the Thomson interaction point, outside the vacuum chamber. Therefore, the X-ray beam must pass through a 200 µm-thick aluminium window to enter air from vacuum and it travels about 4.9 m through the air before reaching the HEXITEC detector. To block low-energy radiation, an additional 1.5 mm-thick aluminium plate is placed in front of the detector chip during the experiment. In the Geant4 simulations [186], Gaussian input spectra with various mean energies and bandwidths were considered. They were propagated to the X-ray detector, which calculates the energy deposited in the detector chip. By comparing the input spectrum and the spectrum collected by the detector, the measured spectra in the experiment can be corrected back to the original spectrum.

Figure 9.11 shows the collected spectra compared to the input spectra with a mean energy of 70 keV and FWHM bandwidths of 14.13 keV (Fig. 9.11a) and 23.55 keV (Fig. 9.11b). The measured spectrum shows an escape peak at a lower energy of about 25 keV due to the fluorescence of CdTe. For bandwidths less than 25/2 keV, the main spectrum and its replica are generally distinguishable. In the case of large bandwidths, however, the replica merges with the main spectrum (see Fig. 9.11b), making the recorded total distribution appear broadened. Furthermore, due to attenuation in aluminium, air and the detector chip, higher X-ray energies are less likely to be

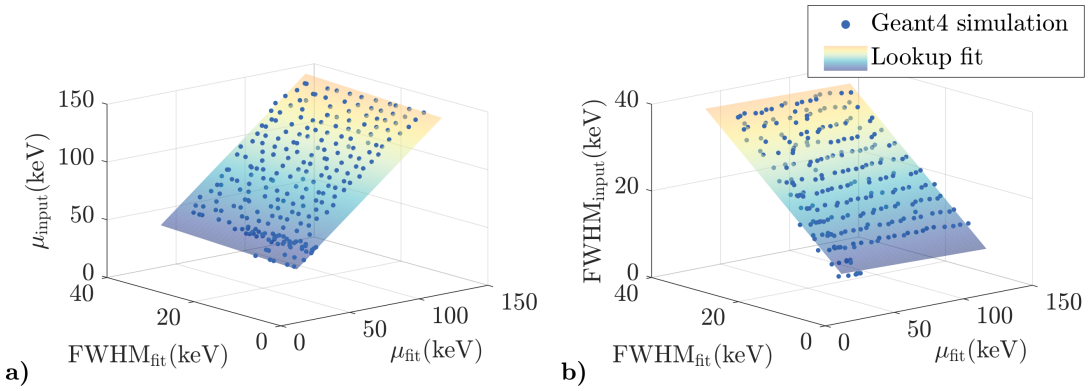

Figure 9.12: Mean position and FWHM bandwidth of the input X-ray spectrum as a function of the fitted mean position and bandwidth of the output spectrum. Geant4 was used to simulate the reconstruction effects, which are described by a two-dimensional linear lookup fit that can be applied to the measured spectra.

detected. When compared to the input spectrum, the mean energy appears to be shifted to lower energies, and the spectral width is reduced for the X-ray energies under consideration. Since the simulation assumes Gaussian spectral profiles, the measured data was described using a Gaussian fit. However, energies of less than 2/3 of the FWHM relative to the peak energy are excluded from the fitting to reduce artificial broadening due to the escape peak. Additionally, because of the fluorescence peaks of CdTe, energies below 30 keV were excluded from the fitting routine. The larger the bandwidth, the more severe the peak energy shift and change in measured bandwidth. The FWHM of the input spectrum in Fig. 9.11a is 14.13keV, and the fitted output spectrum is shifted by about 1 keV with a bandwidth reduction of about 0.3 keV. For an input bandwidth of 23.55 keV, however, the measured peak is shifted by about 2 keV and the bandwith is reduced by about 1 keV (see Fig. 9.11b).

The X-ray detector in the experiment measures a spectrum analogous to the Geant4 output spectrum, but the input spectrum is the actual spectrum from the source. To account for these effects, a two-dimensional scan comprised of several Geant4 simulations, such as shown in Fig. 9.11, was performed. The change in reconstructed mean position and bandwidth was determined for mean energies ranging from 35 keV to 140 keV and FWHM bandwidths ranging from 7 keV to 35 keV. Figures 9.12a and 9.12b show the mean position and FWHM bandwidth of the input spectrum as a function of the bandwidth and mean position of the fitted function. A two-dimensional linear model was used to describe the distribution as a lookup fit. The mean energies and bandwidths are generally lower than in the actual spectrum for the X-ray energies under consideration. After using the same fitting routine for the measured spectra in the experiment, the spectra are corrected by applying the result of the lookup fit.

9.5 MEASUREMENT PROCEDURE

Several procedures and optimisations must be performed in order to set up the Thomson source and measure the signal from the X-ray photons. At the start of a laser experiment, the laser beam alignment and focal spot quality of both the main laser beam and the Thomson laser beam are checked. If necessary, optimisation is carried out. To avoid saturation of the X-ray detector by the overall photon flux, which is primarily caused by bremsstrahlung, the electron source is operated at low electron beam charge. Because electron beams define the propagation axis of generated Thomson radiation, they are optimised for stability and central pointing. The plasma lens is driven onto the beam axis and used to focus the electron beam, once again ensuring proper electron beam pointing.

After optimising the electron source, the spatial and temporal overlap of the focused electron beam and the Thomson laser beam must be realised. While the Thomson laser beam is blocked, the spatial overlap diagnostic system is positioned in the interaction plane, where the polychromatic electron focal position is imaged and marked (see Sec. 9.3.1). The LPA driver laser beam is then blocked, and the Thomson laser beam focal spot is observed on the overlap diagnostic system. By adjusting the folding mirror with motorised stepper motors, the laser beam focal spot is moved to the position of the electron beam focal spot. Because the focused electron energy has a larger beam size than the laser beam focal spot, the spatial overlap is less sensitive to electron beam shot-to-shot fluctuations.

To determine temporal overlap, the diagnostic based on spatial interference between both laser beams is used (see Sec. 9.3.2). The delay stage of the LPA driver laser beam is adjusted so that both laser beams are temporally overlapped at the interaction plane position. To compensate for uncertainties in the temporal overlap, such as a longitudinal offset between the spatial and temporal overlap diagnostics, a fine timing scan is required. The spectrum measured by the HEXITEC detector (see Sec. 9.4.1) was used to perform this fine timing scan. The delay stage was scanned in 10 fs increments until the signal from TS was measured over the background radiation. When the Thomson signal was first measured, the X-ray detector was moved transversally so that the measured photon spectrum had the maximum peak energy and the lowest bandwidth, as expected in the on-axis spectrum.

At this point, the electron beam profile was characterised (see Sec. 4), and the electron spectrum was measured in combination with the beam emittance (see Sec. 7). After the Thomson signal has been optimised for a given discharge current in the APL, the focusing strength of the APL can be changed to tune the resulting X-ray spectrum.

The changed APL strength has no effect on spatial overlap, and was not checked throughout the measurements. The scattering laser beam can be blocked to measure background radiation without affecting electron beam production or propagation.

10 THOMSON SOURCE STUDIES

The goal of the work described in this thesis is the realisation and characterisation of a tunable Thomson source with reduced spectral bandwidth. This section discusses the experimentally measured photon spectra, and compares them with results from simulation and analytical predictions.

Section 10.1 introduces the simulation tools that were used to mimic the experiment, while the measured spectra are presented and analysed in Sec. 10.2. In particular, the spectral bandwidth contributions and the photon yield of the spectra are highlighted. Section 10.3 concludes with a discussion of possibilities for future X-ray source optimisation. The question of what can be done to reduce the spectral bandwidth even further and increase the photon yield will be addressed.

10.1 SIMULATION TOOLS

To comprehend, study, and optimise an experiment, it is useful to compare it to existing theory or simulations. While the theoretical foundations presented in Sec. 8 are helpful for understanding the dependencies and scaling laws of various effects, several assumptions must be made. For example, the laser strength parameter and beam divergence are not constants and vary according to the specific setup. Attempts have previously been made to describe these parameters using effective quantities [165]. In general, the fundamental theory fails to predict the precise spectral shape of the produced X-ray beam. Therefore, numerical simulations are essential in order to interpret experimental results.

A start-to-end simulation pipeline on the basis of **Wake**field particle **T**racker (Wake-T) [187], **F**ourier-**B**essel **P**article-**I**n-**C**ell (FBPIC) [49, 50], and synchrad [188] was developed [189] and benchmarked against previously used simulation codes [40, 163]. The main advantages in this pipeline over the previously used codes are its flexibility and decreased computing times. It is divided into three parts. The electron bunch is first generated and transported to the interaction plane via the APL. The scattering laser beam's interaction with the electron bunch is then simulated. In the final step, the generated radiation is computed from the electron trajectories in the electric field of the laser pulse. The simulation pipeline and the inputs used are further described below.

10.1.1 Electron Bunch Propagation

The simulation starts with electron bunch generation and propagation to the interaction plane using Wake-T. Wake-T is a tracking code for laser- and beam-driven plasma wakefield accelerators that provides a fast, simplified alternative to **P**article-**i**n-**c**ell (PIC) simulations. Furthermore, conventional beam optics and the APL are implemented in order to simulate complex beamlines [187].

The simulation uses the measured electron beam characteristics described in Sec. 7.2. A total bunch charge of 4.5 pC is distributed in 50000 macroparticles according to the reconstructed electron energy spectrum (see Sec. 7.2.1). However, because the Thomson interaction's effective electron energy spread limits the required charge distribution, only a range of $\pm 20\%$ around the focused energy is simulated. The initial beam size and emittance in the horizontal plane are set to the fitted parameters from Sec. 7.2.2, and the electron beam is assumed to be matched, i.e. $\langle xx' \rangle = 0\,\mu\text{m mrad}$. The average energy slice has a beam size is about 2.9 µm and a normalised emittance of about 0.4 mm mrad. Due to the increased electron beam divergence in the polarisation plane of the laser beam, an increased emittance along that axis, i.e. along the vertical, is expected. To consider that in the simulation, the vertical emittance was doubled compared to the horizontal emittance while keeping the same source beam size. The electron beam travels 7.4 cm in free drift before being focused by an APL with a length of 4 cm and a radius of 1 mm to image the central electron energy. The output of the simulation is the particle distribution at the interaction plane 23 cm after the APL exit.

10.1.2 The Electron-Laser Interaction

The next step is to calculate the electron trajectories in the electric field of the scattering laser beam. The interaction and the laser beam profile is simulated in FBPIC [49, 50]. FBPIC is a PIC code that is used to study plasma-based acceleration by simulating the interaction of charged particles and electromagnetic fields. As in Wake-T, the charged particles are represented by macroparticles, but the fields are calculated on a grid. A set of 2D radial grids is used to represent the azimuthal modes of the 3D problem. This makes the code fast, but it is only applicable in situations with close-to-cylindrical symmetry. Discrete time steps are used to simulate the time evolution. The following calculations are carried out within a single time step [190]:

- The values from the electric and magnetic fields are gathered from the grid onto the macroparticles.

- The particles are pushed by one time step determined by their velocity.
- The macroparticles' charge and current are deposited on the grid.
- The electric and magnetic fields are recalculated using the updated grid.

The measured properties of the scattering laser beam are described in Sec. 9.1. FBPIC provides numerous options for realising a custom laser pulse. In this case, a transverse and temporal profile are defined separately. The total laser pulse energy is distributed over the entire laser profile to obtain the required laser strength parameter. The temporal profile is assumed to be described by a Gaussian pulse with a FWHM pulse duration of 32.2 fs. However, in the code, the spectral bandwidth is given by the Fourier-limited bandwidth. By introducing a chirp of 176.5 fs^2 for a Gaussian pulse with a pulse duration of 19 fs, a temporal profile with 32 fs pulse duration and a spectral bandwidth of 8.8 % was obtained. The central wavelength was set to 800 nm.

A simple description using Gaussian profiles is not possible for the transverse laser profile. As presented in Sec. 9.1, the focal spot is asymmetric. While the peak laser strength parameter was measured to be $a_0 = 0.81$, there is additional intensity outside of the main peak that reaches $a_0 = 0.3$. To describe the entire intensity distribution, the measured transverse profile was decomposed into its **H**ermite **G**aussian (HG) modes, as previously done in [191]. A single HG mode in the transverse axis x is defined by [71]

$$u_n(x) = \sqrt{\frac{\sqrt{2/\pi}}{2^n\, n!\, w_0}} H_n\left(\frac{\sqrt{2}x}{w_0}\right) \exp\left(-\frac{x^2}{w_0^2}\right), \tag{10.1}$$

with n describing the order of the mode and w_0 being the laser beam waist. The Hermite polynomial of degree n is defined by

$$H_n(x) = (-1)^n e^{x^2} \frac{d^n}{dx^n} e^{-x^2}. \tag{10.2}$$

Then the normalised transverse electric field is given by the product of the waveforms in both axes, i.e. $u_{n,m}(x,y) = u_n(x) \cdot u_m(y)$. The total order of HG modes is defined by $N = m + n$. Figure 10.1 depicts the intensity profile for the first nine HG profiles. Modal decomposition requires calculating the coefficients $c_{n,m}$ by projecting each HG mode $u_{n,m}$ onto the measured laser field profile [192]. The superposition of the HG modes

$$\tilde{u}_{N_{max}}(x,y) = \sum_{n=0}^{N_{max}} \sum_{m=0}^{N_{max}-n} c_{n,m} \cdot u_n(x) u_m(y) \tag{10.3}$$

results in the reconstruction of the initial profile, where N_{max} specifies the maximum number of HG modes with $N = 0, 1, 2, ..., N_{max}$. A theoretically perfect reconstruction

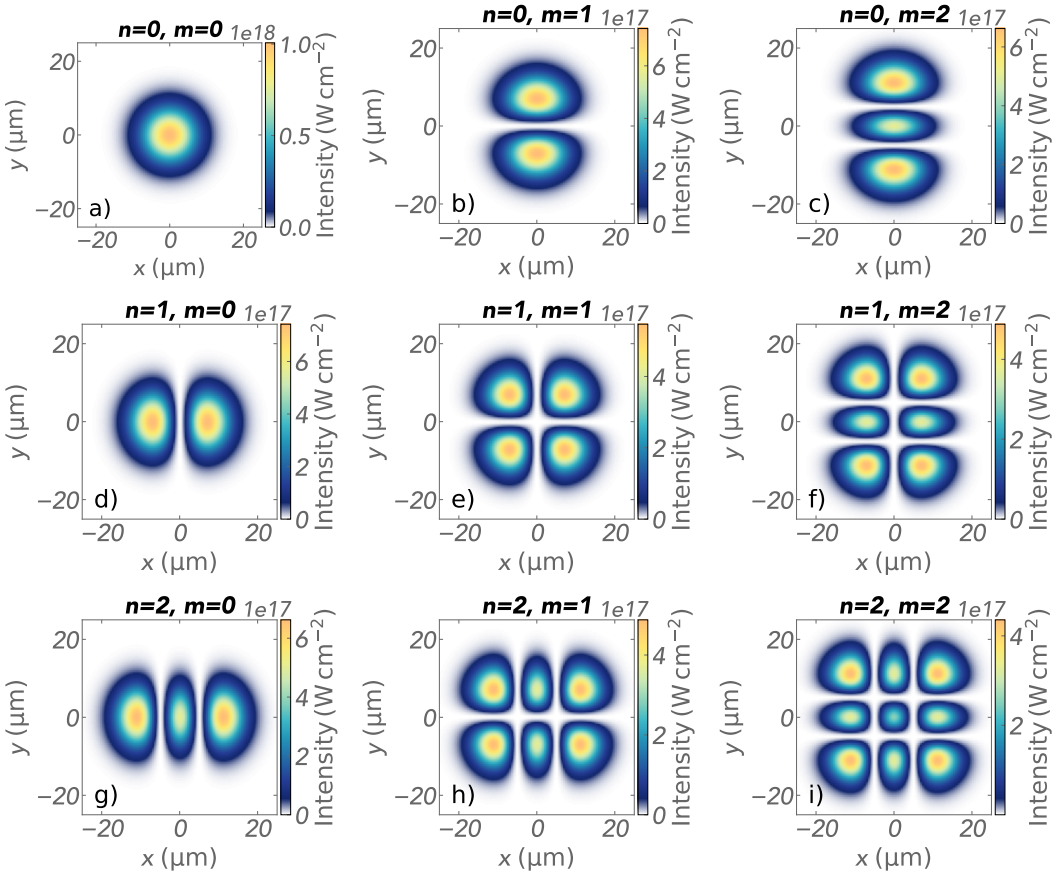

Figure 10.1: Intensity profiles for the first nine HG profiles. The calculation of the intensity assumes a wavelength of 800 nm, a pulse energy of 50.8 mJ, a pulse duration of 32 fs and a focal waist of $w_0 = 10\,\mu m$.

of any arbitrary distribution is obtained for $N_{max} \to \infty$. For $N_{max} = 0$ is $n = m = 0$ and the profile is described by a two dimensional Gaussian distribution. Figure 10.2a depicts this scenario, in which the measured intensity profile is described by simple Gaussian distributions. The residual intensity to the initial profile is shown in Fig. 10.2b, indicating that Gaussian distributions do not adequately describe the initial profile. As the number of available modes N_{max} increases, the initial profile is reconstructed with more details, and the residual intensity decreases. Figures 10.2c-10.2h illustrate the reconstructed profiles for $N_{max} \in \{5, 10, 30\}$.

To assess the significance of single modes, Fig. 10.3a depicts the share for a pair of (n, m)—modes to the total reconstruction in the case of $N_{max} = 30$. The mode with $n = m = 0$ contributes the most to the description of the intensity profile, while higher modes are used to describe deviations. As the number of modes increases, the

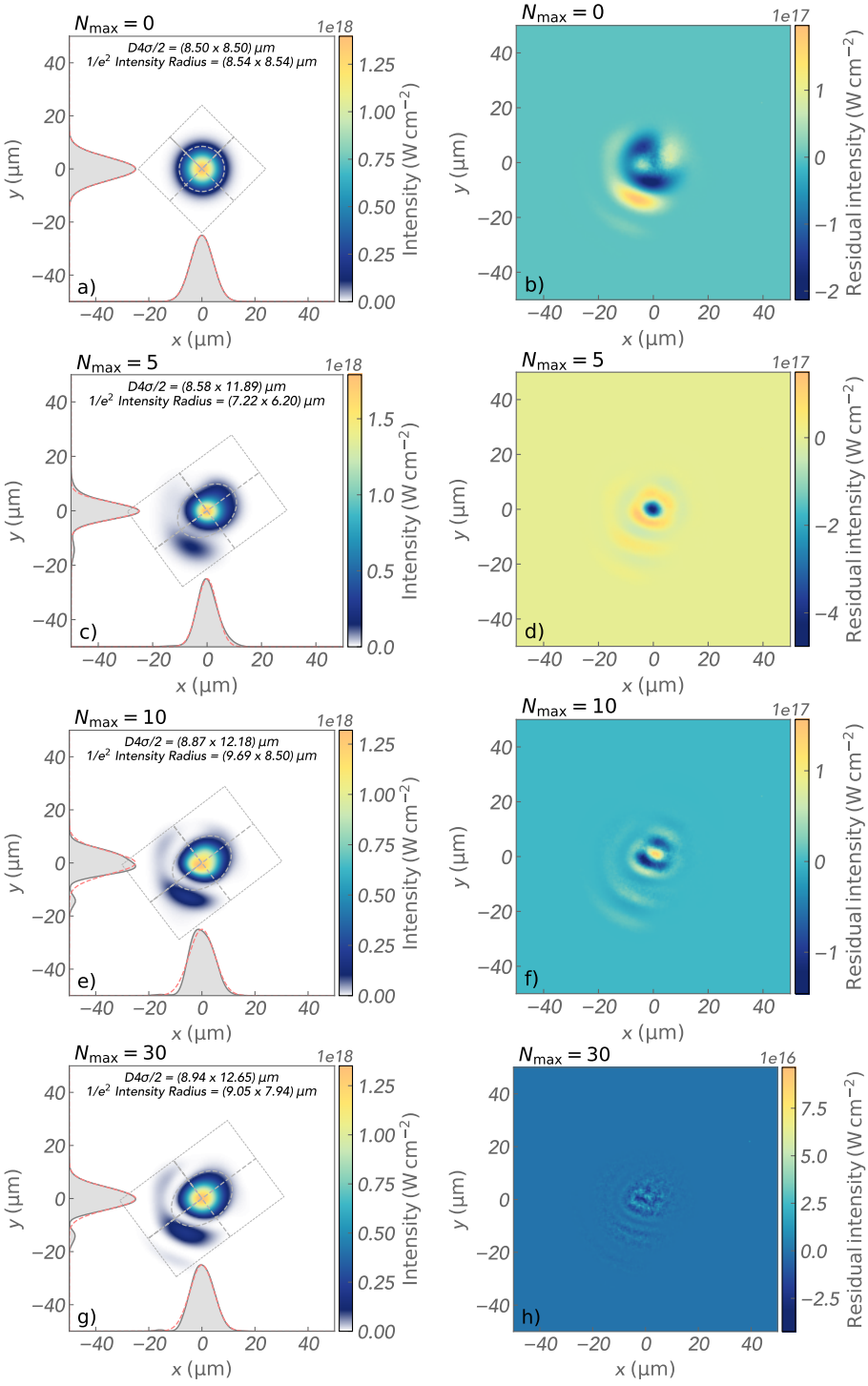

Figure 10.2: Reconstruction of the Thomson laser intensity profile at focus using a superposition of HG modes up to N_{max}. The reconstructed intensity according to Eq. 10.3 for $N_{max} \in \{0, 5, 10, 30\}$ is shown in (a), (c), (e) and (g), respectively. A comparison with the initial profile yields in the residual intensity shown in (b), (d), (f) and (h).

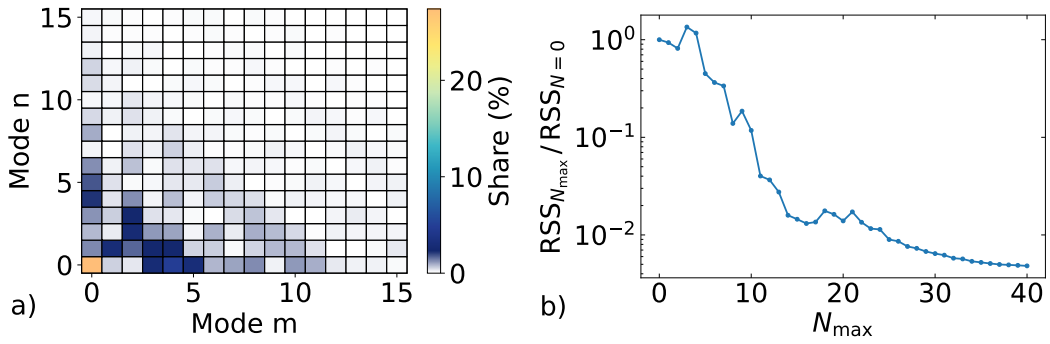

Figure 10.3: Individual HG mode contributions to the reconstruction of the Thomson laser intensity profile in focus with an $N_{max} = 30$ (a) and evaluation of residual intensities compared a simple Gaussian reconstruction (b).

importance of each mode decreases. To quantify the intensity profile reconstruction for different N_{max}, the **R**esidual **S**um of **S**quares (RSS) is defined as

$$RSS = \sum_i (I_{init,i} - I_{reco,i})^2, \tag{10.4}$$

with I_{init} being the initial intensity profile and I_{reco} being the reconstructed profile for a specified N_{max}. The sum is evaluated over all camera bins i. Figure 10.3b illustrates the relative RSS-value when comparing the reconstruction to a simple Gaussian description ($N_{max} = 0$). In general, as $N_{max} = 0$ increases, the reconstruction improves. A $N_{max} = 30$ was used for the measured laser beam profile, which improves the RSS-value by a factor of about 100 when compared to a simple Gaussian model. Including more orders does not impact the simulation significantly but it does increase the computing time. The reconstructed intensity profile is shown in Fig. 10.2g and the field construction by HG modes was imported to FBPIC. In the simulation, the peak laser strength parameter was fixed to $a_0 = 0.81$.

Since the Thomson laser beam collided with the electron beam at an angle of 10°, the electron beam axis was rotated relative to the laser beam propagation axis. The electrons interact with the fields of the scattering laser beam, resulting in modulated trajectories and thus photon emission. This simulation step calculates the electron trajectories in the laser field.

10.1.3 Radiation Calculations

The final simulation step is to calculate the emitted radiation using the electron trajectories. This is accomplished using the open source code synchrad [188]. This tool processes the 3D trajectories of charged point-like particles and computes the

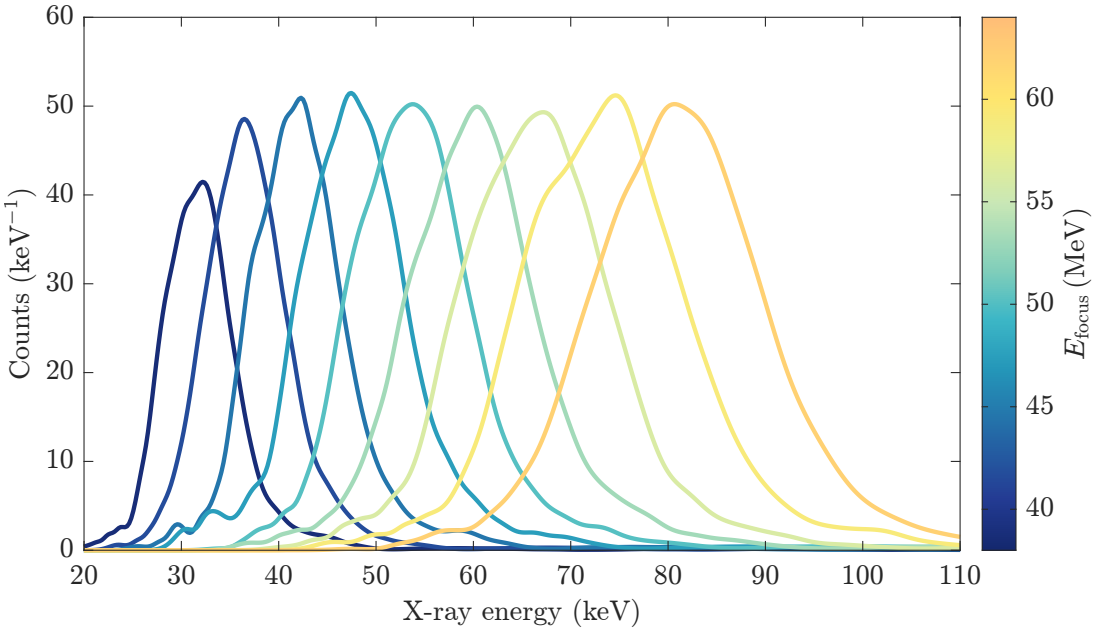

Figure 10.4: Simulated X-ray spectra for various electron energies in focus. The APL current was tuned in the simulation to vary the electron energy E_{focus} in focus.

energy density of synchrotron radiation in the 3D spectral domain using Fourier transformed Lienard-Wiechert potentials [193]. The X-ray spectrum that reaches the HEXITEC detector is simulated by limiting the opening radiation cone to 2.61 mrad. A set of simulated X-ray spectra is shown in Fig. 10.4. The various spectra result from assuming different focusing strengths in the APL in order to have a different electron energy E_{focus} in focus. The simulated and measured X-ray spectra are analysed and compared in Sec. 10.2.

10.2 TUNABLE X-RAY SOURCE

After the Thomson source was set up and optimised using the procedures described in Sec. 9.5, the HEXITEC detector was used to measure X-ray spectra. The measurement of various Thomson spectra is covered in Sec. 10.2.1. Section 10.2.2 studies the individual contributions to the total spectral bandwidth by comparing the spectra to numerical simulations and the analytical model. Finally, Sec. 10.2.3 discusses the measured and expected photon yield.

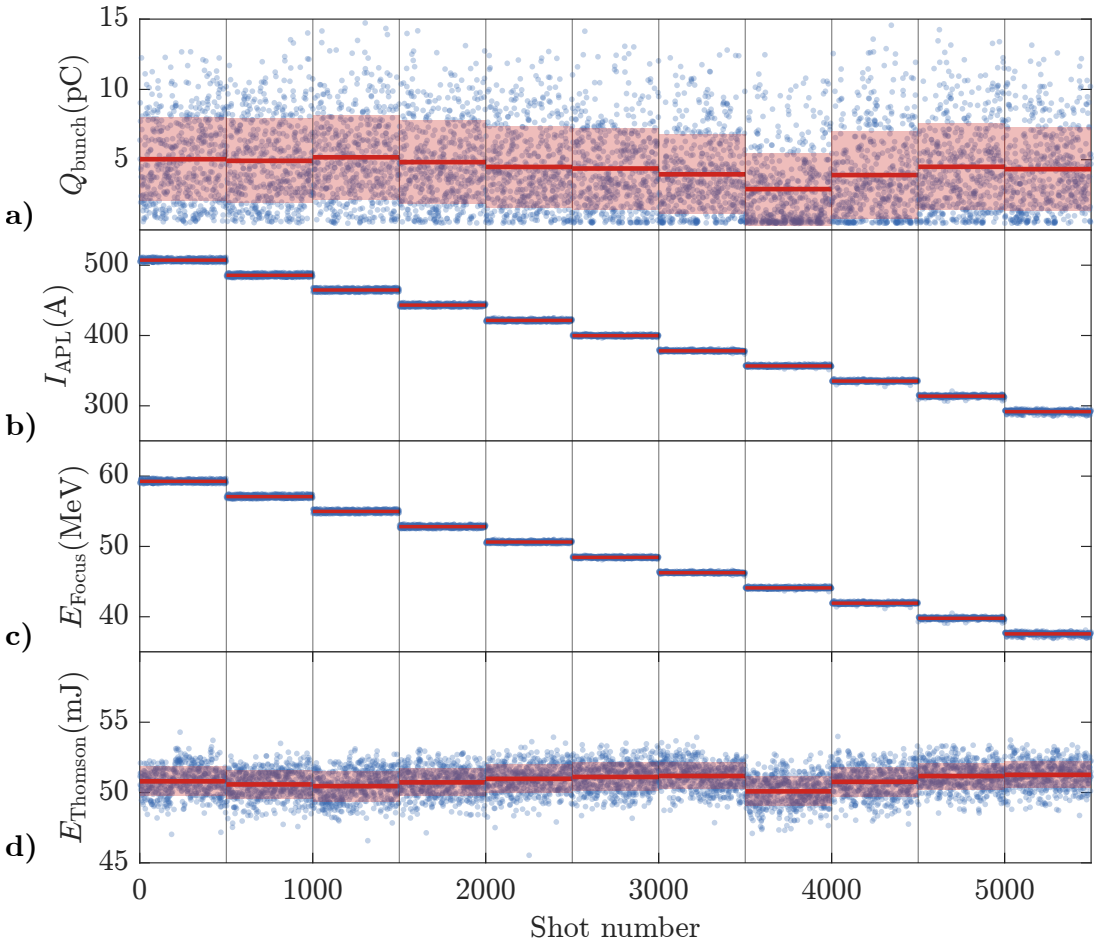

Figure 10.5: Electron energy focal scan to tune the energies of the produced Thomson photons. The APL current I_{APL} is changed (b) in order to vary the electron energy in focus E_{Focus} (c), influencing the electron beam properties in the Thomson interaction. 500 consecutive shots are displayed for each setting. The total bunch charge Q_{bunch} and the pulse energy in the Thomson laser beam $E_{Thomson}$ are shown in (a) and (b), respectively. The average value of each setting is depicted by the horizontal red line, while the standard deviation is represented by the red transparent area. The average total bunch charge is (4.5 ± 3.0) pC and the average laser pulse energy is (50.8 ± 2.2) mJ.

10.2.1 Thomson Spectrum Measurement

The purpose of the realised Thomson source is to provide a proof-of-principle experiment demonstrating a reduced spectral bandwidth and easy tuning the mean X-ray energy. Tuning was accomplished by varying the APL current in order to change the electron energy in focus. Figure 10.5b depicts the APL current of 500 consecutive shots for each setting, whereas Fig. 10.5c depicts the calculated focused electron energy for each shot. During the measurement, the APL current was decreased stepwise, and each setting resulted in a single measurement of a summed X-ray spectrum. The total electron beam charge during the Thomson interaction is shown in Fig. 10.5a. It results in an average beam charge of (4.5 ± 3.0) pC. In addition, Fig. 10.5d shows the laser pulse energy of the Thomson scattering laser beam, yielding an average energy of (50.8 ± 2.2) mJ.

Due to low photon yield and low efficiency in detecting X-ray photons with the HEXITEC detector, each spectrum is the combined signal of a 5 min measurement with a repetition rate of 2.1 Hz, yielding a total shot number of 630. Figure 10.6 depicts the measured X-ray spectra for five different focused electron energies E_{Focus}. The photon spectra shown in Fig. 10.6 are not corrected for X-ray beam attenuation or the HEXITEC detector's quantum efficiency. The TS interaction was turned off by blocking the scattering laser beam in order to record the background radiation generated by electron beam propagation. This was done for four different electron energies in focus, with no visible change in shape. The background spectrum depicted is the average of these measurements.

Figure 10.7 depicts the measured X-ray spectra after background subtraction for focused electron energies ranging from 40 MeV to 62 MeV. The photon counts are corrected for X-ray beam attenuation and the quantum efficiency of the HEXITEC detector, as described in Sec. 9.4.3. Section 10.2.2 compares the recorded spectra to simulation results and their underlying theory.

10.2.2 Composition of Spectral Bandwidth

To interpret the measured spectra, it is necessary to compare the experimental data to simulations and existing theory. The mean X-ray energy and the FWHM spectral bandwidth are the focus of this investigation. Background subtraction was performed on the uncorrected spectra in Fig. 10.6. Following that, the fitting routine and corrections described in Sec. 9.4.3 were used to analyse these spectra, yielding the mean energy and FWHM bandwidth of each spectrum. Analogue to the experimental measurements,

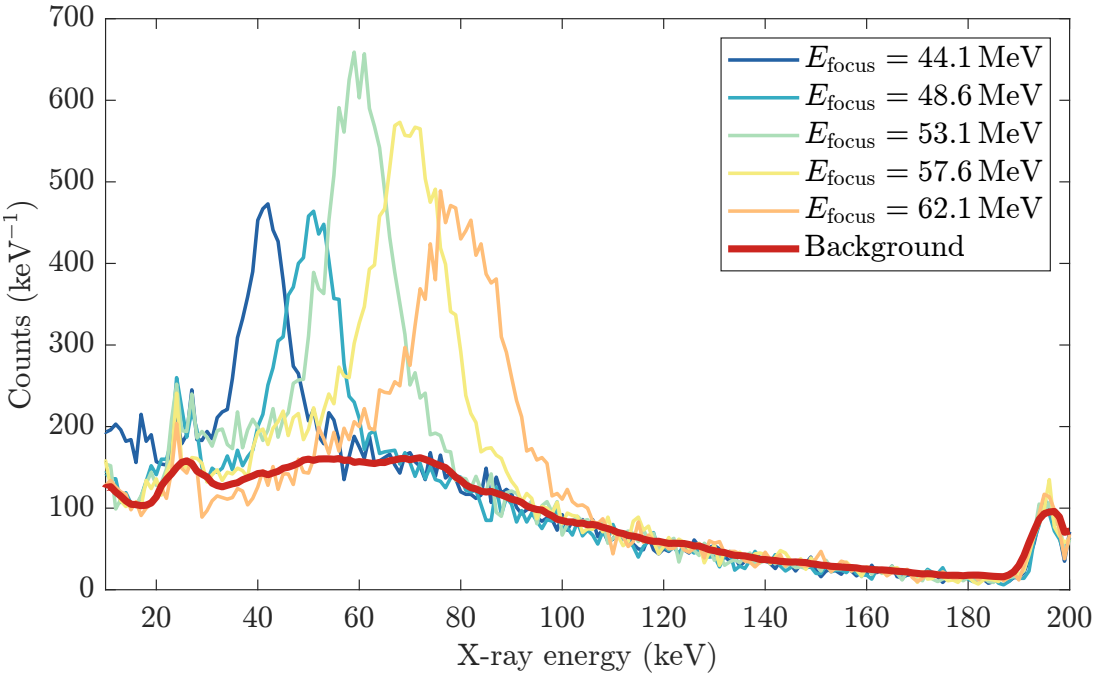

Figure 10.6: Experimentally measured X-ray spectra with background radiation. For five different electron energies focused into the Thomson interaction plane, the uncorrected X-ray spectra are recorded using the HEXITEC detector. The background radiation (red line) was measured for a blocked scattering laser beam, thus, no TS interaction occurred but the electron beam propagated in the same way.

the simulated spectra in Fig. 10.4 are analysed using the same routine. No correction for X-ray beam attenuation and the quantum efficiency of the HEXITEC detector are needed for the simulated X-ray spectra. Figure 10.8 depicts the measurement and simulation results as a function of the electron energy in focus.

Furthermore, the analytical model with the effective quantities of the scattering process presented in Sec. 8.2 is used to study the individual broadening contributions. Equation 8.9 was used to calculate the mean X-ray beam energy in Fig. 10.8a. In the TS process, the electron energy in focus was used as the defining electron energy, whereas the scattering laser has a wavelength of 800 nm. When considering the interaction volume of the electron beam and laser beam, effective values for the laser strength parameter and beam divergence must be used (see Sec. 8.2.4). Because the electron beam size is greater than the laser beam size, the laser strength parameter yields an effective quantity of about $a_{0,\text{eff}} \approx 0.48$. Likewise, the electron beam divergence is effectively reduced to about $\sigma_{\theta,\text{eff,rms}} \approx 0.3\,\text{mrad}$. Electron beam imaging with the APL contributes to the total reduction of the beam divergence. Furthermore, the interaction angle between the electron and laser beams is 10°. As can be seen in Fig. 10.8a, the simulation and analytical model results agree with the measurement within

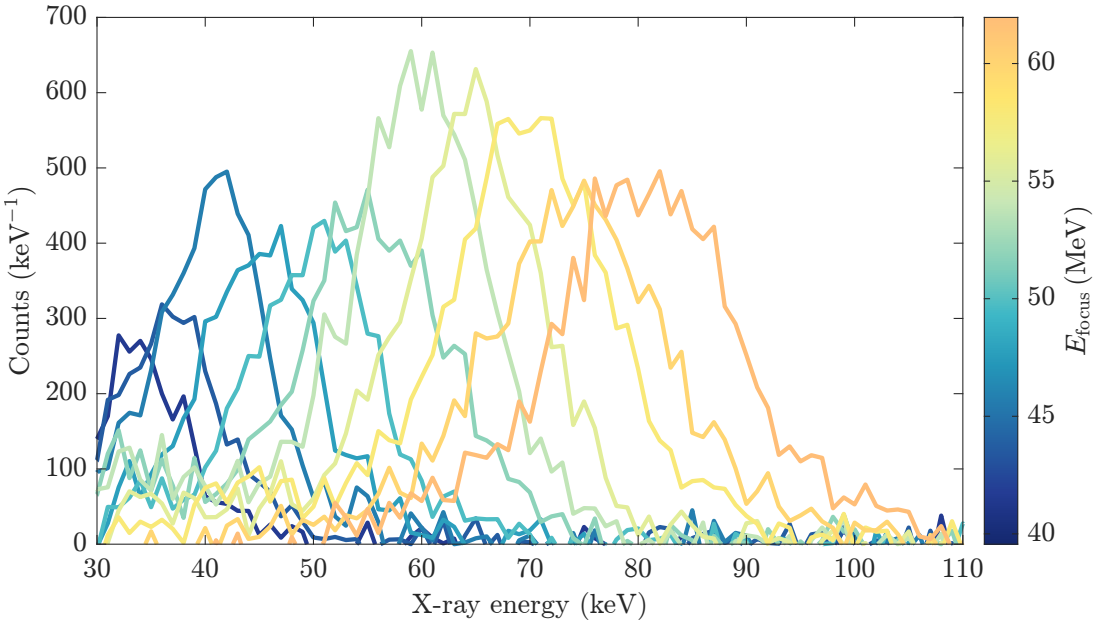

Figure 10.7: X-ray spectra measured after background subtraction and correction for X-ray beam attenuation, as well as the quantum efficiency of the HEXITEC detector. The electron energy focused into the TS interaction plane was set to values between 40 MeV and 62 MeV by varying the focusing strength of the APL. The focused electron energy for each spectrum is represented by the line colour that appears in the colour bar. Each spectrum is the accumulation of photon counts from operating the TS source with a repetition rate of 2.1 Hz for 5 min.

the error bars. This is because the scattered electron energy primarily determines the average photon energy with a quadratic dependency. Conversely, this means that the calculated focused electron energy is correct as it matches the X-ray spectra generated.

The achievable X-ray energy is mainly limited by the electron energy and needs to be tuned with the APL for a specific X-ray radiation application. Nevertheless, many applications have additional maximum X-ray bandwidth limits in order to function. Figures 10.8b and 10.8c depict the absolute and relative FWHM bandwidths, respectively. The weighted mean of all X-ray bandwidths measured is (25.6 ± 2.5) %. Within this error range, the bandwidths of the simulated spectra agree with the measurement. For a bandwidth examination, all individual contributions must be understood. The broadening effects that occur in the case of the realised Thomson source are listed in Tab. 10.1, along with their contribution to the relative bandwidth according to Eqs. 8.14 and 8.15. Unless explicitly stated otherwise, the total bandwidth is the root sum square of all individual bandwidth contributions shown.

The two main causes of spectral broadening determined by electron beams are beam divergence and electron energy spread. Both are reduced by chromatically

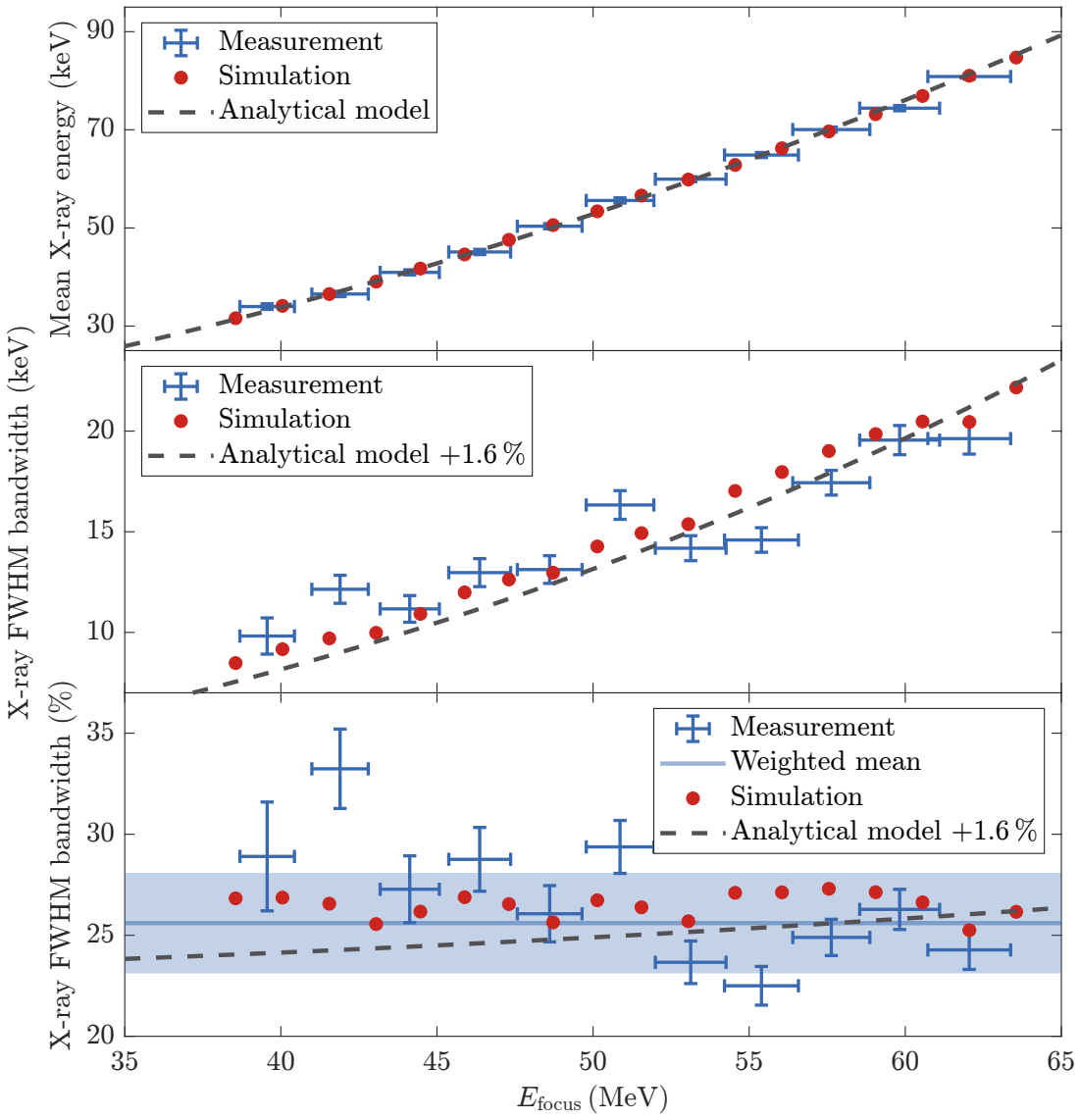

Figure 10.8: Characteristics from measured X-ray spectra for various electron energies in focus. In addition, the characteristics obtained from simulations (red) and an analytical model (black) are shown. The X-ray spectra are characterised by their mean energy (a), absolute FWHM bandwidth (b), and relative FWHM bandwidth (c). Furthermore, the weighted mean (blue line) and weighted standard deviation (blue area) of the measurement are depicted in the case of the relative bandwidth.

Table 10.1: Individual FWHM bandwidth contributions from the measured X-ray spectra. The total bandwidth of the generated X-ray spectrum is calculated as the root sum square of the individual contributions, as done in Eqs. 8.14 and 8.15. It should be noted that spectral broadening due to electron beam divergence, electron energy spread, and X-ray beam collimation are all affected by electron energy. However, this dependency has only a minor impact on the broadening contribution due to beam divergence in the experiment.

SPECTRAL BROADENING DUE TO	CONTRIBUTION TO FWHM BANDWIDTH
Effective electron beam divergence	$\left(\frac{\Delta\omega}{\omega}\right)_{\sigma_{\theta,\mathrm{eff}}} \approx 1\,\%$
Effective electron energy spread (energy-dependent)	$7.5\,\% \lesssim \left(\frac{\Delta\omega}{\omega}\right)_{\gamma_e} \lesssim 11.5\,\%$
Laser bandwidth	$\left(\frac{\Delta\omega}{\omega}\right)_{\omega_{\mathrm{Laser}}} \approx 8.8\,\%$
Effective laser strength	$\left(\frac{\Delta\omega}{\omega}\right)_{a_{0,\mathrm{eff}}} \approx 19.5\,\%$
Confined detection collimation (energy-dependent)	$1\,\% \lesssim \left(\frac{\Delta\omega}{\omega}\right)_{\mathrm{coll}} \lesssim 4\,\%$

imaging the electron beam into the TS interaction plane. The effective electron energy spread describes the electron energies that participate in the TS interaction after chromatic filtering. It can be estimated using the model of a head-on collision between an electron beam and a Gaussian laser pulse described in Sec. 9.2. It increases linearly with the electron energy in focus and contributes 7.5 % - 11.5 % to the bandwidth of the X-ray spectra (see Fig. 9.4) in the range of the measurement. As mentioned above, the electron beam divergence is effectively reduced to about 0.3 mrad due to the effective TS interaction volume with a focused electron beam. This amounts to a bandwidth contribution of approximately 1 %. However, because of electron beam pointing jitter, this effect may be underestimated. When the electron beam angle varies, the interaction angle of the scattering process and the observation angle for a fixed position of the X-ray detector change. For summing numerous X-ray beams to measure a spectrum, these effects can be described as an increased effective beam divergence.

The laser beam significantly contributes to the total bandwidth. On the one hand, the laser's bandwidth of 8.8 % contributes directly to the generated X-ray spectrum. On the other hand, the higher the laser intensity of the scattering laser, the more broadening from the laser strength parameter there is. Even though the laser strength parameter is effectively reduced to $a_{0,\mathrm{eff}} \approx 0.48$, the bandwidth contribution is approximately 19.5 %. One consequence of this effect can be seen in Fig. 10.4, where

an additional shoulder formed on the low-energy side of each X-ray spectrum is visible. In addition, as explained in Sec. 9.1, the X-ray spectrum generated broadens due to non-negligible intensity outside of the scattering laser focal spot.

TS simulations comparing transverse laser profiles described by an ideal Gaussian distribution and the experimentally measured distribution revealed that the non-uniform intensity distribution increases the FWHM bandwidth on average by about 1.6 %. The simulations include full start-to-end simulations, as described in Sec. 10.1. The normalised vector potential peak and pulse duration were kept constant when the transverse intensity profile was changed, and the Gaussian distribution was described by the fitted focal spot size. It should be noted that this bandwidth contribution is directly added to the total bandwidth.

The spectral broadening effects discussed so far describe the on-axis bandwidth. However, both the photon energy and the photon number decrease with larger observation angle. In the case of the 1.61 mrad opening angle of the HEXITEC detector, the bandwidth increases up to 4 % for a focused electron energy of about 62 MeV. As can be seen in Eq. 8.15, this contribution varies with electron energy and decreases as electron energy decreases.

Figures 10.1b and 10.1c depict the total bandwidth of the X-ray spectra predicted by the analytical model. It differs by up to 2 % from the simulation results and rather underestimates the total bandwidth. Underestimation can be caused by uncertainties in effective scattering quantities, assumptions in Gaussian distributions and head-on collisions, or the fact that broadening effects are asymmetrical in reality. Further to that, the electron beam pointing jitter was not taken into account, and that can result in an increased effective beam divergence.

The laser effects contribute the most to the total bandwidth of the generated X-ray spectrum, accounting for 19.5 % from the laser strength parameter and 8.8 % from the laser bandwidth. The effective electron energy spread is the next most significant component. This contribution increases for higher focused electron energies in an energy-tuned X-ray source and is the primary cause of the bandwidth increase in the analytical model shown in Fig. 10.8c. In this setup, it contributes up to 11.5 %. Due to scattering off an electron beam focus and the focusing geometry used, the electron beam divergence has only a minor contribution of 1 %. Both electron beam effects are heavily influenced by the initial electron beam parameters and electron beam focusing geometry, which will be discussed in greater detail in Sec. 10.3.1.

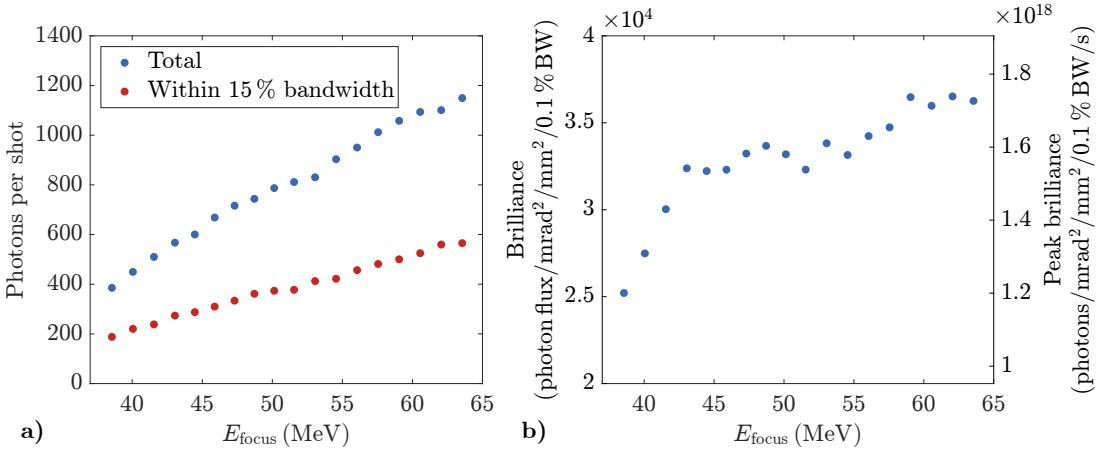

Figure 10.9: Photon production and brilliance of the simulated X-ray spectra. The simulated X-ray spectra shown in Fig. 10.4 are used in this evaluation. The total number of photons per shot and within a spectral bandwidth of 15 % are calculated for various electron energies in focus during the TS interaction (a). (b) depicts the brilliance of an X-ray source defined as photon flux per mrad^2 and mm^2 within a 0.1 % bandwidth for a repetition rate of 2.1 Hz. In addition, the peak brilliance in the case of a 40 fs long X-ray beam is shown.

10.2.3 Photon Yield

Typical X-ray radiation applications often require a certain photon flux in addition to a maximum spectral bandwidth limit. While the design bandwidth must be met in each shot, the photon number does not necessarily have to be. In other words, a lower photon yield can be compensated for by more shots per second or measuring for longer periods of time. The HEXITEC detector is well suited to measuring X-ray spectra with energies up to 200 keV and a resolution of < 1 keV. However, because the detector operated close to saturation, an unknown fraction of the total photon yield was registered. The X-ray spectra in Fig. 10.7 are made up of 630 individual shots. This means that the detector recorded between 5 and 20 photons per shot. The following analysis is based on the results of the TS simulations presented in Sec. 10.1. The laser beam and electron beam parameters measured during the experiment are used to obtain information about absolute photon numbers. A separate diagnostic, such as one based on a CsI(Tl) scintillator array, would be required for a direct measurement of photon yield [77, 194–196].

In the simulation, the HEXITEC detector area is represented by an opening cone with a radius of 1.61 mrad. Based on the Thomson simulations, Fig. 10.9a depicts the total number of photons per shot and within a spectral bandwidth of 15 % for various electron energies in focus. Depending on the electron energy imaged, the entire X-ray

spectrum consists of about 400 to 1000 photons. On the other hand, within a 15 % bandwidth, there are approximately 200 to 600 photons. Because the effective electron energy spread increases linearly with the electron energy in focus, the number of electrons participating in the TS interaction increases. Therefore as the imaged electron energies increase, so does the photon yield. The TS interaction involves about 5 % of the total number of electrons in the bunch. To quantify the interaction itself and as potential optimisation parameter, the effective photon production μ_{eff} can be used. It is defined as the number of photons emitted per electron into a confined cone with a fixed bandwidth [40]. Averaged over the simulated tuning range, $(3.6 \pm 0.6) \cdot 10^{-4}$ photons per electron are emitted into a cone of ± 1.61 mrad and a FWHM bandwidth of 15 %.

One of the key parameters used to compare different X-ray radiation sources is the source's brilliance. It is defined as

$$\frac{\text{photon flux}}{\text{mrad}^2 \cdot \text{mm}^2 \cdot 0.1\,\% \,\text{bandwidth}} \tag{10.5}$$

and describes the photon flux of a specific wavelength per unit of solid angle concentrated on a spot. The term 'mrad²' describes the angular divergence of the photons, 'mm²' gives the cross-sectional area of the X-ray beam, and '0.1 % bandwidth' includes the photons within a bandwidth of 0.1 % of a central energy. The photon flux is calculated by multiplying the determined photon number by the source's repetition rate of 2.1 Hz. Since this photon flux is contained within an opening cone with a radius of 1.61 mrad, the angular divergence term is given by $\pi \cdot (1.61\,\text{mrad})^2$. The source area is defined by the scattering laser's FWHM focal spot size, which was determined to be approximately 10 µm. Figure 10.9b shows the calculated brilliance and peak brilliance of the simulated Thomson spectra. The peak brilliance is given by

$$\frac{\text{photons per shot}}{\text{mrad}^2 \cdot \text{mm}^2 \cdot 0.1\,\% \,\text{bandwidth} \cdot \text{pulse duration}}. \tag{10.6}$$

In contrast to average brilliance, the peak brilliance considers the number of photons generated per shot per X-ray pulse duration rather than the photon flux. The duration of the electron beam mainly determines the X-ray pulse duration of the X-ray beam generated. It is assumed to be 10 fs. The peak brilliance of the simulated X-ray source averaged over the entire tuning range is approximately $1.6 \cdot 10^{18}$ photons/mrad²/mm²/0.1 % bandwidth/s.

10.3 CONSIDERATIONS FOR SOURCE OPTIMISATION

The realised proof-of-principle Thomson X-ray source has an average FWHM bandwidth of $(25.6 \pm 2.5)\,\%$ at a repetition rate of 2.1 Hz, with simulations predicting a production of $200 - 500$ photons within 15 % bandwidth per shot within ± 1.61 mrad. Because X-ray applications often have stricter requirements for spectral bandwidth and photon yield, additional optimisation may be required. In the case of XFI with GNPs as tracers, an incident X-ray energy of 90 keV is required, with a relative FWHM spectral bandwidth of less than 15 %. Furthermore, an X-ray flux of approximately 10^9 photons per second within a ± 0.5 mrad opening cone is required [14, 15]. For a specific application, the question of what properties should be optimised for an X-ray source must be answered. The majority of modifications to the setup affect both the spectral bandwidth and the photon production. As a result, a light source's spectral bandwidth, total photon yield, or photon yield within a given bandwidth can all be optimised and necessitate different approaches. The TS simulations revealed an average effective photon production of $3.6 \cdot 10^{-4}$ photons emitted per electron in a ± 1.61 mrad opening cone and a FWHM bandwidth of 15 %. A design study of a comparable Thomson source predicted an effective photon production of up to $7.2 \cdot 10^{-3}$ photons emitted per electron within a ± 0.5 mrad opening cone and a FWHM bandwidth of 15 % [40]. This demonstrates that optimising the X-ray source can result in a twentyfold increase in effective photon production, even in an about tenfold smaller cross section. In the following sections, the main individual mechanisms that can be used to reduce bandwidth or increase photon flux XFI with GNPs are discussed. The electron energy in focus is assumed to be 65 MeV to generate X-ray photons with a mean energy of about 90 keV required for GNPs, which can be easily achieved by adjusting the APL's focusing strength accordingly.

10.3.1 Bandwidth Reduction

The FWHM bandwidth for XFI with GNPs should be less than 15 %. All individual contributions to the bandwidth of the produced X-ray spectra were examined in Sec. 10.2.2 and must be investigated separately. However, treating broadening effects separately can lead to incorrect conclusions because effects can affect various contributions. The following general modifications are based on the electron beams and laser system that were available in the experimental environment. Further advancements can be accomplished, for example, by employing an imaging system for the electron beam that consists of several beam imaging devices.

X-Ray Beam Opening Cone

The X-ray spectrum measurements were carried out on the HEXITEC detector, which has a chip area of 2 cm by 2 cm, resulting in an opening cone of about 1.61 mrad. However, XFI with GNPs necessitates the use of pencil X-ray beams of about 1 mm for scanning. Thus, X-ray beam collimation is needed. The actual collimation angle is determined by how far the X-ray beam is collimated from the X-ray source. Equation 8.15 indicates that for a collimation angle of 1.61 mrad and an electron energy of 65 MeV, beam collimation contributes 4 % to the spectral bandwidth. When the X-ray beam is collimated to 0.5 mrad or 0.1 mrad, the bandwidth contribution drops to about 0.4 % and 0.02 %, respectively. However, this comes at the expense of drastically reducing the usable photon yield.

Scattering Laser Pulse

The scattering laser pulse has a direct impact on three aspects that broadens the generated X-ray spectrum. (i) The X-ray spectrum inherits the initial bandwidth of the laser beam. (ii) The laser strength parameter quadratically increases the X-ray bandwidth. (iii) The laser beam's focal waist size affects the broadening contribution due to effective electron energy spread. Furthermore, the relative spatial overlap of the electron beam and laser beam influences the effective quantities of the laser strength parameter and the electron beam divergence (see Sec. 8.2.4).

The effect of the laser beam's relative spatial overlap with the electron beam is independent of the other effects. In general, as the laser beam waist size differs from the electron beam focal spot size, the bandwidth contributions from effective laser strength and beam divergence are reduced. While it reduces spectral broadening, it also reduces the total photon yield because fewer electrons are included in the scattering process of mismatched beam sizes. In the experimental setup, the spatial overlap between the electron beam and laser beam can reduce the bandwidth contribution by up to 4 % when compared to its maximum contribution. This relationship is explained further below using the electron beam size relative to a fixed laser focal spot.

The optimisation of the scattering laser beam's focal spot is one improvement that should reduce the total FWHM bandwidth. The excessive laser intensity outside the main focal point is currently contributing to the scattering process with 1.6 % (compare Sec. 9.1).

As shown in Tab. 10.1, the constant bandwidth contributions due to the laser bandwidth and laser strength are among the largest. Because the laser system is based on **C**hirped **P**ulse **A**mplification (CPA), the laser beam has a few percent bandwidth.

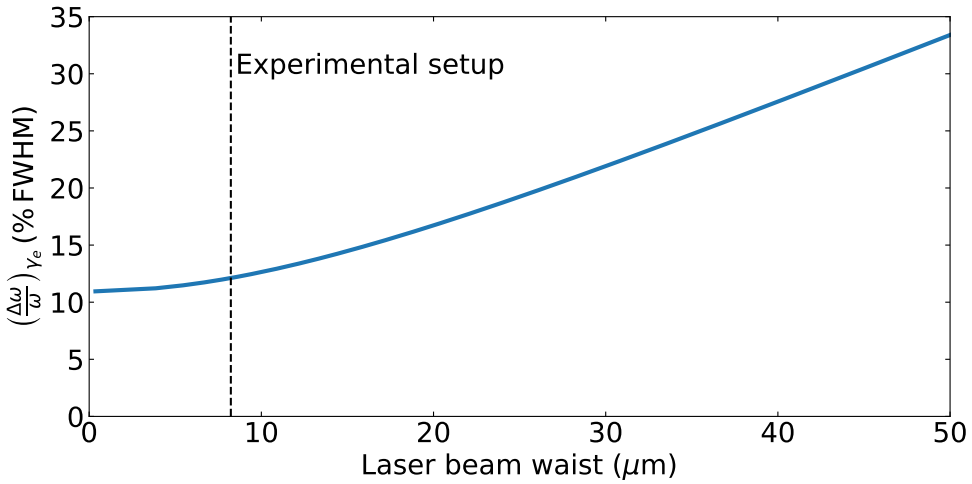

Figure 10.10: Spectral broadening contribution due to effective electron energy spread for various laser beam waists in the case fixed laser strength parameter, pulse duration, and pulse energy. During the Thomson scattering interaction, the laser beam waist relative to the electron focal spot size influences the effective electron energy spread and thus its spectral broadening contribution. A 0.43 mm mrad normalised emittance, a 3.3 µm initial beam size, and a focused electron energy of 65 MeV were used in the calculation. As a result, the RMS electron beam focal spot size is about 8.7 µm. The vertical dashed line represents the laser beam waist that was used in the experiment.

This contribution can be reduced by using a separate laser system with smaller spectral bandwidth or spectral filtering at the expense of laser intensity. Furthermore, depending on the electron-laser overlap, stretching the laser pulse via a longitudinal chirp can result in a reduced effective laser bandwidth $\Delta\omega_{\text{eff}} < \Delta\omega$ [40, 171, 172].

The scattering laser beam has a laser strength parameter of $a_0 = 0.81$, resulting in the largest bandwidth contribution of this Thomson X-ray source with about 19.5 %. In general, moderate values of $a_0 < 0.5$ are recommended to avoid non-linear effects in the scattering process that cause broadening. Photon production, on the other hand, is reduced for smaller laser strength parameters. The reduction of a_0 is accomplished by lowering the laser intensity at the focus. For example, a different focusing optic can be used to increase the laser beam's focal spot size, or attenuation can be used to lower the laser pulse energy. Furthermore, the laser intensity can also be reduced by temporally stretching the laser pulse. This can be accomplished, for example, by introducing a longitudinal chirp using chirped mirrors.

The electrons involved in the TS interaction which define the effective electron energy spread are affected by the relative size of the laser beam waist and the electron focal spot size, among other things. In the experimental setup, this results in a

bandwidth broadening of about 12 % for an electron beam with a focused energy of 65 MeV. This contribution is depicted in Fig. 10.10 as a function of the laser beam waist for a fixed laser strength parameter, pulse duration, and pulse energy. For a larger laser beam waist, more off-focus electrons with energies different from the focused energy are involved in the scattering process, thereby increasing the effective electron energy spread. However, the chromatic dispersion introduced by the APL primarily determines the effective electron energy spread and, even when the laser beam waist size is reduced in the experiment, it only leads to a minor improvement on the X-ray bandwidth. To reduce this contribution, the electron parameters or the electron beam focusing geometry must be changed.

Electron Beam Focusing Geometry

One advantage of focusing the electron beam with an APL is that the electron beam parameters in the TS interaction can be controlled independently of the scattering laser beam. The focusing geometry determines the electron beam size, beam divergence, and chromatic filtering in focus. Optionally, the electron beam source would have to be modified to meet the requirements of the scattering process, but his is considerably less flexible. Broadening caused by effective energy spread increases for higher focused electron energies, while broadening caused by beam divergence decreases, and vice versa. Therefore, an optimisation is performed for a specific electron energy that might not be valid for the entire electron energy range. The optimisation is performed here for an electron energy of 65 MeV, as required for XFI with GNPs.

In the experiment, electron beam imaging into focus magnifies the electron beam size by a factor of 2.6 and reduces the beam divergence by about 62 %. As a result, spectral broadening caused by beam divergence is reduced to a contribution of about 1 %. While shot-to-shot fluctuations in the electron beam direction can result in an increased effective beam divergence when examining X-ray spectra from multiple shots, this effect has no consequences on the bandwidth of the individual X-ray shots. This is beneficial for a scanning modality such as XFI, where individual X-ray beams must meet a minimum bandwidth of 15 % rather than the X-ray spectrum of multiple shots.

The electrons involved in the TS process determine the effective electron energy spread, and thus its contribution to spectral broadening. It depends on the overlap between of the laser beam and the electron beam, as shown in Fig. 10.10. For a broad electron energy spectrum, chromatic imaging with an APL reduces the effective electron energy spread in the Thomson interaction. There are two main approaches to reducing the effective electron energy spread even further. On the one hand, the

chromaticity introduced by the APL can be increased, leading to a greater chromatic dependence of electron beam size during the scattering process. However, this implies that there are more electrons that do not partake in the scattering process. On the other hand, a lower initial electron beam energy spread than that obtained from imaging chromaticity results in a lower effective electron energy spread without reducing the electron charge participating in the scattering. LPA with more localised injection can result in electron beams with a narrower spectral width. Examples of schemes with localised injection are self-truncated ionisation injection [61, 62], shock-front injection [35, 63, 64], or injection using multiple laser pulses [59, 60]. However, because the electron beam has a limited energy spread, the tunability of the mean X-ray beam energy based on changing the imaged electron energy would also be limited if the mean electron energy could not be controlled at the same time [28]. Furthermore, more control over the scattering interaction could be gained by imaging the electron beam with multiple APLs. Multiple APLs allow for controlling the bunch properties separately in the scattering interaction. For example, the beam imaging can be adjusted to further reduce the effective energy spread without increasing the beam divergence in focus, and vice versa. Another advantage is that the scattering interaction plane can be fixed in this case, meaning that the effective bunch characteristics can be changed without moving the focal plane of the scattering laser beam. Because the objective of this optimisation is to improve the Thomson source based on the existing electron source, changes in the electron beam focusing geometry using a single APL are discussed.

The scattering characteristics of the electron beam can be adjusted by varying the drift lengths from the electron source to the APL and from the APL to the Thomson interaction plane. Three effects that are dependent on the beam focusing geometry influence the bandwidth of the resulting X-ray beam: (i) the chromatic imaging and the focal spot size of the electron beam change the effective electron energy spread, (ii) the electron beam divergence at the focal position changes, and (iii) the relative spatial overlap between the electron beam and laser beam determines the contribution of the effective laser strength parameter (and of the effective beam divergence). However, the third effect is the least problematic and can, in principle, be decoupled from the electron bunch properties. As discussed above, the scattering laser properties can be independently adjusted to accomplish this. Figure 10.11 depicts the X-ray beam bandwidth contributions for various drift lengths before and after the APL. The laser is assumed to be defined by a pulse energy of 50.8 mJ, a pulse duration of 32 fs and a laser strength parameter of 0.81. Furthermore, an electron beam with a normalised emittance of 0.43 mm mrad and an initial beam size of 3.3 µm has an energy of 65 MeV

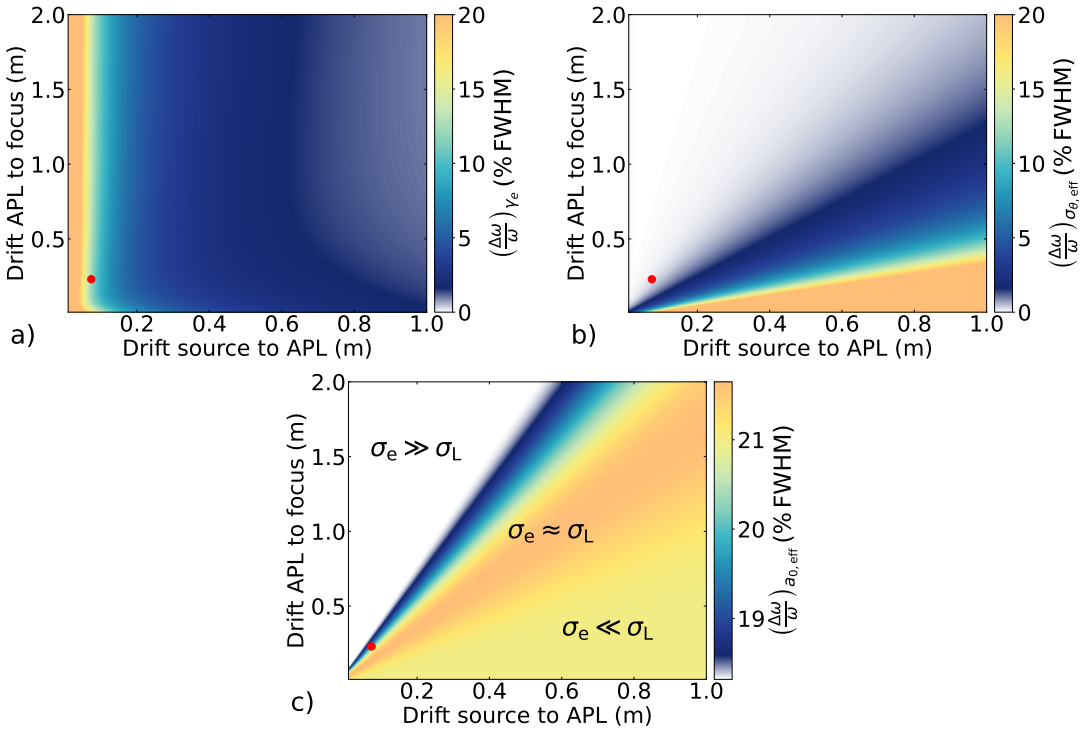

Figure 10.11: Spectral broadening due to effective electron energy spread, effective beam divergence, and effective laser strength, depending on the focusing geometry used to image the electron beam. An APL focuses an electron beam with a normalised emittance of 0.43 mm mrad, an initial beam size of 3.3 µm and a central energy of 65 MeV into the TS interaction plane. The laser beam is defined by a pulse energy of 50.8 mJ, a pulse duration of 32 fs and a laser strength parameter of 0.81. The drift lengths before and after the electron beam imaging device influence the electron parameters at focus, such as beam size and beam divergence. According to these parameters, the bandwidth contribution from effective electron energy spread $\left(\frac{\Delta\omega}{\omega}\right)_{\gamma_e}$ (a), effective beam divergence $\left(\frac{\Delta\omega}{\omega}\right)_{\sigma_{\theta,\mathrm{eff}}}$ (b), and effective laser strength $\left(\frac{\Delta\omega}{\omega}\right)_{a_{0,\mathrm{eff}}}$ (c) varies. Spectral broadening due to $a_{0,\mathrm{eff}}$ is determined by the electron beam size σ_e relative to the laser beam size σ_L. The red dot marks an initial drift length of 7.4 cm to the APL and a 23 cm long drift length from APL to the electron focus, as used in the experiment.

focused into the Thomson interaction point. As the various broadening effects must be balanced in an optimisation, the individual effects are explained further below.

In the case of fixed initial electron beam parameters and a fixed scattering laser beam, electron beam imaging determines the effective electron energy spread. This holds true only when the initial energy spread is larger than the effective energy spread caused by chromaticity. Figure 10.11a depicts the contribution of electron energy spread to the FWHM bandwidth of generated X-ray beams. The red dot marks an initial drift length of 7.4 cm to the APL and a 23 cm long drift length from APL to the electron focus, as used in the experiment. A theoretical bandwidth contribution of 12 % is present there. The effective energy spread can be reduced by increasing the drift length from the electron source to the APL. The main cause of this decrease is the imaging chromaticity introduced by the APL. As described in Sec. 6.2.2, the chromatic amplitude growth in a thin lens can be approximated as

$$\Delta W_x = \frac{x_{rms}^2}{\epsilon_x f}, \tag{10.7}$$

where x_{rms} is the electron beam size in the APL, ϵ_x is the geometrical beam emittance and f is the focal length of the APL. The chromatic amplitude growth increases quadratically with the electron beam size at the imaging device, and the larger the initial drift length, the larger the beam size will be. Therefore, a larger drift to the APL produces a more chromatic focal spot of the electron beam, thus reducing the effective electron energy spread in the TS interaction. However, when only the drift length from the APL to the Thomson interaction point is changed, the effective electron energy spread remains approximately constant. Only drift lengths of < 0.1 m in this setup increase the energy spread on a sub-percentage scale because the imaged electron beam size becomes smaller than the scattering laser beam focal spot. To summarise, increasing the imaging chromaticity is necessary to effectively reduce the electron energy spread in a setup consisting of a single imaging device. The most practical way to accomplish this is to increase the electron beam size at the APL. It might be necessary to increase the APL aperture to prevent charge loss and the production of additional bremsstrahlung. Furthermore, in order to compensate for a larger focal length and a larger APL radius, the APL focusing strength must be increased, either through higher discharge currents or by increasing the capillary length.

In the experiment, X-ray spectrum broadening caused by effective energy spread was more severe than broadening caused by beam divergence, accounting for about 1 % of the total FWHM bandwidth. When decreasing the effective energy spread by changing the electron beam focusing geometry, it is necessary to prevent the effective beam divergence at the Thomson interaction point from dominating the

Thomson bandwidth. Figure 10.11b depicts the spectral bandwidth contribution due to effective electron beam divergence for various focusing geometries. The red dot again represents the electron beam imaging used in the experiment, at which the beam divergence is reduced by approximately 62 %. In contrast to the effect of electron energy spread, spectral broadening caused by beam divergence worsens as the drift length from the electron source to the APL increases. The broadening owing to beam divergence becomes more severe as the beam divergence increases. The change in beam divergence can be assessed in terms of imaging magnification[1] M. A magnification of $M > 1$ results in a reduction in beam divergence, whereas $M < 1$ results in an increase in beam divergence. The factor $1/M$ can be used to estimate the change in beam divergence. As a result, for larger drift lengths to the APL, the broadening due to beam divergence increases as the beam divergence in the focus increases. On the other hand, larger drift lengths between the APL and the Thomson interaction point reduce beam divergence and thus the broadening effect.

The third effect that the electron beam focusing geometry indirectly influences is the effective laser strength parameter and should only be considered when no independent control over the scattering laser beam is available. It depends on the interaction volume of the scattering laser beam and the electron beam, which is primarily determined by their relative transverse beam sizes. The contribution to the bandwidth of the X-ray beam due to the effective laser strength is shown in Fig. 10.11c. When compared to beam broadening caused by beam divergence and beam energy spread, the variations are less consequential. The size of the electron focal spot is determined by the beam imaging, whereas the laser beam waist remains constant. When both transverse beam sizes are comparable ($\sigma_e \approx \sigma_L$), the bandwidth contribution for a laser strength parameter of $a_0 = 0.81$ is approximately 22 %. A mismatch in the sizes of both beams effectively reduces the broadening. When the size of the electron beam is smaller than that of the laser beam ($\sigma_e \ll \sigma_L$), the contribution drops to about 21 %, while for $\sigma_e \gg \sigma_L$ it can drop to about 18 %. To further reduce this broadening effect, the laser strength parameter must be reduced, as should be done in general.

1 Using the thin lens model, imaging magnification is defined as $M = d_2/d_1$, where d_1 is the drift length from the source to the imaging device and d_2 is the drift length from the imaging device to the focal position.

Estimation of the Minimum Bandwidth

The minimum spectral bandwidth of the generated X-ray beams are estimated using the analytical calculations from Eqs. 8.14 and 8.15 are used. Because of the complexity and asymmetries of the various effects in the scattering process, numerical simulations are indispensable for a detailed optimisation. This section demonstrates how to optimise and uncover the limits of the setup used by employing fundamental analytical relations. The estimate presented is based on the electron beams produced and the existing scattering laser setup.

The scattering laser beam has a focal waist of 8.5 µm and a pulse duration of 32 fs. Then, to obtain a laser strength parameter of 0.5, the laser pulse energy can be reduced or the laser beam can be stretched in time to match its Rayleigh length for an additional increase in photon production. The scattering laser's bandwidth is kept constant, accounting for 8.8 % of the total X-ray beam bandwidth. With a contribution of about 4 %, the detection collimation angle is still taken into account. The total spectral bandwidth of the X-ray beam $\left(\frac{\Delta\omega}{\omega}\right)_{\text{total}}$ is then given by including the broadening contributions from the effective electron energy spread and effective beam divergence.

Figure 10.12 depicts the total FWHM bandwidth for various beam imaging geometries. The areas with the greatest bandwidth contribution from effective electron energy spread and effective electron beam divergence are highlighted, respectively. A red contour line represents the limit for the minimum FWHM bandwidth of 15 % required by XFI with GNPs. To meet the bandwidth limit, an imaging geometry behind this line must be used. In general, a drift length of > 15 cm between the electron source and the APL is required to suppress the broadening caused by electron energy spread. Furthermore, the drift length from the APL to the Thomson interaction point must be greater than 0.4 cm to decrease contribution of the beam divergence. Increasing both drift lengths further improves the overall bandwidth of the X-ray beam. For an initial drift length of about 0.3 cm to the APL followed by a drift length of about 1 m to the interaction point, the combined broadening from electron energy spread and beam divergence is less than 1 %.

In principle, the maximum drift length from the APL to the Thomson interaction point is only limited by the available space in the LPA chamber. It is possible to use a drift length of about 0.4 cm, but this may require rearranging the scattering laser arm. On the other hand, a drift length of > 15 cm before the APL is more challenging. The total electron beam size at the plasma lens entry will be larger than the capillary diameter. This causes charge loss in the beam optic as well as on-axis bremsstrahlung, which must be avoided. It is advantageous to reduce the electron beam pointing

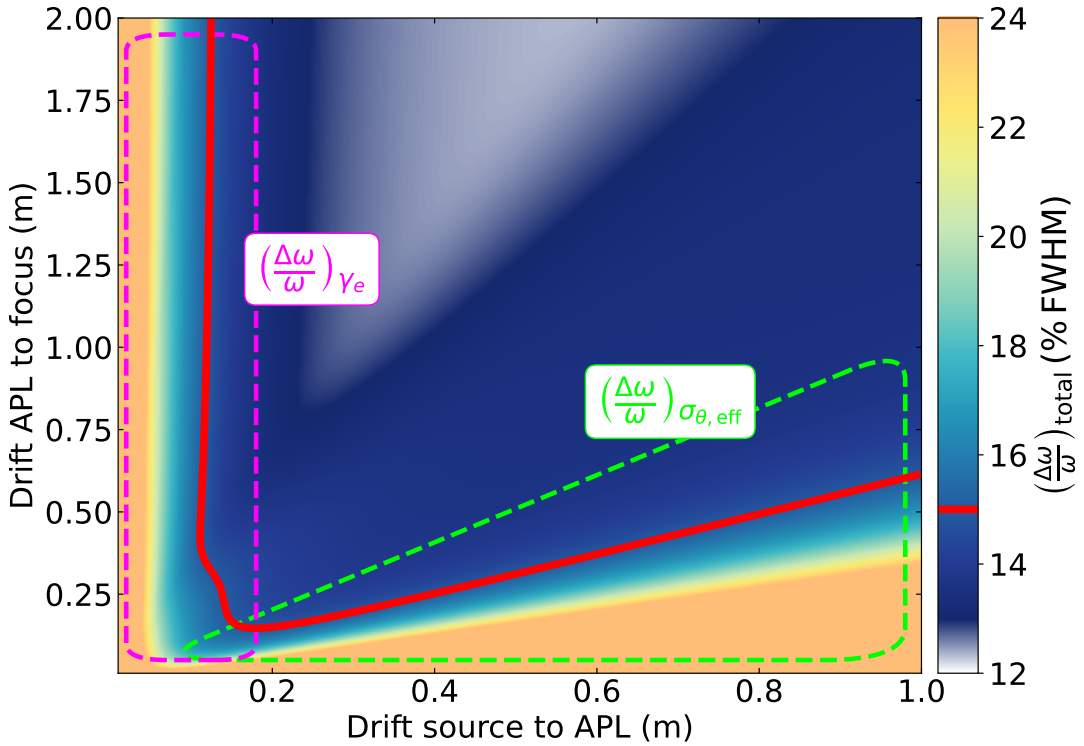

Figure 10.12: Total FWHM spectral bandwidth of the generated Thomson spectra depending on the electron beam imaging geometry. The total broadening is the result from the quadratic sum of all individual contributions based on Eqs. 8.14 and 8.15, which includes the following origins: effective electron beam divergence, effective electron energy spread, scattering laser bandwidth, effective laser strength and the confined detection angle. The calculations are based on an electron beam with a normalised emittance of 0.43 mm mrad, an initial beam size of 3.3 µm that has a focused energy of 65 MeV to interact with a laser beam. The laser beam is defined by a beam waist of 8.5 µm, a pulse duration of 32 fs and a laser strength parameter of 0.5. In contrast to previous assumptions, the laser pulse energy is reduced in order to achieve the lower a_0. When the focusing geometry is changed, the contributions from the effective electron energy spread $\left(\frac{\Delta\omega}{\omega}\right)_{\gamma_e}$ and the effective electron beam divergence $\left(\frac{\Delta\omega}{\omega}\right)_{\sigma_{\theta,\mathrm{eff}}}$ are those primarily influenced. Magenta and green regions highlight the areas where these effects are most prominent. The red contour denotes the location at which the total X-ray beam bandwidth is 15 %.

jitter for this purpose. However, in order to capture the entire beam charge, the aperture of the APL must be enlarged. A larger APL diameter of about 4 mm may require additional testing to ensure stable operation. Furthermore, a larger diameter reduces the focusing strength quadratically and increases the gas load into vacuum, which must be compensated for. Because rather moderate APL discharge currents were used in the experiment, the focusing strength can be increased by increasing the APL current. If the APL current cannot be increased any further, the APL length must be increased.

So far, ways to reduce the bandwidth contributions from electron energy spread and beam divergence have been discussed. The scattering laser beam was assumed to have a laser strength parameter of 0.5. Neglecting the variation in the broadening caused by the laser strength, a constant bandwidth contribution due to effective laser strength, laser bandwidth and detection collimation emerges. These contributions, which amount to about 12 %, are almost independent of the geometry of the electron beam focusing. They contribute the most to the total X-ray bandwidth. Lower X-ray bandwidth can be achieved by further reducing the laser strength parameter by decreasing the pulse energy, increasing the focal waist, or increasing the pulse duration. Increased laser pulse duration, in particular, has the advantage of not reducing photon production as much as described below. In addition, a lower bandwidth of the scattering laser is advantageous to the spectral width of the generated X-ray beam. The laser bandwidth can be effectively reduced, for example, by stretching the laser pulse via a longitudinal chirp, so that $\Delta\omega_{\text{eff}} < \Delta\omega$ [40, 171, 172].

10.3.2 Enhanced Photon Yield

The Thomson source presented has the advantage of reducing the spectral bandwidth by chromatically filtering the electron energy with an APL. However, because fewer electrons are involved in the scattering process, the total photon production rate also decreases. In addition, because XFI requires pencil X-ray beams of approximately 1 mm in diameter, additional beam collimation is required, further reducing the number of X-ray photons. More developments are required to achieve the ultimate goal of producing quasi-monochromatic X-ray spectra at high fluxes. Only X-ray photons within the bandwidth limit specified by the application can be used in applications. Therefore, increased photon production without drastically increased bandwidth is required. While a more intense scattering laser pulse increases the total number of photons, it also broadens the X-ray spectrum more. This section discusses the possibilities and future prospects for developing higher photon flux X-ray sources.

Electron Bunch Charge

One method for increasing the photon yield per shot is to increase the spectral charge density of the electron bunch. The number of X-ray photons increases in direct proportion to the number of electrons involved in the interaction. However, to avoid saturating the X-ray detector and allowing spectra to be measured, the total beam charge was intentionally kept low in this experiment, at about 4.5 pC. Additionally, in a setup where the electron beam charge is filtered chromatically, the effective electron energy spread, not the total bunch charge, limits the available electrons. The effective energy spread can be increased by designing the electron beam imaging correspondingly, but this results in increased spectral broadening.

The electron beam source based on LPA relied on the technique of ionisation injection to trap electrons in the plasma wakefield. This is a reliable method in which electrons are continuously injected, resulting in electron energy spectra that are generally broad. Large energy spreads are advantageous for tuning the mean X-ray energy because numerous electron energies can be focused into the Thomson interaction point. However, in applications requiring X-ray photons with a specific energy and photon number, electron beams with a low energy spread are preferable. The X-ray beam energy tuning is then limited, but the scattering process has a higher electron charge density. The use of a shock-front in the gas jet to inject electrons is one method that could be implemented into the existing setup [35, 63, 64]. For this a plasma density gradient with decreasing density in the laser propagation direction is used to localise the charge injection process and produce low energy spread electron beams. The density shock-front can be generated, for example, by inserting a knife edge laterally into the gas jet. Using such a technique, stable electron beams with spectral densities greater than 10 pC/MeV can be generated [36]. Examples of other methods with a localised injection are self-truncated ionisation injection [61, 62] or injection using multiple laser pulses [59, 60]. Also, the mean energy of a narrowband electron beam can be tuned, for example, by shifting the charge injection point in localised injection methods or by using adjustable gas cells[25, 28, 197, 198]. This allows for the mean X-ray beam energy to be tuned again.

Spatial Overlap

The APL enables control of electron beam parameters during scattering interactions. These include the beam size, beam divergence, and effective electron energy spread. The transversal overlap is particularly important for photon production. When the electron and laser beams are matched in size and the spatial and temporal overlap is

optimised, the most photons are produced. The electron beam imaging magnification allows the electron beam size to be matched to the focal waist size of the scattering laser. Alternatively, the laser's focusing optic must be replaced to change the focal waist size. To ensure that both beams are spatially overlapped, a reliable diagnostic system for measuring the total photon number must be developed. Due to shot-to-shot electron-beam fluctuations and the electron beam's size being larger than the laser beam's size, the spatial overlap in this experiment could not be optimised well. In the case of less background radiation from bremsstrahlung, the total photon yield could be measured using a CsI(Tl) scintillator array [77, 194–196]. To accurately measure photon flux from an X-ray source, silicon pin diodes could be used [199]. These detectors are already in use at synchrotrons and in the hard X-ray regime [200].

Pulse Duration of the Scattering Laser

One advantage of an all-optical Thomson source is that the same laser system is used for both the LPA driver laser beam and the TS laser beam, making synchronisation easier. Because the electron source requires a laser pulse duration of about 30 fs, the scattering laser pulse has a duration of the same order. By lengthening the scattering interaction of the electron and laser beams, the total photon production increases. Because the interaction length is determined by the pulse durations of both beams, a longitudinally stretched scattering laser pulse will increase the number of X-ray photons emitted. It should be noted that photon production scales quadratically with laser strength (see Eq. 8.16), which is reduced by stretching the laser pulse. However, the laser power parameter can be high in LPA-experiments, and a reduction may be required for the scattering laser beam to fulfil particular minimum bandwidth limitations. This is true for the experiment conducted to meet bandwidth requirements for XFI with GNPs. An intense laser pulse can be stretched by passing it through a dispersive medium, such as a glass block, or by utilising chirped mirrors [163].

Laser Repetition Rate

While the effects described so far can enhance the photon production per shot, the X-ray source's repetition rate can also be increased to boost total photon flux.Although the available laser system can provide a repetition rate of up to 10 Hz, the proof-of-principle experiment was carried out at 2.1 Hz. Additional testing is required to run the X-ray source at the laser's full repetition rate. The heating effects of the compressor grating [97], as well as thermal lensing, can cause the laser focal spot to change over time [201]. Beside that, the total gas load from the gas jet into vacuum increases, but the differential pumping system has been tested and found to be capable of handling

a gas load of up to 10 Hz. Using the laser system's maximum repetition rate increases the photon flux by a factor of about 5. For a higher photon flux the laser system would eventually need to evolve to a kHz-laser system, such as the KALDERA-laser, which is currently under construction [202]. The photon flux would increase by a factor of 400 as a result.

11 SUMMARY AND OUTLOOK

In this thesis, a new concept for a tunable Thomson source based on a laser-plasma accelerator was demonstrated and characterised as part of a proof-of-principle experiment. The realisation of this X-ray source was motivated by **X**-ray **F**luorescence **I**maging (XFI) with **g**old **n**ano**p**articles (GNPs), which requires an X-ray source of high quality and specific parameters, preferably in a compact design to allow future implementation at medical facilities. The generated X-ray beam should be tuneable to a mean X-ray energy of about 90 keV and have a **F**ull **W**idth at **H**alf **M**aximum (FWHM) spectral bandwidth of less than 15 %. The designed Thomson X-ray source is the result of combining **L**aser-**P**lasma **A**cceleration (LPA) to generate relativistic electron beams and **T**homson **S**cattering (TS) to generate the X-ray radiation. An **A**ctive **P**lasma **L**ens (APL) is used to obtain independent control over the properties of the electron bunch in the scattering process. By imaging the polychromatic electron beam from the LPA stage, the beam divergence and energy spread, which contribute to the X-ray beam bandwidth, are effectively reduced. Furthermore, the electron beam focal spot can be matched to the scattering laser focal spot to enhance photon production within the effective electron energy spread. The contents of this thesis can be divided into three parts: (i) electron beam generation using LPA, (ii) design of an APL for beam characterisation and the Thomson X-ray source, and (iii) construction and demonstration of the X-ray source.

For electron beam generation, an LPA electron source based on ionisation injection was set up and characterised. It was run at a repetition rate of 2.1 Hz and produced electron beams with beam charges of about 4.5 pC, which was artificially limited by the detection of the X-ray beams. Higher beam charges produce a larger Bremsstrahlung background caused by electrons scattering at objects near the beam axis, and this radiation background quickly saturates the X-ray detector. An APL was specifically designed and successfully implemented to meet the requirements of the experiment. It is capable of imaging the electron beam into the Thomson scattering point as well as into the electron energy spectrometer. By imaging individual electron energies into the electron spectrometer, the electron spectrum was piecewise reconstructed. The technique of an imaging electron spectrometer provides a more thorough insight into the spectral charge distribution since beam-divergence would otherwise result

in broadening and averaging effects on the measured electron spectrum. Wiggles in the electron energy spectrum were observed, which hint at a variable charge injection during the LPA stage using ionisation injection, which were previously observed in simulations [100] but could not be resolved without the improved diagnostic. The electron beam has a mean energy of about 51 MeV and an FWHM energy spread of about 69 MeV. The tunability of the radiated energies in the X-ray source scheme presented is determined by the width of the electron energy spectrum.

Furthermore, electron beam foci dispersed in the electron spectrometer can be used to reconstruct the initial phase-space of the electron beam in the dispersive axis of the spectrometer, as first proposed by Weingartner et al. [107]. The electron bunch parameters were determined in order to validate the experimental results of the TS experiment and its optimisation. In the energy range of 42 MeV to 85 MeV, an average normalised emittance of $0.43^{+0.12}_{-0.33}$ mm mrad was measured, which is comparable but about a factor of three lower than recently published results from ionisation injection [155]. The average **R**oot **M**ean **S**quare (RMS) beam size at the electron source was measured to be $2.92^{+0.28}_{-0.86}$ µm, and the average RMS beam divergence was determined to be $1.16^{+0.32}_{-0.86}$ mrad. The normalised slice emittance and the imaged beam charge were observed to have a small correlation, with a higher charge density resulting in a larger beam emittance. While it was determined that emittance growth due to space charge effects is negligible, an indirect correlation can explain this behaviour. A higher laser pulse energy, for example, causes more charge to be injected while also resulting in a larger phase-space volume into which charge is injected, leading to an increase in emittance. Fluctuations in the plasma density of the LPA stage can have a similar effect. Higher plasma densities result in stronger plasma focusing, which increases the ionised charge as well as the emittance of the beam.

An X-ray source based on TS was established by overlapping a scattering laser beam and an electron beam focused using an APL with µm-precision in space and fs-precision in time. The implementation of the APL to the setup enabled an unprecedented control over the final X-ray energy by scattering off various electron energies in focus. X-ray beams with mean energies ranging from 34 keV to 81 keV were generated and measured. Scattering on an electron beam with an energy spread of $> 100\,\%$ results theoretically in a highly broadband X-ray beam [14, 92]. As a result of beam imaging with the APL, the electron energy spread was effectively reduced to about 5 % (FWHM), while also reducing the initial beam divergence by a factor of approximately 2.6. The detected X-ray spectra have an average relative bandwidth of $(25.6 \pm 2.5)\,\%$, an improvement over bandwidths previously achieved in the same laboratory with no APL by a factor of approximately 4 [14, 92]. To validate and study the experimental

results, they were compared to start-to-end simulations, which revealed excellent agreement with the mean X-ray energies. Within their uncertainty, the bandwidths of the simulated X-ray spectra agree with the average X-ray bandwidths from the experiment.

For a comprehensive X-ray bandwidth investigation, the individual contributions were studied in detail. This was accomplished through the use of an analytical model that agrees with the measured average X-ray bandwidths within its error. The contributions of spectral broadening due to effective electron beam divergence and effective electron energy spread were estimated to be between 8 % and 13 % (FWHM), depending on the focused electron energy. The scattering laser causes the most severe broadening, with the laser bandwidth accounting for about 8.8 % (FWHM) and the effective laser strength accounting for about 19.5 % (FWHM).

While chromatic imaging with the APL proved a reduction of spectral broadening owing to beam divergence and beam energy spread is possible, the measured total bandwidth is too large for the application of XFI. However, in the demonstrated setup, the x-ray bandwidth is no longer dominated by parameters of the electron bunch, and further improvement of the X-ray source necessary for use with XFI should be concentrated on shaping parameters of the scattering laser pulse. It was shown that adjusting the focusing geometry for the electron beam can significantly reduce the bandwidth contributions from beam divergence and energy spread (down to about 1 % (FWHM)). On the other hand, reducing the effective electron energy spread also reduces the electron charge participating in the scattering process, thus lowering the total photon yield. To further minimise the total X-ray bandwidth, the contributions originating from the scattering laser must be reduced. A scattering laser with a laser strength parameter of 0.81 ± 0.02 was used in the experiment. Since the contribution of the laser intensity to the X-ray bandwidth is of a quadratic nature, it is advisable to use moderate laser strength parameters of 0.5 or less. The laser strength parameter can be reduced by decreasing the energy of the laser pulse, increasing the laser focal spot size, or stretching the laser pulse in time. Particularly, the latter should be pursued in order to maintain high photon production. When the laser strength parameter is reduced to 0.5 and the electron beam focusing geometry is changed, the Thomson X-ray source from the experiment can theoretically produce X-ray beams with FWHM bandwidths of less than 15 %. To suppress spectral broadening from electron energy spread, the drift length from the electron source to the APL should be increased to 15 cm or more. The drift length from the APL to the electron beam focus needs to be larger than 40 cm to suppress broadening from beam divergence. To compensate for the increased electron beam size at the APL, a larger aperture may be required

to prevent electron charge loss and the additional generation of bremsstrahlung. In applications requiring X-ray spectra with smaller bandwidths, the laser strength parameter must be reduced further, as must the broadening contribution from the scattering laser's bandwidth. Depending on the electron-laser overlap, stretching the laser pulse via a longitudinal chirp can result in a reduced effective laser bandwidth $\Delta\omega_{\text{eff}} < \Delta\omega$ [40, 171, 172].

The total photon yield of the X-ray source could not be measured with the X-ray detector used here. According to simulations, approximately 200 to 600 photons were produced per shot within a 15 % bandwidth. This results in a peak brilliance of the X-ray source of approximately $1.6 \cdot 10^{18}$ photons/mrad²/mm²/0.1 %bandwidth/s for a repetition rate of 2.1 Hz. The TS simulations also revealed an average effective photon production of $3.6 \cdot 10^{-4}$ photons emitted per electron in a ± 1.61 mrad opening cone and a FWHM bandwidth of 15 %. A design study of a comparable Thomson source, specifically for XFI with GNP, predicted an effective photon production of up to $7.2 \cdot 10^{-3}$ photons emitted per electron within a ± 0.5 mrad opening cone and a FWHM bandwidth of 15 % [40]. This demonstrates that optimising the X-ray source can result in a twentyfold increase in effective photon production, even in an about tenfold smaller cross section. In the future, a separate diagnostic device, such as one based on a CsI(Tl) scintillator array, would be required for a direct measurement of the photon production. The next steps towards a high-flux Thomson X-ray source are higher laser repetition rates, increased electron charge density, and longer pulse duration of the scattering laser. Because photon flux scales linearly with laser repetition rate, switching to a kHz laser system increases flux by about three orders of magnitude, reducing the measuring times of an application accordingly. Stretching the laser pulse via a longitudinal chirp increases the interaction length of the scattering process, thus maintaining a high number of photons while improving the bandwidth due to a reduced laser strength parameter. When the decrease in the laser strength parameter is compensated for, the number of photons produced per shot increases. Similarly, as the electron beam's spectral density increases, so does the number of scattered electrons. LPA with a more localised injection scheme, such as shock-front injection, can result in electron beams with a narrower energy spread and a higher charge density. While this increases photon production, it decreases the tunability of the X-ray source, which is determined by the spectral width of the electron beam. Ideally, narrowband electron beams with adjustable mean energy are generated at the electron source. This is possible in injection schemes that allow the charge injection point to be shifted, such as shock-front injection or colliding pulse injection. Alternatively, adjustable gas cells can be used. The combination of a narrowband electron beam

source and an APL would be highly beneficial for a TS X-ray source. Then, both the electron source and the APL support X-ray beam energy tuning, with the photon source benefiting from increased stability and photon production by imaging with the APL.

The X-ray source described in this thesis can generate X-ray beams with reduced divergence and bandwidth as well as increased photon yield within the effective electron energy spread. It was shown that after optimisation, the setup would be able to fulfil the requirements for XFI with GNPs. If necessary, further optimisations may result in even smaller spectral bandwidths and higher photon production. Future advancements in high-power laser technologies may increase the source photon yield, paving the way for a wide range of scientific and medical applications. Due to their small spatial dimensions, these high brilliance, narrowband, tunable photon sources have the potential to be installed in universities and medical facilities, promoting X-ray radiation research and treatment.

BIBLIOGRAPHY

[1] B. H. Kevles. *Naked To The Bone: Medical Imaging In The Twentieth Century*. Basic Books, 1998. ISBN: 9780201328332.

[2] W. C. Röntgen. "Ueber eine neue Art von Strahlen." In: *Annalen der Physik* 300.1 (1898), pp. 12–17. DOI: https://doi.org/10.1002/andp.18983000103. URL: https://onlinelibrary.wiley.com/doi/abs/10.1002/andp.18983000103.

[3] David Attwood and Anne Sakdinawat. *X-Rays and Extreme Ultraviolet Radiation: Principles and Applications*. 2nd ed. Cambridge University Press, 2017. DOI: 10.1017/CBO9781107477629.

[4] Eric A. Simiele et al. "Precision radiotherapy using monochromatic inverse Compton x-ray sources." In: *Medical physics* (2020).

[5] Henry N. Chapman et al. "Femtosecond X-ray protein nanocrystallography." English. In: *Nature* 470.7332 (Feb. 2011), pp. 73–77. ISSN: 0028-0836. DOI: 10.1038/nature09750.

[6] I. D. Cullum, Peter J. Ell, and John P. Ryder. "X-ray dual-photon absorptiometry: a new method for the measurement of bone density." In: *The British journal of radiology* 62 739 (1989), pp. 587–92.

[7] P. Boisseau and Lee Grodzins. "Fluorescence tomography using synchrotron radiation at the NSLS." In: *Hyperfine Interactions* 33 (1987), pp. 283–292.

[8] W. Thomlinson, Helene Elleaume, Liisa Porra, and P. Suortti. "K-edge subtraction synchrotron X-ray imaging in bio-medical research." In: *Physica Medica* 49 (May 2018), pp. 58–76. DOI: 10.1016/j.ejmp.2018.04.389.

[9] Roberto Cesareo and Sergio Mascarenhas. "A new tomographic device based on the detection of fluorescent x-rays." In: *Nuclear Instruments and Methods in Physics Research Section A: Accelerators, Spectrometers, Detectors and Associated Equipment* 277.2 (1989), pp. 669–672. ISSN: 0168-9002. DOI: https://doi.org/10.1016/0168-9002(89)90802-4. URL: https://www.sciencedirect.com/science/article/pii/0168900289908024.

[10] Seong-Kyun Cheong et al. "X-ray fluorescence computed tomography (XFCT) imaging of gold nanoparticle-loaded objects using 110 kVp x-rays." In: *Physics in Medicine and Biology* 55.3 (Jan. 2010), pp. 647–662. DOI: 10.1088/0031-9155/55/3/007. URL: https://doi.org/10.1088/0031-9155/55/3/007.

[11] Florian Schulz et al. "Gold nanoparticles functionalized with a fragment of the neural cell adhesion molecule L1 stimulate L1-mediated functions." In: *Nanoscale* 5 (21 2013), pp. 10605–10617. DOI: 10.1039/C3NR02707D. URL: http://dx.doi.org/10.1039/C3NR02707D.

[12] Liqiang Ren et al. "Three-dimensional x-ray fluorescence mapping of a gold nanoparticle-loaded phantom." In: *Medical Physics* 41.3 (2014), p. 031902. DOI: https://doi.org/10.1118/1.4863510. URL: https://aapm.onlinelibrary.wiley.com/doi/abs/10.1118/1.4863510.

[13] Nivedh Manohar et al. "Quantitative imaging of gold nanoparticle distribution in a tumor-bearing mouse using benchtop x-ray fluorescence computed tomography." In: *Scientific Reports* 6 (Feb. 2016), p. 22079. DOI: 10.1038/srep22079.

[14] Theresa Maria Staufer. "X-Ray Fluorescence Imaging with a Laser-Driven X-Ray Source." Dissertation, Universität Hamburg, 2020. Dissertation. Hamburg: Universität Hamburg, 2020. URL: https://ediss.sub.uni-hamburg.de/handle/ediss/8499.

[15] T. Staufer et al. "Development of a laser-wakefield Thomson x-ray source for x-ray fluorescence imaging." In: *Laser Acceleration of Electrons, Protons, and Ions V*. Ed. by Eric Esarey, Carl B. Schroeder, and Jörg Schreiber. Vol. 11037. International Society for Optics and Photonics. SPIE, 2019, pp. 38 –47. DOI: 10.1117/12.2520685. URL: https://doi.org/10.1117/12.2520685.

[16] Florian Grüner et al. "Localising functionalised gold-nanoparticles in murine spinal cords by X-ray fluorescence imaging and background-reduction through spatial filtering for human-sized objects." In: *Scientific reports* 8.1 (2018), p. 16561. ISSN: 2045-2322. DOI: 10.1038/s41598-018-34925-3. URL: https://bib-pubdb1.desy.de/record/416705.

[17] F. R. Arutyunian and V. A. Tumanian. "The Compton effect on relativistic electrons and the possibility of obtaining high energy beams." In: *Physics Letters* 4.3 (1963), pp. 176–178. ISSN: 0031-9163. DOI: https://doi.org/10.1016/0031-9163(63)90351-2. URL: https://www.sciencedirect.com/science/article/pii/0031916363903512.

[18] F. R. Arutyunyan and V. A. Tumanyan. "Quasi-monochromatic and polarized high-energy gamma rays." In: *Soviet Physics Uspekhi* 7.3 (Mar. 1964), pp. 339–357. DOI: 10.1070/pu1964v007n03abeh003669. URL: https://doi.org/10.1070/pu1964v007n03abeh003669.

[19] O. F. Kulikov, Y. Y. Telnov, E. I. Filippov, and M. N. Yakimenko. "Compton effect on moving electrons." In: *Physics Letters* 13.4 (1964), pp. 344–346. ISSN: 0031-9163. DOI: https://doi.org/10.1016/0031-9163(64)90040-X. URL: https://www.sciencedirect.com/science/article/pii/003191636490040X.

[20] A.W. Chao, K. Mess, M. Tigner, and F. Zimmermann. *Handbook of Accelerator Physics and Engineering: 2nd Edition*. Jan. 2013. ISBN: 978-981-4415-84-2 , 978-981-4417-17-4.

[21] T. Tajima and J. M. Dawson. "Laser Electron Accelerator." In: *Phys. Rev. Lett.* 43 (July 1979), pp. 267–270. DOI: 10.1103/PhysRevLett.43.267. URL: https://link.aps.org/doi/10.1103/PhysRevLett.43.267.

[22] Donna Strickland and Gerard Mourou. "Compression of amplified chirped optical pulses." In: *Optics Communications* 55.6 (1985), pp. 447 –449. ISSN: 0030-4018. DOI: https://doi.org/10.1016/0030-4018(85)90151-8.

[23] K. Ta Phuoc et al. "All-optical Compton gamma-ray source." In: *Nature Photonics* 6.5 (Apr. 2012), pp. 308–311. DOI: 10.1038/nphoton.2012.82. URL: https://doi.org/10.1038%2Fnphoton.2012.82.

[24] S. Chen et al. "MeV-Energy X Rays from Inverse Compton Scattering with Laser-Wakefield Accelerated Electrons." In: *Phys. Rev. Lett.* 110 (Apr. 2013), p. 155003. DOI: 10.1103/PhysRevLett.110.155003. URL: https://link.aps.org/doi/10.1103/PhysRevLett.110.155003.

[25] Nathan Powers et al. "Quasi-monoenergetic and tunable X-rays from a laser-driven Compton light source." In: *Nature Photonics* 8 (Nov. 2013), pp. 28–31. DOI: 10.1038/nphoton.2013.314.

[26] Cheng Liu et al. "Generation of 9 MeV γ-rays by all-laser-driven Compton scattering with second-harmonic laser light." In: *Opt. Lett.* 39.14 (July 2014), pp. 4132–4135. DOI: 10.1364/OL.39.004132. URL: http://opg.optica.org/ol/abstract.cfm?URI=ol-39-14-4132.

[27] G. Sarri et al. "Ultrahigh Brilliance Multi-MeV γ-Ray Beams from Nonlinear Relativistic Thomson Scattering." In: *Phys. Rev. Lett.* 113 (Nov. 2014), p. 224801. DOI: 10.1103/PhysRevLett.113.224801. URL: https://link.aps.org/doi/10.1103/PhysRevLett.113.224801.

[28] K. Khrennikov et al. "Tunable All-Optical Quasimonochromatic Thomson X-Ray Source in the Nonlinear Regime." In: *Phys. Rev. Lett.* 114 (May 2015), p. 195003. DOI: 10.1103/PhysRevLett.114.195003. URL: https://link.aps.org/doi/10.1103/PhysRevLett.114.195003.

[29] S. P. D. Mangles et al. "Monoenergetic beams of relativistic electrons from intense laser-plasma interactions." In: *Nature* 431.7008 (Sept. 2004), pp. 535–538. ISSN: 1476-4687. DOI: 10.1038/nature02939. URL: https://doi.org/10.1038/nature02939.

[30] J. Faure et al. "A laser-plasma accelerator producing monoenergetic electron beams." In: *Nature* 431.7008 (Sept. 2004), pp. 541–544. ISSN: 1476-4687. DOI: 10.1038/nature02963. URL: https://doi.org/10.1038/nature02963.

[31] J. Faure et al. "Controlled injection and acceleration of electrons in plasma wakefields by colliding laser pulses." In: *Nature* 444.7120 (Dec. 2006), pp. 737–739. ISSN: 1476-4687. DOI: 10.1038/nature05393. URL: https://doi.org/10.1038/nature05393.

[32] S. P. D. Mangles et al. "On the stability of laser wakefield electron accelerators in the monoenergetic regime." In: *Physics of Plasmas* 14.5 (2007), p. 056702. DOI: 10.1063/1.2436481. URL: https://doi.org/10.1063/1.2436481.

[33] J. Osterhoff et al. "Generation of Stable, Low-Divergence Electron Beams by Laser-Wakefield Acceleration in a Steady-State-Flow Gas Cell." In: *Phys. Rev. Lett.* 101 (8 Aug. 2008), p. 085002. DOI: 10.1103/PhysRevLett.101.085002. URL: https://link.aps.org/doi/10.1103/PhysRevLett.101.085002.

[34] B. B. Pollock et al. "Demonstration of a Narrow Energy Spread, ~ 0.5 GeV Electron Beam from a Two-Stage Laser Wakefield Accelerator." In: *Phys. Rev. Lett.* 107 (July 2011), p. 045001. DOI: 10.1103/PhysRevLett.107.045001. URL: https://link.aps.org/doi/10.1103/PhysRevLett.107.045001.

[35] K. Schmid et al. "Density-transition based electron injector for laser driven wakefield accelerators." In: *Phys. Rev. ST Accel. Beams* 13 (Sept. 2010), p. 091301. DOI: 10.1103/PhysRevSTAB.13.091301. URL: https://link.aps.org/doi/10.1103/PhysRevSTAB.13.091301.

[36] A Buck et al. "Shock-Front Injector for High-Quality Laser-Plasma Acceleration." In: *Physical review letters* 110 (May 2013), p. 185006. DOI: 10.1103/PhysRevLett.110.185006.

[37] W. K. H. Panofsky and W. R. Baker. "A Focusing Device for the External 350-Mev Proton Beam of the 184-Inch Cyclotron at Berkeley." In: *Review of Scientific Instruments* 21.5 (1950), pp. 445–447. DOI: 10.1063/1.1745611. URL: https://doi.org/10.1063/1.1745611.

[38] E. Boggasch et al. "z-pinch plasma lens focusing of a heavy-ion beam." In: *Phys. Rev. Lett.* 66 (Apr. 1991), pp. 1705–1708. DOI: 10.1103/PhysRevLett.66.1705. URL: https://link.aps.org/doi/10.1103/PhysRevLett.66.1705.

[39] J. van Tilborg et al. "Active Plasma Lensing for Relativistic Laser-Plasma-Accelerated Electron Beams." In: *Phys. Rev. Lett.* 115 (Oct. 2015), p. 184802. DOI: 10.1103/PhysRevLett.115.184802. URL: https://link.aps.org/doi/10.1103/PhysRevLett.115.184802.

[40] Theresa Brümmer et al. "Design study for a compact laser-driven source for medical x-ray fluorescence imaging." In: *Physical Review Accelerators and Beams* 23.3 (2020). http://link.aps.org/pdf/10.1103/PhysRevAccelBeams.23.031601, p. 031601. DOI: 10.1103/physrevaccelbeams.23.031601. URL: https://app.dimensions.ai/details/publication/pub.1125318605.

[41] T. Brümmer et al. "Compact all-optical precision-tunable narrowband hard Compton X-ray source." In: *Scientific Reports* 12.1 (Sept. 2022), p. 16017. ISSN: 2045-2322. DOI: 10.1038/s41598-022-20283-8. URL: https://doi.org/10.1038/s41598-022-20283-8.

[42] W. P. Leemans et al. "GeV electron beams from a centimetre-scale accelerator." In: *Nature Physics* 2 (2006), pp. 696 –699. DOI: doi:10.1038/nphys418.

[43] Chen, F. *Introduction to Plasma Physics and Controlled Fusion*. Springer, 2016. ISBN: 978-3-319-22309-4. DOI: 10.1007/978-3-319-22309-4.

[44] Stroth, U. *Plasmaphysik*. Vieweg+Teubner Verlag, 2011. ISBN: 978-3-8348-8326-1. DOI: 10.1007/978-3-8348-8326-1.

[45] R. J. Goldston and P. H. Rutherford. "Plasmaphysik." In: *Vieweg+ Teubner* (1998).

[46] Osterhoff, Jens. "Stable, ultra-relativistic electron beams by laser-wakefield acceleration." PhD thesis. 2009.

[47] E. Esarey, C. B. Schroeder, and W. P. Leemans. "Physics of laser-driven plasma-based electron accelerators." In: *Rev. Mod. Phys.* 81 (Aug. 2009), pp. 1229–1285. DOI: 10.1103/RevModPhys.81.1229. URL: https://link.aps.org/doi/10.1103/RevModPhys.81.1229.

[48] V. Malka et al. "Principles and applications of compact laser–plasma accelerators." In: *Nature Physics* 4 (June 2008), pp. 447–453. DOI: 10.1038/nphys966.

[49] Rémi Lehe et al. "A spectral, quasi-cylindrical and dispersion-free Particle-In-Cell algorithm." In: *Computer Physics Communications* 203 (2016), pp. 66–82. ISSN: 0010-4655. DOI: https://doi.org/10.1016/j.cpc.2016.02.007. URL: https://www.sciencedirect.com/science/article/pii/S0010465516300224.

[50] S. Jalas et al. "Accurate modeling of plasma acceleration with arbitrary order pseudo-spectral particle-in-cell methods." In: *Physics of Plasmas* 24.3 (2017), p. 033115. DOI: 10.1063/1.4978569. URL: https://doi.org/10.1063/1.4978569.

[51] A. Pukhov and J. Meyer-ter Vehn. "Laser wake field acceleration: the highly non-linear broken-wave regime." In: *Applied Physics B* 74.4 (Apr. 2002), pp. 355–361. ISSN: 1432-0649. DOI: 10.1007/s003400200795. URL: https://doi.org/10.1007/s003400200795.

[52] A. G. Khachatryan et al. "Conceptual design of a laser wakefield acceleration experiment with external bunch injection." In: *Nuclear Instruments and Methods in Physics Research Section A: Accelerators, Spectrometers, Detectors and Associated Equipment* 566.2 (2006), pp. 244 –249. ISSN: 0168-9002. DOI: https://doi.org/10.1016/j.nima.2006.07.007. URL: http://www.sciencedirect.com/science/article/pii/S0168900206012551.

[53] S. Bulanov, N. Naumova, F. Pegoraro, and J. Sakai. "Particle injection into the wave acceleration phase due to nonlinear wake wave breaking." In: *Phys. Rev. E* 58 (Nov. 1998), R5257–R5260. DOI: 10.1103/PhysRevE.58.R5257. URL: https://link.aps.org/doi/10.1103/PhysRevE.58.R5257.

[54] E. Esarey, B. Hafizi, R. Hubbard, and A. Ting. "Trapping and Acceleration in Self-Modulated Laser Wakefields." In: *Phys. Rev. Lett.* 80 (June 1998), pp. 5552–5555. DOI: 10.1103/PhysRevLett.80.5552. URL: https://link.aps.org/doi/10.1103/PhysRevLett.80.5552.

[55] E. Oz et al. "Ionization-Induced Electron Trapping in Ultrarelativistic Plasma Wakes." In: *Phys. Rev. Lett.* 98 (Feb. 2007), p. 084801. DOI: 10.1103/PhysRevLett.98.084801. URL: https://link.aps.org/doi/10.1103/PhysRevLett.98.084801.

[56] M. Chen et al. "Theory of ionization-induced trapping in laser-plasma accelerators." In: *Physics of Plasmas* 19.3 (2012), p. 033101. DOI: 10.1063/1.3689922. URL: https://doi.org/10.1063/1.3689922.

[57] Min Chen, Zheng-Ming Sheng, Yan-Yun Ma, and Jie Zhang. "Electron injection and trapping in a laser wakefield by field ionization to high-charge states of gases." In: *Journal of Applied Physics* 99.5 (2006), p. 056109. DOI: 10.1063/1.2179194. URL: https://doi.org/10.1063/1.2179194.

[58] S. K. Barber et al. "Measured Emittance Dependence on the Injection Method in Laser Plasma Accelerators." In: *Phys. Rev. Lett.* 119 (Sept. 2017), p. 104801. DOI: 10.1103/PhysRevLett.119.104801. URL: https://link.aps.org/doi/10.1103/PhysRevLett.119.104801.

[59] F. Li et al. "Generating High-Brightness Electron Beams via Ionization Injection by Transverse Colliding Lasers in a Plasma-Wakefield Accelerator." In: *Phys. Rev. Lett.* 111 (July 2013), p. 015003. DOI: 10.1103/PhysRevLett.111.015003. URL: https://link.aps.org/doi/10.1103/PhysRevLett.111.015003.

[60] N. Bourgeois, J. Cowley, and S. M. Hooker. "Two-Pulse Ionization Injection into Quasilinear Laser Wakefields." In: *Phys. Rev. Lett.* 111 (Oct. 2013), p. 155004. DOI: 10.1103/PhysRevLett.111.155004. URL: https://link.aps.org/doi/10.1103/PhysRevLett.111.155004.

[61] C Kamperidis et al. "Low energy spread electron beams from ionization injection in a weakly relativistic laser wakefield accelerator." In: *Plasma Physics and Controlled Fusion* 56.8 (July 2014), p. 084007. DOI: 10.1088/0741-3335/56/8/084007. URL: https://doi.org/10.1088/0741-3335/56/8/084007.

[62] M. Mirzaie et al. "Demonstration of self-truncated ionization injection for GeV electron beams." In: *Scientific Reports* 5.1 (Oct. 2015), p. 14659. ISSN: 2045-2322. DOI: 10.1038/srep14659. URL: https://doi.org/10.1038/srep14659.

[63] C. G. R. Geddes et al. "Plasma-Density-Gradient Injection of Low Absolute-Momentum-Spread Electron Bunches." In: *Phys. Rev. Lett.* 100 (May 2008), p. 215004. DOI: 10.1103/PhysRevLett.100.215004. URL: https://link.aps.org/doi/10.1103/PhysRevLett.100.215004.

[64] K. Schmid et al. "Density-transition based electron injector for laser driven wakefield accelerators." In: *Phys. Rev. ST Accel. Beams* 13 (2010), p. 091301. DOI: 10.1103/PhysRevSTAB.13.091301.

[65] *Courtesy of Simon Bohlen.*

[66] Richard D'Arcy et al. "FLASHForward: plasma wakefield accelerator science for high-average-power applications." In: *Philosophical Transactions of the Royal Society A: Mathematical, Physical and Engineering Sciences* 377 (Aug. 2019), p. 20180392. DOI: 10.1098/rsta.2018.0392.

[67] A. Aschikhin et al. "The FLASHForward facility at DESY." In: *Nuclear Instruments and Methods in Physics Research Section A: Accelerators, Spectrometers, Detectors and Associated Equipment* 806 (2016), pp. 175–183. ISSN: 0168-9002. DOI: https://doi.org/10.1016/j.nima.2015.10.005. URL: https://www.sciencedirect.com/science/article/pii/S0168900215012103.

[68] R. D'Arcy et al. "Tunable Plasma-Based Energy Dechirper." In: *Phys. Rev. Lett.* 122 (Jan. 2019), p. 034801. DOI: 10.1103/PhysRevLett.122.034801. URL: https://link.aps.org/doi/10.1103/PhysRevLett.122.034801.

[69] A. Knetsch et al. "Stable witness-beam formation in a beam-driven plasma cathode." In: *Phys. Rev. Accel. Beams* 24 (Oct. 2021), p. 101302. DOI: 10.1103/PhysRevAccelBeams.24.101302. URL: https://link.aps.org/doi/10.1103/PhysRevAccelBeams.24.101302.

[70] Jean-Claude Diels and Wolfgang Rudolph. *Ultrashort laser pulse phenomena*. Elsevier, 2006.

[71] Anthony E Siegman. *Lasers*. University science books, 1986.

[72] Wolfgang Kaiser and David H Auston. *Ultrashort laser pulses: generation and applications*. Springer, 1993.

[73] *Courtesy of Song Li.*

[74] S. Semushin and V. Malka. "High density gas jet nozzle design for laser target production." In: *Review of Scientific Instruments* 72.7 (2001), pp. 2961–2965. DOI: 10.1063/1.1380393. URL: https://doi.org/10.1063/1.1380393.

[75] J.-H. Röckemann et al. "Direct measurement of focusing fields in active plasma lenses." In: *Phys. Rev. Accel. Beams* 21 (Dec. 2018), p. 122801. DOI: 10.1103/PhysRevAccelBeams.21.122801. URL: https://link.aps.org/doi/10.1103/PhysRevAccelBeams.21.122801.

[76] Martin Meisel. "Emittance Measurement of Electron Beams from Laser Wakefield Acceleration using an Active Plasma Lens." Masterarbeit. Hamburg: Universität Hamburg, 2018, p. 91. DOI: 10.3204/PUBDB-2018-03854. URL: https://bib-pubdb1.desy.de/record/414292.

[77] Jonathan Schwardt. "Flux measurement of a Thomson source." Masterarbeit. University of Hamburg, 2022.

[78] Ralph A. Alpher and Donald R. White. "Optical Refractivity of High-Temperature Gases. II. Effects Resulting from Ionization of Monatomic Gases." In: *The Physics of Fluids* 2.2 (1959), pp. 162–169. DOI: 10.1063/1.1705907. URL: https://aip.scitation.org/doi/abs/10.1063/1.1705907.

[79] D. E. T. F. Ashby and D. F. Jephcott. "Measurement of Plasma Density Using a Gas Laser as an Infrared Interferometer." In: *Applied Physics Letters* 3.1 (1963), pp. 13–16. DOI: 10.1063/1.1723556. URL: https://doi.org/10.1063/1.1723556.

[80] E. A. McLean and S. A. Ramsden. "Optical Interferometric and Spectroscopic Measurements of Electron Density in a Plasma." In: *Phys. Rev.* 140 (Nov. 1965), A1122–A1129. DOI: 10.1103/PhysRev.140.A1122. URL: https://link.aps.org/doi/10.1103/PhysRev.140.A1122.

[81] Jason Mark Cole. "Diagnosis and application of laser wakefield accelerators." Dissertation, Imperial College London, 2016. Dissertation. 216. DOI: 10.25560/42222. URL: http://hdl.handle.net/10044/1/42222.

[82] Fastlite. *Dazzler - Ultrafast pulse shaper*. https://fastlite.com/produits/dazzler-ultrafast-pulse-shaper/. [Online; accessed 20-July-2022].

[83] Fastlite. "Wizzler manual, V2.0." In: ().

[84] T. Oksenhendler et al. "Self-referenced spectral interferometry." In: *Applied Physics B* 99.1 (Apr. 2010), pp. 7–12. ISSN: 1432-0649. DOI: 10.1007/s00340-010-3916-y. URL: https://doi.org/10.1007/s00340-010-3916-y.

[85] N. Minkovski et al. "Nonlinear polarization rotation and orthogonal polarization generation experienced in a single-beam configuration." In: *J. Opt. Soc. Am. B* 21.9 (Sept. 2004), pp. 1659–1664. DOI: 10.1364/JOSAB.21.001659. URL: http://opg.optica.org/josab/abstract.cfm?URI=josab-21-9-1659.

[86] Thomas Kurz et al. "Calibration and cross-laboratory implementation of scintillating screens for electron bunch charge determination." In: *Review of Scientific Instruments* 89.9 (2018), p. 093303. DOI: 10.1063/1.5041755. URL: https://doi.org/10.1063/1.5041755.

[87] J.-P. Schwinkendorf et al. "Charge calibration of DRZ scintillation phosphor screens." In: *Journal of Instrumentation* 14.09 (Sept. 2019), P09025–P09025. DOI: 10.1088/1748-0221/14/09/p09025. URL: https://doi.org/10.1088/1748-0221/14/09/p09025.

[88] Bergoz. "Integrating Current Transformer, User's Manual, Rev. 4.0." In: (2018).

[89] D. et al. Lipka. "Dark Current Monitor for the European XFEL." In: *Proceedings of DIPAC2011, Hamburg, Germany*. Vol. WEOC03. 2011.

[90] D. et al. Lipka. "Resonator for Charge Measurement at REGAE." In: *Proceedings of IBIC2013, Oxford, UK*. Vol. WEPF25. 2013. ISBN: 978-3-95450-127-4.

[91] M. C. Downer et al. "Diagnostics for plasma-based electron accelerators." In: *Rev. Mod. Phys.* 90 (Aug. 2018), p. 035002. DOI: 10.1103/RevModPhys.90.035002. URL: https://link.aps.org/doi/10.1103/RevModPhys.90.035002.

[92] Simon Bohlen. "Measurement of Electron Parameters using Thomson Scattering." Dissertation. Hamburg: Universtät Hamburg, 2021, p. 158. DOI: 10.3204/PUBDB-2020-05030. URL: https://bib-pubdb1.desy.de/record/453194.

[93] C. Patrignani et al. "Review of Particle Physics." In: *Chin. Phys.* C40.10 (2016), p. 100001. DOI: 10.1088/1674-1137/40/10/100001.

[94] Gero Kube et al. "Transverse Beam Profile Imaging of Few-Micrometer Beam Sizes Based on a Scintillator Screen." In: Jan. 2016.

[95] Paul Pourmoussavi. "Studies on a feedback loop system for the optimisation of Laser Wakefield Acceleration." Masters Thesis, University of Hamburg, 2018. Masters thesis. University of Hamburg, 2018.

[96] Yannick Ruske, Jens Osterhoff, and Florian Gruener. "Präzise spektrale Analyse von Elektronenpaketen aus einemLaser Plasma Wakefield Beschleuniger." Bachelorarbeit, University of Hamburg, 2019. Bachelorarbeit. University of Hamburg, 2019, p. 48. URL: https://bib-pubdb1.desy.de/record/426729.

[97] Jan Lukas Dresselhaus. "Paving the way of high repetition rate laser wakefield acceleration by solving heat induced grating deformation issues." Masterarbeit. University of Hamburg, 2020, p. 62. DOI: 10.3204/PUBDB-2020-05063. URL: https://bib-pubdb1.desy.de/record/453227.

[98] Robin Brabants. "Longitudinal Bunch Profile Diagnostics at a Laser-Driven Plasma Wakefield Acceleration Experiment." Masterarbeit. University of Hamburg, 2020, p. 83. DOI: 10.3204/PUBDB-2020-04239. URL: https://bib-pubdb1.desy.de/record/450225.

[99] Matthias Czimmeck. "Optimization study of a laserdriven Thomson X-ray source for medium Z fluorescence imaging." Masterarbeit. University of Hamburg, 2021.

[100] Simon Bohlen et al. "Stability of ionization-injection-based laser-plasma accelerators." In: *Phys. Rev. Accel. Beams* 25 (Mar. 2022), p. 031301. DOI: 10.1103/PhysRevAccelBeams.25.031301. URL: https://link.aps.org/doi/10.1103/PhysRevAccelBeams.25.031301.

[101] S. Bohlen et al. "In Situ Measurement of Electron Energy Evolution in a Laser-Plasma Accelerator." In: *Phys. Rev. Lett.* 129 (24 Dec. 2022), p. 244801. DOI: 10.1103/PhysRevLett.129.244801. URL: https://link.aps.org/doi/10.1103/PhysRevLett.129.244801.

[102] C. B. Schroeder et al. "Physics considerations for laser-plasma linear colliders." In: *Phys. Rev. ST Accel. Beams* 13 (Oct. 2010), p. 101301. DOI: 10.1103/PhysRevSTAB.13.101301. URL: https://link.aps.org/doi/10.1103/PhysRevSTAB.13.101301.

[103] Kazuhisa Nakajima. "Towards a table-top free-electron laser." In: *Nature Physics* 4.2 (Feb. 2008), pp. 92–93. ISSN: 1745-2481. DOI: 10.1038/nphys846. URL: https://doi.org/10.1038/nphys846.

[104] R. Hajima et al. "Detection of radioactive isotopes by using laser Compton scattered γ-ray beams." In: *Nuclear Instruments and Methods in Physics Research Section A: Accelerators, Spectrometers, Detectors and Associated Equipment* 608.1, Supplement (2009), S57–S61. ISSN: 0168-9002. DOI: https://doi.org/10.1016/j.nima.2009.05.063. URL: https://www.sciencedirect.com/science/article/pii/S0168900209009693.

[105] A. R. Maier et al. "Demonstration Scheme for a Laser-Plasma-Driven Free-Electron Laser." In: *Phys. Rev. X* 2 (Sept. 2012), p. 031019. DOI: 10.1103/PhysRevX.2.031019. URL: https://link.aps.org/doi/10.1103/PhysRevX.2.031019.

[106] Zhirong Huang, Yuantao Ding, and Carl B. Schroeder. "Compact X-ray Free-Electron Laser from a Laser-Plasma Accelerator Using a Transverse-Gradient Undulator." In: *Phys. Rev. Lett.* 109 (Nov. 2012), p. 204801. DOI: 10.1103/PhysRevLett.109.204801. URL: https://link.aps.org/doi/10.1103/PhysRevLett.109.204801.

[107] R. Weingartner et al. "Ultralow emittance electron beams from a laser-wakefield accelerator." In: *Phys. Rev. ST Accel. Beams* 15 (Nov. 2012), p. 111302. DOI: 10.1103/PhysRevSTAB.15.111302. URL: https://link.aps.org/doi/10.1103/PhysRevSTAB.15.111302.

[108] P. Antici et al. "Laser-driven electron beamlines generated by coupling laser-plasma sources with conventional transport systems." In: *Journal of Applied Physics* 112.4 (2012), p. 044902. DOI: 10.1063/1.4740456. URL: https://doi.org/10.1063/1.4740456.

[109] M. Migliorati et al. "Intrinsic normalized emittance growth in laser-driven electron accelerators." In: *Phys. Rev. ST Accel. Beams* 16 (Jan. 2013), p. 011302. DOI: 10.1103/PhysRevSTAB.16.011302. URL: https://link.aps.org/doi/10.1103/PhysRevSTAB.16.011302.

[110] F. Löhl. "Measurements of the Transverse Emittance at the VUV-FEL." DESY-THESIS 2005-014 and TESLA-FEL 2005-03. Diploma Thesis. Department of Physics of the University of Hamburg, 2005.

[111] H. Wiedemann. "Particle Accelerator Physics." In: (2007). DOI: 10.1007/978-3-540-49045-6.

[112] Andy Bolzmann. "Investigation of the longitudinal charge distribution of electron bunches at the VUV-FEL using the transverse deflecting cavity LOLA." Dipl. Hamburg: Bayerische Julius-Maximilians Universität Würzburg, 2005, p. 44. DOI: 10.3204/DESY-THESIS-2005-046. URL: http://bib-pubdb1.desy.de/record/288705.

[113] Pisin Chen. "Grand Disruption: A Possible Final Focusing Mechanism for Linear Colliders." In: *Part. Accel.* 20 (1987), pp. 171–182.

[114] J. B. Rosenzweig, B. Breizman, T. Katsouleas, and J. J. Su. "Acceleration and focusing of electrons in two-dimensional nonlinear plasma wake fields." In: *Phys. Rev. A* 44 (Nov. 1991), R6189–R6192. DOI: 10.1103/PhysRevA.44.R6189. URL: https://link.aps.org/doi/10.1103/PhysRevA.44.R6189.

[115] J. S. T. Ng et al. "Observation of Plasma Focusing of a 28.5 GeV Positron Beam." In: *Phys. Rev. Lett.* 87 (Nov. 2001), p. 244801. DOI: 10.1103/PhysRevLett.87.244801. URL: https://link.aps.org/doi/10.1103/PhysRevLett.87.244801.

[116] S. Kuschel et al. "Demonstration of passive plasma lensing of a laser wakefield accelerated electron bunch." In: *Phys. Rev. Accel. Beams* 19 (July 2016), p. 071301. DOI: 10.1103/PhysRevAccelBeams.19.071301. URL: https://link.aps.org/doi/10.1103/PhysRevAccelBeams.19.071301.

[117] C. A. Lindstrøm et al. "Emittance Preservation in an Aberration-Free Active Plasma Lens." In: *Phys. Rev. Lett.* 121 (Nov. 2018), p. 194801. DOI: 10.1103/PhysRevLett.121.194801. URL: https://link.aps.org/doi/10.1103/PhysRevLett.121.194801.

[118] K. N. Sjobak et al. "Strong focusing gradient in a linear active plasma lens." In: *Phys. Rev. Accel. Beams* 24 (Dec. 2021), p. 121306. DOI: 10.1103/PhysRevAccelBeams.24.121306. URL: https://link.aps.org/doi/10.1103/PhysRevAccelBeams.24.121306.

[119] Dengming Xiao. "Fundamental Theory of Townsend Discharge." In: *Gas Discharge and Gas Insulation*. Berlin, Heidelberg: Springer Berlin Heidelberg, 2016, pp. 47–88. ISBN: 978-3-662-48041-0. DOI: 10.1007/978-3-662-48041-0_3. URL: https://doi.org/10.1007/978-3-662-48041-0_3.

[120] F. Paschen. *Über die zum Funkenübergang in Luft, Wasserstoff und Kohlensäure bei verschiedenen Drucken erforderliche Potenzialdifferenz*. Barth, 1889. DOI: 10.1002/andp.18892730505.

[121] M. A. Lieberman and A. J. Lichtenberg. *Principles of Plasma Discharges and Materials Processing*. Wiley, 1994. ISBN: 9780471005773.

[122] J. K. Lim et al. "Adjustable, short focal length permanent-magnet quadrupole based electron beam final focus system." In: *Phys. Rev. ST Accel. Beams* 8 (July 2005), p. 072401. DOI: 10.1103/PhysRevSTAB.8.072401. URL: https://link.aps.org/doi/10.1103/PhysRevSTAB.8.072401.

[123] Jan-Hendrik Röckemann. "Experimental and theoretical studies on electron-beam focusing using active plasma lenses." Dissertation, University of Hamburg, 2020. Dissertation. University of Hamburg, 2020, p. 105. DOI: 10.3204/PUBDB-2020-05067. URL: https://bib-pubdb1.desy.de/record/453231.

[124] G. Golovin et al. "Intrinsic beam emittance of laser-accelerated electrons measured by x-ray spectroscopic imaging." In: *Scientific Reports* 6.1 (Apr. 2016), p. 24622. ISSN: 2045-2322. DOI: 10.1038/srep24622. URL: https://doi.org/10.1038/srep24622.

[125] C. A. Lindstrøm and M. Thévenet. "Emittance preservation in advanced accelerators." In: *Journal of Instrumentation* 17.05 (May 2022), P05016. DOI: 10.1088/1748-0221/17/05/p05016. URL: https://doi.org/10.1088%2F1748-0221%2F17%2F05%2Fp05016.

[126] Martin Reiser. *Theory and design of charged particle beams; Second, updated and expanded edition*. Weinheim: Wiley-VCH Verlag, 2008, XXVII, 647 pages : illustrations. ISBN: 9783527407415. DOI: 10.1002/9783527622047. URL: https://bib-pubdb1.desy.de/record/371845.

[127] F. J. Grüner et al. "Space-charge effects in ultrahigh current electron bunches generated by laser-plasma accelerators." In: *Phys. Rev. ST Accel. Beams* 12 (Feb. 2009), p. 020701. DOI: 10.1103/PhysRevSTAB.12.020701. URL: https://link.aps.org/doi/10.1103/PhysRevSTAB.12.020701.

[128] Karlheinz Schindl. "Space charge." In: (2006). DOI: 10.5170/CERN-2006-002.305. URL: https://cds.cern.ch/record/941316.

[129] Floettmann, Klaus. "ASTRA: A Space Charge Tracking Algorithm." In: (2017). URL: https://www.desy.de/~mpyflo/.

[130] C. A. Lindstrøm and E. Adli. "Design of general apochromatic drift-quadrupole beam lines." In: *Phys. Rev. Accel. Beams* 19 (July 2016), p. 071002. DOI: 10.1103/PhysRevAccelBeams.19.071002. URL: https://link.aps.org/doi/10.1103/PhysRevAccelBeams.19.071002.

[131] Carl A. Lindstrøm. "Staging of plasma-wakefield accelerators." In: *Phys. Rev. Accel. Beams* 24 (Jan. 2021), p. 014801. DOI: 10.1103/PhysRevAccelBeams.24.014801. URL: https://link.aps.org/doi/10.1103/PhysRevAccelBeams.24.014801.

[132] N. Kirby et al. "Emittance growth from Multiple Coulomb Scattering in a plasma wakefield accelerator." In: *2007 IEEE Particle Accelerator Conference (PAC)*. 2007, pp. 3097–3099. DOI: 10.1109/PAC.2007.4440680.

[133] Bryan W. Montague. "Emittance growth from multiple scattering in the plasma beat-wave accelerator." In: (Dec. 1984). DOI: 10.5170/CERN-1985-007.208. URL: http://cds.cern.ch/record/625633.

[134] C. B. Schroeder, E. Esarey, C. Benedetti, and W. P. Leemans. "Control of focusing forces and emittances in plasma-based accelerators using near-hollow plasma channels." In: *Physics of Plasmas* 20.8 (2013), p. 080701. DOI: 10.1063/1.4817799. URL: https://doi.org/10.1063/1.4817799.

[135] Jonas Björklund Svensson. "Direct measurements of emittance growth from Coulomb scattering on neutral gas atoms in a plasma lens." In: 20th Advanced Accelerator Concepts Workshop, Hauppauge (New York), 6 Nov 2022 - 11 Nov 2022. Nov. 2022. URL: https://indico.classe.cornell.edu/event/2108/contributions/2051/.

[136] Carl A. Lindstrøm and Erik Adli. *Analytic plasma wakefield limits for active plasma lenses*. 2018. DOI: 10.48550/ARXIV.1802.02750. URL: https://arxiv.org/abs/1802.02750.

[137] Carl Andreas Lindstrøm. "Emittance growth and preservation in a plasma-based linear collider." PhD thesis. Oslo U., 2019.

[138] N. A. Bobrova et al. "Simulations of a hydrogen-filled capillary discharge waveguide." In: *Phys. Rev. E* 65 (Dec. 2001), p. 016407. DOI: 10.1103/PhysRevE.65.016407. URL: https://link.aps.org/doi/10.1103/PhysRevE.65.016407.

[139] J. van Tilborg et al. "Nonuniform discharge currents in active plasma lenses." In: *Phys. Rev. Accel. Beams* 20 (Mar. 2017), p. 032803. DOI: 10.1103/PhysRevAccelBeams.20.032803. URL: https://link.aps.org/doi/10.1103/PhysRevAccelBeams.20.032803.

[140] B. H. P. Broks, K. Garloff, and J. J. A. M. van der Mullen. "Nonlocal-thermal-equilibrium model of a pulsed capillary discharge waveguide." In: *Phys. Rev. E* 71 (Jan. 2005), p. 016401. DOI: 10.1103/PhysRevE.71.016401. URL: https://link.aps.org/doi/10.1103/PhysRevE.71.016401.

[141] Gregory Boyle et al. "Electron temperature relaxation and emittance conservation in active plasma lenses." In: 60th Annual Meeting of the APS Division of Plasma Physics, Portland (Oregon), 5 Nov 2018 - 9 Nov 2018. Nov. 2018. DOI: 10.3204/PUBDB-2018-04761. URL: https://bib-pubdb1.desy.de/record/416287.

[142] Wim Leemans. "Limits and Possibilities of Laser Wakefield Accelerators." In: *7th International Particle Accelerator Conference*. 2016, MOYBA01. DOI: 10.18429/JACoW-IPAC2016-MOYBA01.

[143] M. J. V. Streeter and Z. Najmudin. "Compton recoil effects in staging of laser wakefield accelerators." In: *Phys. Rev. Accel. Beams* 23 (July 2020), p. 071602. DOI: 10.1103/PhysRevAccelBeams.23.071602. URL: https://link.aps.org/doi/10.1103/PhysRevAccelBeams.23.071602.

[144] Borland, M. "elegant: A Flexible SDDS-Compliant Code for Accelerator Simulation." In: (2000).

[145] Lars Goldberg. "Laser-Based Discharge Ignition for Capillary Waveguides." MS. Hamburg: Universität Hamburg, 2013.

[146] Alan Dower Blumlein. *Improvements in or relating to apparatus for generating electrical impulses*. Patent GB589127A, 1947.

[147] Romanelli John. *Pulse forming network*. U.S. Patent 2904706, 1958.

[148] Niels Matthias Delbos. "High Repetition Rate Laser-Plasma Accelerator: 5 Hz Electron Beam Generation and Advanced Target Design." en. Universität Hamburg, 2017.

[149] Zhirong Huang, Yuantao Ding, and Carl B. Schroeder. "Compact X-ray Free-Electron Laser from a Laser-Plasma Accelerator Using a Transverse-Gradient Undulator." In: *Phys. Rev. Lett.* 109 (Nov. 2012), p. 204801. DOI: 10.1103/PhysRevLett.109.204801. URL: https://link.aps.org/doi/10.1103/PhysRevLett.109.204801.

[150] Christopher M. S. Sears et al. "Emittance and divergence of laser wakefield accelerated electrons." In: *Phys. Rev. ST Accel. Beams* 13 (Sept. 2010), p. 092803. DOI: 10.1103/PhysRevSTAB.13.092803. URL: https://link.aps.org/doi/10.1103/PhysRevSTAB.13.092803.

[151] A. Cianchi et al. "Challenges in plasma and laser wakefield accelerated beams diagnostic." In: *Nuclear Instruments and Methods in Physics Research Section A: Accelerators, Spectrometers, Detectors and Associated Equipment* 720 (2013). Selected papers from the 2nd International Conference Frontiers in Diagnostic Technologies (ICFDT2), pp. 153–156. ISSN: 0168-9002. DOI: https://doi.org/10.1016/j.nima.2012.12.012. URL: https://www.sciencedirect.com/science/article/pii/S0168900212015458.

[152] G. R. Plateau et al. "Low-Emittance Electron Bunches from a Laser-Plasma Accelerator Measured using Single-Shot X-Ray Spectroscopy." In: *Phys. Rev. Lett.* 109 (Aug. 2012), p. 064802. DOI: 10.1103/PhysRevLett.109.064802. URL: https://link.aps.org/doi/10.1103/PhysRevLett.109.064802.

[153] S. Kneip et al. "Characterization of transverse beam emittance of electrons from a laser-plasma wakefield accelerator in the bubble regime using betatron x-ray radiation." In: *Phys. Rev. ST Accel. Beams* 15 (Feb. 2012), p. 021302. DOI: 10.1103/PhysRevSTAB.15.021302. URL: https://link.aps.org/doi/10.1103/PhysRevSTAB.15.021302.

[154] Paul Viktor Winkler. "Emittance Measurements at Laser-Wakefield Accelerators." Dissertation, University of Hamburg, 2019. Dissertation. University of Hamburg, 2020, p. 145. URL: https://bib-pubdb1.desy.de/record/437970.

[155] S. K. Barber et al. "Measured Emittance Dependence on the Injection Method in Laser Plasma Accelerators." In: *Phys. Rev. Lett.* 119 (Sept. 2017), p. 104801. DOI: 10.1103/PhysRevLett.119.104801. URL: https://link.aps.org/doi/10.1103/PhysRevLett.119.104801.

[156] S. K. Barber et al. "Parametric emittance measurements of electron beams produced by a laser plasma accelerator." In: *Plasma Physics and Controlled Fusion* 60.5 (2018), p. 054015. URL: http://stacks.iop.org/0741-3335/60/i=5/a=054015.

[157] R. Ariniello et al. "Transverse beam dynamics in a plasma density ramp." In: *Phys. Rev. Accel. Beams* 22 (Apr. 2019), p. 041304. DOI: 10.1103/PhysRevAccelBeams.22.041304. URL: https://link.aps.org/doi/10.1103/PhysRevAccelBeams.22.041304.

[158] Yujian Zhao et al. "Emittance preservation through density ramp matching sections in a plasma wakefield accelerator." In: *Phys. Rev. Accel. Beams* 23 (Jan. 2020), p. 011302. DOI: 10.1103/PhysRevAccelBeams.23.011302. URL: https://link.aps.org/doi/10.1103/PhysRevAccelBeams.23.011302.

[159] S. Corde et al. "Multi-gigaelectronvolt acceleration of positrons in a self-loaded plasma wakefield." In: *Nature* 524.7566 (Aug. 2015), pp. 442–445. ISSN: 1476-4687. DOI: 10.1038/nature14890. URL: https://doi.org/10.1038/nature14890.

[160] Nivedh Manohar et al. "High-sensitivity imaging and quantification of intratumoral distributions of gold nanoparticles using a benchtop x-ray fluorescence imaging system." In: *Opt. Lett.* 44.21 (Nov. 2019), pp. 5314–5317. DOI: 10.1364/OL.44.005314. URL: http://opg.optica.org/ol/abstract.cfm?URI=ol-44-21-5314.

[161] S. J. Riederer and C. A. Mistretta. "Selective iodine imaging using K-edge energies in computerized x-ray tomography." In: *Medical Physics* 4.6 (1977), pp. 474–481. DOI: https://doi.org/10.1118/1.594357. URL: https://aapm.onlinelibrary.wiley.com/doi/abs/10.1118/1.594357.

[162] A. Sarnelli et al. "K-edge digital subtraction imaging with dichromatic x-ray sources: SNR and dose studies." English. In: *Physics in Medicine and Biology* 51.17 (Sept. 2006), pp. 4311–4328. ISSN: 0031-9155. DOI: 10.1088/0031-9155/51/17/012.

[163] Theresa Karoline Brümmer. "Design Study of a Laser-Driven X-ray Source for Medical Fluorescence Imaging." Dissertation, Universität Hamburg, 2017. Dissertation. Hamburg: Universität Hamburg, 2018, p. 171. DOI: 10.3204/PUBDB-2018-01857. URL: https://bib-pubdb1.desy.de/record/402600.

[164] S G Rykovanov et al. "Quasi-monoenergetic femtosecond photon sources from Thomson Scattering using laser plasma accelerators and plasma channels." In: *Journal of Physics B: Atomic, Molecular and Optical Physics* 47.23 (Nov. 2014), p. 234013. DOI: 10.1088/0953-4075/47/23/234013. URL: https://doi.org/10.1088/0953-4075/47/23/234013.

[165] J. Krämer et al. "Making spectral shape measurements in inverse Compton scattering a tool for advanced diagnostic applications." In: *Scientific Reports* 8 (Jan. 2018). DOI: 10.1038/s41598-018-19546-0.

[166] Eric Esarey, Sally K. Ride, and Phillip Sprangle. "Nonlinear Thomson scattering of intense laser pulses from beams and plasmas." In: *Phys. Rev. E* 48 (Oct. 1993), pp. 3003–3021. DOI: 10.1103/PhysRevE.48.3003. URL: https://link.aps.org/doi/10.1103/PhysRevE.48.3003.

[167] Sally K. Ride, Eric Esarey, and Michael Baine. "Thomson scattering of intense lasers from electron beams at arbitrary interaction angles." In: *Phys. Rev. E* 52 (Nov. 1995), pp. 5425–5442. DOI: 10.1103/PhysRevE.52.5425. URL: https://link.aps.org/doi/10.1103/PhysRevE.52.5425.

[168] C. Maroli, Vittoria Petrillo, Paolo Tomassini, and L. Serafini. "Nonlinear effects in Thomson backscattering." In: *Physical Review Special Topics Accelerators and Beams* 16 (Mar. 2013), pp. 30706–. DOI: 10.1103/PhysRevSTAB.16.030706.

[169] M. Chen et al. "Modeling classical and quantum radiation from laser-plasma accelerators." In: *Phys. Rev. ST Accel. Beams* 16 (Mar. 2013), p. 030701. DOI: 10.1103/PhysRevSTAB.16.030701. URL: https://link.aps.org/doi/10.1103/PhysRevSTAB.16.030701.

[170] Marcel Ruijter, Vittoria Petrillo, and Matt Zepf. "Decreasing the bandwidth of linear and nonlinear Thomson scattering radiation for electron bunches with a finite energy spread." In: *Phys. Rev. Accel. Beams* 24 (Feb. 2021), p. 020702. DOI: 10.1103/PhysRevAccelBeams.24.020702. URL: https://link.aps.org/doi/10.1103/PhysRevAccelBeams.24.020702.

[171] S. G. Rykovanov et al. "Controlling the spectral shape of nonlinear Thomson scattering with proper laser chirping." In: *Phys. Rev. Accel. Beams* 19 (Mar. 2016), p. 030701. DOI: 10.1103/PhysRevAccelBeams.19.030701. URL: https://link.aps.org/doi/10.1103/PhysRevAccelBeams.19.030701.

[172] Isaac Ghebregziabher, B. A. Shadwick, and Donald Umstadter. "Spectral bandwidth reduction of Thomson scattered light by pulse chirping." In: *Phys. Rev. ST Accel. Beams* 16 (Mar. 2013), p. 030705. DOI: 10.1103/PhysRevSTAB.16.030705. URL: https://link.aps.org/doi/10.1103/PhysRevSTAB.16.030705.

[173] A. Debus. "Brilliant radiation sources by laser-plasma accelerators and optical undulators." PhD thesis. 2012.

[174] A. D. Debus et al. "Traveling-wave Thomson scattering and optical undulators for high-yield EUV and X-ray sources." In: *Applied Physics B* 100.1 (July 2010), pp. 61–76. ISSN: 1432-0649. DOI: 10.1007/s00340-010-3990-1. URL: https://doi.org/10.1007/s00340-010-3990-1.

[175] Klaus Steiniger et al. "Optical free-electron lasers with Traveling-Wave Thomson-Scattering." In: *Journal of Physics B: Atomic, Molecular and Optical Physics* 47.23 (Nov. 2014), p. 234011. DOI: 10.1088/0953-4075/47/23/234011. URL: https://doi.org/10.1088/0953-4075/47/23/234011.

[176] Klaus Steiniger et al. "Building an Optical Free-Electron Laser in the Traveling-Wave Thomson-Scattering Geometry." In: *Frontiers in Physics* 6 (2019). ISSN: 2296-424X. DOI: 10.3389/fphy.2018.00155. URL: https://www.frontiersin.org/articles/10.3389/fphy.2018.00155.

[177] C. G. Durfee and H. M. Milchberg. "Light pipe for high intensity laser pulses." In: *Phys. Rev. Lett.* 71 (Oct. 1993), pp. 2409–2412. DOI: 10.1103/PhysRevLett.71.2409. URL: https://link.aps.org/doi/10.1103/PhysRevLett.71.2409.

[178] I.V. Pogorelsky, I. Ben-Zvi, X.J. Wang, and T. Hirose. "Femtosecond laser synchrotron sources based on Compton scattering in plasma channels." In: *Nuclear Instruments and Methods in Physics Research Section A: Accelerators, Spectrometers, Detectors and Associated Equipment* 455.1 (2000). Proceedings of the Int. Symp. on New Visions in Laser-Beam, pp. 176–180. ISSN: 0168-9002. DOI: https://doi.org/10.1016/S0168-9002(00)00727-0. URL: https://www.sciencedirect.com/science/article/pii/S0168900200007270.

[179] D. J. Corvan et al. "Optical measurement of the temporal delay between two ultra-short and focussed laser pluses." In: *Opt. Express* 24.3 (Feb. 2016), pp. 3127–3136. DOI: 10.1364/OE.24.003127. URL: https://opg.optica.org/oe/abstract.cfm?URI=oe-24-3-3127.

[180] M. C. Veale, P. Seller, M. Wilson, and E. Liotti. "HEXITEC: A High-Energy X-ray Spectroscopic Imaging Detector for Synchrotron Applications." In: *Synchrotron Radiation News* 31.6 (2018), pp. 28–32. DOI: 10.1080/08940886.2018.1528431. URL: https://doi.org/10.1080/08940886.2018.1528431.

[181] Gopal B. Saha. "Scintillation and Semiconductor Detectors." In: *Physics and Radiobiology of Nuclear Medicine*. New York, NY: Springer New York, 2006, pp. 81–107. ISBN: 978-0-387-36281-6. DOI: 10.1007/978-0-387-36281-6_8. URL: https://doi.org/10.1007/978-0-387-36281-6_8.

[182] W.T. Elam, B.D. Ravel, and J.R. Sieber. "A new atomic database for X-ray spectroscopic calculations." In: *Radiation Physics and Chemistry* 63.2 (2002), pp. 121–128. ISSN: 0969-806X. DOI: https://doi.org/10.1016/S0969-806X(01)00227-4. URL: https://www.sciencedirect.com/science/article/pii/S0969806X01002274.

[183] S. Agostinelli et al. "Geant4 — a simulation toolkit." In: *Nuclear Instruments and Methods in Physics Research Section A: Accelerators, Spectrometers, Detectors and Associated Equipment* 506.3 (2003), pp. 250–303. ISSN: 0168-9002. DOI: https://doi.org/10.1016/S0168-9002(03)01368-8. URL: https://www.sciencedirect.com/science/article/pii/S0168900203013688.

[184] J. Allison et al. "Geant4 developments and applications." In: *IEEE Transactions on Nuclear Science* 53.1 (2006), pp. 270–278. DOI: 10.1109/TNS.2006.869826.

[185] J. Allison et al. "Recent developments in Geant4." In: *Nuclear Instruments and Methods in Physics Research Section A: Accelerators, Spectrometers, Detectors and Associated Equipment* 835 (2016), pp. 186–225. ISSN: 0168-9002. DOI: https://doi.org/10.1016/j.nima.2016.06.125. URL: https://www.sciencedirect.com/science/article/pii/S0168900216306957.

[186] Theresa Staufer. *All Geant4 simulations were set up and performed by Theresa Staufer*.

[187] A Ferran Pousa, R Assmann, and A Martinez de la Ossa. "Wake-T: a fast particle tracking code for plasma-based accelerators." In: *Journal of Physics: Conference Series* 1350.1 (Nov. 2019), p. 012056. DOI: 10.1088/1742-6596/1350/1/012056. URL: https://dx.doi.org/10.1088/1742-6596/1350/1/012056.

[188] Igor Andriyash. *Synchrotron Radiation calculator via openCL*. https://github.com/hightower8083/synchrad. 2022.

[189] Maxence Thévenet and Kristjan Poder. *The pipline for Inverse Compton Scattering simulations was set up by Maxence Thévenet and Kristjan Poder*.

[190] FBPIC contributors. *FBPIC algorithm features*. 2016. URL: https://fbpic.github.io/overview/pic_algorithm.html (visited on 10/27/2022).

[191] L. T. Dickson et al. "Mechanisms to control laser-plasma coupling in laser wakefield electron acceleration." In: *Phys. Rev. Accel. Beams* 25 (Oct. 2022), p. 101301. DOI: 10.1103/PhysRevAccelBeams.25.101301. URL: https://link.aps.org/doi/10.1103/PhysRevAccelBeams.25.101301.

[192] Xin Xue, Haiqing Wei, and Andrew G. Kirk. "Intensity-based modal decomposition of optical beams in terms of Hermite–Gaussian functions." In: *J. Opt. Soc. Am. A* 17.6 (June 2000), pp. 1086–1091. DOI: 10.1364/JOSAA.17.001086. URL: https://opg.optica.org/josaa/abstract.cfm?URI=josaa-17-6-1086.

[193] John David Jackson. *Classical electrodynamics*. 3rd ed. New York, NY: Wiley, 1999. ISBN: 9780471309321. URL: http://cdsweb.cern.ch/record/490457.

[194] S. Chen et al. "MeV-Energy X Rays from Inverse Compton Scattering with Laser-Wakefield Accelerated Electrons." In: *Phys. Rev. Lett.* 110 (15 Apr. 2013), p. 155003. DOI: 10.1103/PhysRevLett.110.155003. URL: https://link.aps.org/doi/10.1103/PhysRevLett.110.155003.

[195] Simon Bohlen. "Detection of Inverse Compton Scattering in Plasma Wakefield Experiments." Masterarbeit. Hamburg: Universität Hamburg, 2016, p. 112. DOI: 10.3204/PUBDB-2016-05732. URL: https://bib-pubdb1.desy.de/record/315263.

[196] Z. Mianowska et al. "The light response of CsI:Tl crystal after interaction with gamma radiation study using analysis of single scintillation pulses and digital oscilloscope readout." In: *Nuclear Instruments and Methods in Physics Research Section A: Accelerators, Spectrometers, Detectors and Associated Equipment* 1031 (2022), p. 166600. ISSN: 0168-9002. DOI: https://doi.org/10.1016/j.nima.2022.166600. URL: https://www.sciencedirect.com/science/article/pii/S0168900222001693.

[197] G. Golovin et al. "Tunable monoenergetic electron beams from independently controllable laser-wakefield acceleration and injection." In: *Phys. Rev. ST Accel. Beams* 18 (1 Jan. 2015), p. 011301. DOI: 10.1103/PhysRevSTAB.18.011301. URL: https://link.aps.org/doi/10.1103/PhysRevSTAB.18.011301.

[198] Henrik Ekerfelt et al. "A tunable electron beam source using trapping of electrons in a density down-ramp in laser wakefield acceleration." In: *Scientific Reports* 7.1 (Sept. 2017), p. 12229. ISSN: 2045-2322. DOI: 10.1038/s41598-017-12560-8. URL: https://doi.org/10.1038/s41598-017-12560-8.

[199] Robin L. Owen, James M. Holton, Clemens Schulze-Briese, and Elspeth F. Garman. "Determination of X-ray flux using silicon pin diodes." In: *Journal of Synchrotron Radiation* 16.2 (Mar. 2009), pp. 143–151. DOI: 10.1107/S0909049508040429. URL: https://doi.org/10.1107/S0909049508040429.

[200] S. C. Lee, H. B. Jeon, K. H. Kang, and H. Park. "Study of silicon PIN diode responses to low energy gamma-rays." In: *Journal of the Korean Physical Society* 69.10 (Nov. 2016), pp. 1587–1590. ISSN: 1976-8524. DOI: 10.3938/jkps.69.1587. URL: https://doi.org/10.3938/jkps.69.1587.

[201] Sebastian Faas, Daniel J. Foerster, Rudolf Weber, and Thomas Graf. "Determination of the thermally induced focal shift of processing optics for ultrafast lasers with average powers of up to 525 W." In: *Opt. Express* 26.20 (Oct. 2018), pp. 26020–26029. DOI: 10.1364/OE.26.026020. URL: https://opg.optica.org/oe/abstract.cfm?URI=oe-26-20-26020.

[202] Wim Leemans. “KALDERA - High average power laser plasma accelerator project at DESY.” In: 4th European Advanced Accelerator Concepts Workshop. Sept. 2019.

ACKNOWLEDGEMENTS

This thesis is the outcome of not just my scientific work but also a result of the support and impact of the people I worked with.
First and foremost, I want to express my deepest gratitude to my supervisor, **Jens Osterhoff**, for his continuous support, insight, and patience over the last four years and earlier. I would also like to thank **Wolfgang Hillert** for his interest in my research and for agreeing to be the second supervisor of my thesis.
These acknowledgements would be incomplete without sincerely thanking **Kris**, **Simon**, and **Theresa** for their valuable contributions to the experiments. They helped and supported me from the moment I walked into the lab until I completed my thesis. Many thanks to **Jon** and **Lucas** for their contributions and helpful advice.
I gratefully acknowledge the assistance of **Kai**, **Andrej**, **Amir**, and **Frank**, who always helped with all technical issues, including designing and building new components and maintaining the infrastructure in our laboratories. Many thanks to **Sven** and **Sandra** for numerous server revivals and camera installations, to **Vladimir** for fixing the DAQ, and to **Maik** for his work on the laser system to ensure that our experiments could be carried out.
I would like to extend my thanks to everyone in **FLA** and **MPA** for providing a great work atmosphere and always being willing to help where they can.
I would also like to thank **Desmond** and **Simon** for proof-reading my thesis.
Last but not least, I am thankful for the precious support of my **family** and **friends**. Thanks to my sister **Nathalie** for encouraging me on since I was little and walking up the path in front of me. I am sincerely grateful to my parents, **Christian** and **Ursula**, for their unconditional love and constant support.

EIDESSTATTLICHE VERSICHERUNG / DECLARATION OF OATH

Hiermit versichere ich an Eides statt, die vorliegende Dissertationsschrift selbst verfasst und keine anderen als die angegebenen Hilfsmittel und Quellen benutzt zu haben.

Die eingereichte schriftliche Fassung entspricht der auf dem elektronischen Speichermedium.

Die Dissertation wurde in der vorgelegten oder einer ähnlichen Form nicht schon einmal in einem früheren Promotionsverfahren angenommen oder als ungenügend beurteilt.

Hamburg, 09. Februar 2023

Martin Meisel